Ministry of Environment
of Denmark
Environmental
Protection Agency

Ancient Root Macropores and Fractures in Glacial till and Their Contribution to Pesticide Vulnerability of Groundwater in Low and High-ground Agricultural Landscape

PESTPORE2

Pesticide Research
no 207

February 2022

Publisher: The Danish Environmental Protection Agency

Authors:
Peter R. Jørgensen, PJ-Bluetech ApS
Paul Henning Krogh, Aarhus University
Jiayi Qin, Aarhus University
Luca Modesti, PJ-Bluetech ApS
Ida Broman Nielsen, University of Copenhagen
Frederik Seersholm, University of Copenhagen
Natascha Wagner, Georg-August-University of Göttingen
Anders Johannes Hansen, University of Copenhagen
Jesper Olsen, Aarhus University
Bjarne Strobel, University of Copenhagen
Søren Hansen, University of Copenhagen
Jacob Gudbjerg, University of Copenhagen
Carsten T. Petersen, University of Copenhagen
Marine Lacoste, INRA
Isabelle Cousin, INRA
Evelyn Keaveney, Quenn´s Univerity Belfast
Gerard Barrett, Quenn´s Univerity Belfast

ISBN: 978-87-7038-376-9

The Danish Environmental Protection Agency publishes reports and papers about research and development projects within the environmental sector, financed by the Agency. The content of this publication do not necessarily represent the official views of the Danish Environmental Protection Agency. By publishing this report, the Danish Environmental Protection Agency expresses that the content represents an important contribution to the related discourse on Danish environmental policy.

Sources must be acknowledged

Contents

Preface

This study was carried out in the period 2016 - 2020 by PJ-Bluetech ApS (project leader) in collaboration with University of Copenhagen (Globe Institute, Section for Geogenetics; and Department of Plant and Environmental Sciences); Aarhus University (Department of Ecoscience, Department of Physics and Astronomy, and Department of Environmental Science); Albrecht-Haller-Institute for Plant Sciences Georg-August-University of Göttingen, Germany; INRA, Orleans, France; and Quenn´s Univerity Belfast, Engineering and Physical Sciences. The study was funded by the Danish Ministry of Environment's Research Program for Pesticides (MST no. 667-00106).

The project work was followed by a steering and review committee with the participants:

- Ph.D. Henrik F. Brødsgaard, Danish Environmental Protection Agency, (Chairman)
- Ph.D. Anne Louise Gimsing, Danish Agriculture & Food
- Ph.D. Philip Grinder Pedersen, Danish Environmental Protection Agency
- Ph.D. Steen Marcher, Danish Environmental Protection Agency
- Professor Merete Styczen, Dept. of Plant and Environmental Sciences, University of Copenhagen
- Department Head Niels Lindemark, Danish Plant Protection
- Advisor Walter Brüsch, Danish Society for Nature Conservation
- Senior scientist Vibeke Ernstsen, The National Geological Survey for Denmark and Greenland, GEUS
- Professor Poul L. Bjerg, Dept. of Water and Environmental Technology, DTU
- Professor Hans Chr. Bruun Hansen, Department of Plant and Environmental Sciences, University of Copenhagen
- Professor Carsten Suhr Jacobsen, Environmental Science, Aarhus University.

The project group wishes to thank Merete Styczen (Department of Plant and Environmental Sciences, University of Copenhagen), Philip Grinder Pedersen and Jakob Lanstorp (Danish Environmental Agency), Klaus Mosthaf (Danish Technical University, DTU), and Anne Louise Gimsing (Danish Agriculture & Food) for reviewing and providing suggestions for improvement of the report. We would further like to thank Carsten Suhr Jacobsen for advising about G2 DNA/RNA Enhancer for aDNA extractions, cand. silv. Svend J. Christensen and cand. silv. Karsten Raae for identification of live tree species in the study sites, and cand. scient. Jesper Bruhn Nielsen for providing aerial photos of the study area. Finally, we wish to thank owners Niels Eskildsen (Salløv site) and Anne Thea Preytz (Bulbro site) for allowing field work and excavations on their properties.

Summary and Conclusions

This study investigates pesticide vulnerability of groundwater in glacial clayey till due to subsoil preferential flow (from approximately 1 m depth below ground surface) in a high and low-ground agricultural landscape near Havdrup, Sjælland.

The investigation adds to a series of previous studies across Denmark (including the predecessor PESTPORE project by Jørgensen et al. 2017) in which groundwater flow in fractures and root channels were investigated as separate flow paths. These studies suggests that potentially very deep root channels, presumably from pre-historic trees, greatly dominate preferential flow and control pesticide vulnerability in surficial aquitards, while the influence of fractures as flow paths was minor or absent because they were largely closed from shallow depths. This challenges the recognized perception among groundwater scientists that rapid flow in fractures determines pesticide vulnerability of groundwater in the glacial till aquifers underneath the tills.

In this study, we explored the new findings by using a field-scale approach to investigate the natural groundwater vulnerability in the moraine landscape. This integrates multi-disciplinary studies, which include geological and hydrogeological mapping, flow and dye-tracer field experiments, geochemical and mineralogical analyzes, X-ray tomography, radiocarbon dating and stable isotopes, eDNA and aDNA sequencing and groundwater modeling.

The investigation provides three major results:

- Fossil roots and root channels from widespread pre-historic native forest were found locally to more than 6 m depth and were shown to control rapid preferential flow and pesticide vulnerability of shallow-groundwater.
- Fractures were largely closed below 1-2 m depth, unless they were enlarged by root channels inside the fractures.
- Underneath maximum rooting depths the dominant role to flow and pesticide vulnerability was not fractures, but embedded sand layers, sand lenses, sand pockets and other sedimentary heterogeneity in the tills.

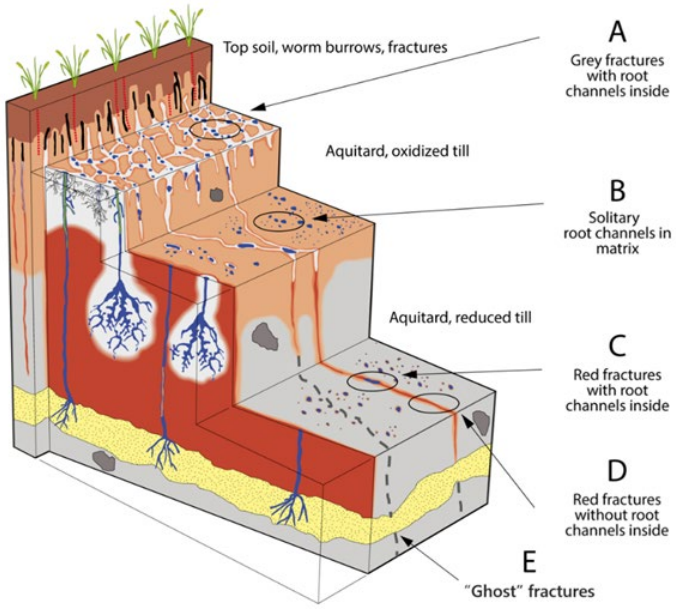

Conceptual diagram showing subsoil macropore flow paths (blue) in glacial clayey till.

Fractures, relic root channels and sand lenses

In the high-ground site of the study (Salløv, 42-45 MSL), we carried out three 4-6 m deep excavations in which the clayey tills were oxidized and intensively weathered to > 8 m depth and contained high frequencies of naturally stained, prominent fractures and deep relic macropores from roots. The root channels were found locally throughout the depth of the excavated profiles.

Field mapping and X-ray tomography revealed that the subsoil root channels and isolated voids in the tills had diameters between 1-10 mm, which were overall decreasing with depth below the soil surface. In the upper 3-3.5 m, the fractures and root channels had grey rims (grey fractures) due to reductive dissolution of Fe/Mn-oxides (A in block diagram), and below this depth they were reddish (red fractures) due to reprecipitation of the dissolved Fe/Mn-oxides leached from above (C and D in block diagram). This vertical sequence resembles the typical appearance of fractures, which are found widespread in clayey tills. The root channel macropores occurred locally to at least 6 m depth, however, were masked by occurring mainly inside the fractures, in which they formed dense patterns of macropore flow channels (see block diagram). The observed depths of the root channels in the high-ground site (ca. 3 hectares) followed, to some degree, the maximum seasonal decline of the groundwater table in the clay, which varied between 1.5 and > 8 m depth across the site. This behavior of the root channels corroborates observations in the previous PESTPORE study (Jørgensen et al. 2017) and descriptions in the literature.

The Fe/Mn-oxide staining and filling of fractures were observed locally to more than 8 m in till samples from wells next to the excavations. The time required to precipitate the observed amount of Fe/Mn-oxides in the fractures and root channels was estimated to more than 2,000 years, based on geochemical mass balance calculations and Fe- concentrations in the infiltration. This dated the root channels inside the fractures to be likely many thousand years old.

Another three excavations were carried out in the low-ground Bulbro site (ca. 1.5 hectare area, 25-28 MSL), in which the grey and red staining of the fractures occurred to only 1.5-2 m depth due to permanent high groundwater table. Those were the only visible fracture type, while deep non-visible tectonic fractures (“ghost-fractures”) were identified from the shapes and patterns of deep fossil roots that penetrated along those fractures (E in block diagram).

The fossil tree-roots and related relic root channels had diameters from 1 to 18 mm and were found abundantly across the entire Bulbro site locally to 3.2 m depth. In a previous study they were found to 5 m depth at Marebæk about 1.5 km further south in the low ground area. In both of the low-ground sites, the channels penetrated several meters below the groundwater table into unweathered (grey) till, in which they connected with randomly embedded sand lenses or sand layers of various thickness and spatial orientation. Those layers and sand pockets (together hereafter referred to as sand lenses) together with other sedimenary heterogeneity were abundant in the tills across the entire high and low-ground study area and were intercepted by the root channels and fractures both in the high and low-ground excavations.

Thus, while the depth of the root channels in the high-ground to some degree followed the current maximum seasonal decline of the ground water table, this was not the case in the low-ground, where the ancient roots consistently targeted saturated sand lenses underneath the groundwater table. This difference was suggested by the aDNA analyses to be due to the tree species, which had dominated pre-historically in the respective landscape positions.

Origin of fossil roots and relic root channels

Radiocarbon dating and aDNA sequencing of the fossil roots in the low-ground revealed that they dated 2,900 to 7,200 years BP and originated from *Alnus glutinosa* (Common alder, in Danish “Rødel”). The main habitat of *A. glutinosa* is low-ground moist locations, but it occurs in

both low and high-ground landscapes. It was one of the four most abundant trees in the native forest, which covered most of Denmark during mid-Holocene climatic optimum from roughly 7,000 to 3,000 years BP. *A. glutinosa* possess an extensive root system of both surface and deep branches (which was confirmed by the study) and is the only tree species in Denmark to have roots significantly below-groundwater tables. As already mentioned, in the Bulbro site the fossil roots and open channels extended several meters below-groundwater tables to 2.5-3.2 m depth, and similar root channels, presumably also from *A. glutinosa,* occurred several m below the groundwater table in the Marebæk site, both places in unoxidized tills.

We found no recognizable fossil roots in the high-ground Salløv-site, which was presumably due to the deep intensive weathering and oxidation (governed by the high elevation in the landscape) combined with probably early clearing of the pre-historic forest. However, we found aDNA from the Salix subgroup Chamaetia/Vetrix (Willow family) in Fe/Mn filled root channels and adjacent matrix in reduced pockets of the clayey till in 5-6 m depth. The S. chamaetia/vetrix subgroup includes the species *Salix caprea* (Seljepil), *Salix cinerea* (Gråpil) and *Salix myrsinifolia (Sort pil)* together with shrubs from colder climates, which could not be distinguished due to small differences in the genome and age-related extensive damage of the DNA. The 3 species of willow tress pioneered the open landscape in early post glacial time 11,000-10,000 years BP. It was not possible to accurately radiocarbon date the *Salix sp.* aDNA due to weathering and heterogeneity of the organic carbon in the soil materials. However, an origin of the aDNA and channels from the native forest was indicated by (i) complete absence of recent radiocarbon in the root channel organo-mineral fillings, (ii) age-related extreme damage of the identified *Salix sp.* aDNA and (iii) the estimated age of more than 2,000 years for the precipitated Fe/Mn-oxides in the channels.

Knowledge about rooting depths of trees in Danish soils is sparse beyond the current findings of relic root channels in this and the previous related studies. It is, however, well known that rooting is highly variable for different tree species and some have enormous plasticity in response to environment and local hydrological conditions. Until more information becomes available, local rooting depth to about 9 m depth are expected to be realistic, based on random observations reported in the literature and the observed depth of the relic root channels in the current study.

Hydrologic role of relic root channels, fractures, and sand lenses

We conducted a total of 12 dye tracer infiltration experiments in the excavations. In the high-ground, the dye tracer infiltration revealed that potentially very rapid vertical preferential flow (> 20 m/day in the experiments) was controlled by worm burrows and root channels (https://mst.dk/media/210348/pestpore2video1.mp4) in the upper 1.5 m and by the relic root channels to 3-3.5 m depth. As mentioned, the majority of the root channels were concealed as macropore flow paths inside grey fractures, which were only open flow channels in the upper 3.5 m of the till aquitard (https://mst.dk/media/210350/pestpore2video2.mp4). Below 3-3.5 m depth, the root channels and fractures were clogged with the precipitated Fe/Mn-oxides (red fractures), which made them both largely inactive as preferential flow paths. This created a sharp hydrological barrier in the till, which reduced vertical hydraulic conductivity several orders of magnitude and thereby created perched groundwater conditions in the till aquitard. The integrity of the barrier was locally disrupted by the random sand lenses with excessive vertical discharge. This caused shifting between perched and leaky aquitard condtions across the high ground field with permanent high and local decline of the water tables in summer to more than 8 m depth. Consequently, the vertical groundwater recharge and supposedly groundwater vulnerability changed within short range across the field. Similar clogging of deep fractures and root channels was shown to have developed in the other 9 sites that have been investigated in the previous related studies, which suggests that similar local hydrological barriers may cause reduced vertical flow and vulnerability in many clayey tills.

In the low-ground Bulbro site, rapid preferential flow occurred widespread in the abundant root channels and fossil roots. In the upper 1-1.5 m depth, the root channels sometimes occurred inside grey fractures, while below this depth the root channels with active flow occurred mostly in the solid matrix and had no internal precipitation of Fe/Mn oxides due to permanent shallow groundwater tables. Due to the moister conditions, activation of the root channels as preferential flow paths was more likely to occur rain storms in summer than in the high-ground places with deep groundwater tables where possible surplus of precipitation would become absorbed by the less moist matrix. Consequently, pesticide groundwater risks due to rain storms in summer were likely higher in the low ground area.

As mentioned, underneath the visible fractures we also identified “ghost fractures”. We found no evidence of active flow along the “ghost-fractures” in the dye tracer experiments in this or the previous field studies. The deep root channels alone controlled flow through the till into local sand lenses and layers several meters below the groundwater table, which was in agreement with the previous nearby low-ground experiments in the Marebæk site, in which more than 90 % of groundwater recharge and migration of mobile pesticides were controlled by open root channels into a sand layer in 5-6 m depth. The lack of Fe/Mn clogging of the deep root channels in both low-ground sites (as opposed to the observed clogging of root channels in high-ground) suggested that ground water vulnerability due to deep root channel macropore flow was generally higher in the low-ground than in high-ground. However, this apparent pattern was contradicted by the previous high-ground PESTPORE study (Jørgensen et al. 2017), which exhibited rapid preferential flow and pesticide transport to similar depths through unrestricted root channels. This suggests that there is no simple correlation between the landscape elevation and occurrence of open or closed root channels, which is apparently controlled by multiple factors that are currently unclear.

The observed occurrence of deep root channels from *A. Glutinosa* and *Salix sp.* that originated from the ancient native forest, suggest that similar deep macropore root channel systems occur widely in moraine landscapes. This was supported by the series of previous related studies, in which rapid preferential flow and pesticide migration in deep residual root channels were abundant. Consequently, particularly groundwater risks to pesticide pollution may be anticipated in areas where the thickness of clay layers above aquifers is smaller than the ancient rooting depths.

The brilliant blue (BB) infiltration experiments revealed that deep fractures, which were not enlarged by internal root channels, had very small hydraulic apertures (< 10 µm). Those apertures were in the same range as the apertures, which has been determined for fractures without root channels inside in the previous 9 clayey till sites mentioned above. This provides growing evidence that fractures below maximum depth of historical rooting from trees, contributes only marginally to bulk flow in the tills in comparison with heterogeneities of the clay matrix and embedded sand lenses.

We tested this evidence by using the aperture data determined for the fractures without internal root channels (apertures = 5-14 µm) to re-evaluate older studies in which fractures were concluded, on the basis of indirect hydrogeological observations, to be major flow paths in unweathered clayey till aquitards. The re-evaluation indicated that the small fracture apertures would only account for a minor portion of the hydraulic conductivities (from 10^{-8} - 10^{-5} m/s) in the aquitards. This disagree with the perception that fractures are causing the observed several orders of magnitude higher hydraulic conductivities of the bulk aquitards than that of the unfractured clay matrix material of the aquitards. Instead, the result suggests that embedded sand lenses and other common geological heterogeneities in the tills were most likely the major control of flow in the aquitards.

Groundwater vulnerability

We evaluated the vulnerability of groundwater to mobile non-degradable pesticides underneath clayey till aquitards by model simulation of pesticide fluxes into the groundwater (pesticide mass/m^2/year) under water saturated conditions. The models were rigorously calibrated to simulate the observed pesticide transport in field and lab experiments with natural fractures and root channel macropores from this and the previous series of related studies, including the "Clayfrac" study by Aamand et al. (in prep. 2020). The simulations showed that the greatest pesticide vulnerability of groundwater occurred underneath till aquitards with fully penetrating root channels, while for aquitards thicker than rooting depths, the vulnerability was greatest underneath those with the highest vertical hydraulic conductivity. In those tills with a hydraulic conductivity above 10^{-8} m/s, the influence of pesticide transport in the fractures (assuming the small fractures without internal root channels) was negligible because the pesticide flux from the fractures were obliterated by the pesticide fluxes from other flow paths required to simulate the high hydraulic conductivities of those tills. As previously mentioned, within the upper 1-8 m depth of the tills with unsaturated conditions, the study suggests that pesticide vulnerability by activation of the root channels as macropore flow paths by rain storms in summer would likely be higher in the low-ground due to moister clay matrix near the soil surface than in the high-ground.

Perspectives

The study emphasizes that flow and pesticide migration in the clayey tills is very heterogenous, random and variable within the scale of individual farmed fields in the landscape. In the current study area, the lithological heterogeneity was high, despite the fact that the dominant till type was lodgement till, which is considered the least heterogenous of common till types in Denmark. This implies that groundwater underneath clayey tills should in general be considered vulnerable to pesticide pollution. Thus, leached pesticides from topsoils, which are not strongly adsorbed and very slowly degraded in the subsoil environment, should be expected to eventually migrate with the groundwater flow into underlying aquifers (except in areas with upward groundwater flow).

The study implies that particular high vulnerability will occur in areas with the following subsoil characteristics or combination of characteristics:

- *Areas with clay thicknesses of less than approximately 10 m.* These layers are shallower than the expected maximum depths of root channels. Actual maximum depths of the relic root channels in landscapes are unknown, and it is unclear under which conditions the channels are closed or remain open as active deep flow paths. Further research is needed in order to clarify this.

- *Low-ground areas near well-heads with intensive water abstraction*. These are indicated to have abundant deep root channels from ancient forest that may provide rapid flow and pesticide transport directly into the anaerobic groundwater zone. Moreover, pesticide risk and vulnerability due to root channel macropore flow being activated by rain storms in summer is enhanced due to typically higher soil moisture content above groundwater tables than in many high-ground sites. The groundwater vulnerability is suggested to be further enhanced by intense water abstraction from underlying aquifers. Further research is required to investigate the importance of these aspects to the groundwater vulnerability.

- *Areas with high vertical hydraulic conductivity and/or recharge in the tills underneath maximum current and historical rooting depths.* Modeling studies indicate that groundwater vulnerability (expressed as pesticide fluxes into aquifers) will vary orders of magnitude as a function of the distribution of aquifer recharge and redox conditions as a consequence of flow in vertically connected sand layers or vertical fractures, even if the aquitard thickness in catchments is relatively constant (Blessent et al., 2014; Cherry et al. 2006; Jørgensen et al., 2004c). This

vulnerability is anticipated to further increase in areas where hydraulic pressure heads in underlying aquifers have been lowered significantly by intensive water abstraction. Hence, differences in aquitard thickness and amount of groundwater recharge in combination are suggested to represent useful key parameters for pointing out areas with overall contrasting groundwater vulnerability. This approach has been utilized with promising results in previous studies (Jørgensen et al. 2003b; Miljøstyrelsen, 2002, 2005.

The distribution of aquitard thickness and aquifer recharge has been mapped in many clayey till areas in the national groundwater mapping using geological/geophysical mapping and catchment water balance modeling (Miljøstyrelsen 2020). The investigation suggests that these existing data may be utilized or further improved to point out overall clayey till areas with particular aquifer vulnerability to pesticide pollution. Such an approach will be limited by the absence of information on the very local scale variability of aquitard hydraulic conductivity and vulnerability shown in the current study. There are currently no large-scale field methods or maps available to identify such places. More research and development are required in order to provide this.

Sammenfatning og konklusion

Dette projekt omhandler grundvandsstrømning i makroporer og sprækker i moræneler under ca. 1 mu.t og betydningen af disse for grundvandets sårbarheden over for pesticidforurening. Projekteret er udført ved Roskilde i et hhv. topografisk højt- og lavtliggende bundmoræneland-skab med landbrugsdrift. Betegnelsen ”lavtliggende” (”low-ground” i rapporten) dækker topografisk lavtliggende landskab i bred forstand i forhold til det omkringliggende landskab og dermed ikke kun egentlige lavbundsjorde. Projektet føjer sig til en række tidligere undersøgelser inklusiv projektet PESTPORE (Jørgensen et al. 2017), hvor sprækker og rodkanaler i moræneler er undersøgt som særskilte strømningsveje i lerlagene. Disse undersøgelser har vist, at relikte rodkanaler kan gå ned til mindst 5-6 mu.t. og fungere som præferentielle strømningsveje bl.a. for hurtig pesticidnedsivning, mens sprækker fra 1-2 mu.t. i de undersøgte moræner kun har haft ringe eller ingen betydning fordi de var tilnærmelsesvis lukkede.

Dette sætter spørgsmålstegn ved den udbredte opfattelse, at strømning i sprækker er den afgørende hydrologiske faktor for sårbarheden af grundvand under moræneler, hvorfor der næsten udelukkende har været fokus på disse i hydrogeologisk forskning og udpegning af grundvandssårbarhed i moræneler. I dette projekt er de nye resultater undersøgt nærmere i et morænelandskab vha. en multidisiplinær tilgang med geologisk og hydrogeologisk kortlægning, flow- og tracerforsøg, geokemiske og mineralogiske analyser, røntgentomografi, kulstof-14-datering og stabile isotoper, eDNA- og aDNA-sekventering og grundvandsmodellering.

Undersøgelsen har givet følgende tre hovedresultater:

- Rodkanaler fra forhistorisk skov kontrollerede hurtig præferentiel strømning og pesticidsårbarhed af grundvandet ned til mindst 3-6 mu.t.
- Sprækker lukkede til med dybden i takt med stigende jordtryk, og at de rodkanaler, der fandtes i sprækkerne, forsvandt eller var tilstoppet med Fe/Mn udfældninger. Under den maximale roddybde havde sprækkerne ringe eller ingen betydning for grundvandsstrømningen og pesticidudvaskningen i sammenligning med andre strømningsveje i moræneleren.
- Undersøgelsen indikerer, at de vigtigste strømningsveje til det dybere grundvand under rodkanalerne ikke er sprækker, men indlejrede sandlinser, sandlag, sandlommer og andre typer sedimentær heterogenitet i morænerne.

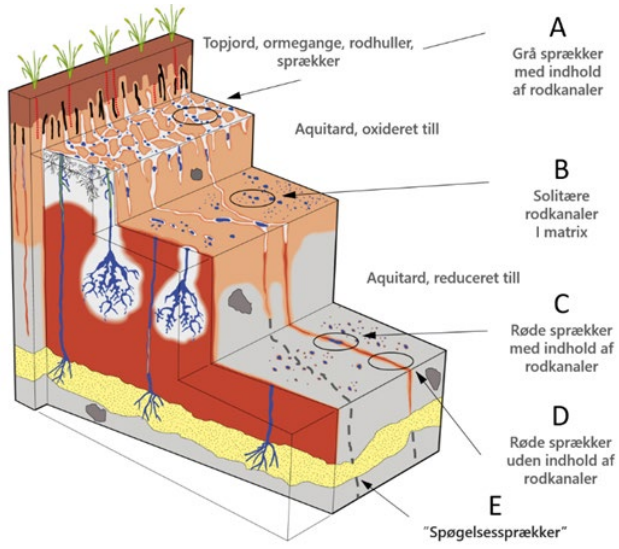

Konceptuelt diagram der viser hurtige makropore strømningsveje (blå) i moræneler.

Sprækker, relikte rodkanaler of sandlinser

På undersøgelsens topografisk højt beliggende område (Salløv i 42-45 moh) udførtes tre 4-6 m dybe udgravninger fordelt på ca. 3 ha. I alle udgravningerne var moræneleren oxideret og intensivt forvitret og havde høj frekvens af dybe tektoniske sprækker og makroporer efter orme og dybe rødder (bioporer). Hyppigheden af sprækkerne og bioporene svarede til den generelle forekomst i moræneler (se blokdiagram).

Bioporene havde diametre fra 1-10 mm i øverste 1-1.5 m (https://mst.dk/media/210347/pestpore2video3.mp4) og faldt herunder til 1-2 mm for de dybe rodkanaler. I de øverste 3-3.5 m havde sprækkerne og rodkanalerne grå rande, som var dannet ved reduktiv opløsning (pseudogley-proces) af lerets indhold af sekundære Fe/Mn-oxider (”A” i blokdiagram). Under de grå sprækker var sprækkerne og rodkanalerne rustfarvede (røde sprækker) og helt eller delvist udfyldte med genudfældede Fe/Mn-oxider fra de grå sprækker ovenover i profilen (”C” og ”D” i blokdiagram). De fleste rodkanaler var ikke umiddelbart synlige, fordi de fandtes inde i sprækkerne, hvori de dannede tætte mønstre af strømningsaktive makroporer i de grå sprækker, mens de var næsten lukkede i de røde sprækker pga. Fe/Mn udfældningerne (blokdiagram). Ud fra geokemiske massebalanceberegning af omfordeling af Fe langs sprækker og rodkanaler samt grundvandets indhold af totalt Fe (jern) blev det estimeret, at opbygningen af Fe-indholdet i de røde sprækker og rodkanaler har taget mere end 2.000 år, der således indikerer en minimumsalder af de udfyldte rodkanaler i sprækkerne.

Dybden af rodkanalerne varierede fra 3 mu.t. til > 6 mu.t. (max. dybde af udgravningerne) i udgravningerne. Endvidere blev der i boringer udført ved siden af udgravningerne observeret rustfarvede sprækker og dermed potentielt rodkanaler lokalt ned til mindst 8 mu.t. Dybden af rodkanalerne fulgte til en vis grad årsvariationen af grundvandsspejlets dybde i morænen (1.5 m til > 8 mu.t. på udgravningsstederne). Da grundvandsspejlets dybde var styret af grundvandsinfiltrationen i morænen (dvs. den vertikale hydrauliske ledningsevne), faldt de største roddybder sammen den største lokal grundvandsdannelse og grundvandssårbarhed, som igen var kontrolleret af tilstedeværelsen af vandførende sandlinser, sandlag og sandlommer (herefter kaldet sandlinser) samt texturel grovere lermatrix i morænen. De indlejrede sandlinser forekom hyppigt og tilfældigt fordelt i morænen i hele projektområdet og var stedvis skråtstillede pga. glacialtektoniske forstyrrelser.

Der blev udført yderligere 3 udgravninger på projektets topografisk lavtliggende Bulbro-lokalitet på et ca. 1.5 ha stort område beliggende 25-28 moh. Pga. relativt stabilt højtliggende grundvand i dette område var synlige tektoniske sprækker kun udviklet ned til 1.5-2 mu.t., som overfladiske grå og rustfarvede sprækker. Herunder forekom der ikke synlige sprækker, men der blev indentificeret såkaldte usynlige "spøgelsessprækker", ud fra mønstret og formen af fossile rødder, der var trængt ned langs disse i moræne (”E” i blokdiagram).

De fossile rødder og rodkanaler havde meget høj frekvens, men heterogen fordeling på Bulbro-lokaliteten med diametre op til 2 cm i de øverste 1.8-2 mu.t. Herfra udgik tyndere dybe rødder og rodkanaler lokalt til 3.2 mu.t. med diameter på 1-4 mm. Tilsvarende rodkanaler ned til 5 mu.t. er fundet tidligere ved Marebæk ca. 1.5 km længere mod syd i samme lavtliggende område.

Mens dybden af rodkanalerne som nævnt overvejende fulgte det dybeste sæsonbetingede grundvandsspejl på den højtliggende Salløv lokalitet, var dette ikke tilfældet i det lavtliggende område med Bulbro- og Marebæk- lokaliteterne. På begge de sidstnævnte var rodkanalerne trængt 1-2 meter ned under det lavtliggende grundvandsspejl og dannede hydraulisk kontakt til lokale sandlinser i det underliggende grå lavpermeable moræneler med primært anaerobe forhold (blokdiagram). Undersøgelsens kulstof-14 og aDNA bestemmelser af rødderne og ka-

nalerne indikerer, at forskellen i rodnedtrængningen under grundvandspejlet mellem det topografisk højt- og lavtliggende område kan relateres til træarternes habitatområder i det forhistoriske landskab (se nedenfor).

Oprindelse og forekomst af fossile rødder og rodkanaler

Kulstof-14-dateringen og aDNA-sekventeringen af de fossile rødder fra de 3 udgravninger Bulbro-lokaliteten viste, at de var 2.900 til 7.200 år gamle og alle stammede fra Rødel (*Alnus glutinosa)*. Rødel har et omfattende rodsystem af både overfladenære og dybe rødder (hvilket blev bekræftet af undersøgelsen) og er den eneste træart i Danmark med rødder, der vokser under grundvandsspejlet, hvilket svarer til den fundne forekomst flere meter under grundvandsspejlet i Bulbro og Marebæk. Rødel var blandt de mest udbredte træarter i egeblandingsskoven, der har dækket det meste af Danmark for 7.000 til 3.000 år siden. Hovedhabitaten for Rødel er fugtige, og dermed særligt lavtliggende områder, men Rødel forekom også på højtliggende områder med udbredte vandlidende forhold før kunstig dræning. Dermed må relikte rodkanaler efter Rødel forventes generelt udbredt i moræneler i hele Danmark, men særligt i lavtliggende landskabsområder.

Vi fandt ingen fossile rødder bevaret på Salløv-lokaliteten og intet aDNA fra planter i den oxiderede zone af morænen. Dette skyldtes antageligt den intensive forvitring og oxidation som følge af den høje landskabsbeliggenhed samt formentlig tidlig rydning af den oprindelige skov i området. Vi fandt dog aDNA fra Salix-familien *Chamaetia/Vetrix* (Piletræ familien) i forbindelse med rodkanaler i lommer af reduceret moræneler i 5-6 mu.t. *S. chamaetia/vetrix* inkluderer arterne Seljepil (*S. caprea*), Gråpil (*S. cinerea*) og Sortpil (*S. myrsinifolia*) sammen med arter af pilekrat fra koldere klimaer. Disse kunne ikke skelnes på grund af små forskelle i genomet og udtalte aldersrelaterede skader på DNA'et. De tre piletræ-arter bredte sig i det åbne landskab efter istiden allerede for 11.000-10.000 år siden. Det var ikke muligt nøjagtigt at datere fundene af *Salix sp.* aDNA' et på grund af forvitringen og heterogenitet af det organiske kulstof i morænematerialet, men der blev indikeret en meget gammel oprindelse af rodkanalerne ud fra (i) fravær af ungt kulstof-14, (ii) estimerede alder på over 2.000 år af Fe/Mn udfyldningerne i rodkanalerne samt (iii), ekstrem beskadigelse af DNA' et pga. aldersbetinget nedbrydning.

Ud over de aktuelle fund af fossile rødder og relikte rodkanaler til 5-6 mu.t. er viden om roddybder fra træer generel og, i dansk jord i særdeleshed, meget sparsom og usikker. Undersøgelser af træers rodnet har tidligere primært haft fokus på rødderne i den øverste ca. 0.5 m. Nyere undersøgelser viser, at trærødder kan gå meget dybere, end man hidtil har troet, og der er eksempler på meget dybe rødder hos træarter beslægtet med de danske, herunder Eg og Elm. Den foreliggende viden viser, at træers roddybde er meget variabel afhængig af træart, og at rodsystemer har ekstrem tilpasningsevne i forhold til jordmiljø og lokal hydrologiske forhold. I canadiske undersøgelser har man tilfældige fund af levende rødder i moræneler ned til 9 mu.t. Indtil der fremkommer mere information om roddybder for danske forhold, må tilsvarende roddybder forventes realistiske i Dansk moræneler.

Grundvandsstrømning i rodkanaler, sprækker og sandlinser

Vi udførte samlet 12 infiltrationsforsøg med farvetraceren "Brilliant Blue" i udgravningerne. I både det højt-og lavtliggende område blev der målt meget hurtig præferentiel strømning (hastigheder > 20 m/dag) i rodkanalerne i sprækkerne og rodkanaler der fandtes i matrixen ned til 3-3,5 mu.t. ("B" i blokdiagram og https://mst.dk/media/210349/pestpore2video4.mp4). Dette svarer til tidligere laboratorieforsøg med sprækker fra 8 andre morænelokaliteter, der havde hydrauliske sprækkeaperturer på 40 - > 100 µm pga. interne rodkanaler i sprækkerne og dermed et stort potentiale for meget hurtig strømning og transport af mobile pesticider.

Omvendt blev der i infiltrationsforsøgene bestemt meget små sprækkeaperturer på 3-6 µm for de dybere røde sprækker udfyldt med Fe/Mn-oxider uden rodkanaler, og 10 µm for sprækker med rodkanaler helt eller delvis var udfyldt med Fe/Mn-oxider. Disse aperturer svarer til de

aperturer der blev målt for sprækker uden rodkanaler på de nævnte 9 andre lokaliteter. Da strømningen i sprækkerne afhænger af sprækkeaperturen i 3. potens, betyder de små aperturer, at der er meget lille strømning i sprækkerne uden indhold af rodkanaler og et tilsvarende lille potentiale for strømning og pesticidtransport pga. sprækker under max. roddybde.

For yderligere at teste denne evidens anvendte vi de små sprækkeaperturer for sprækkerne uden indhold af rodkanaler (sprækkeaperturer = 5-14 µm) til at revurdere ældre undersøgelser, hvor høje hydrauliske ledningsevner (Ksat = 10^{-8}- 10^{-5} m/s) i uforvitrede morænelag, er tolket som værende resultat af sprækkestrømning. Beregninger med de nye sprækkedata viste at disse kun kunne forklare en lille del af strømningen i lerlagene. Dette modsiger, at de observerede høje hydrauliske ledningsevner skulle være forårsaget af sprækkestrømning. I stedet er det formentlig indlejrede sandlinser og anden sedimentær heterogenitet i morænematerialet, der er den primære årsag til høje hydrauliske ledningsevner (dvs. Ksat > 10^{-8} m/s) i lerlagene, når de findes under maximal roddybde. Betydningen af disse grovere indslag som strømningsveje støttes af flere nye og ældre undersøgelser.

På den højtliggende Salløv lokalitet bevirkede udfyldningen af de røde sprækker med Fe/Mn-oxider og deraf følgende små sprækkeaperturer (3-10 µm), at der omkring 3-3.5 mu.t. skete et brat fald på flere størrelsesordner af morænelagets hydrauliske ledningsevne til de samme værdier som det usprækkede ler. Dette fald skabte en hydrologisk barriere, som dannede lokale hængende grundvandsspejl øverst i morænen, hvorfra der var minimal nedsivning til underliggende grundvand. Dette kom til udtryk ved, at der var et meget begrænset fald i grundvandsspejlet fra vinter- til sommersæson. Den hydrologiske barriere var afbrudt af afstrømning i tilfældige skråstillede sandlinser, som ved en af udgravningerne bevirkede mere end 8 m afsænkning af grundvandsspejlet i løbet af sommersæsonen. Målingerne viser dermed, at den vertikale afstrømning gennem morænen (og dermed sårbarheden) varierede betydeligt over korte afstande på det undersøgte markareal, hvilket også er påvist i tidligere undersøgelser bl.a. på den nærliggende Marebæk lokalitet.

Mens rodkanalernes dybde i nogen grad fulgte grundvandsspejlet maximale dybde i morænen på Salløv lokaliteten, fortsatte de fossile rodkanaler fra Elletræerne som åbne makroporer under grundvandspejlet på lavtliggende Bulbro, hvor der skete meget hurtig strømning direkte ned i lokale sandlinser til 1-2 meter under grundvandsspejlet.

Vi fandt ingen tegn på strømning i de dybere spøgelsessprækker, hvilket er i overensstemmelse med tidligere tracerforsøg i Flakkebjerg (PESTPORE projektet) og Marebæk, hvor tilsvarende spøgelsessprækker også blev identificeret uden tegn på aktiv strømning.

Grundvandssårbarhed over for pesticider

Vi evaluerede grundvandets sårbarhed overfor mobile pesticider, der ikke nedbrydes under øverste meter i det geologiske profil, ved at modelsimulere pesticidfluxen gennem et vandmættet heterogent lerlag indeholdende sprækker med og uden indhold af rodkanaler. Modellerne blev sat op med de hydrauliske data for sprækker og lermatrix i denne og rækken af tidligere undersøgelser, hvor der foreligger samtidige målinger af pesticidtransport og direkte strømningsbestemmelser i sprækker og bioporer. Herved blev modellerne kalibreret, så de beregnede den konkret målte sammenhæng mellem strømning og pesticidtransport i disse undersøgelser og eksperimenter.

Modelsimuleringerne viste, at grundvandets sårbarhed over for pesticiderne (udtryk som størrelsen af pesticidmassen, der transporteres ned i grundvandet i µg/m^2/år) var markant størst under lerlag med fuld gennemtrængning af rodkanaler. Under rodkanalerne var grundvandsårbarheden størst i lerlag med de højeste Ksat værdier (hydraulisk ledningsevne). I disse lerlag var indflydelsen af pesticidtransporten i sprækkerne (sprækker uden indhold af rodkanaler) uden betydning, hvis lerlagets Ksat værdi var over ca. 10^{-8} m/s, fordi pesticidbidraget fra

sprækkerne blev overskygget af pesticidbidraget (µg/m^2/år) igennem de andre strømningsveje, dvs. i indlejrede sandlinser og texturel heterogen lermatrix. Tidligere forskning har vist, at pesticidtransport i forstnævnte i nogle tilfælde kan have lige så stor effekt på pesticidsårbarheden som strømning i store åbne sprækker.

Endeligt betyder typisk højere jordfugtighed i sommersæsonen på lavtliggende end højtliggende terræn, at der på førstnævnte antageligt ofte er større risiko for aktivering af makroporestrømning i topjord og umættet zone og dermed pesticidudvaskning i forbindelse med kraftige regnbyger og ekstremregn om sommeren.

Perspektiver

Undersøgelsen understreger, at muligheden for pesticidtransport ned i grundvandet er yderst heterogent og tilfældigt fordelt selv inden for den enkelte mark i landskabet, selvom morænen består af bundmoræne, der regnes for en af de mindst sedimentært heterogene blandt de almindelige danske morænetyper. Dette betyder, at grundvandsressourcen under moræneler generelt må betragtes som sårbar over for pesticidforurening i den forstand, at pesticider, der udvaskes fra topjorden og ikke bindes eller nedbrydes i den underliggende moræne, med tiden vil transporteres med grundvandets strømning til underliggende grundvandsmagasiner (bortset fra i områder med opadrettet grundvandstrømning).

Undersøgelsen peger på, at der vil være særlig stor sårbarhed (potentiale for særlig stor masseflux af pesticider til grundvandsmagasiner under lerlagene) i områder med følgende egenskaber eller kombination af egenskaber i morænerne under topjorden:

- *Områder med lertykkelser der er mindre end ca.10 m.* Disse lag er tyndere end den forventede maksimale dybde af bevarede rodkanaler fra forhistorisk skov. Den maksimale dybde af de relikte rodkanaler og dennes fordeling i landskabet er ukendt, og det er uklart, under hvilke forhold rodkanalerne er lukkede eller bevaret som åbne dybe strømningsveje. Yderligere forskning er nødvendig for at kunne afklare dette.

- *Lavtliggende områder særligt nær større kildepladser med intensiv grundvandindvinding.* De lavtliggende områder har med overvejende sandsynlighed en udbredt forekomst af rodkanaler fra bl.a. forhistoriske Elletræer (Rødel), der kan danne dybe åbne rodkanaler med potentielt hurtig strømning og pesticidtransport til under grundvandsspejlet. Desuden vil der antageligt mange steder være en forøget pesticidudvaskningsrisiko på grund af makroporestrømning i umættet zone i sommersæsonen, der i højere grad end i højtliggende terræn aktiveres af regnbyger og ekstremregn. Det antages, at nedadrettet strømning, og dermed sårbarheden, endvidere kan forstærkes af intens vandindvinding af underliggende grundvand. Yderligere forskning vil være påkrævet for at undersøge betydningen af disse sårbarhedsaspekter, og om de er tilstrækkeligt repræsenteret i varslingen af pesticidudvaskning.

- *Områder med høj vertikal hydraulisk ledningsevne og/eller stor grundvandsdannelse i lerlag under maksimal historisk roddybde*. Modelstudier baseret på felt- og laboratorieforsøg har vist, at grundvandssårbarheden (udtrykt som den vertikale pesticidflux til grundvandsmagasiner) varierer flere størrelsesordener som funktion af grundvandsdannelsens størrelse og redoxforhold ved strømning i forbundne sandlinser og/eller sprækker (Blessent et al., 2014; Cherry et al., 2006; Jørgensen et al., 2004c). Disse viser dermed, at forskelle i lerlagstykkelser og størrelsen af grundvandsdannelse i kombination vil være nyttige nøgleparametre til udpegning af kontrasterende grundvandssårbarhed. Dette approach er anvendt med lovende resultater i tidligere undersøgelser af grundvandssårbarhed under moræneler (Jørgensen et al., 2003b; Miljøstyrelsen 2002, 2005) og understøttes yderligere af dokumentationen i den nærværende undersøgelse.

Fordelingen af lerlagstykkelser og grundvandsdannelse i grundvandsmagasiner er kortlagt i mange morænelersområder i den nationale grundvandskortlægning ved hjælp af geologisk/geofysisk kortlægning og vandbalancemodellering (Miljøstyrelsen, 2020). Disse data vil formentlig kunne udnyttes eller udbygges yderligere til en overordnet udpegning af morænelersområder med særligt sårbart grundvand over for pesticidforurening. En sådan tilgang vil være begrænset af manglende data om sårbarhedens variation inden for markskala, der er vist at være betydelig i den aktuelle undersøgelse. Mere forskning og udvikling er påkrævet for at kunne opskalere kortlægningen af denne lokal sårbarhed til oplandsskala.

1. Introduction

Groundwater in Denmark has become widely polluted with residues of pesticides and biocides, which deteriorates drinking water resources. This is a general problem across Denmark, however, is particularly widespread in aquifers underneath geological layers of glacial clayey till (so-called aquitards) in which approximately 30% of water abstraction wells are polluted (GEUS, 2019). Some of the pesticides and biocides are leached from farmland, others originate from urban and industrial areas.

It is well documented that pesticide leaching from farmland can occur rapidly along large biogenic macropores, such as worm burrows and root channels in the clayey soils (e.g., Jensen et al., 1999; Hansen et al., 2012a,b; Petersen et al., 2013; Jørgensen et al., 2017). Rosenbom (2005) and Jørgensen et al. (2017) showed that surficial worm burrows and root channels may connect with underlying fractures, which are widely recognized as major preferential flow paths in clayey till subsoils. The fractures occur abundantly as surficial bleached (grey) and deeper Fe/Mn-oxide stained (red) structures to about 10 m depth and occasionally more in the tills. Jørgensen and Fredericia (1992), and Jørgensen et al. (2004a,b, 2017) showed that the bleaching of the grey surficial fractures was determined by degradation of root residuals and associated with root channels inside the fractures. Moreover, non-visible fractures (so-called ghost fractures) were suggested to provide widely spaced active preferential flow paths, which may control groundwater vulnerability to even greater depth (Cherry, 1989; Harrison et al., 1992; Cherry et al. 2006).

The recognition of fractures as major flow paths in the glacial tills was established 3-4 decades ago from field studies using indirect hydrogeological observations such as hydraulic head responses to pumping and deep migration of bomb tritium in aquitards. Those were supported by observations of widespread prominent fractures and water dripping from fractures in excavations (e.g., Cherry, 1989; Fredericia, 1990; Jørgensen, 1990; Ruland et al., 1991; Jørgensen and Fredericia, 1992; Cherry et al., 2006). Based on those observations it was concluded that fractures were the most likely explanation to common occurrences of several orders of magnitude higher hydraulic conductivities of the till aquitards than of the unfractured diamicton clay material of the aquitards (e.g., Cherry et al., 2006). Beside the fractures, subsoil relic root channels together with sand layers, sand lenses, micro sand layers, and sand pockets (hereafter collectively termed sand lenses) were also observed in the tills in many of the original studies (e.g., Cherry et al., 1989; Ruland et al., 1991), however, those were not considered to be of significant importance as flow paths below the upper few meters of the aquitards (e.g., Cherry et al., 1989; McKay and Fredericia, 1995).

Following those studies, McKay et al. (1993a,b, 1999); Sidle et al. (1998); and Harrar et al. (2007) carried out various field hydraulic and tracer infiltration experiments. In all of those experiments they observed rapid preferential transport of the tracers in the subsoil, which was attributed to flow in fractures. However, the flow paths in the tills were not investigated with dye tracers, and consequently, the actual type of preferential flow paths, including possible flow in root channels along fractures, were not documented. Additional field experiments by Rosenbom et al. (2008) used infiltration of dye tracers to documented rapid preferential flow along deep fractures, however, the possible influence of root channels as flow paths inside the fractures below soil depths, was not investigated.

In order to quantify and study the flow processes in the tills in greater detail, Jørgensen et al. (1993, 1998, 2019) developed the LUC method (large undisturbed column method). By this

method flow and transport of contaminants in fractures and macropores can be investigated directly under well-defined experimental conditions that includes effective soil stress.

The LUC studies questioned fractures being the major flow paths in the tills as they are supposed to be, based on the early field studies. Instead, the LUC studies revealed that excessive flow in the fractures was controlled by root channels located inside the fractures, while the fractures themselves were nearly or entirely closed from shallow depth in the investigated tills that included 10 sites across Denmark (e.g., Jørgensen et al., 2002a, 2004a,b; Butzbach, 2007: Jørgensen et al., 2016a; Aamand et in prep., 2020.; Jørgensen et al. in prep., 2020).

The LUC results were supported by field studies in which subsoil flow paths including root channels inside fractures were investigated by infiltration of dye tracers followed by excavation of the experimental fields and the inside of the fractures (e.g., Jørgensen et al., 2002a, and the previous PESTPORE study by Jørgensen et al., 2017). By combining LUC with dye tracer techniques in the field experiments by Jørgensen et al. (2002a), it was estimated that 91% of total vertical groundwater flow through the clayey till aquitard into a local aquifer in 5-6 m depth was controlled by relic root channels (presumable from trees) localized inside fractures that connected with the aquifer (Figure 1). Flow and pesticide transport in the abundant prominent fractures without root channel inside, however, were nearly closed, had no connected aperture channels, and played a very minor role to the observed bulk flow and pesticide transport in the experiment.

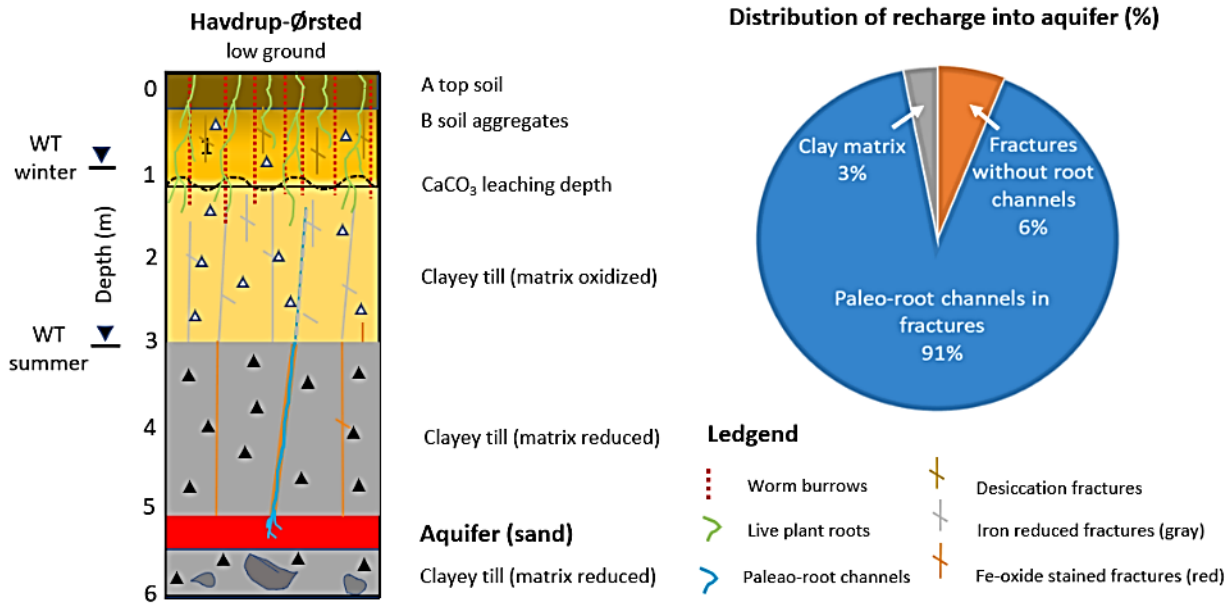

FIGURE 1. Groundwater flow and recharge through glacial till into a local sand aquifer in Marebæk near the current study sites (Figure 2). The diagram to the right shows the distribution of total vertical flow (ground water recharge) into the aquifer as percentages between fractures, fossil root channels along fractures and clay matrix in the glacial till (from Jørgensen et al., 1998a, 2002a).

Consistent results with those experiments were obtained in the PESTPORE study by Jørgensen et al. (2017) in which an experimental arable field was sprayed with various pesticides and

infiltration was monitored over 18 months before a dye tracer was infiltrated, and the experimental field was excavated. In this study, rapid preferential flow and migration of mobile pesticides in the clayey till occurred within few hours to few days along relic root channels extending to 4-6 m depth, when the experimental field was exposed to heavy rain in autumn after spraying. Also, in this study, groundwater flow, dye tracer, and pesticide transport were absent in the deep fractures without distinct root channels inside.

As mentioned, the occurrence of relic root channels, presumably from trees, in subsoil glacial tills is well known (e.g., Cherry, 1989; Ruland et al., 1991; Jørgensen and Fredericia, 1992; McKay and Fredericia, 1995; Klint and Gravesen, 1999; Cherry et al., 2006). Specific knowledge about deep rooting of trees is, however, sparse and uncertain due to small attention having been paid to the deep portion of tree root systems in past research (Canadell et al., 1996). Rooting is, however, known to be highly variable for different tree species, some of which have great ability to adapt to local environment and hydrological conditions, which further complicates collecting representative data (e.g., Fan et al., 2017; Xi et al., 2018). Jackson et al. (1999) recorded ecosystem rooting to greater depth than 5 m for at least six tree species, and to 22 m for Texas live Oak (*Q. fusiformis)* in limestones caves in Texas, US. Among the few random observations of deep roots in glacial tills, Ruland et al. (1991) reported live roots in 9 m depth in a Canadian till. Similar rooting depths may be expected possibly also in Danish glacial tills based on the previous finding of residual root channels to more than 5-6 m depth in the studies of e.g., Jørgensen et al. (2002a,b, 2017).

Objectives and hypothesis

In this study we explore the new findings by taking a multidisciplinary approach to natural groundwater vulnerability in the till landscape, which include geological and hydrogeological mapping, flow and dye-tracer field experiments, geochemical and mineralogical analyzes, X-ray tomography, radiocarbon dating and stable isotopes, eDNA and aDNA sequencing and groundwater modeling.

The overall objective of the study is to improve documentation of subsoil root channels and their role as ground water flow paths relative to other flow paths in high and low-ground agricultural landscapes. Specific objectives are to:

1. Investigate the occurrence and characterize worm burrows, root channels and fractures by field and laboratory methods (field mapping, X-ray tomography (XRT) and geochemical/mineralogical analyses).
2. Investigate water flow in various subsoil root channels and fracture types using dye tracer infiltration experiments. Special attention is given to the possibility of water flow in non-visible vertical extensions of chemically stained fractures (ghost fractures).
3. Determine the age and origin of worm burrows and deep root channels using ^{14}C, $\delta^{13}C$, eDNA and aDNA methods.
4. Investigate the influence of weathering/chemical diagenetic processes on flow capacity in deep root channels and fractures.
5. Evaluate flow and pesticide transport by using numerical modeling based on the project data and data from LUC experiments.

Hypotheses of the study are:

1. Subsoil root channels in the glacial tills originate mainly from pre-historic forest and may therefore be expected to occur widely in moraine landscapes.
2. Root channels dominate deep (> 3-6 m) preferential flow in naturally well drained areas (high-ground), while they are absent or very shallow features in originally moist areas (low-ground) that are now well drained arable land.
3. Ground water is more vulnerable in high-ground terrains than in low-ground due to the deeper relic root channels from prehistoric forest.
4. Fractures without root channels inside are, in general, minor contributors to groundwater flow in the subsoil of the glacial tills below the upper 1-2 m in the landscape.

Study area

Figure 2a shows the study sites and study area which is dominated by low-ground moraine plain to the south (near to the town of Havdrup), and high-ground moraine hills to the north. The study sites of the investigation are the Salløv and Bulbro sites, while the Marebæk site has previously been investigated by Jørgensen (1990); Jørgensen and Fredericia (1992); Jørgensen and Spliid (1998a,c); Hildebrandt (2000); Rivad et al. (2001); Jørgensen et al, (2002a,b, 2003a, 2004c); Stenemo et al. 2005; Regionernes Videnscenter (2008). The Salløv and Bulbro sites have not previously been investigated.

The surface geology and landscape in the area are dominated by basal moraines (mainly lodgement till). Figure 2b shows a geological cross-section of the main aquifer of Paleocene and Danien limestones, which are overlain by Quaternary glacial deposits of clayey till and local sand layers. In wells near the current Salløv and Bulbro study sites, the thickness of the glacial layers above the main aquifer is 14-18 m and locally less. The origin of the lower clayey till units in the profile is uncertain and may be from pre-Weichsel glaciations, while the till unit (TC) directly underneath the SC sand layer is from the late Weichsel main ice advance (23-20 kyr BP). Above the SC sand, the tills are from the young Baltic ice advances (17-19 kyr BP), (Jørgensen and Fredericia, 1992; Hildebrandt, 2000; GEUS, 2005). Between deposition of the TC and TD ice advances, the land surface was exposed in a subaerial period with tundra, which caused local weathering and oxidation of the top in the TC unit. The deposition of the SC sand occurred in front of the advancing TD Baltic glacier at the end of this period (Hildebrandt 2000), which also created the glacial pavement with rocks and boulders in the transition. The SC sand layer is found locally in most of the Havdrup area and have been used together with the glacial pavement to make the correlations shown in the cross section. Lenses and layers of sand and gravel are abundant embedded features with variable extension and orientations in and across the till units.

Since early the 1950s, the hydrogeology, water tables and vertical hydraulic gradients in the study area has been significantly influenced by water abstraction from the nearby well-field of Thorsbro waterworks (Figure 2). Groundwater abstraction in the early years from 1951 was 3 million m^3/year until 1972 and thereafter decreased to approximately half of the original amount. The current permission is 2.5 million m^3/year (Solrød kommune, 2016). The abstraction has lowered the pressure head in the main aquifer with up to 7 m in the study area (Krüger A/S, 1989). Thereby, the water tables and pressure heads in the glacial layers above the main aquifer have been influenced, however to the authors best knowledge, there is no historical record available to quantify this. Significant influence, however, is suggested by reported drying out of steams and local farmers shallow wells, the latter in which the water disappeared within few weeks after the water abstraction was initiated in 1951 (personal communication in 1987 by farmer Henry Jessen, Marebæk site).

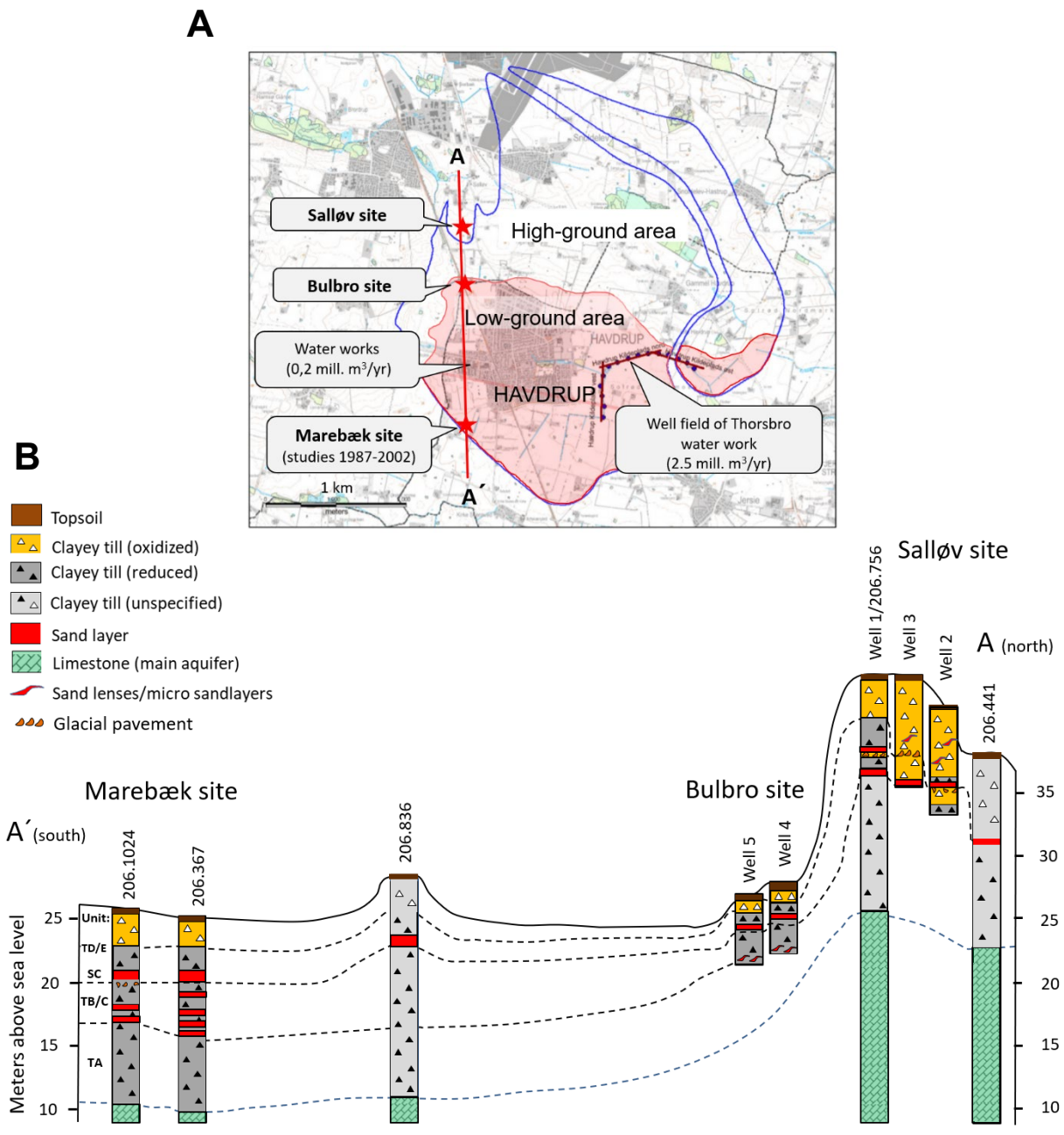

FIGURE 2. Location of the study sites Salløv and Bulbro and the previous Marebæk site in the Havdrup area. (A) The blue line shows the groundwater catchment of the Havdrup water abstraction well field (2.5 mill. m³/yr in 2002) (belonging to Thorsbro water work) (Solrød kommune, 2016). The surface geology and landscape are dominated by basal moraines (lodgement till). The landscape consists of hills (45-50 m above sea level) in the high-ground and plains (20-27 m above sea level) in the low-ground. (B) Geological cross section from the Marebæk site to the Salløv site showing till units representing different ice advances during ice ages; TA and TB: are possibly from older ice ages, TC: Late Weichsel main advance (23-20 kyr BP), TD: Young Baltic advance (19 kyr BP), Young Baltic re-advance (18-17 kyr BP).

2. Materials and Methods

2.1 Study sites, excavations and monitoring wells

Figure 3 shows the EM38 survey at the Salløv and Bulbro sites used for guiding where to the place the excavations of the study. Before final excavation, hand-auguring was carried out to ensured that representative clayey till profiles would be presented. Three excavations (E1-3) were established in the Salløv high-ground site, and three were established (E4-6) in the low-ground Bulbro site. Nests of monitoring wells were established 10-15 m from each excavation, with screens in 1-3 m depth and in 6-8 m depth. The monitoring wells were carried out by 6" dry auguring, except for the shallow wells by E1 and E3, which were established by 3" hand-auguring. Soil samples were collected every 0.5 m and from layers in between during auguring. The screens were packed with sand and sealed with bentonite to 1 m depth below the soil surface. Description of bore profiles, well screens and soil mechanical properties obtained from the wells are shown in Appendix 1.

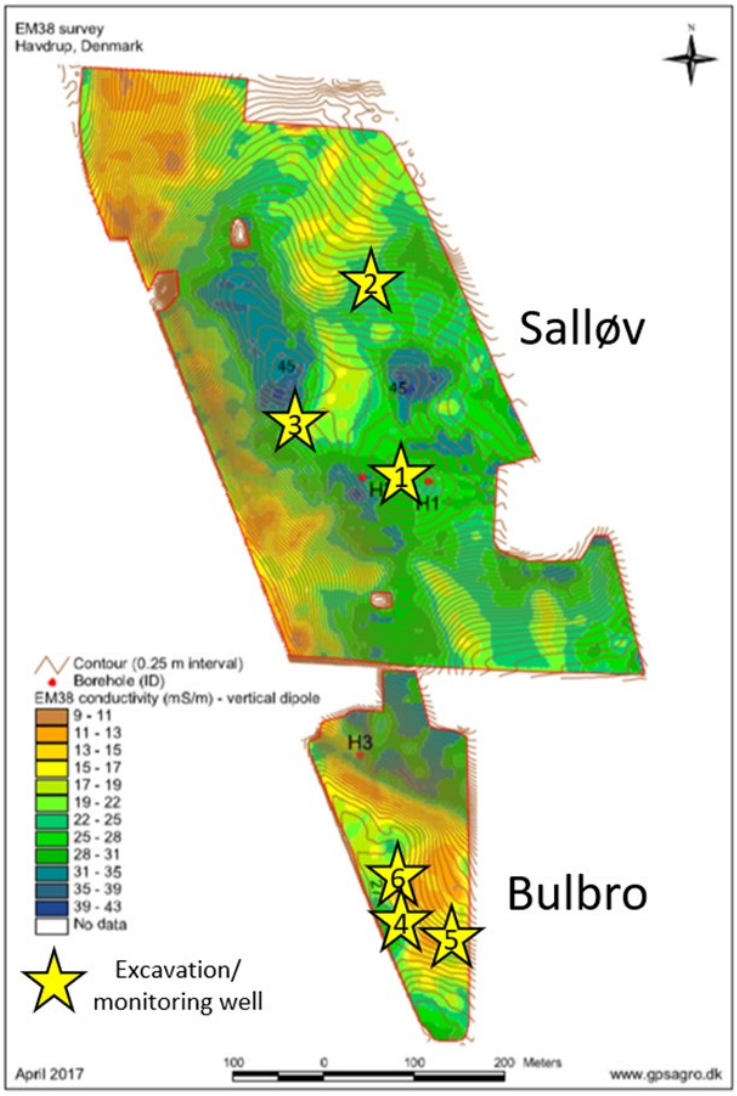

FIGURE 3. E38 map with location of excavations (E1-E6) and monitoring wells. The EM38 map shows the electric conductivity and, hence, clay content in the upper approximately 1 m of the soil. Conductivity = 19-22 mS/m equals ca. 12% clay.

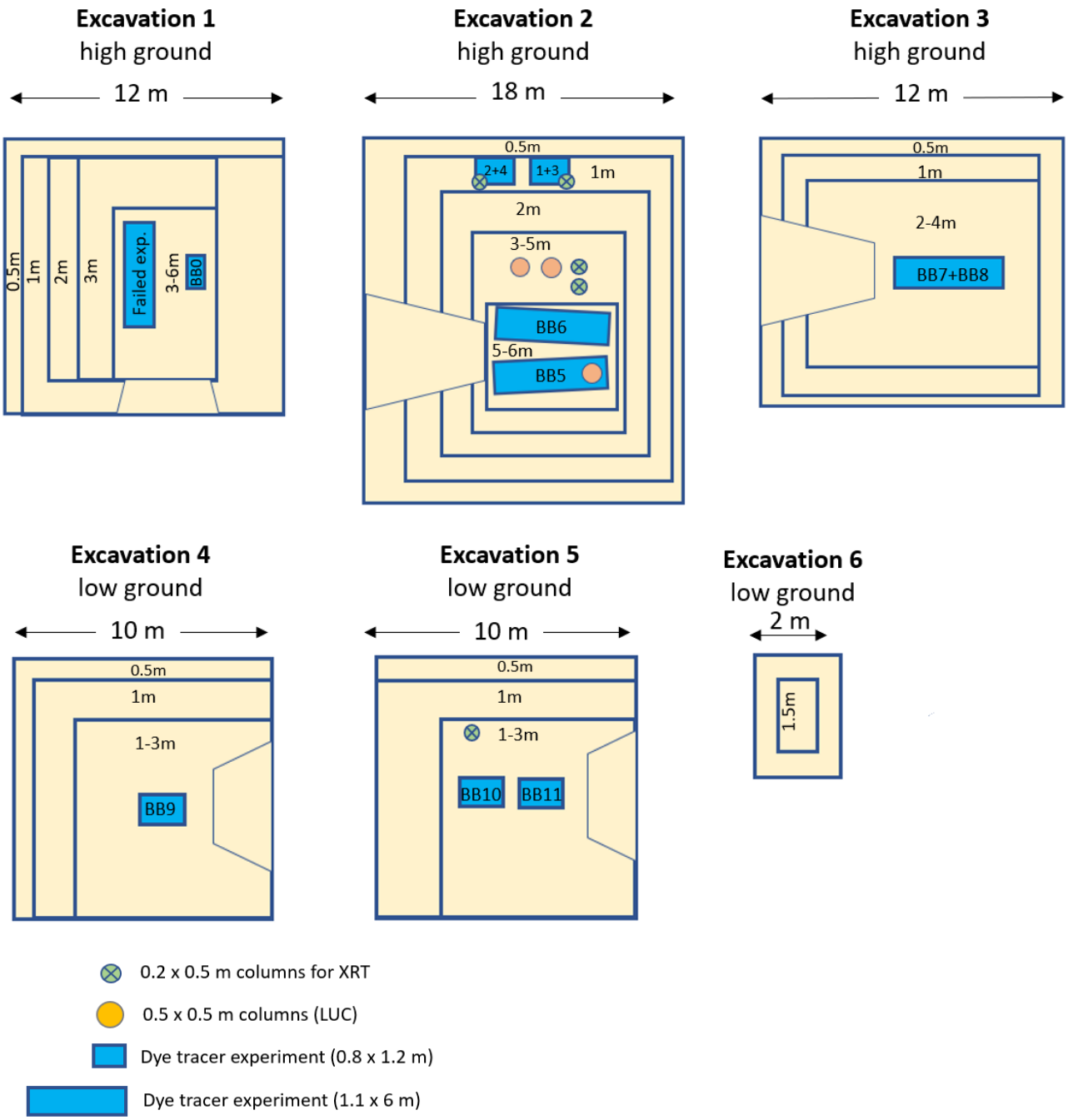

FIGURE 4. Plan view of excavations and dye tracer infiltration experiments. The dye tracer experiments used Brilliant Blue dye tracer (BB). Non-invasive macropore studies were carried out with CT-scanning of intact samples (XRT). Hydraulic and pesticide transport experiments were carried out with Large Undisturbed Columns (LUC) in the "Clayfrac" project by Aamand et al. in prep. (2020).

Figure 4 shows a plan view of the excavations (E in the following) with indicated locations of Brilliant Blue (BB) dye tracer experiments, sampling of intact cores for X-ray tomography (XRT) and large undisturbed columns for LUC experiments (large undisturbed columns), the latter being used for hydraulic and pesticide transport experiments in the "Clayfrac" project (Aamand et al. in prep., 2020).

Figure 5 shows the excavation of E2 with preparation for Brilliant Blue (BB) dye tracer experiments in the bottom. As mentioned, this excavation was shared with the “Clayfrac” project, in which soil samples for pesticide determinations and large undisturbed columns (LUC in Figure 5) for hydraulic and pesticide transport experiments were collected (Aamand et al. in prep., 2020).

FIGURE 5. High-ground excavation E2 in Salløv. Ongoing preparation of the dye infiltration experimental fields BB5 and BB6 in the bottom of the excavation (5.2 m depth).

2.2 Geological description and mapping of biopores and fractures

Geological layers and boundaries in the excavations were recorded and described in horizontal and vertical profiles. Frequencies and diameters of biopores together with live roots contained in the biopores were counted manually in 1-2 m^2 horizontal fields in 0.1, 0.5 and 1 m depth and in the surfaces of the dye tracer experiments. Furthermore, fracture frequencies and biopore patterns were inspected and mapped on 2-70 m^2 horizontal surfaces in the grey and red fracture vertical zones of the excavations in order to establish representative dye tracer experiments and provide fracture frequencies for Fe/Mn-oxide mass balance calculations (section 2.3) and hydraulic calculations (section 3.5.3). Dip and strike of fractures were measured with compass and GEOid iPhone app or manually with a geologist compass. The fracture measurements were plotted in stereographic projections. Further details about applied methods for the mapping of the fractures and biopores are described by Jørgensen et al. (2017). Texture, porosity and hydraulic conductivity of the clayey till matrix were determined with 70 mm intact cores. Those were collected as sub-samples from the large intact columns (LUC) in E2 and shared with the “Clayfrac” project, Aamand et al. in prep. (2020), Table 1. The intact core hydraulic measurements were carried out by an external laboratory (consulting company GEO) in triaxial permeameter cells.

TABLE 1. Saturated hydraulic conductivity (Ksat), porosity and texture of unfractured 70 mm intact clayey till cores collected from excavation E2.

Excavation (Till unit and matrix weathering)	**Depth, m**	**Hydraulic conductivity, Ksat, m/s**	**Porosity**	**Texture %**			
				Clay	Silt	Sand	Gravel
				0.001-0.002 mm	>0.002-0.06 mm	>0.06-2 mm	>2 mm
E2 (Till-TD oxidized)	2.8-2.9	3.2E-9	0,30	15	35	46	4
E2 (Till-TD oxidized)	3.4-3.9	2.5E-9	0,30	17	31	42	10
E2 (Till TD oxidized)	4.4-4.9	2.8E-9	0,27	17	32	49	2
E2 (Till TD reduced)	5.45-5.5	1.7E-9	0,23	19	33	46	2
E2 (Till TC oxidized)	5.8-5.9	4.9E-9	0,21	16	29	52	3
E2 (Till TC oxidized)	5.8-5.9	2.3E-8	0,31	13	32	43	12

2.3 Geochemistry

Fe-oxide in soil and water samples by CBD method

Samples for chemical analysis across fractures were collected from the Sallløv E2 excavation as blocks of approx. 15×15 cm and brought to the lab wrapped in foil to avoid disrupton of the structure during transport. In the lab, fractures were located precisely and dimensions of the grey fracture and the red Fe-oxide rim were measured. The blocks were carefully opened in the fracture, leaving two halves with a grey fracture face (Westergaard and Hansen, 1997). The grey material was carefully scratched from the fracture face with a sharp scalpel, and material from both halves was combined. After all grey material was sampled, the red Fe-oxide rim material was collected in the same way and combined from both sides of the fracture. From the fractures with red infilling, the infilling was scarped out. Finally, material was sampled from the matrix in the center between fractures. Fractures were sampled from soil depth 1.5 m, 3.0 m and 3.7 m, and several blocks and fractures was combined for each depth. Samples were carefully ground in an agate mortar with a pestle of polyoxymethylene and ready for extraction for chemical analysis.

For extraction, 0.10 g ground soil sample was weighed into a 15 ml vial and mixed with 4.0 mL of 0.3 M Na-citrate and 0.5 mL 1 M $NaHCO_3$ at pH 8. The vial was placed in a waterbath at 70 °C and after addition of 0.1 g Na-dithionite extracted for 10 minutes. The citrate-bicarbonate extraction was repeated twice and all three fractions combined (Mehra and Jackson, 1960). The extracts were diluted 10 × with 3.5% HNO_3 to avoid complexation and stored cold until determination by ICP-OES. The stock solution CPI international (P/N 4400-132565) is a mixture of elements in concentration ratios relevant for soil, and water analysis was used for external calibration curve for the following elements: Al, B, Ca, Cd, Co, Cr, Cu, Fe, K, Mg, Mn, Mo, Ni, P, Pb, V, Zn. The results are shown in Appendix 2, Table A2.1.

Total Fe in pore water

Water samples were collected every week from the E2 wells in the period 20. October 2017 to 24. April 2018 for analyses of total Fe. Before sampling, the wells were pumped dry. Water samples were hereafter collected from ground water that recharged into the wells. Content of Fe in the water samples was determined by Atomic Absorption Spectrometry (AAS). The results are shown in Appendix 2, Table A2.2).

Dissolution of Fe-oxides before eDNA extraction

The efficiency of DTT (Dithiothreitol) (Cleland's reagent) to dissolve Fe-oxides in the Fe-oxide rim during the eDNA extraction was tested for 0.03 g (amount in the standard method for eDNA extraction in section 2.7) and 0.1 g DTT addition instead of dithionate in the CBD method. The results were compared with Fe extracted by the CBD method to test the efficiency of opening the Fe-oxide structure that might protect captured eDNA and aDNA inside Fe-oxides from being extracted.

2.4 Dye tracer experiments and hydraulic measurements

Preparation and Installations

A total of 12 Brilliant Blue FCF (E-133; CI 42090, Flury and Flühler (1995)) dye tracer infiltration experiments (BB experiments) were carried out between 1-6 m depth in the till profiles. Applied concentration, amount and time length of BB infiltration together with overall experimental conditions are shown in Table *2*. Locations of the experiments in excavations E1-E5 are shown in Figure 4. Figure 5 and Figure 6 show the preparation of the of the 6x1 m dye tracer experimental fields. These were excavated and leveled by using a fabricated steel frame on which the excavator could move back and forth and excavate a 20 cm deep trench within the frame without disturbing the surface of the experimental fields (Figure 6A and B). The final levelling of the bottom in the trench was carried out by using a sharpened excavator shovel to removed smearing and closing of fractures and macropores (Figure 6B). To remove any smearing left by the excavator shovel, the clay was thereafter chipped of with knifes along the fractures (Figure 6C) and vacuumed. Hereby groves along the fractures were created, which were filled with coarse filter sand (Figure 6D). Following this, the surface was covered with stainless steel mesh (1 mm mesh size), which was covered with a 2-4 cm layer of gravel (Figure 6E). In order to obtain free downward drainage of the infiltrated dye tracer solution, a drain tube with a diameter of 160 mmm was established 1-2 m underneath the experimental surfaces (Figure 6F). The technique used for establishing the drain was utilizing a specialized cutting reamer developed in the predecessor PESTPORE study (Jørgensen et al., 2017) to removed smearing from the borehole wall, which has been shown to prevent outflow from macropores into borings and drain tubes (D´Astrous et al., 1989). The method and devices are described in detail by Jørgensen et al. (2017). The 1 m^2 dye tracer experiments shown in Figure 4 were prepared with the same procedures and installations as in the large experiments, however, by using hand tools.

TABLE 2. Specifications of Brilliant Blue (BB) infiltration experiments.

Excavation	**1**	**2**	**2**	**2**	**2**	**2**	**2**	**3**	**3**	**4**	**5**	**5**
Experiment	**BB 0**	**BB 1**	**BB 2**	**BB 3**	**BB 4**	**BB 5**	**BB 6**	**BB 7**	**BB 8**	**BB 9**	**BB 10**	**BB 11**
Area of BB-infiltration basin, m^2	1	0.5	1	1	1	6.6	6.6	6.6	6.6	1	1	1
Depth of BB-infiltration basin (bottom) below soil surface, m	5.0	1.1	1.1	2.4	2,4	5.2	5.2	2.05	3.1	1	0.6	0.6
BB ponding in infiltration basins, cm	10	2	2	2	2	10	10	10	10	4	8	8
Depth of drain tube below soil surface, m	-	2.1	1.8	4.0	4.0	-	-	3.8	3.8	3	3	3
Depth of GW table below bottom of BB-basin, m	3.0	6.9	6.9	5.6	5.6	3	3	2	1	0.7	1	1
BB dye concentration, mg/L	2	2	2	2	2	2	2	2	2	2	2	2
Length of BB-experiment, days	8,0	1,0	1,0	1,0	5,0	15	15	12	10	0,04	10	10

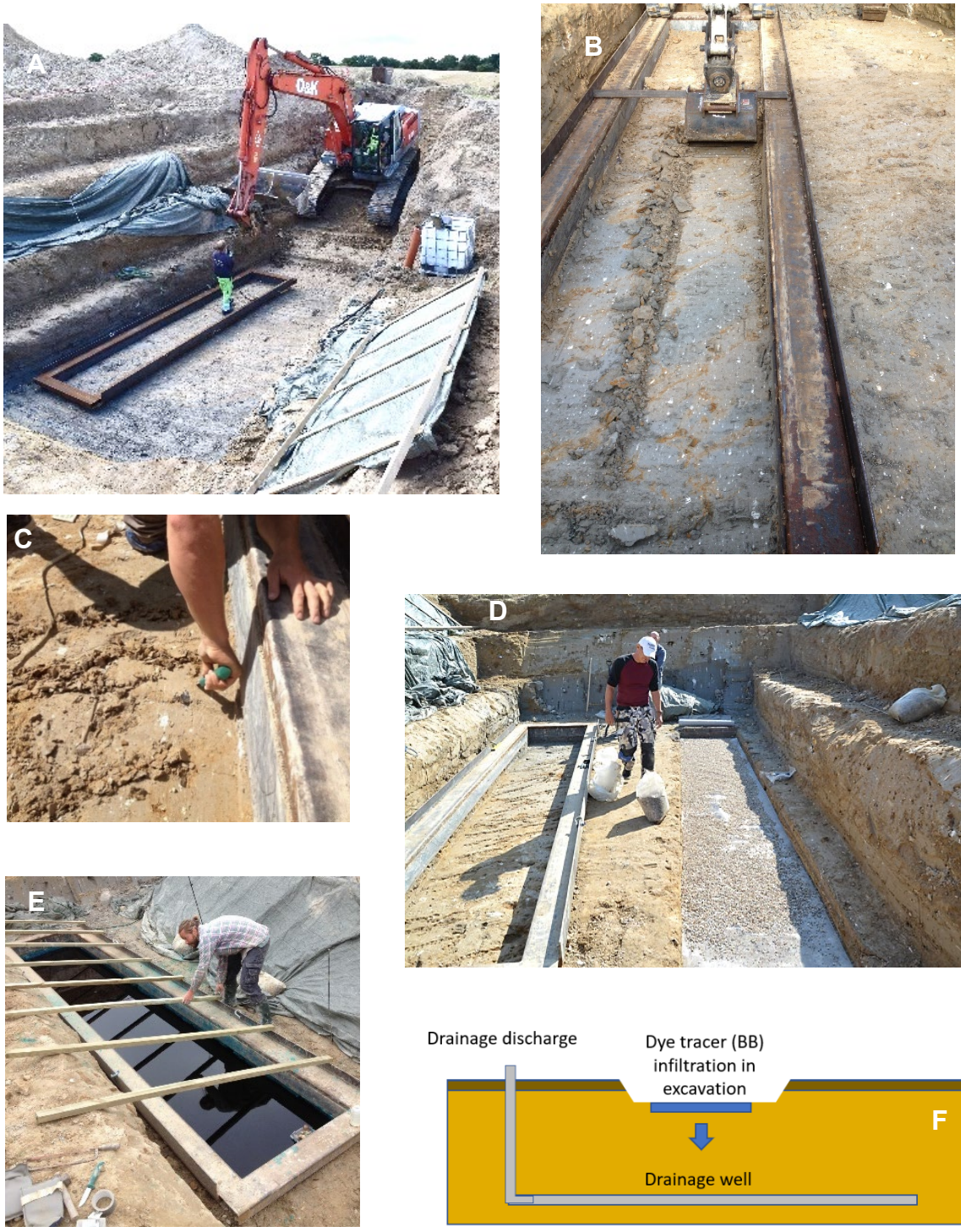

FIGURE 6. Preparation of BB5 and BB6 dye tracer experimental fields in excavation E2, which was shared between PESTPORE2 and the "Clayfrac" project. (A) Installation of steel frame from which the excavator could excavate the experimental field without disturbing the surface (see figure 5). (B) Final levelling of the experimental surface using a sharpened shovel to minimize smearing and thereby avoid closing of fractures and macropores. (6C) "Chipping" of clay along fractures with knives to remove any remaining smearing. (D9) Covering the experimental surfaces with stainless steel mesh and 2-4 cm gravel. (E) Cover of experimental field

about to be established over BB6 experimental field with Brilliant Blue dye tracer. (F) Drain tube installed 1-2 m below experimental fields.

Due to appearance of rock boulders in infiltration fields BB0, BB5 and BB6, the installation of drain tubes had to be omitted in these experiments. In BB5 and BB6, the groundwater table was more than 1 m below the infiltration surfaces. In order to avoid filling up dead-end macropores with water that would potentially drain off very slowly and thereby prevent infiltration of the dye, the BB5 and BB6 fields were not water saturated before the dye infiltration and infiltration measurements. Hence the macropores were unsaturated at the start of dye infiltration, which may have retarded the initial infiltration. The BB5 and BB6 infiltration experiments were covered with plastic tarpaulins, and infiltration rates were determined from the daily drop in water table in the infiltration trenches (Thalund-Hansen, 2018). Evaporation determined in trays with water placed underneath basin covers was subtracted. The BB6 cover turned out not to be water tight against heavy rain, which occurred during the period of measurement. Consequently, infiltration was only estimated for the BB5 experiment. Due to possible effects from the initially unsaturated condition of macropores, the measurements of infiltration rates obtained from the first 2 days were omitted from flow rate calculations. When the BB5 and BB6 experiments were excavated after the dye infiltration, it was revealed that the BB5 and BB6 experimental fields were naturally drained by inclining sand layers occurring 0.3-1 m below the infiltration fields (Figure 19). In the BB0 experiment, the till was naturally water saturated in the top (till TD) by perched water table and shifted to unsaturated condition in the underlying till TC (see section 3.1).

In the remaining dye tracer infiltration experiments (BB1, BB2, BB3, BB4, BB7, BB8, BB9, BB10, BB11), drain tubes were installed 1-2 m below the infiltration fields, and they were water saturated for 1-3 days before application of the dye tracer solution. After BB had been infiltrated, the infiltration experiments were excavated, and dyed flow paths were mapped on transparent plastic sheets and photo documented. Samples were collected from the dyed and non-dyed flow paths and macropores for radiocarbon dating, C-isotopes and aDNA analyses. XRT and LUC columns were collected from the BB experiential fields or immediately adjacent to them (Figure 4).

Fracture aperture estimation

The aperture of fractures in the dye tracer experiments were estimated by numerical modeling of the observed maximum depths of BB infiltration in fractures by Thalund-Hansen (2018). This novel approach utilized that the applied BB concentrations in the experiments were 2g/L (Table 2), while the lowest visible BB concentrations in fractures were 20 mg/L. The fracture apertures were then determined as the simulated aperture value for which the simulated depth of the BB concentration = 20 mg/L was equal to the visually observed maximum depth of BB in the fracture. Retardation of the BB by adsorption (R=3) was determined from combined bromide and BB transport data obtained from LUC experiments with similar clayey till to the till in the current study site (Urup, 2001). Figure 7 shows the simulated BB infiltration depths in fractures as a function of the hydraulic gradient, time length of infiltration and fracture aperture.

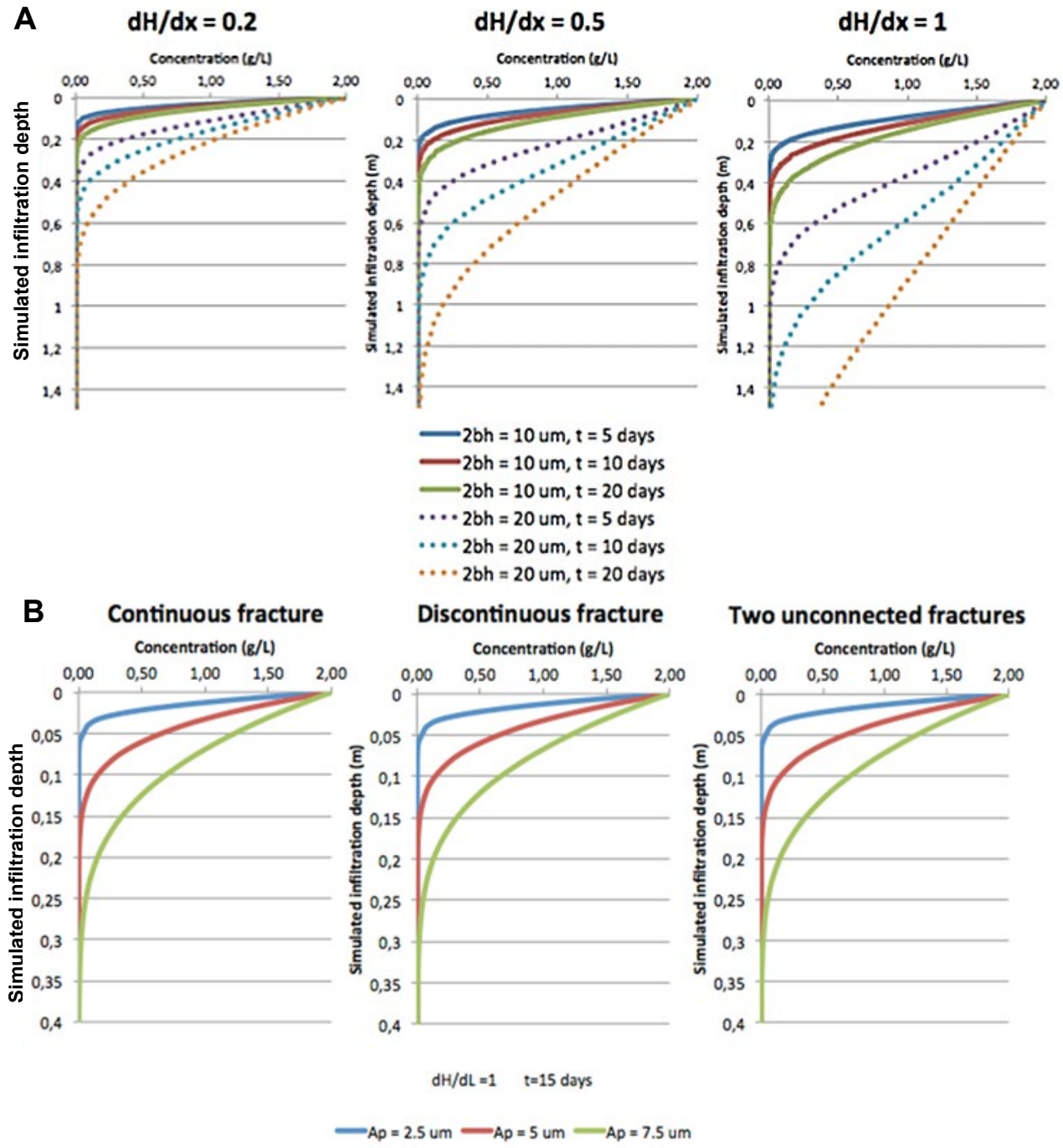

FIGURE 7. Model simulations of Brilliant blue infiltration depths as a function of the fracture aperture (Ap) for water saturated fractures with free drainage of flow into drains or natural sand layers underneath the infiltration fields. Infiltration depths are shown as a function of (A) fracture aperture, different hydraulic gradients (dH/dx) and length of infiltration time. (B) Continuous, discontinuous and unconnected fractures for three fracture apertures in 15 days and dH/dx =1 (from Thalund-Hansen, 2018).

Figure 7 shows that the simulated BB infiltration depth varied most strongly as a function of the fracture aperture, while the hydraulic gradient had a smaller impact on infiltration depth (and, hence calculated apertures). The difference is due to the fact that the hydraulic gradient is first order variable of flow, while the flow scales with the aperture cubed (Snow, 1968; Witherspoon

et al., 1980), which means that the aperture has strong impact on visible BB infiltration depth. This makes the approach highly sensitive to the aperture and consequently provides reasonable accurate estimates of aperture values when based om direct observation of the BB tracer. Further details of the modeling are given by Thalund-Hansen (2018).

2.5 X-ray tomography (XRT)

Two types of intact soil samples were collected for XRT soil columns and soils blocks (Table 3). The soil samples were transported from Denmark to France (INRAE, Orléans) by a car with air suspension to assure minimum disturbance and then kept in a cold chamber (4°C) to preserve them from degradation.

Image acquisition by X-ray computed tomography

X-ray imaging was performed at the CIRE platform by INRA in France (INRAE Val de Loire, Nouzilly, UMR PRC). We used a medical X-ray tomograph (Siemens Somatom Definition AS) operating at an energy level of 200 kV and a current of 140 mA. The advantage of such a scanner is that large samples can be imaged, and image acquisition is fast (less than one minute). The resolution of the obtain image depends on the diameter of the sample (Table 3). Images are delivered in 16-bits, but converted to 8-bits for analyse.

TABLE 3. List of samples and corresponding images acquired by CT-SCAN

Sample description	**Excavation and Brilliant Blue infiltration (BB)**	**Image acquisition**	**Image resolution (mm)**
Column 1 (1.10-1.60 m). Yellowish brown oxidized till with grey fractures.	E2, high-ground, BB1	Whole column	x= y = 0.430 z= 0.1
Column 2 (2.40-2.90 m) Yellowish brown oxidized till with red fractures	E2, high-ground, BB3	Whole column	x= y = 0.430 z= 0.1
Block 1 (3.00-3.50 m). Yellowish brown oxidized till with red fractures	E2, high-ground, BB6	Whole block	x= y = 0.977 z= 0.1
		Square zoom 1	x= y = 0.451 z= 0.2
		Square zoom 2	x= y = 0.146 z= 0.6
Block 2 (4.00-4.50 m). Yellowish brown oxidized till with red fractures	E2, high-ground, BB6	Whole block	x= y = 0.977 z= 0.1
		Square zoom 1	x= y = 0.367 z= 0.6
		Square zoom 2	x= y = 0.146 z= 0.6
Column 3 (2.30– 2.80 m). Yellowish brown oxidized till with grey fractures	E3, high-ground, BB7	Whole column	x= y = 0.369 z= 0.6
		2 square zooms	x= y = 0.176 z= 0.6
Column 4 (1.80 – 2.30 m). Grey reduced till without visible fractures	E5, low-ground, BB10	Whole column	x= y = 0.369 z= 0.1
		Square zoom	x= y = 0.176 z= 0.1

Image analysis for columns

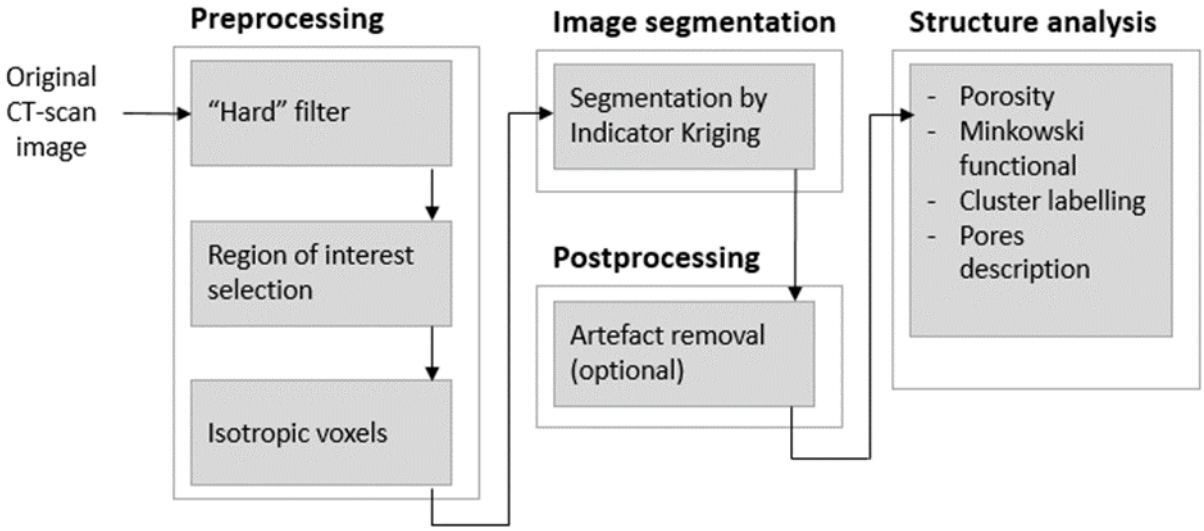

FIGURE 8. Workflow diagram for columns' image processing (adapted from Schluter et al., 2014).

Images acquired from the column soil samples were analysed following the workflow of Figure 8:

Preprocessing: preparation of the image for analysis.

- "*Hard" filter*: in this project, the images were delivered by the CIRE platform after applying an iterative reconstruction algorithm released by Siemens and named SAFIRE (Sinogram Affirmed Iterative Reconstruction)(Ghetti *et al.*, 2013). Two different filters were applied separately, a soft filter (I31s) and a hard filter (I70h), with noise reduction as the main purpose. Only the images that experienced the hard filter were used for further analysis.
- *Region of interest selection (ROI)*: this step allows removing all the elements of the image we do not want to include in the analysis (PVC cylinder, extremities of the soil samples disturbed during sampling). This step was achieved using the ImageJ free software (Schneider *et al.*, 2012; Rueden *et al.*, 2017).
- *Isotropic voxels*: the images delivered by the CIRE platform do not have isotropic voxels, i.e. voxels have different resolution in the x, y and z directions. However, some of the algorithms used for image analysis required images with isotropic voxels. A transformation was then applied to rescale the images along the z-axis so the voxels' depth was the same as the voxels' width. This step was achieved using ImageJ (*Make Isotropic* plugin, https://imagej.nih.gov/ij/plugins/make-isotropic/index.html).

Image segmentation: conversion of the grey image to a binary image that allows making the distinction between two phases, i.e. the soil matrix and the pore network. Images were segmented using the Indicator Kriging method, based on auto threshold determination by the Schlüter-Weller-Vogel method (Oh & Lindquist, 1999; Schluter *et al.*, 2010; Houston *et al.*, 2013). Indicator Kriging is part of locally adaptive segmentation methods, which account for some kind of neighbourhood statistic for class assignment in order to smooth object boundaries, avoid noise objects or compensate for local intensity changes. Indicator Kriging was successfully applied to porous media images in previous studies.

Postprocessing: due to sampling and/or transportation, some soil samples show artefacts that did not reflect the real soil structure. For example, one soil column showed fractures that were clearly related to sampling. These artefacts were removed from the segmented image to

avoid biased analysis of the soil structure, e.g., porosity overestimation. This step was achieved using ImageJ.

Structure analysis: different quantitative descriptors of soil structure were calculated.

- *Porosity estimation*. This step was achieved using ImageJ.
- *Minkowski functionnals* that provide information on the size of pores and aggregates, the pore surface area and the pore topology having the potential to be linked to physical properties. Indicators are calculated: porosity, surface density, mean curvature and Euler number. In particular, the Euler number informs about the connectivity of the pore space (a negative Euler number indicates a connected pore network). It can be calculated by taking into account only the voxels connected by the faces (Euler6) or the voxels connected by the faces and by the corners (Euler26). Surface density and mean curvature give an idea of the complexity of the pore network. This step was achieved using the Quantim toolbox (Vogel, 2008; https://www.ufz.de/index.php?en=39198).
- *Cluster labelling*, allowing the identification and the description of each pore seen as an independent group of connected voxels. This step was achieved using the BoneJ plugin (Doube *et al.*, 2010; http://bonej.org/) through ImageJ.
- *Pore network analyse*. Percolation of the pore network, connectivity of the to the top part of the soil sample and critical pore diameter was analysed using SoilJ (Koestel, 2018; https://github.com/johnkoestel/soilj) run under Fiji (Schindelin *et al.*, 2012).
- *Pore network tortuosity* was estimated using the Tortuosity plug-in (Roque & Costa, 2020).
- For each sample, some *individual pores were extracted* to allow a more precise description. Pore length and diameter were achieved using ImageJ in combination with Smartroot (Lobet *et al.*, 2011; https://smartroot.github.io/) run under Fiji.

Image analysis for the blocks

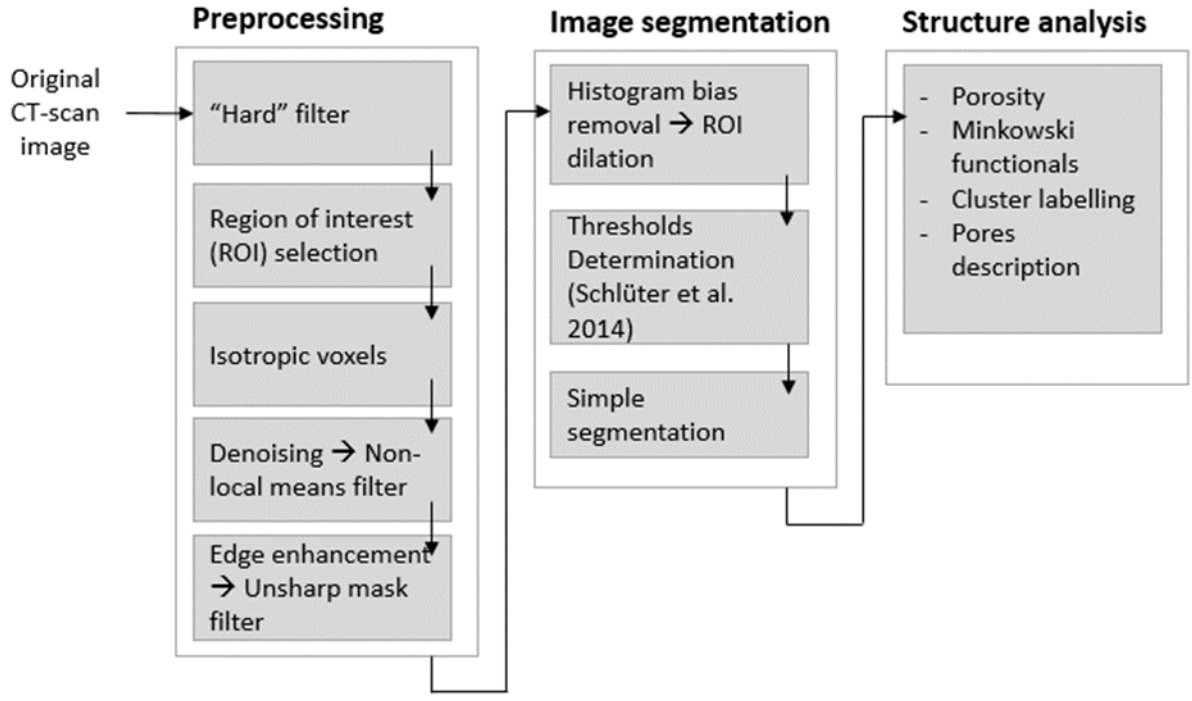

FIGURE 9. Workflow diagram for blocks' image processing (adapted from Schluter et al., 2014).

Images acquired from the block soil samples presented less porosity. They were then analysed following another workflow (Figure 9):

-Preprocessing: preparation of the image for analysis.

- “Hard” filter: in this project, the images were delivered by the CIRE platform after applying an iterative reconstruction algorithm released by Siemens and named SAFIRE (Sinogram Affirmed Iterative Reconstruction)(Ghetti et al., 2013). Two different filters were applied separately, a soft filter (I31s) and a hard filter (I70h), with noise reduction as main purpose. Only the images that experienced the hard filter were used for further analysis.
- Region of interest selection (ROI): this step allows removing all the elements of the image we do not want to include in the analysis (PVC cylinder, extremities of the soil samples disturbed during sampling…). This step was achieved using the ImageJ free software (Schneider et al., 2012; Rueden et al., 2017).
- Isotropic voxels: the images delivered by the CIRE platform do not have isotropic voxels, i.e. voxels have different resolution in the x, y and z directions. However, some of the algorithms used for image analysis required images with isotropic voxels. A transformation was then applied to rescale the images along the z-axis so the voxels’ depth is the same as the voxels’ width. This step was achieved using ImageJ (Make Isotropic plugin, https://imagej.nih.gov/ij/plugins/make-isotropic/index.html).
- Denoising: a non-local means filter (NL) was applied. It is a linear filter, i.e. the grey value at the current location is the average of grey values at other locations. According to Schulter et al. (2014), this filter sufficiently denoises along edges while smoothing across the edges is inhibited. As a consequence, an additional treatment of rugged surfaces after edge enhancement is not necessary. This step was achieved using the Non Local Means Denoise tool with Fiji (https://imagej.net/Non_Local_Means_Denoise).
- Edge enhancement: this step is important if image edges do not show a crisp intensity step, but rather a gradual intensity change spanning several voxels. A standard method to sharpen the image, i.e. to enhance the intensity gradient locally, is unsharp masking. Unsharp masking will also enhance noise, so the image should be denoised first. This step was achieved using Fiji.

-Image segmentation:

- ROI dilation (method adapted from (Schluter et al., 2014)): Some images exhibit unimodal histograms due to very imbalanced class proportions, i.e., a very small volume fraction of a certain phase and a very large volume fraction of the background. A balanced frequency distribution can be obtained with a new, semiautomatic algorithm: (i) pick a threshold manually that detects the class with lowest volume fraction as the region of interest (ROI) and binarize the image. (ii) Dilate the thus obtained mask. (iii) Multiply the original image with the mask in order to compute the ROI histogram. (iv) If it is not yet clearly bimodal (multimodal), return to step (ii). This step was achieved using ImageJ. Three dilation loops were applied.
- Threshold determination: global thresholding was performed following Schluter et al. (2014). In this approach, classes are assigned to voxels by histogram evaluation only. Five threshold detection methods were used: Maximum Variance, Minimum Error, Maximum Entropy, Fuzzy C-means and Shape. These methods allow multiphase segmentation. The obtained thresholds from were outlier-corrected averaged to determine the final threshold used for image segmentation.

-Structure analysis: different quantitative descriptors of soil structure were calculated.

- Porosity estimation. This step was achieved using ImageJ.
- Minkowski functionnals that provide information on the size of pores and aggregates, the pore surface area and the pore topology having the potential to be linked to physical properties. In particular, the Euler number informs about the connectivity of the pore space. This step was achieved using the Quantim toolbox (Vogel, 2008; https://www.ufz.de/index.php?en=39198).
- Cluster labelling, allowing the identification and the description of each pore seen as an independent group of connected voxels. This step was achieved using the BoneJ plugin (Doube et al., 2010; http://bonej.org/) through ImageJ.
- Pore network analysis. Percolation of the pore network, connectivity of the top part of the soil sample and critical pore diameter was analysed using SoilJ (Koestel, 2018;

https://github.com/johnkoestel/soilj) run under Fiji (Schindelin et al., 2012). Pore network tortuosity was estimated using the Tortuosity plug-in (Roque & Costa, 2020).

- For each sample, some individual pores were extracted to allow a more precise description. Pore length and diameter were achieved using ImageJ in combination with Smartroot (Lobet et al., 2011; https://smartroot.github.io/) run under Fiji. The diameters were in general estimated as the diameter of the greatest sphere that fits within the structure. It is thus an approximation for the pores which are not cylindrical.

2.6 ^{14}C dating and C-isotopes

The ^{14}C dating and C-isotope analysis were carried out in parallel samples with the aDNA analysies (Appendix 3). From bulk samples of clayey till, the carbonate content was removed using 1M HCl. Subsequently, humic acids were dissolved with 0.5M NaOH. This was repeated until no colouring of the supernatant occurred, and the supernatant for each was collected. From the supernatant, the humic acid (HA) fraction was precipitated using 1M HCl rinsed with MilliQ water and freeze dried. The sediments, the humin fraction leftover from the HA extraction, was treated with 1M HCl, rinsed with MilliQ water and freeze dried. Plant macrofossil samples (roots) were pre-treated with acid-base-acid to remove carbonate and humic acids, rinsed with MilliQ water and freeze dried. All samples were then transferred to evacuated glass vials containing CuO for combustion to CO_2, which were subsequently reduced using H_2 to graphite. The graphite was then used for ^{14}C analysis at the 1MV Tandetron accelerator at the Department of Physics, Aarhus University (Olsen et al., 2017).

^{14}C analysis of Fe/Mn-oxide concretions and infillings from fractures by ramped pyroxidation samples was determined by Ramped Pyroxidation at Queen's University Belfast (QUB) in collaboration with Gerard Barrett and Evelyn Keaveney (Keaveney et al 2020). The samples were placed in a pre-baked quartz tube and heated incrementally to 600 °C, at 3-4 °C per minute, in a furnace with a continuous flow of Ultra-high purity He (35 ml/minute). Pyroxidation products flowed into a second furnace where they were oxidised by a continuous stream of Ultra-high purity O_2 (3 ml/minute hand a Cu/Ni/Pt wire catalyst. A Sable Systems CA-10 infrared CO2 detector was used to quantify the CO_2 evolved during the Pyroxidation process. Peaks of CO_2 produced were identified by this detector and selected fractions of CO_2 were cryogenically collected for ^{14}C analysis and transferred for graphitisation (Vogel et al., 1987) under vacuum to a connected H2 graphite line.

All ^{14}C dates are reported as uncalibrated^{14}C ages BP normalized to −25‰ according to international convention using online ^{13}C/^{12}C ratios (Stuiver and Polach, 1977), where BP is before present and present is defined as 1950CE.

The ^{14}C ages are calibrated to calendar years using the calibration curve IntCal13 (Reimer et al., 2013) and are reported as calibrated ages calBP. The online calibration program OxCal is used for calibrating the ^{14}C ages into calendar years (Bronk Ramsey, 2009).

Due to small sample sizes, FTIR or IRMS analyses are only performed on selected samples. Stable δ^{13}C isotopes were measured using a continuous-flow IsoPrime IRMS coupled to an ElementarPyroCube elemental analyser at the Aarhus AMS Centre (AARAMS), Aarhus University, Denmark. An in-house standard Gel-A was used as primary standard, yielding ±0.2‰ for carbon analysis. Further, secondary in-house and international standards were used to check the normalization to the VPDB scale. FTIR spectra were obtained using an Agilent Technologies Cary 630 ATR-FTIR instrument. Scans were performed in the range from 4000–650 cm^{-1} with a resolution of 2 cm^{-1}.

Fourier-transform infrared spectroscopy (FTIR)
FTIR analysis is used to identify chemical properties and functional groups of organic materials. Here, FTIR was applied to identify possible traces of Brilliant Blue in samples from the dye

tracer experiments used for radiocarbon dating. Because Brilliant Blue is an organic dye (C37H34N2Na2O9S3), samples for radiocarbon analysis may be contaminated (see Figure 10). The 14C age of Brilliant Blue is 17345±51 14C years BP. Brilliant Blue FTIR analysis shows peaks at 1570, 1382, 1327, 1156, 1030, 911, 611 cm-1. These lines are shown in the FTIR spectra of raw sediments, the humic and humin fraction (Figure 11). Only for the raw sediments are there indications of a possible Brilliant Blue contamination around 1350 cm-1. For humic and humin fractions, no FTIR peaks associated with Brilliant Blue can be observed. This suggests that if Brilliant Blue is present, this will be in very dilute concentrations and hence have little influence of 14C ages determined.

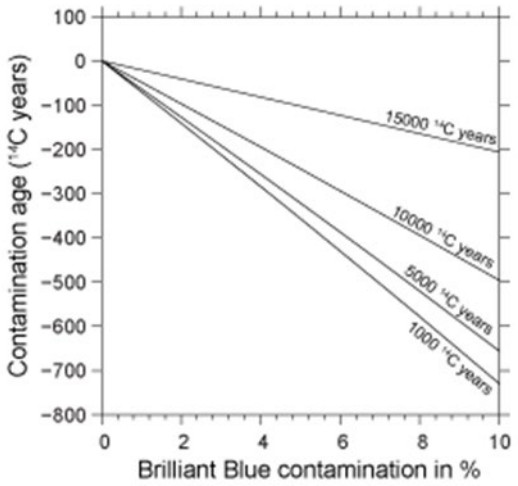

FIGURE 10. Mass balance calculations of the effect of Brilliant Blue contamination on samples for ^{14}C analysis with different ages. The contamination age is calculated as the true ^{14}C age minus ^{14}C age of the contaminated Brilliant Blue sample. If the Brilliant Blue contamination is lower than 1%, then the ^{14}C age error is less than 50 ^{14}C years.

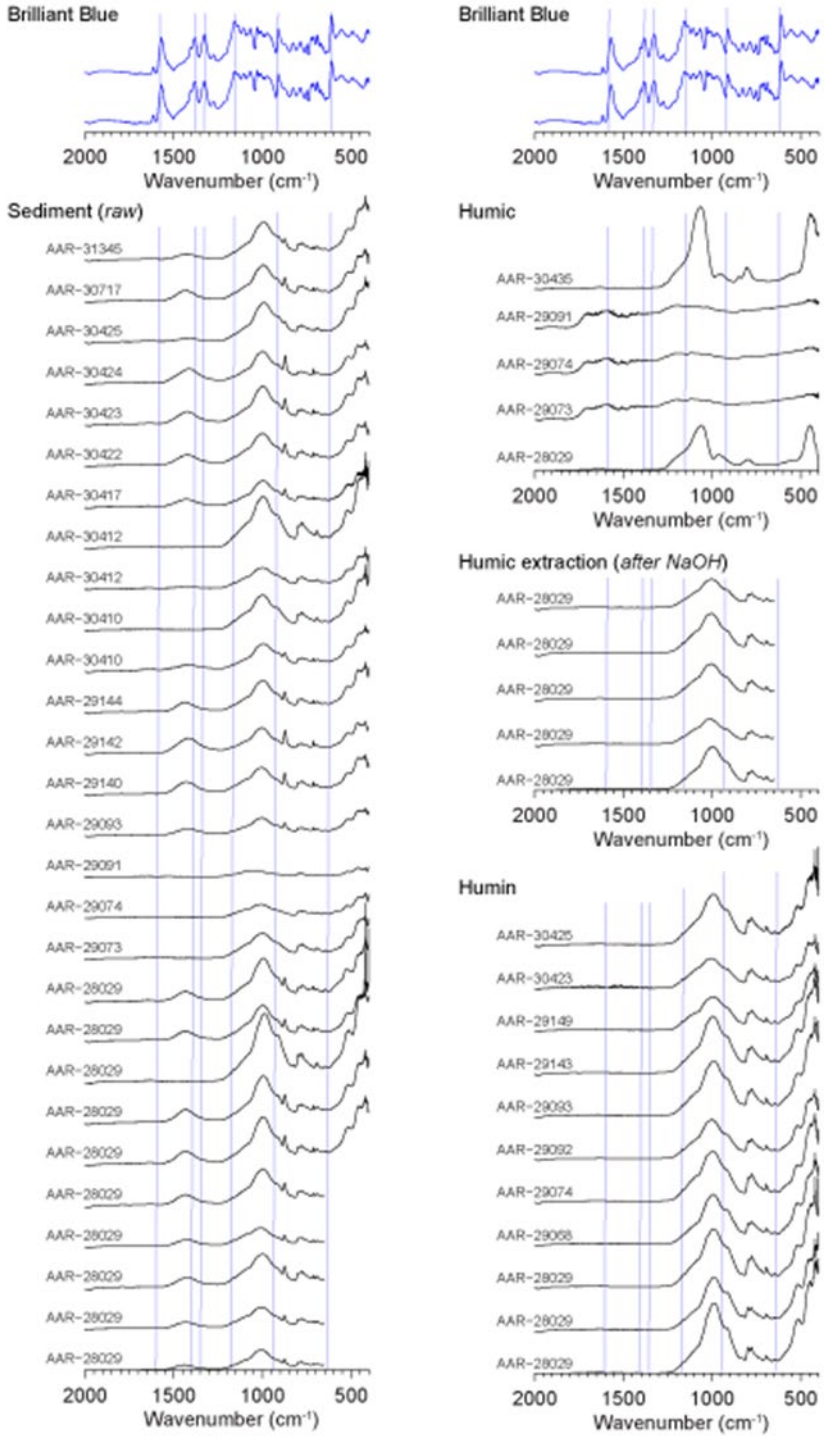

FIGURE 11. FTIR analysis of the sedimentary humic and humin fractions. The top panel shows the FTIR spectra of Brilliant Blue. The Brilliant Blue FTIR peaks are hardly visible in the raw sediment samples, and for pre-treated sample fractions the Brilliant Blue peaks are not visible, suggesting the Brilliant Blue contamination to be low.

2.7 eDNA

Screening of earthworm DNA in soil from burrow linings

Environmental DNA, eDNA, is a complex mixture of genomic DNA from many different organisms found in an environmental sample typically soil and water samples. eDNA is used to

identify the organisms in the sample and assign a taxonomic name. All eDNA work was carried out at the Department of Bioscience, Aarhus University. Soil samples were collected from earthworm burrow lining and infillings and other material from biopores in fractures and reference matrix soil in E2 (see Table 4). We used the DNeasy PowerMax Soil Kit (QIAGEN) to obtain total environmental DNA (eDNA) from the soil samples. Three primer sets targeting three close regions of the mitochondrial 16S region were selected for amplification of these three earthworm DNA markers (Figure 12) (Bienert et al., 2012; Jackson et al., 2017). If the longest sequence of ≈383 bp addressed by the ewA/ewE primer would not amplify, we have included an additional PCR ewB/ewC in our final assessment of earthworm soil eDNA to detect short-chained eDNA of ≈30 bp occurring due to degradation and/or low concentration of long undegraded DNA templates.

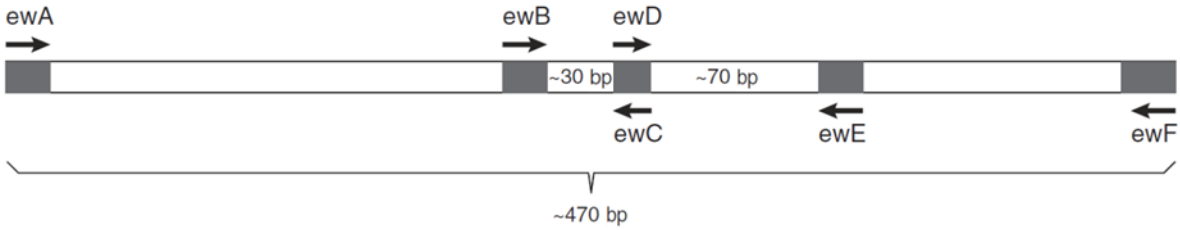

FIGURE 12. A map of the 16s mtDNA region from Bienert et al. (2012), including the long 16S earthworm barcode (ewA/ewE) and the two shorter minibarcodes of 30 and 70 bp. The ewA/ewE primers were used in our study for a medium length barcode and ewB/ewC for the short metabarcode. The primer sections are the shaded areas.

Negative controls (Table 4) were created from quarts sand ignited at 550 °C. They were interspersed between processing of real samples created from the PP2-1 soil block (EW05 and EW06) (Figure 13) and PP2-21 (EW-22 and EW23) soil collected from the ploughing layer.

1. Soil DNA isolation kit: Qiagen DNeasy® PowerMax® Soil Kit
2. Accuprime™ SuperMix II, ThermoFischer
3. 5x HOT FIREPol® EvaGreen® qPCR Supermix
4. Fine sand

in silico testing of earthworm primers

An *in silico* test was run using FastPCR software (Kalendar *et al.*, 2017) with the primers for the long and the short metabarcodes, i.e. to assess the coverage of earthworms by the ewA/ewE and ewB/ewC primer sets obtained from Bienert *et al.* (2012). The FastPCR *in silico* run confirmed that both the long amplicons produced by ewA/ewF (428 bp excl. primers) and ewA/ewE (342 excl. primers) cover all common earthworms. Thus, the earthworm species inhabiting the Sallløv field (Table 4) are all detectable by these primers. Moreover, NCBI primer BLAST (Ye *et al.*, 2012), www.ncbi.nlm.nih.gov/tools/primer-blast/, was also used to assess the specificity, and it was concluded that ewA/ewE should be selected for qPCR, as this primer set was more specific for Clitellata, targeting both Lumbricidae and Enchytraeidae, while ewA/ewF created more taxonomically broad coverage addressing Metazoa.

TABLE 4. Sample information and concentration of DNA extracts.

					DNA extraction		
Sample source	**Depth m u.t.**	**Sample**	**Weight, g**	**Content**	**Volume, mL**	**Conc. Qubit ng/µL**	**ng/g**
PP2-1	2.8	EW01	8.303	Matrix soil	5	Too low	
PP2-1	2.8	EW02	0.123	Fracture pore lining	30 µL	0.26	63
PP2-1	2.8	EW03	0.199	Pseudogley	30 µL	Too low	
PP2-1	2.8	EW04	0.074	Fracture	30 µL	0.13	53
PP2-1	2.8	EW05	5.687	PP2-1 Neg.	5	Too low	
PP2-1	2.8	EW06	8.406	PP2-1 Neg.	5	Too low	
Blanks		EW07	2.147	Blank	5	Too low	
Blanks		EW08	3.439	Blank	5	Too low	
PP2-10	1.1-1.2	EW09	9.897	Infilling	5	3.14	1,586
PP2-11	1.1-1.2	EW10	9.254	Infilling	5	3.98	2,150
PP2-12	1.1-1.2	EW11	9.454	Infilling	5	3.05	1,613
PP2-13	1.2	EW12	9.258	Infilling	5	0.449	242
PP2-14	1.2	EW13	9.44	Matrix soil	5	0.277	147
PP2-15	1.2	EW14	9.468	Burrow lining	5	3.67	1,938
PP2-16	1.2	EW15	10.168	Matrix soil	5	0.4	197
PP2-17	1.2	EW16	10.08	Burrow lining	5	0.703	349
PP2-18	1.2-1.30	EW17	0.067	Burrow lining	30 µL	2.89	1,294
PP2-21	0.1	EW18	10.449	Topsoil	5	14.1	6,747
PP2-21	0.1	EW19	9.398	Topsoil	5	15.9	8,459
PP2-21	0.1	EW20	10.118	Topsoil	5	11.8	5,831
PP2-21	0.1	EW21	9.846	Topsoil	5	8.14	4,134
		EW22	9.034	PP2-21 Neg	5	Too low	
		EW23	9.592	PP2-21 Neg	5	Too low	
PP2-1	2.8	EW24	10.083	Matrix soil	5	Too low	
		EW25	0	extraction negativ0109	5	Too low	
		EW26	0	extraction negativ0105	5	Too low	
Negative Control	Matrix soil	Topsoil	Burrow lining and others				

FIGURE 13. Soil lump PP2-1 of about 10 kg dug out from excavation E2 at 2.8 m depth. The grey colour is pseudogley covering an exposed fracture with clear casts of ≈ 0.5 mm wide, and broad, 3 mm wide, root biopores with organo-mineral fillings.

Sample collection and DNA extraction

Four subsamples were collected from topsoil lump PP2-21 and five subsamples from lump PP2-1 (Figure 13) following our protocol on how to handle soil samples while avoiding contamination. Four types of material were identified and sampled from PP2-1 (Figure 14): 1. Matrix soil the large bulk part of the till; 2. Light grey fracture lining of the opened fracture; 3. Pseudogley just underneath the fracture surface; 4. Fracture pore lining.

FIGURE 14. Sampling of the fracture/biopore lining and fracture surface of PP2-1 and three types of material sampled from the block and fracture.

For negative controls, we prepared fine sand by ignition at 550 ˚C for 2 h in in crucibles covered by tin foil, which was when the sand entered into the first procedure step of soil sample handling for DNA extraction. These negative control samples were handled in parallel to the true samples according to the protocol to avoid contamination, ensuring that the contamination risks of the negative controls were identical to the real samples. For positive controls, we used an identical volume compared to the other soil extracts of earthworm tissue DNA extracts,

which were used as positive controls for the earthworm DNA template PCR reactions. Soil DNA was extracted by the DNeasy® PowerMax® DNA isolation kit according to the manufacturer's instruction of the PowerMax DNA isolation kit (QIAGEN, 2016). The DNA concentration was determined with a Qubit 3.0 fluorometer (Thermo Fisher).

Gradient PCR

To optimize the annealing temperature of the PCR with the 16S earthworm marker primer sets, we performed a gradient PCR with the following temperatures for both the soil DNA and earthworm tissue DNA templates with the three primer sets: ewA/ewE (342 bp, 56˚C), ewD/ewE (75 bp, 62˚C), ewB/ewC (30 bp, 61˚C), covering the T_m ranges of either 52 - 64 ˚C or 54 - 64 ˚C (Table 5 and Table 6).

TABLE 5. PCR mix and programme for the gradient PCR.

	Stock Conc.	Volume
H_2O		5
AccuPrime SuperMix II	1x	12
Primer F	10 mM	1.25
Primer R	10 mM	1.25
BSA	10 mg mL^{-}	0.5
DNA	1-10 ng μL^{-1}	5

	95˚C	12 min
38x	95˚C	30 sec
	T_m	30 sec
	72˚C	1 min
	72˚C	7 min

TABLE 6. Sample types for DNA templates and primer sets for the gradient PCR running with T_m from 52 to 64 ºC.

Primer	DNA template material
ewA/ewE	Earthworm tissue DNA
ewB/ewC	
ewD/ewE	
ewA/ewE	Soil DNA from topsoil / EW18[1]
ewB/ewC	
ewD/ewE	

The annealing temperature ranged from 52 ˚C to 64 ˚C. The pure earthworm tissue DNA could not be amplified by those primer sets due to the high DNA concentration, Figure 15. Regarding primer set ewA/ewE, the annealing temperature was between 58˚C - 61˚C, which requires further gradient PCR to test the accurate annealing temperature. An annealing temperature lower than 58 ˚C gives unspecific amplification. The primer set ewD/ewE had an annealing temperature around 60 ˚C. However, it is better to do further gradient PCR to verify it as well, as the range between 58 - 61 ˚C is too big. From the gel image (Figure 15), it is difficult to interpret anything for the primer set ewB/ewC. The annealing temperature for this primer set

[1] See TABLE 4

may be higher than 61 ˚C, as the annealing temperature lower than 61 ˚C produces unspecific amplification.

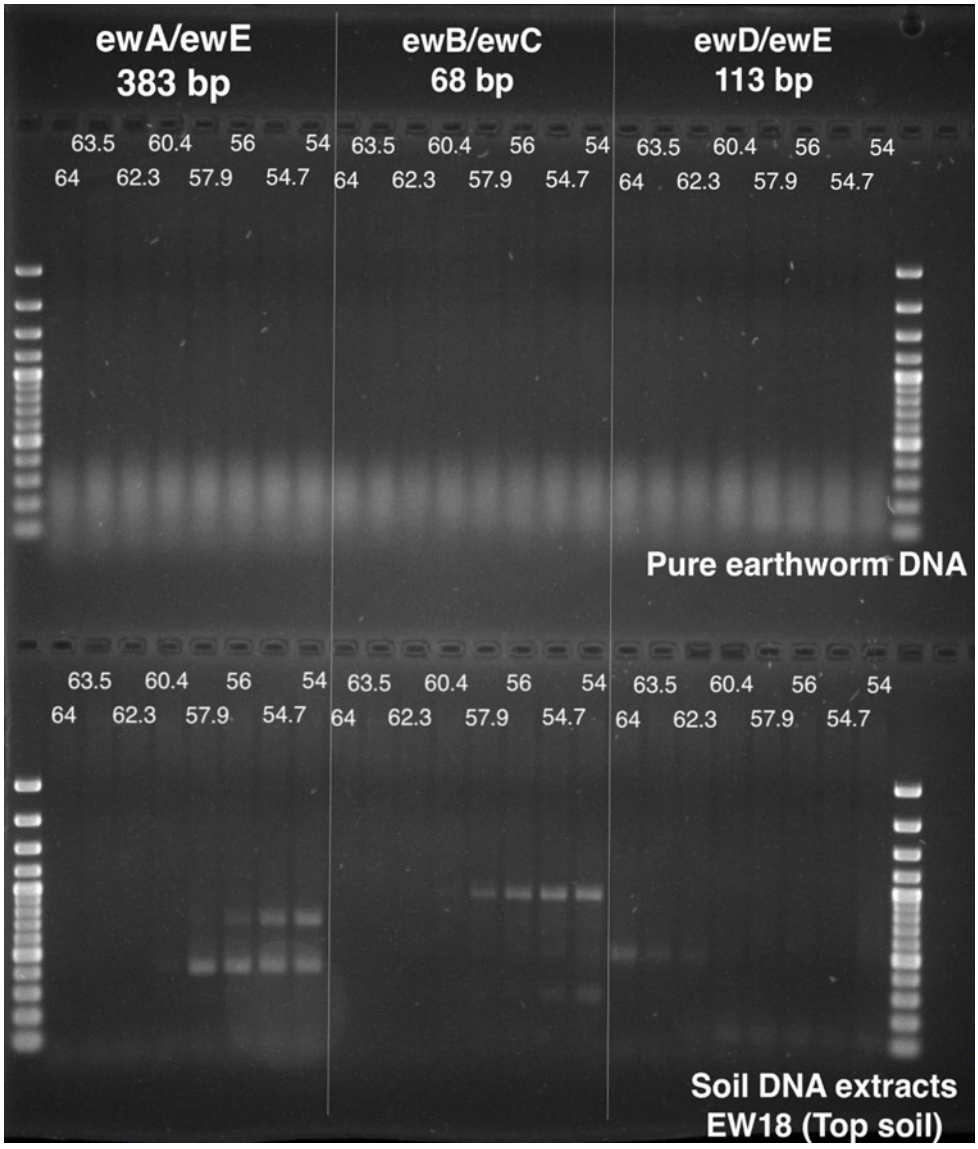

FIGURE 15. Gel showing the PCR products from the earthworm tissue DNA and soil DNA of the temperature gradient created from the three primer sets with approximate DNA string length, bp, including the primer sections: ewA/ewE, 383, ewB/ewC, 68, ewD/ewE, 113, with target regions of length 342, 30 and 75 bp.

qPCR of a short and a long metabarcode

DNA templates from 26 DNA extracts (Table 24) were subject to two qPCR analyses according to the PCR mix and PCR programme shown in Table 7. The selected primer sets and target bp length were ewA/ewE (342 bp) and ewB/ewC (30 bp).

The amplification was performed under thermal cycler conditions displayed in Table 7 in a 25 µL system. The qPCR assays were performed in BioRad CFX Connect™ Real-Time PCR Detection System.

We did not include replicates in the qPCR assay because some samples only had 30 µL DNA extracts, which is not enough to do replication, and the assays aimed for a screening for the presence of earthworm DNA fragments.

TABLE 7. PCR mix and programme for the qPCR.

5x HOT FIREPol® EvaGreen® qPCR Supermix	5 µL	1x
Forward primer 10 µM	1.25 µL	0.5 µM
Reverse primer 10 µM	1.25 µL	0.5 µM
BSA 10 mg mL^{-1} BIO-RON GmbH, Ludwigshafen, Germany	1.5 µL	
Water	11 µL	
DNA template	5 µL	1-10 ng $µL^{-1}$

	Denaturation	95˚C	12 min
50x	Denaturation	95˚C	30 sec
	Annealing	T_m 56 °C ewA/ewE 59 °C ewB/ewC	30 sec
	Extension	72˚C	1 min
	Final extension	72˚C	7 min

2.8 aDNA

Definition of aDNA

"Ancient DNA (aDNA) is DNA isolated from ancient specimens. Due to degradation processes (including cross-linking, deamination and fragmentation) ancient DNA is more degraded in comparison with contemporary genetic material" (Wikipedia).

Sample preparation and DNA extraction

The aDNA analyses were carried out in parallell samples with the ^{14}C and C-isotope analysis (Appendix 3). All aDNA work was carried out at dedicated aDNA laboratory facilities at the Section for GeoGenetics, Globe institute, University of Copenhagen. Samples were delivered in tubes or plastic boxes and brought to our clean lab facilities, while avoiding contamination. See sample list in Appendix 3, Table A3.1 and Table A3.2.

Prior to use and between samples, all materials and working spaces were cleaned with 5% bleach and 70 % EtOH, DNA AWAY™ (Thermo Scientific) and/or UV irradiation.
Up to 200 mg of material was taken from fossil root samples, using sterile scalpels and tweezers, followed by grinding in sterile mortars. For root macropores, soil matrix and Fe-oxide samples up to 500 mg were used for extraction. Macropore linings were carefully scraped off with a sterile scalpel, avoiding the surrounding soil matrix, followed by chopping in aluminium foil or grinding in a mortar to comminute the sample. The same procedure was used for soil matrix samples.

For Fe/Mn-oxide fillings and concretion samples, 500 mg was scraped off using sterile scalpels and was grinded in an agate mortar until pulverized to help release of any captured DNA inside the concretions Fe/Mn-oxides.

For some samples (Table A4.1), *G2 DNA/RNA Enhancer* tubes (Ampliqon PCR Enzymes & Reagents, 1.4 mm beads) were used to increase extraction yield. Two of these samples were extracted twice, one with and one without the use of *G2 DNA/RNA Enhancer* tubes, for comparison of DNA yield. This showed that the *G2 enhancer* was improving the yield with a factor of 8-22.

Digestion and extraction were carried out as described in Wagner et al. 2018 with minor modifications. All samples were digested in duplicates in 1500 µL lysis buffer. To minimize the proportion of modern DNA, root samples were digested for 1 hour, the digestion buffer was then discarded and 1500 µL fresh lysis buffer was added. Extraction was modified for some samples (indicated in Table A4.1) with addition of 2 volumes phenol/chloroform/isoamyl alcohol (25:24:1) added instead of separate phenol and chloroform. These samples were then incubated for 10 min at room temperature followed by centrifugation at 4800 *g* for 10 min. Duplicates were combined on Amicon Ultra 4 centrifugal filters (30 kDa MWCO) (see Wagner et al., 2018). For every 6 samples, a negative control was included for the extraction step.

Post-extraction DNA concentration was estimated on a Qubit 4 Fluorometer (ThermoFisher Scientific) set at High Sensitivity with 1 µL input (Table A4.1).

An inhibitor removal clean-up step was applied for a subset of samples (Table A4.1). This was done using 5 x PB-buffer (MinElute, Qiagen) to 20 µL DNA extract followed by spinning through a Monarch filter tube at 8000 x g for 1 min. Then, 500 µL Inhibitor Removal Buffer from the High pure viral Nucleic Acid large volume kit (Roche) was added to the filter and spun through at 8000 x g for 1 min. 2 rounds of washing was done with 500 µL Wash buffer (MinElute, Qiagen) and spin-down at 8000 x g and a final centrifugation step at 14000 x g for 2 min to dry the filters. After moving filters to new collective tubes, samples were eluted in 30 µL EBT buffer (Qiagen EB-buffer + 0.05 % Tween 20), incubated for 37°C for 15 min and centrifuged for 2 min at 14000 x g.

Library preparation and sequencing

Double-stranded DNA libraries were built following the procedure of the BEST protocol in Carøe et al. (2018) with a final elution volume of 30 µL. Between 7.5 and 32 µL of DNA extract were used as input (> 0.05 – 221.9 ng). Two negative controls were included in the library build.

To determine the optimal number of cycles for the following index PCR (See below), quantitative PCR (qPCR), was performed using an MxPro 3000 qPCR (Agilent Technologies) on the purified libraries in 20 µL reaction mix (1 µL purified library, 10 µL 2 x concentrate Roche LC480 Master Mix (LightCycler® 480 High Resolution Melting Master, Roche), 10 µM of each of forward and revers adaptor targeted primers, and 7 µL Molecular Biology H_2O (Lonza™ Accugene™ Molecular Biology Water). The thermal settings consisted of an initial denaturation step at 95 °C for 10 min, followed by 35 cycles of 30 sec. denaturation at 95°C, 30 sec. annealing at 55°C, and 30 sec elongation at 72°C. This was followed by 1 min. at 95 °C, 30 sec. at 55 °C and 30 sec. at 95 °C with slow ramp to generate a dissociation curve.

Libraries were double indexed and amplified in a 25 µL PCR reaction consisting of 10.5 µL purified library, 12 µL of KAPA HiFi HotStart Uracil+ ReadyMix (2X) and 1 µL of 10 µM forward and reverse primers both with a 6 nucleotide index tag, unique for each sample. Thermal conditions were as follows: 45 sec. at 98 °C for initial denaturation followed by a number of cycles of 15 sec at 98 °C (as determined by qPCR with a maximum of 20 cycles, see Table A3.1), 30 sec. at 65 °C, 30 sec at 72 °C and a final 1 min. at 72 °C. Three negative controls were included in the index PCR.

The amplified libraries were purified using SPRI beads with a sample to bead ratio of 1:6 and a final elution in 35 µL EB-buffer (Qiagen). DNA concentration was estimated on a Qubit 4 Fluorometer as described above followed by further quantification and size estimation on a 2100 BioAnalyzer (Agilent) using the High sensitivity approach.

DNA Sequencing platform

The indexed DNA libraries were pooled in equimolar concentrations in three pools and shotgun sequenced on one lane each on the Illumina Hiseq4000 platform (Illumina®), 80 bp, SR mode. The sequencing was carried out at the Danish National High-Throughput Sequencing Centre, Copenhagen, Denmark.

Data filtering

Adapter sequences were trimmed and paired-end reads were merged using AdapterRemoval (v. 2.3.0)[2]. Using the same program, sequences shorter than 25 bp were discarded and ambiguous bases trimmed at the 5'/3' termini. For metagenomic analyses of plant DNA in the sequencing data, singleton sequences were filtered further with sga preprocess set to filter out low complexity reads with a dust threshold higher than 1.0. This step was implemented to ensure that low complexity DNA in the samples would not result in false positive assignments to species with high contents of simple repeats in the database.

Metagenomic analyses were carried out as described in Seersholm et al. (2016)[3]. Briefly, reads preprocessed by sga were mapped against the NCBI refseq database of full plastid genomes (ftp://ftp.ncbi.nlm.nih.gov/refseq/release/plastid/) using bowtie2[4] set to report up to 500 hits per sequence read. Resulting sam files were then parsed using the getLCA script (https://github.com/frederikseersholm/getLCA), which assigns each read to the taxonomic node of the lowest common ancestor(s) of the best hits to the database.

Phylogenetic analyses and damage patterns

Mapping to the reference chloroplast genome of *Alnus glutinosa* (GenBank acc. no. NC_039930) was carried out using Bowtie2, and analyses of ancient DNA damage patterns were accomplished with mapDamage (Ginolhac *et al.* 2011). Ancient DNA fragments show characteristic DNA damage patterns where particular nucleotid bases are being substituted or transformed towards the ends of the fragment and the extent of such substitutions indicate that the DNA is ancient and not modern precent day DNA. For phylogenetic analyses, mapped reads were sorted (samtools sort) and used to generate consensus sequences (angsd -dofasta 2). Next, consensus sequences in which over 85% of bases could be called were merged with all reference *A.* chloroplast genomes from the NCBI refseq database of full plastid genomes and with the reference genome for *Betula pubescens,* which was included as an outgroup. The resulting fasta file was aligned using mafft (v7.392), and phylogenetic analyses were carried out using MrBayes (v3.2.7a) with a GTR+G substitution model. For each tree, four runs of four MCMC chains were run for 1,000,000 iterations sampling every 1,000 generations. Majority rule consensus trees were constructed using a burnin of 25% (sumt Contype = Allcompat relburnin =yes burninfrac = 0.25) and visualized with FigTree (1.4.2).

Phylogenetic analyses of ribosomal RNA were carried out as described for full chloroplast genomes above, mapping to the ribosomal RNA gene for *A. glutinosa* subsp. *glutinosa* (MF136526). Resulting rRNA sequences were mapped to other *A.* rRNA sequences from Gryta et al. (2017)[6] and to an rRNA sequence of *Malaisia scandens* (MH135781), which was included as an outgroup. In the study fields, there was wheat by E1-E3 in 2017 and 2018. In 2018, there was rape (vinterraps) by E4-E6 and before that wheat.

2.9 Numerical modeling

Numerical modeling of 1D groundwater flow and pesticide migration along fractures and biopores was carried out with the Daisy model (Hansen et al., 2012b). In Daisy, there are two different ways of modelling preferential flow in fractures or macropores, namely "secondary domain" and "biopores". Furthermore, it is possible to model the fractures as a porous medium in a fully discretized way using Daisy in two dimensions.

Overall, the soil is divided into three domains:

1. Primary domain: Matrix, flow is modeled by Richards equation
2. Secondary domain: Small fractures and fractures. Transport is divided with the matrix based on hydraulic conductivity.
3. Tertiary domain: Biopores such as wormholes or old root-channels. Water is moved from high potential to low potential.

Secondary domain model

The secondary domain model corresponds to what is often termed a dual-porosity model or dual-permeability. The column is divided into a primary fraction, representing the matrix, and a secondary fraction, representing the fracture as illustrated in Figure 16.

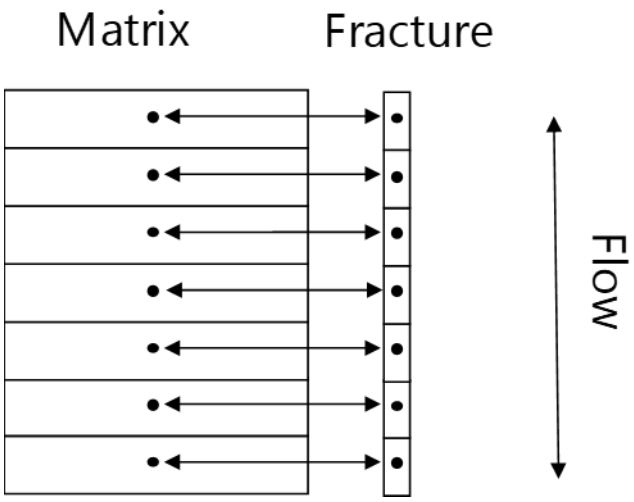

FIGURE 16. Schematic of a one-dimensional dual-porosity model. Horizontal arrows represent mass transfer between primary and secondary domain. Vertical arrow represents water flow.

The model first calculates the flow of water and subsequently the transport of chemical. For the flow of water, the fractures are accounted for by adjusting the hydraulic conductivity and subsequently using the normal 1-dimensional Darcy-equation. The hydraulic conductivity can be adjusted in three ways:

1. By giving the matrix a special hydraulic conductivity - saturation model that accounts for the fracture
2. By setting the conductivity of the factures in the “secondary domain pressure”
3. Or by calculating it using the cubic law-equation, in which case the fracture aperture and the density of the fractures must be provided. It is assumed that fractures are parallel and in one direction:

$$K_{fracture} = \frac{\rho_W g (2b)^3}{12\mu_w} d$$

Where $K_{fracture}$ is the fracture hydraulic conductivity, ρ_w is the density of water, g is the gravitational acceleration, 2b is the fracture aperture, μ_w is the viscosity of water and d is the density of the fractures (inverse of distance between fractures) (Snow, 1968).

In the latter two cases, the models use the maximum of the hydraulic conductivities for either the fracture or the matrix. It could be argued that a more precise way would be to calculate a resulting hydraulic permeability by weighing with the cross-sectional area of the matrix and fracture, respectively. However, the difference in hydraulic conductivities between the two domains is typically orders of magnitude.

To account for unsaturated conditions, the fracture hydraulic conductivity will be zero if the pressure does not exceed a certain limit. When the hydraulic conductivity is provided directly, the pressure limit should also be provided. If the aperture is provided, the pressure limit will be calculated from the equation:

$$h_{limit} = \frac{2\sigma_w}{\rho_w g 2b}$$

where $\sigma_w$is the surface tension of water, ρ_w is the density of water, g is the gravitational acceleration and 2b is the aperture. The equation is based on the assumption of parallel plates.

In the matrix, transport occurs via advection-dispersion. In the fracture, only advection is considered. Since water flow is only calculated for a single domain (a single hydraulic conductivity), this water flow must subsequently be distributed on the two domains to model the transport. The model does this by comparing the hydraulic conductivity at the pressure limit of the fracture with the actual hydraulic conductivity. When the actual hydraulic conductivity is the maximum of the fracture or the matrix hydraulic conductivity, the distribution between matrix and fracture is described by the following equations:

$$q_{matrix} = min\left(1, \frac{K_{matrix}(h_{limit})}{max\left(K_{matrix}(h), K_{fracture}\right)}\right) q_{total}$$

$$q_{fracture} = q_{total} - q_{matrix}$$

This will be inconsistent when the hydraulic conductivity of the matrix is close to or larger than the hydraulic conductivity of the fracture. Because the flow is distributed on both domains, but not directly calculated, the model can be considered a hybrid between a dual-porosity and dual-permeability model.
Mass transfer between the secondary and primary domain is determined by the linear equation:

$$F = \alpha\left(c_p - c_s\right)$$

Where F is the flux between the primary and secondary domain, α is a mass transfer coefficient, c_p and c_s are the concentrations in the primary and secondary domain.

Several processes and effects are lumped into the mass transfer coefficient and should therefore not be seen as a physical parameter that can be measured independently, but rather as a case-specific calibration parameter. In most cases, the mass transfer will be dominated by diffusion, however, the coefficient should also take into account that the primary domain is one single element and not discretized. Consequently, a free water diffusion coefficient cannot be applied directly and, furthermore, the resulting mass transfer coefficient will be flow rate dependent.

Tertiary model (biopores)

In the tertiary domain model or the “Biopore”-model, water is allowed to bypass the matrix by moving directly from one matrix element to another, based on pressure differences when they are connected by a biopore (Figure 17). It is assumed that the hydraulic conductivity of the biopore is so large that there will be no pressure loss in the biopore. The actual pressure in the biopore is calculated from the height of water in the biopore. The flow in the biopore will be limited either by how fast the water can flow out of the matrix at the top or how fast water can flow into the matrix at the bottom. Water can also flow from the bottom to the top.

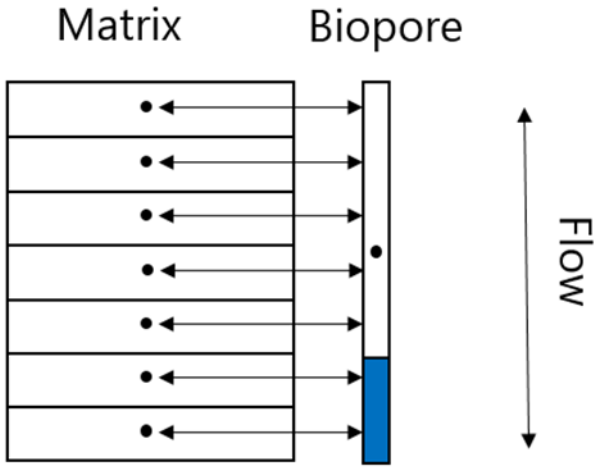

FIGURE 17. Schematic of the “Biopore” model. Arrows represent water flow.

Since the biopore model was developed to model flow in the top soil, it has the limitation that the maximum pressure is equal to the pressure of the corresponding height of a water column. Consequently, one should be careful when using the model for biopores that are not open to the atmosphere. Calibration and evaluation of the model are shown in Appendix 4.

3. Results

3.1 Geology and Groundwater

Figure 18 show the location of excavations and monitoring wells in high-ground (Salløv) and low-ground (Bulbro) study sites, and a North-South geological cross section (A-A´) through the sites.

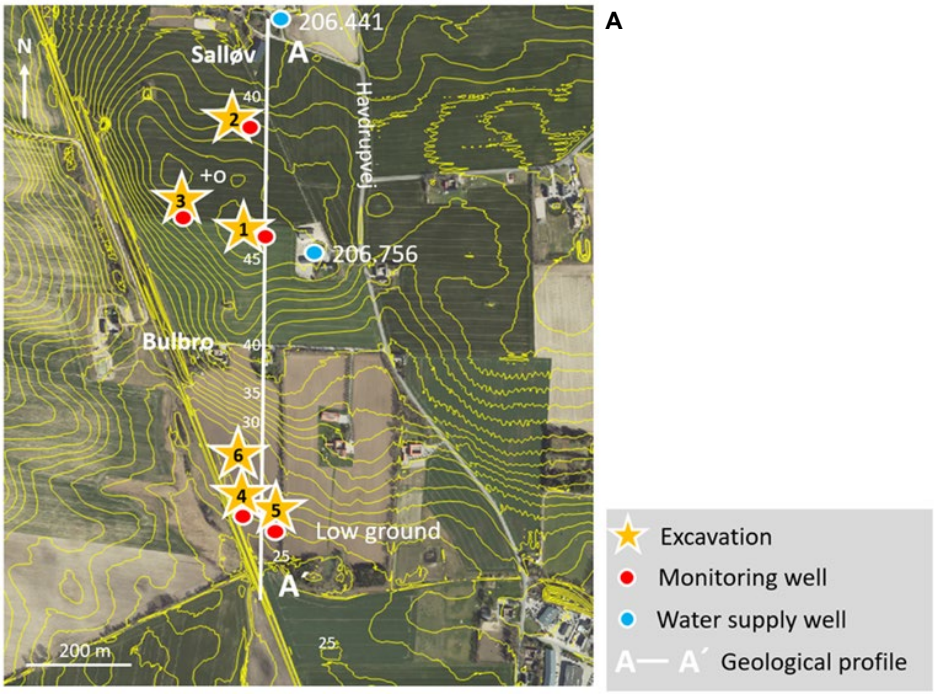

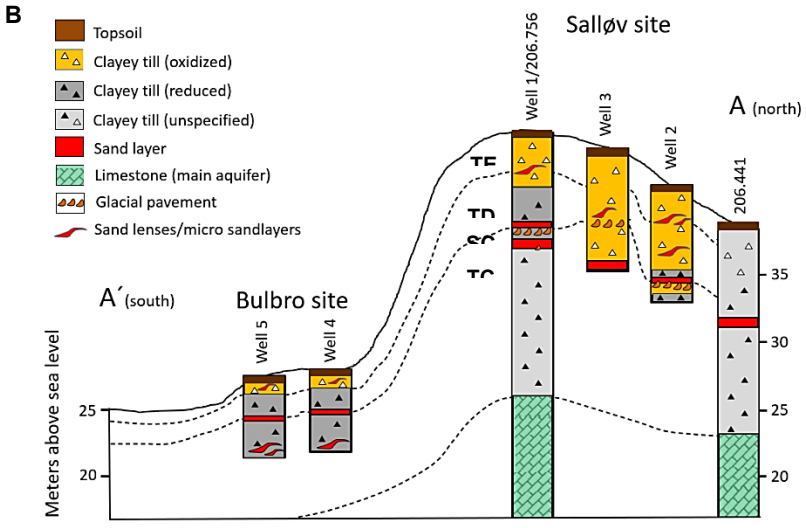

FIGURE 18. Location of excavations/monitoring wells (A) and geological profile (B) of project areas Salløv (high-ground) and Bulbro (low-ground).

In both sites the till layer was dominated by basal moraines (lodgement till). Overall, the till layer was more intensively weathered and oxidized to much greater depth (> 8m) in the high-ground than in the low-ground (< 2 m). The tills exhibited low consolidation in the upper 1-2 m due to weathering, desiccation, biological processes, and local occurrence of ablation till. Below approximately 3 m depth they were generally well-consolidated and dense (Appendix 1). Maximum elevation of the landscape is 42-45 MSL and 25-28 MSL, respectively, for the high and low-ground study sites. The low-ground site is part of the large moraine plain continuing to the south, which includes Havdrup town and the previously investigated Marebæk site (Figure 2). The high-ground is part of a hilly moraine landscape continuing to the north. The geological section A-A´ shows that the surface of the limestone main aquifer in the area largely follows the landscape and is overlain by approximately 14-18 m oxidized and reduced glacial clayey till in the study area. However, large local variation in thickness and composition of the glacial layer, and depth to the limestone aquifer was shown in nearby wells.

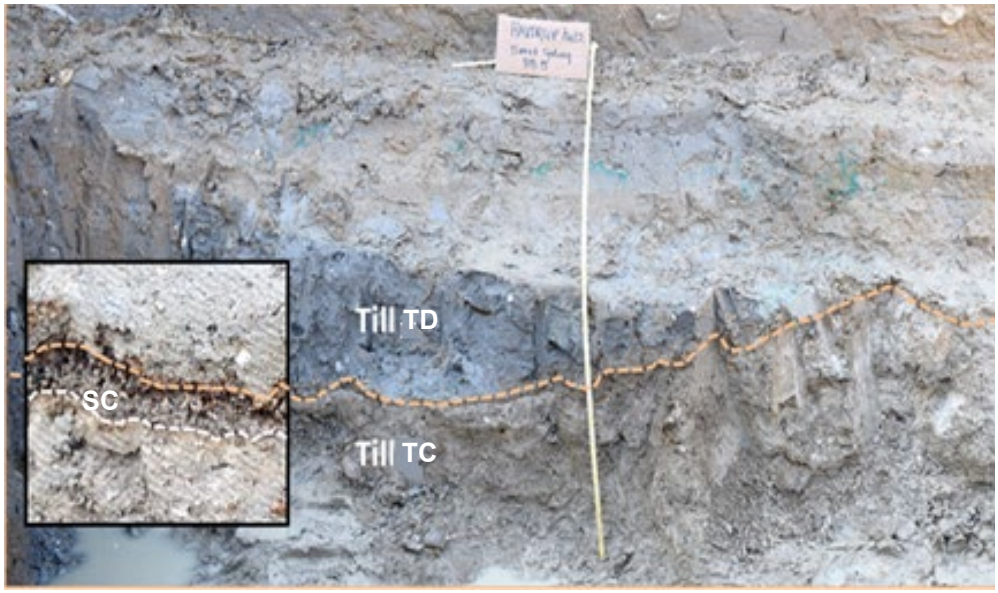

FIGURE 19. Vertical profile in 4.5-6 m depth in excavation E2. Boundary between oxidized (weathered) brown till unit TC (main ice advance in late Weichsel) and overlying pocket of reduced (unweathered) grey till unit TD (Baltic ice advance) (see Figure 2). The two units are separated by the thin SC sand layer (magnified in insert) and marked with dashed line (yard stick is 1.4 m high). The saturated hydraulic conductivity of the clay matix varied with more than 1 order of mangnitude indicating ocurrence of significant heterogenous flow in till matrix. See Figure 18B for explanation of stratigraphic units.

Figure 20 show the geological profiles in the 6 excavations of the study, which were lodgement clayey till, except for excavation 6, which was dominated by meltwater and drift deposits. The high-ground geological profiles (E1-3) were intensively weathered and oxidized locally to more than 8 m depth and dominated by prominent deep vertical and sub-vertical fractures and relic root channes. The profiles had pockets of unweathered reduced till from approximately 3-5 m depth (Figure 19). The saturated hydraulic conductivity of intact cores from the till matrix without fractures or biopores (Table 1) showed differences from $1.7*10^{-9}$ m/s (54 mm/yr) in the reduced pockets to $4.9\text{-}23*10^{-9}$ m/s (155-725 mm/yr) in the oxidized till, which suggest that significant differences of flow in the till was controlled by textural heterogeneity of the matrix. Additionally, sand lenses were common random embedded features in the till sequence, which added further complexity and potential for heterogenous flow. In the low ground, old tree roots and root residual were found along relic root channels to 3.2 m depth. Those are termed paleo-roots or fossil roots in the following.

Figure 21 and Figure 23 show the water tables and hydraulic heads in the monitoring wells (located 10-15 m away from the excavations). In the high-ground there were strong downward hydraulic gradients (Figure 21) and significant difference in seasonally water table fluctuation between the wells; in Well 2 the decline of the water table in summer was > 8 m, while it was only 1-3 m in Well 1 and Well 3. Figure 22 interprets the water tables and hydraulic heads observed in the high-ground wells as representing perched water table conditions in E1 and E3, while the water table in E2 drains off to the underlying aquitard. This suggests that the vertical hydraulic conductivity of the clayey till, and hence, groundwater recharge and vulnerability was higher in the E2 site than in the E1 and E3 sites.

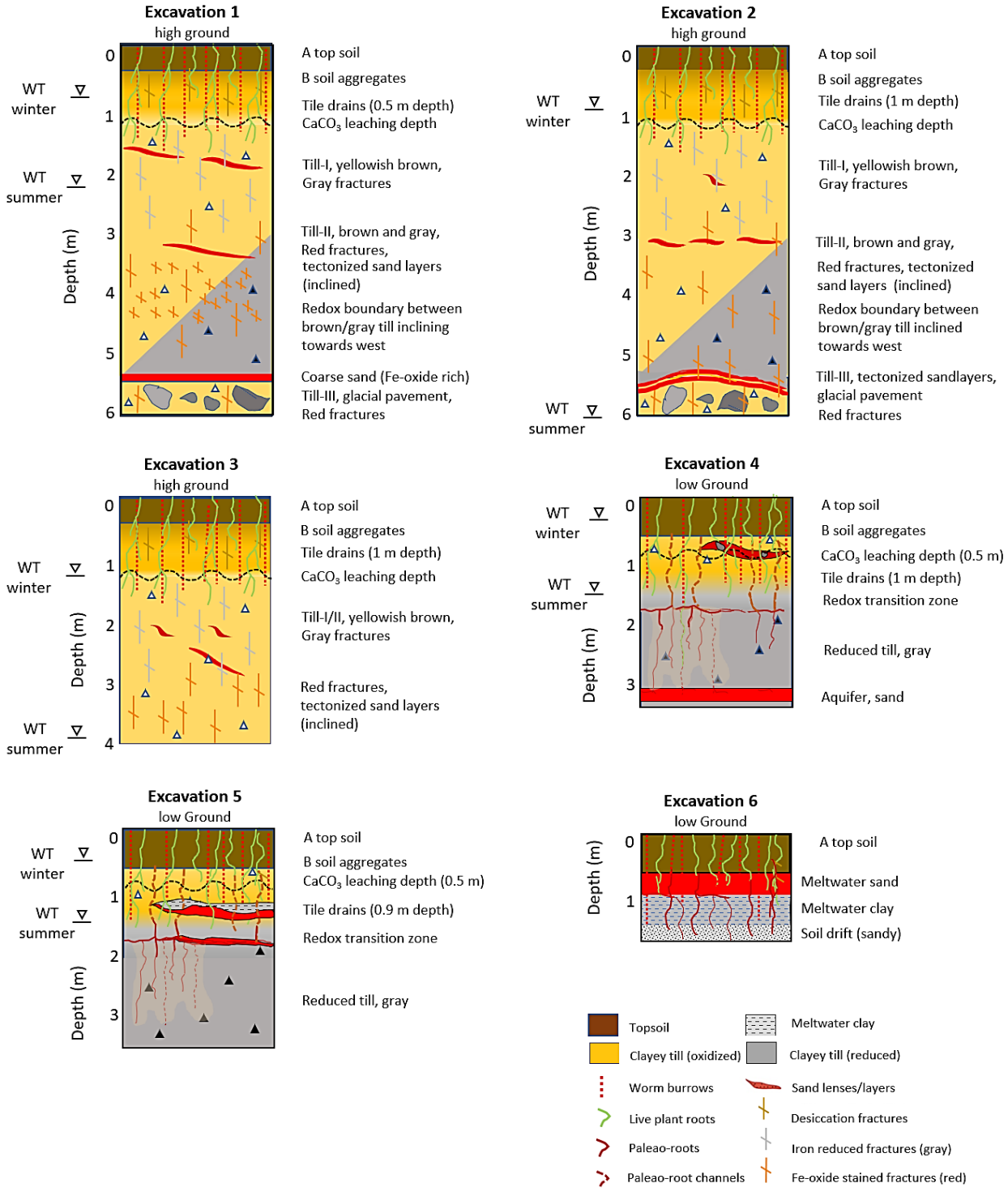

FIGURE 20. Excavations in high and low-ground study sites showing geologic profile, fractures, solitary paleo roots and root channels, live roots and water table fluctuations (WT).

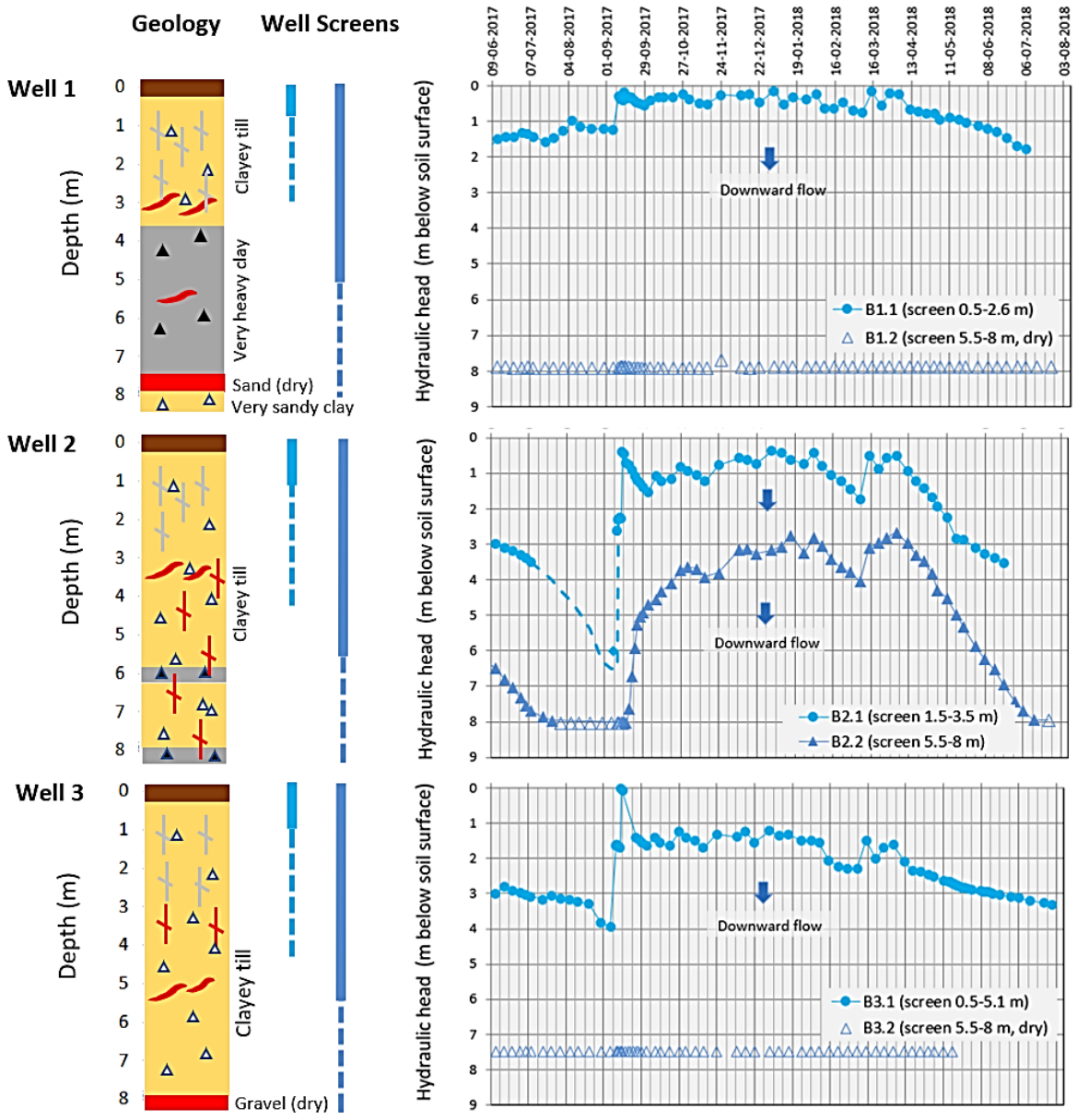

FIGURE 21. Weekly measurements of hydraulic heads and water tables (upper screens) in the high-ground monitoring wells 1 -3. Notice dry lower screens in well 1 and 3 showing perched water tables in till. The wells were located 10-15 m from the excavations.

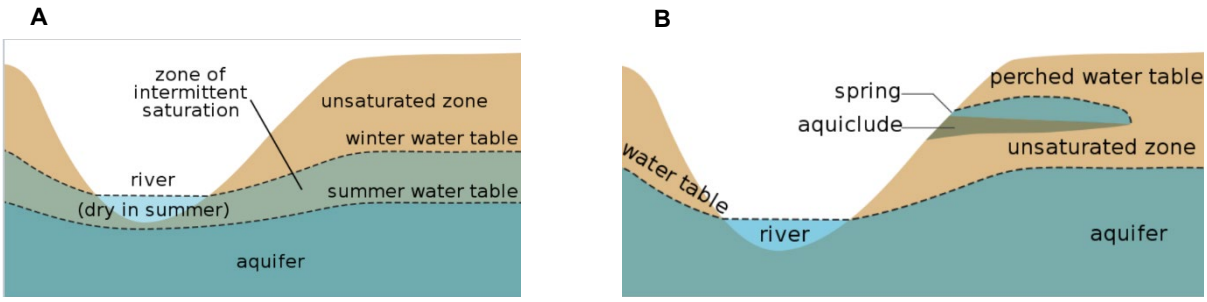

FIGURE 22. Conceptual hydrogeological cross sections representing the observed water tables and pressure heads in the high-ground wells (Wikipedia). (A) Seasonally fluctuating water table in leaky aquitard draining of into underlying aquitard and aquifer (in E2). (B) perched water table with underlying unsaturated zone in aquitard (in E1 and E3).

By contrast, the low-ground excavations in the Bulbro site were dominated by unweathered grey clay from about 1.6-1.8 m depth, which corroborates with the permanent high groundwater tables in this site, Figure 23. Both the water tables and hydraulic heads were governed by the proximity to the hill slope with mainly upward flow controlled by the higher hydraulic heads and groundwater tables in the hill (high-ground area).

The moist conditions had facilitated accumulation of a thicker (and significantly older, see section 3.6) topsoil layer than in the high-ground and visible fractures occurred only to about 2 m depth and were less stained by Fe/Mn-oxides than in the high-ground. Seasonal shift between upward and downward flow was observed in Well 4, while Well 5 had permanent upward flow. Notice also, that the water table in the shallow screen in 1.5 m depth in Well 5 was lower than in the deep screen, which is likely due to tile draining and natural discharge along the abundant sand lenses into the stream by the foot of the hill (Figure 18). By comparison, about 1.5 km further south in the low-ground Marebæk site (Figure 2), groundwater flow was controlled mainly by downward gradients, and the seasonal water table fluctuations were 1-3 m (Jørgensen and Spliid,1998c; Rivad et al., 2001).

Due to the general moist conditions in the low-ground sites as opposed to the Salløv high-ground site, more frequent activation of the root channels as preferential flow paths was likely to occur in the unsaturated zone during summer, than in the high-ground sites with deep seasonal groundwater tables above which any possible surplus of precipitation from e.g., summer rain storms would become absorbed by the less moist matrix to a higher degree (e.g., Jørgensen et al., 1999; Haria et al., 2003; Hansen et al.,2012b).

In both the high and low ground, there was an abundant occurrence of embedded sand layers and lenses with variable size and extension in the tills. The role of such sand layers as flow paths between surficial and deeper ground water was indicated by prominent Fe/Mn-oxide precipitation in some of the inclining sand layers. It is likely that downward flow has been increased by the intense water abstraction from the nearby Thorsbro water wells (Figure 2), which has lowered hydraulic heads in the main aquifer by up to 5-7 m (Krüger A/S, 1989).

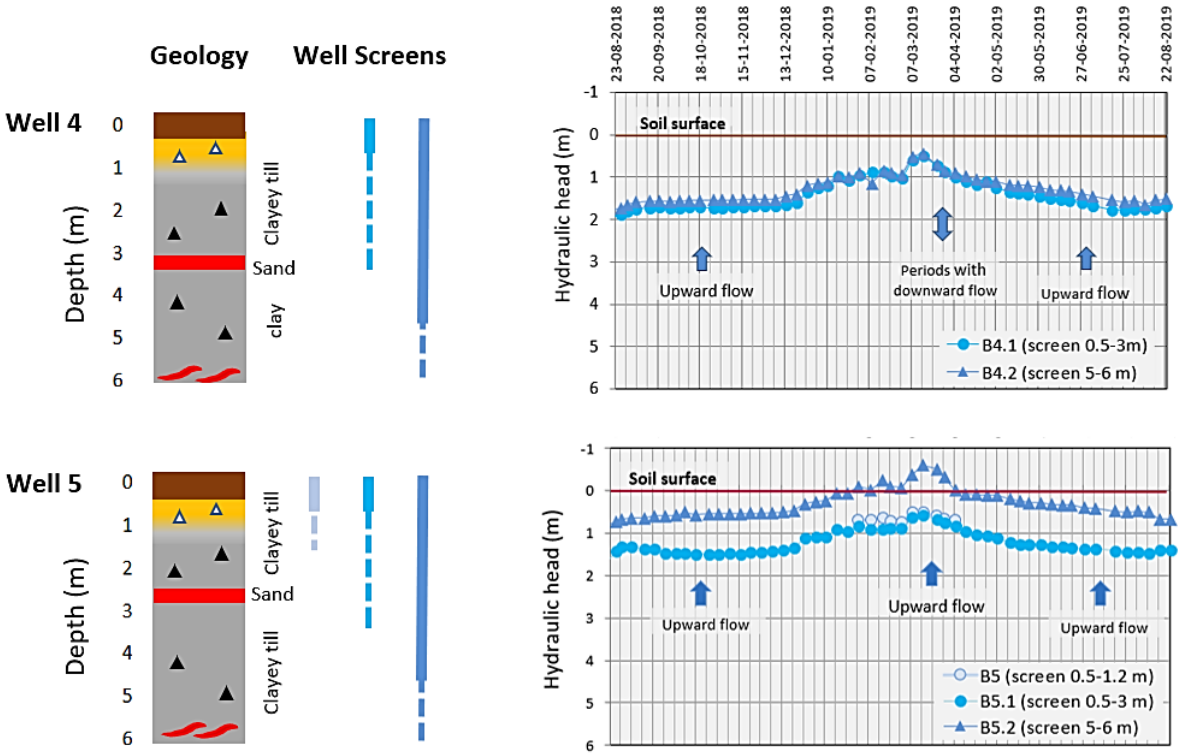

FIGURE 23. Weekly measurements of hydraulic heads and water tables (upper screens) in the low-ground monitoring wells 4 and 5. Notice dominance of upward flow from lower to upper screens and pressure head above the ground surface for the lower screen in well 5. The wells were established 10-15 m from the excavations. Legend in Figure 21.

3.2 Fracture and biopores

In the high-ground excavations, the weathering and downward flow had developed prominent chemical staining of fractures, which were observed locally to more than 8 m depth in monitoring well 2. In contrast, under the unweathered and reducing conditions from shallow depth in the low-ground, fractures were only chemical stained in the upper 1.5-2 m deep.

Figure 24 shows open desiccation fractures in the high-ground E2 profile, which transformed vertically to a grey fracture just below the depth of till drains (1.2 m depth). This profile was also found in the other high-ground excavations. Surficial desiccation fractures followed a polygon pattern with random strike directions to 1.5-2 m depth, while the fractures below were mainly of tectonic origin with directions governed by the depositing glaciers movements (Figure 25). This distribution of fractures resembles previous descriptions from tills by e.g. Jørgensen and Fredericia (1992); Klint and Gravesen (1999); Rosenbom et al. (2005, 2008); Jørgensen et al. (2017); Klint et al. (2013); GEUS (2014).

FIGURE 24. Transition from open brown fractures in the soil to grey fractures in the subsoil environment (high-ground excavation 2). The transition was located immediately below tile drain depth. The grey staining of fractures continued to 2-3.5 m depth.

FIGURE 25. Appearance of Fe/Mn-oxide stained and infilled tectonic fractures (red fractures) in the high-ground excavations. (A) Red fractures on horizontal surface in yellowish brown oxidized till in 3.5 m depth. (B) Red fractures on horizontal surface in grey reduced till in 5 m depth.

In the upper approximately 1-3.5 m of the till profiles, the tectonic fractures were dominated by greyish rims (grey fractures), which were consistently associated with roots and root casts inside the fractures, Figure 26 and Figure 27. Similar grey fracture rims are developed in the upper 2-4 m in most clayey tills and indicates that root channels or casts are occurring inside the fractures. In a transition zone from 2-3.5 m depth, the grey fractures changed to reddish fractures (red fractures) as the result of oxidation of the fracture rims and infilling of the fractures

with secondary Fe/Mn oxides (Figure 25 and Figure 27). Channels after roots were also observed locally inside the red fractures, however, these appeared to be filled or partially filled with Fe/Mn oxides like the fractures (Figure 28).

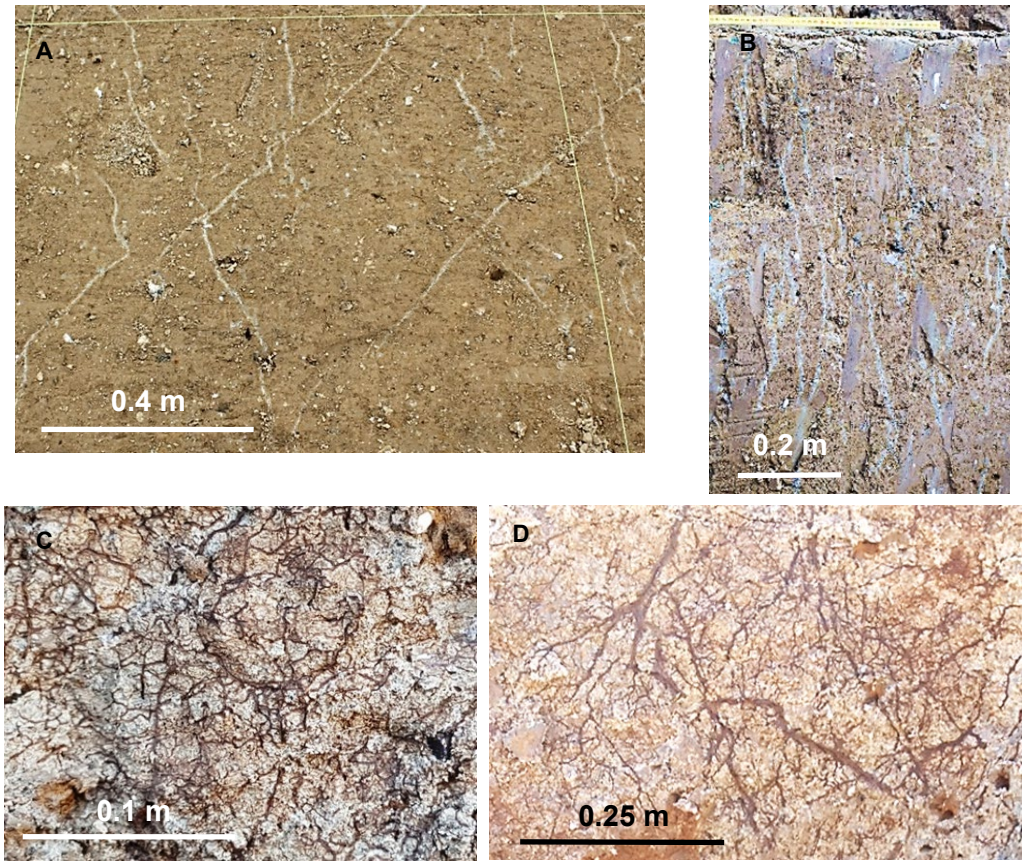

FIGURE 26. Grey fractures and associated root casts in the high-ground glacial till. (A) Horizonal surface with grey tectonic fractures, 2 m depth in excavation 2. (B) Vertical profile with grey fractures, 1.2-2 m depth in excavation 2. (C and D) Examples of root casts inside vertical fractures, 2-2.8 depth in E2 and E3, respectively.

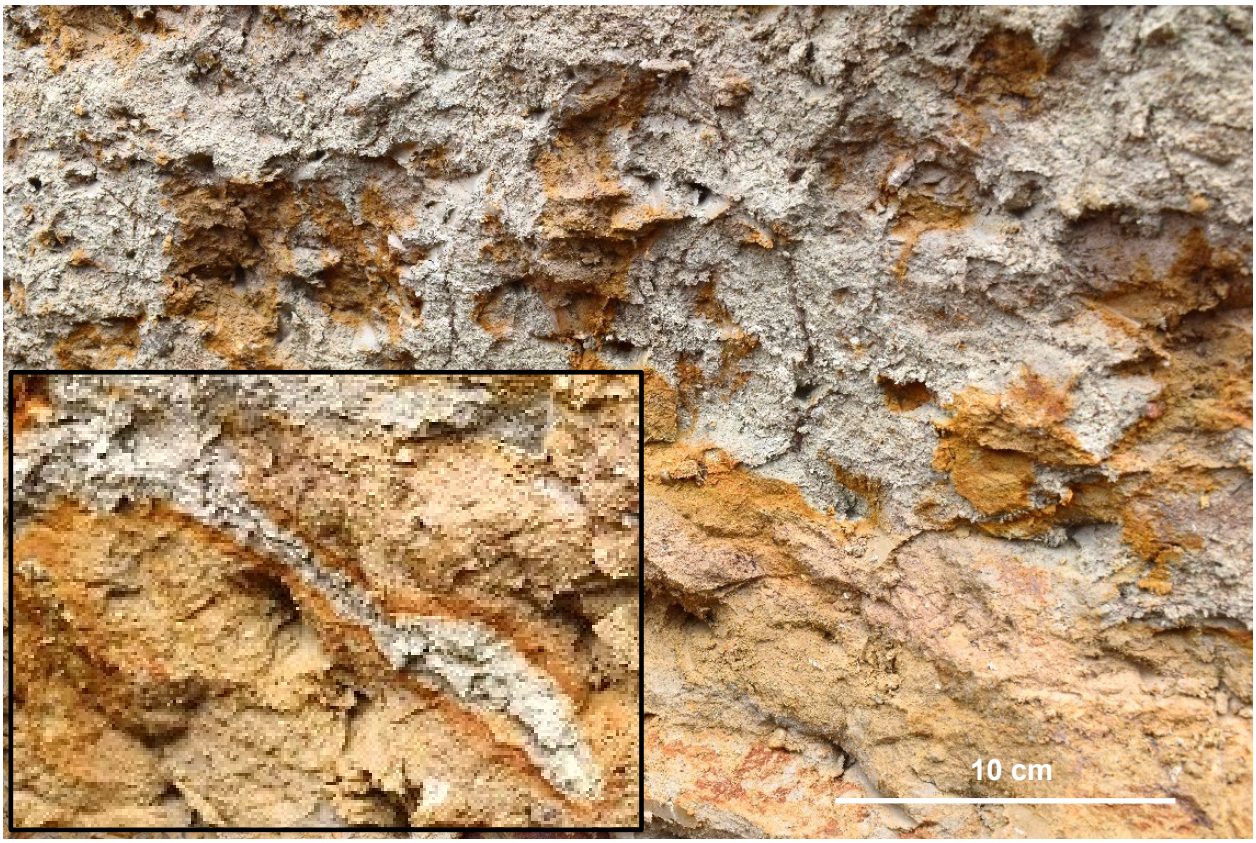

FIGURE 27. Exposed inside of vertical fracture (scale 0.5 m across photo) showing the transition from grey to red fracture staining (2.8-3 m depth in excavation 2). Magnification (x3 in frame) shows details of grey and red redistribution of secondary Fe/Mn-minerals developed around a root-cast by pseudogleying (described further by e.g. Jørgensen and Fredericia 1992 and Jørgensen et al. 2017).

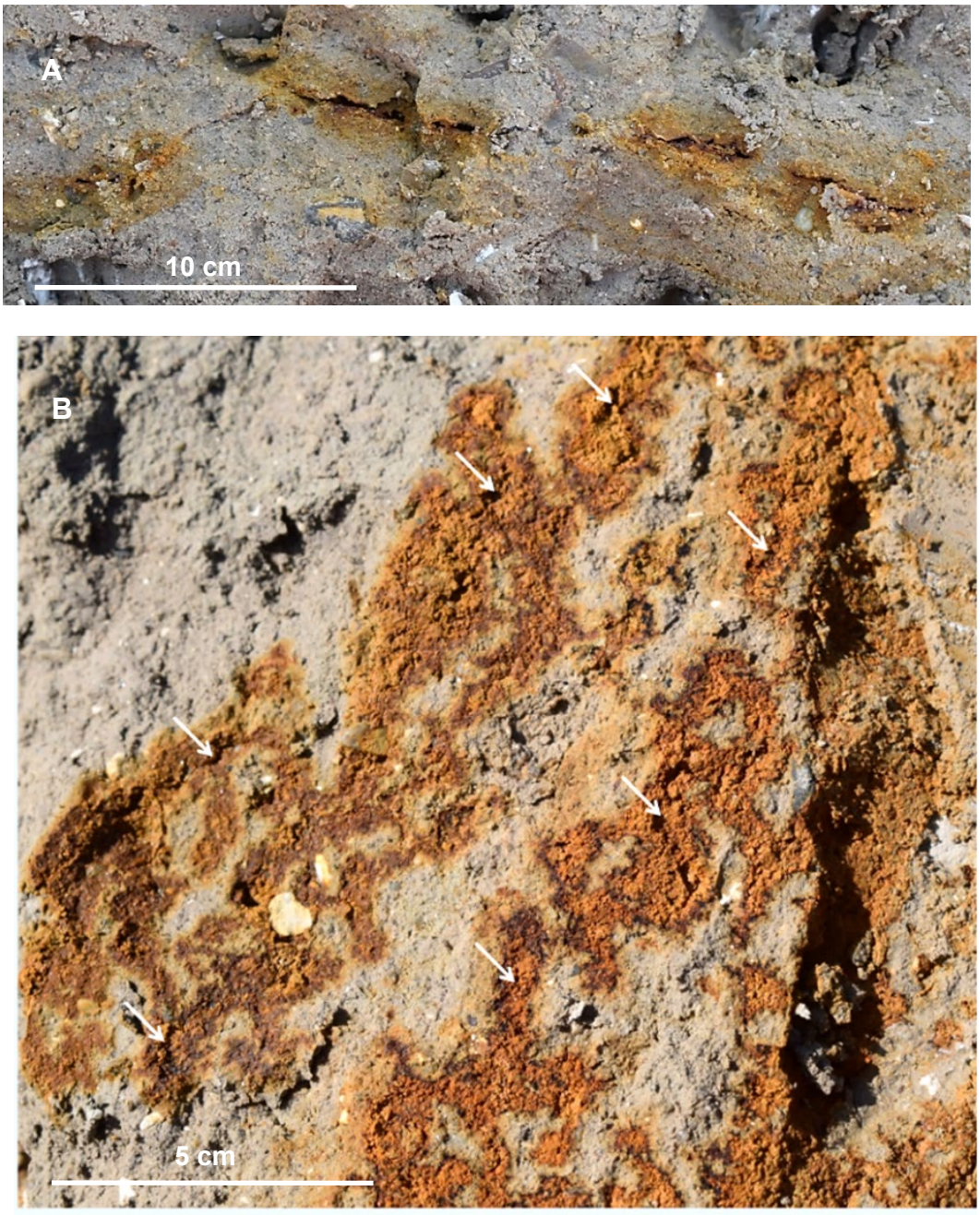

FIGURE 28. Channels inside red fractures (photos 15 cm across). (A) Vertical fracture on horizontal surface in reduced till with partially Fe/Mn-oxide infilled channels. (B) Exposed surface of fracture wall with root channel segments (arrows) infilled with Fe/Mn-oxide precipitate in 5-5.2 m depth. Origin of the channels from ancient willow tress/scrub was suggested from findings of aDNA inside and along the channels (section 3.6.3).

Fracture frequency

Figure 29 shows the overall distribution of fractures on excavated horizontal surfaces in the high-ground excavations. The fracture intersections with the horizontal surface (geological strike) were consistently NW-SE and NE-SW as conjugating sets of fractures. The movement of glaciers that formed the fractures is parallel to the bisector between the two strike direction, which suggests an SE direction of the advancing ice of the deposition. This direction was further supported by fabric analyses of stones in the E2 profile carried out by Aamand et al. (in

prep. 2020), which support an origin of the tills from young Baltic ice advances. Moreover, Figure 31 shows fracture spacings recorded in the high and low-ground excavations. Those reveals that the tills in the high-ground were intensively fractured, while visible fractures only occurred in the upper approximately 1.5-2 m depth in the low-ground. In the previous low-ground study site of Marebæk, 1.5 km further to the south from the hill slope (Figure 2) fracturing similar to the fracturing in the high-ground was observed to 5-6 m depth (Jørgensen et al., 2004c).

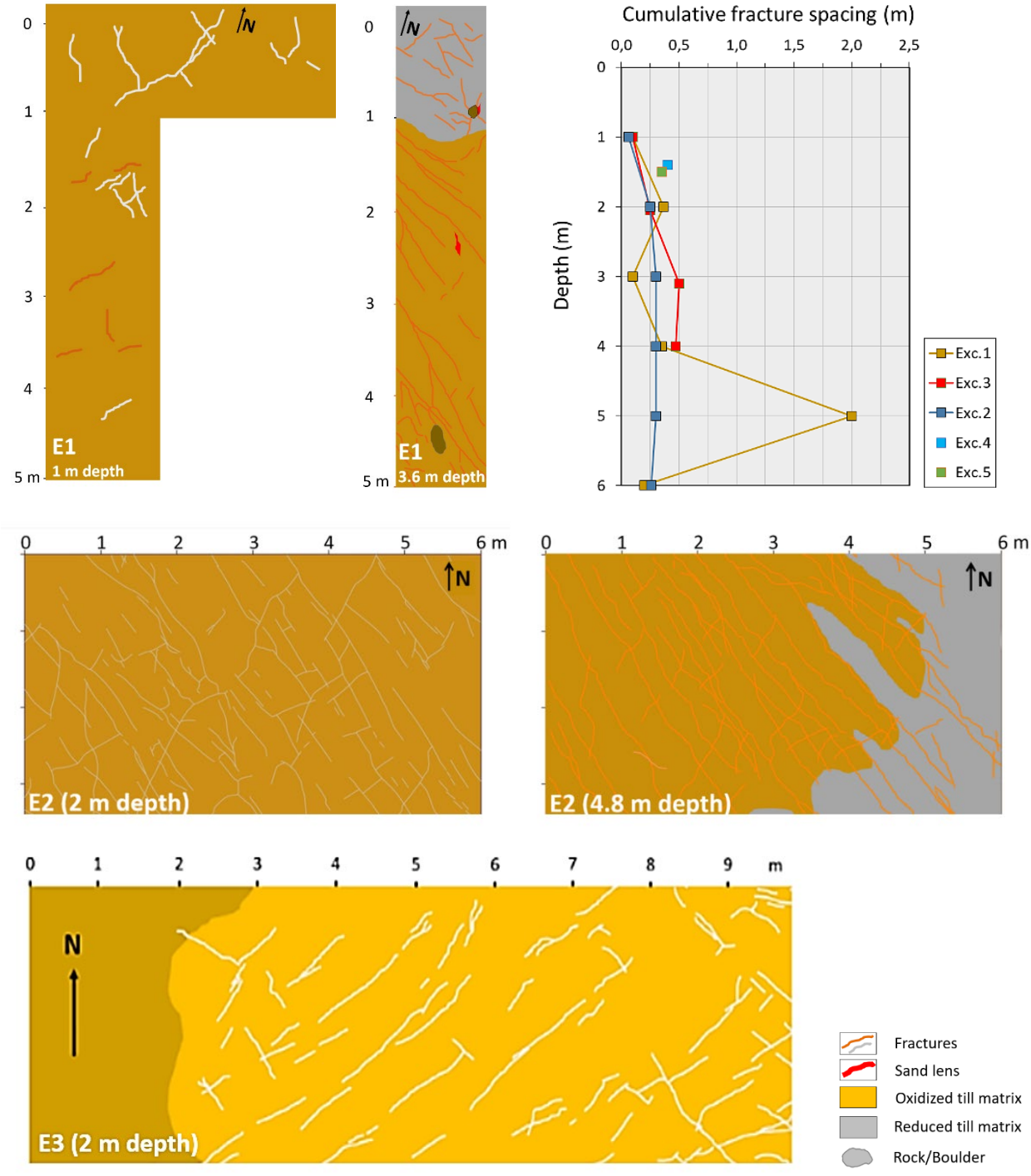

FIGURE 29. Fracture frequencies and spacings measured in excavations E1-E5.

Biopore frequencies

Figure 30 and Figure 31 show the frequency and diameter of biopores in excavations 1-5 and additionally the frequency of root casts along fractures in excavations 1-3. In general, there was a high frequency of solitary biopores in the upper meter dominated by small biopores (< 4 mm) mainly from roots. The frequency had a local minimum in 0.1 m depth (plow layer), which was due to mechanical soil treatment, while a larger number of biopores were preserved immediately below plowing depth (see also Jørgensen et al. 2017).

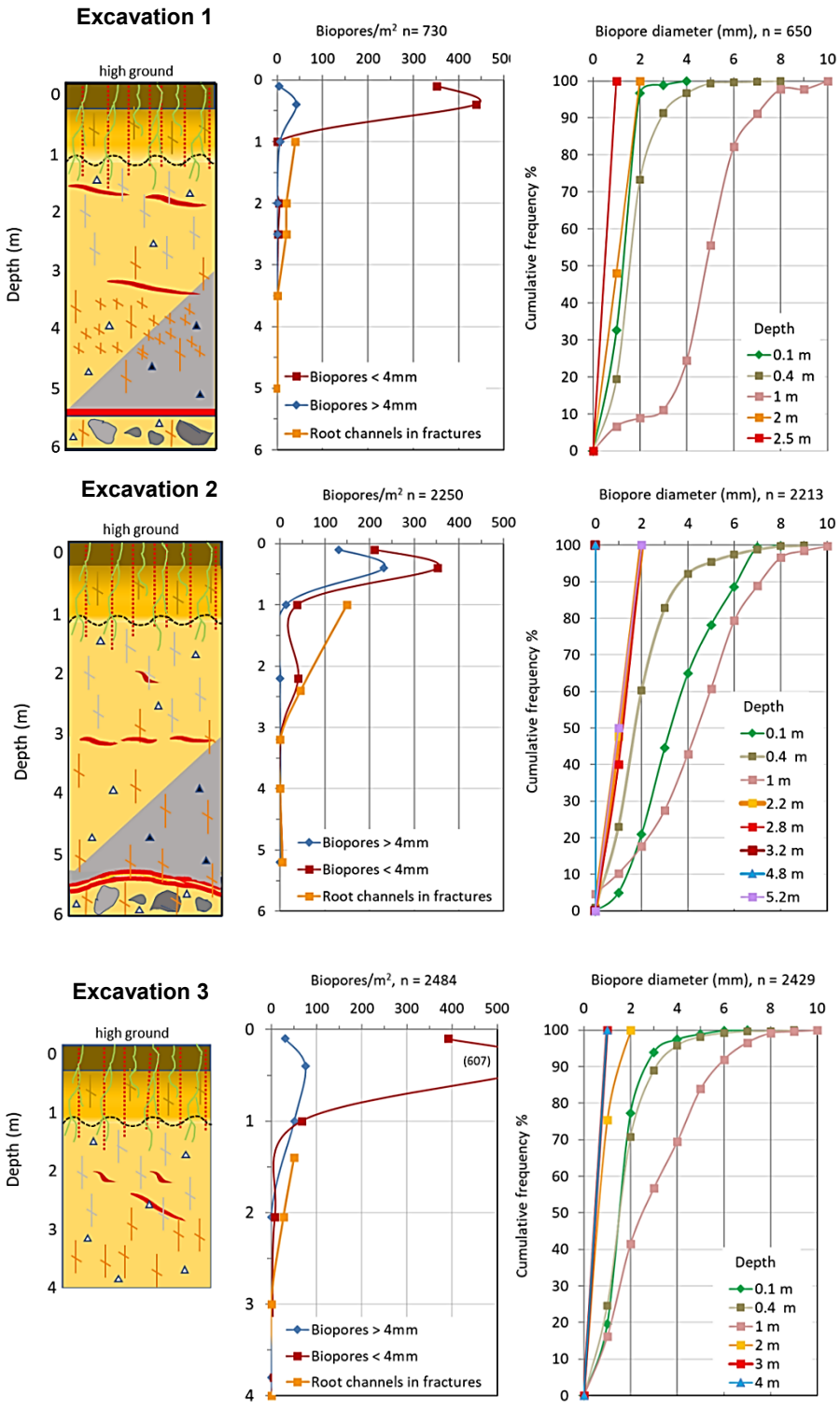

FIGURE 30. Geological profiles, biopore density and pores size distribution versus depth in the high-ground excavations.

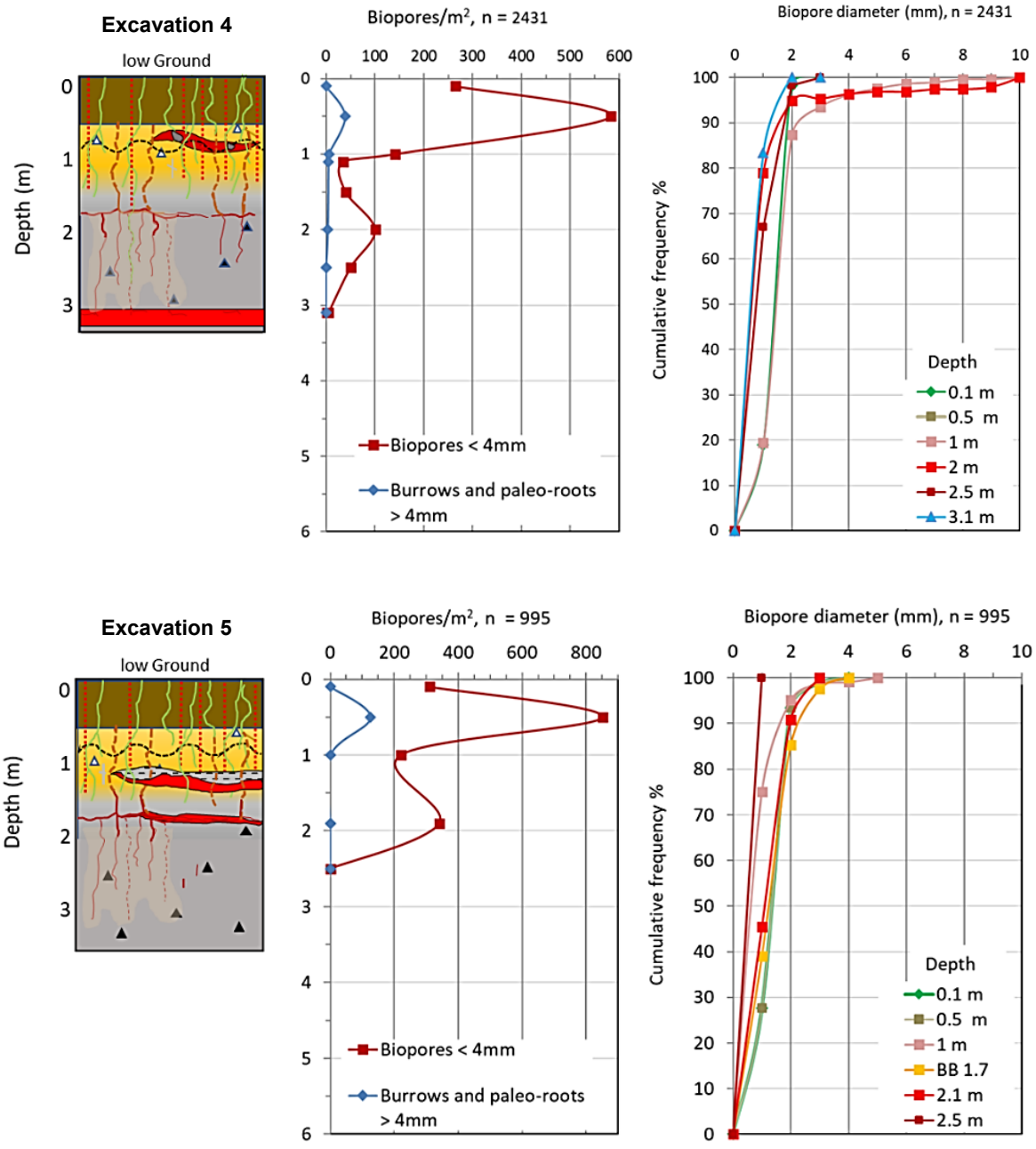

FIGURE 31. Geological profiles, biopore density and pore size distribution versus depth in the low-ground excavations.

The frequency of biopores > 4mm was similar in the high- and low-ground, however, the largest earthworm burrows (6-10 mm) were few or absent in the low-ground (cumulative frequency of diameters in Figure 31). The lack of the largest worm burrows was most pronounced in excavation 5, where the groundwater table is highest and ground water pressure head is above the soil surface in winter. This suggests that the moist conditions in the low-ground are, or have been, unfavorable for large anecic earthworms such as *L.terrestris/herculeus* and *A.longa*.

The maximum depth of biopores in the high-ground excavations was 2.5 to > 5-6 m and were to some degree folllowing the maximum depth of seasonal groundwater table in the tills (Fig-

ure 21). The majority of the biopores were concealed as macropore channels inside the fractures and could not be observed by eye below 2.5-3 m depth because the biopores and fractures were filled with Fe/Mn-oxides (next section). The biopores/root channels were, however, identified by XRT CT-analyses of the intact till blocks collected from the profile (Figure 69 to Figure 73).

3.3 Geochemistry and redistribution of Fe/Mn-oxides

Figure 32 shows the vertical succession of fracture staining from bleached fractures (surficial grey fractures) to Fe/Mn-oxide stained fractures (deep red fractures) in the high-ground excavation E2. The succession from grey to red fractures was in agreement with the conceptual geological model shown in Figure 2. This assumes reductive dissolution of the Fe/Mn-oxides by pseudogleying processes in the grey fractures (Figure 32A and B) and redistribution of the Fe and Mn into the oxidized fracture rims along the grey fractures and deeper in the geological profile by infiltration into the red fractures (Figure 32 A-C) (e.g., Jørgensen and Fredericia, 1992; Westergaard et al., 1997; Jørgensen et al., 2017).

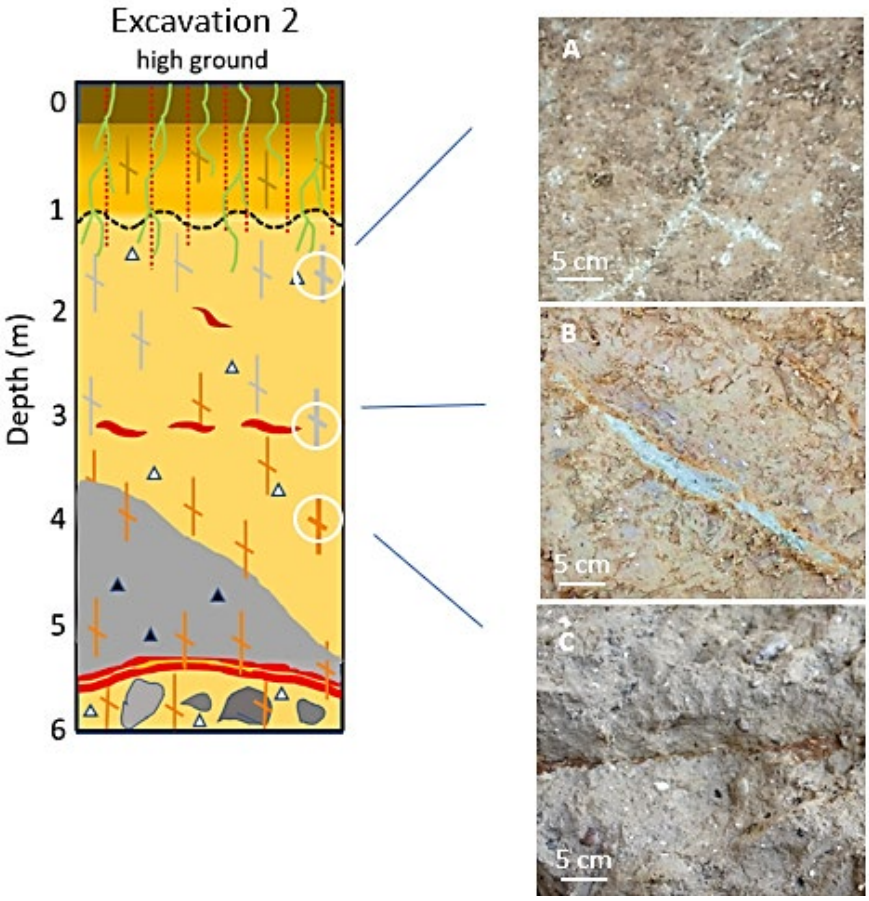

FIGURE 32. Vertical succession of geochemical staining and filling of the fractures investigated in geochemical and XRD analyzes in Excavation 2. (A) Bleached fractures in 1.7 m depth, (B) Fracture with bleached and Fe/oxide enriched rims in 3.0 m depth. (C) Fe/Mn-oxide filled fracture in 3.7 m depth.

Figure 33 shows concentrations of selected chemical elements in profiles across the fractures, fracture rims, and into the matrix in the vertical succession shown in Figure 32 and Appendix 2 (Table A2.1).

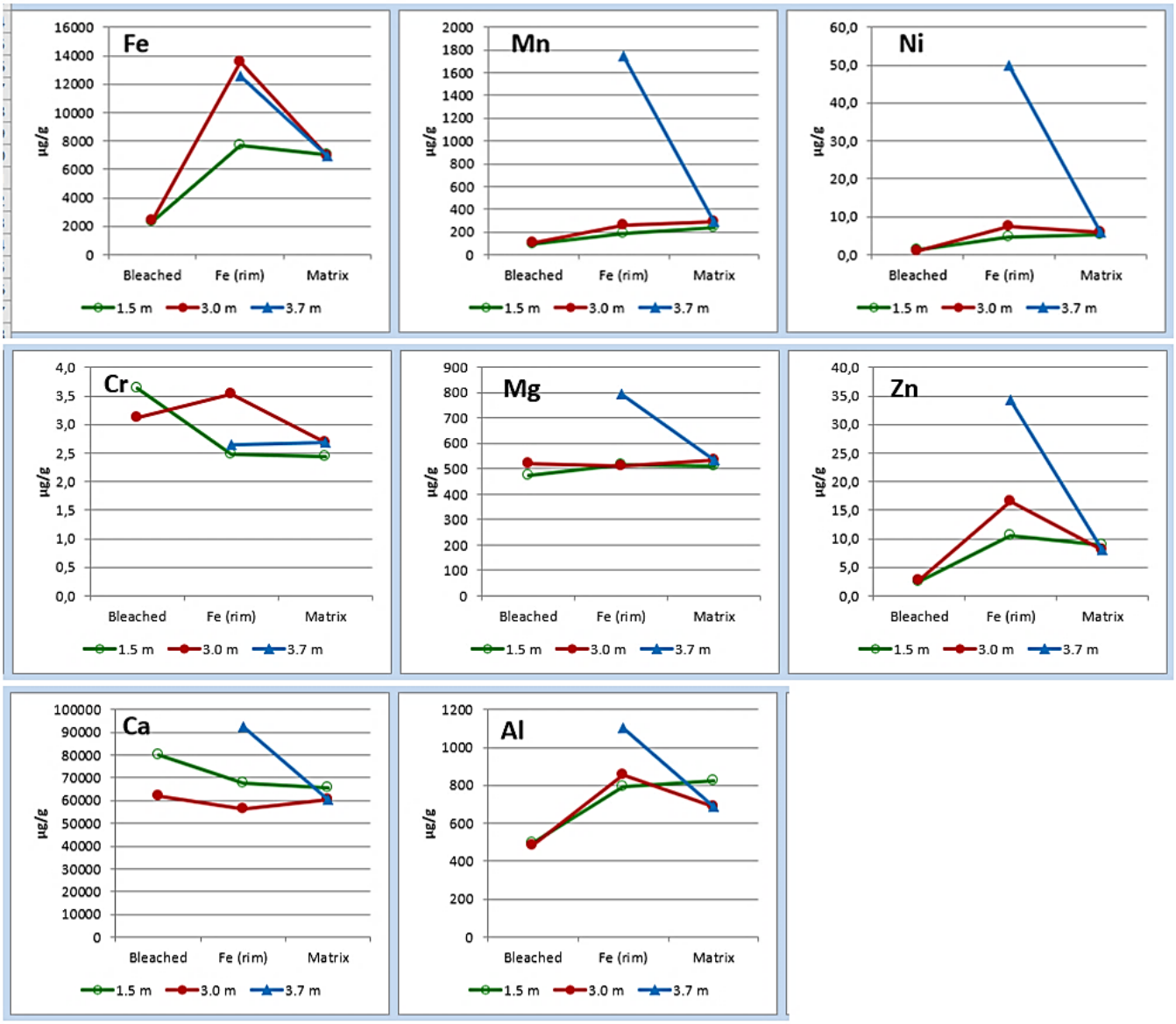

FIGURE 33. Concentration of selected major elements in the fractures, fracture rims and adjacent clay matrix shown in Figure 32.

The observed variation across the fractures is most distinct for Fe associated with the depletion in the bleached material in 1.5 and 3.0 m and accumulation in the Fe-oxide rim in 3.0 m compared to the matrix. In 3.7 m, the Fe-oxides were accumulated inside the narrow fracture with the same content as in the Fe-oxide rim in 3.0 m, and no bleached material was found. The content of Al and Zn followed the same distribution pattern as Fe, but with smaller differences between depletion and accummulation. For Mn and Ni, some depletion was determined in the bleached material in 1.5 and 3.0 m, but only accumulation at the fracture face in 3.7 m. For Mg, the accummulation in 3.7 m was distinct, whereas Ca and Cr show little redistribution. The Ca accummulation in the bleached zone in 1.5 and 3.0 m most likely originates from liming of the agricultural field which showed accummulation at the fracture surfaces at all three soil depths.

Mass balance and time scale of Fe-oxide redistribution

Figure 34 shows the concentrations for Fe and Mn combined with the widths of rims and fillings along the the vertical sequence of grey fractures and red fractures in Figure 32 and Figure 33. Assuming downward vertical transport and re-precipitation of Fe/Mn in the geological profile (described by Jørgensen and Fredericia, 1992, and Jørgensen et al., 2017) the mass-balance was estimated between depleted Fe from grey fractures (upper 3 m) and accumulated Fe in the red fractures (3-8 m depth) based on the total mass of Fe in the fracture rims and fillings (Figure 34).

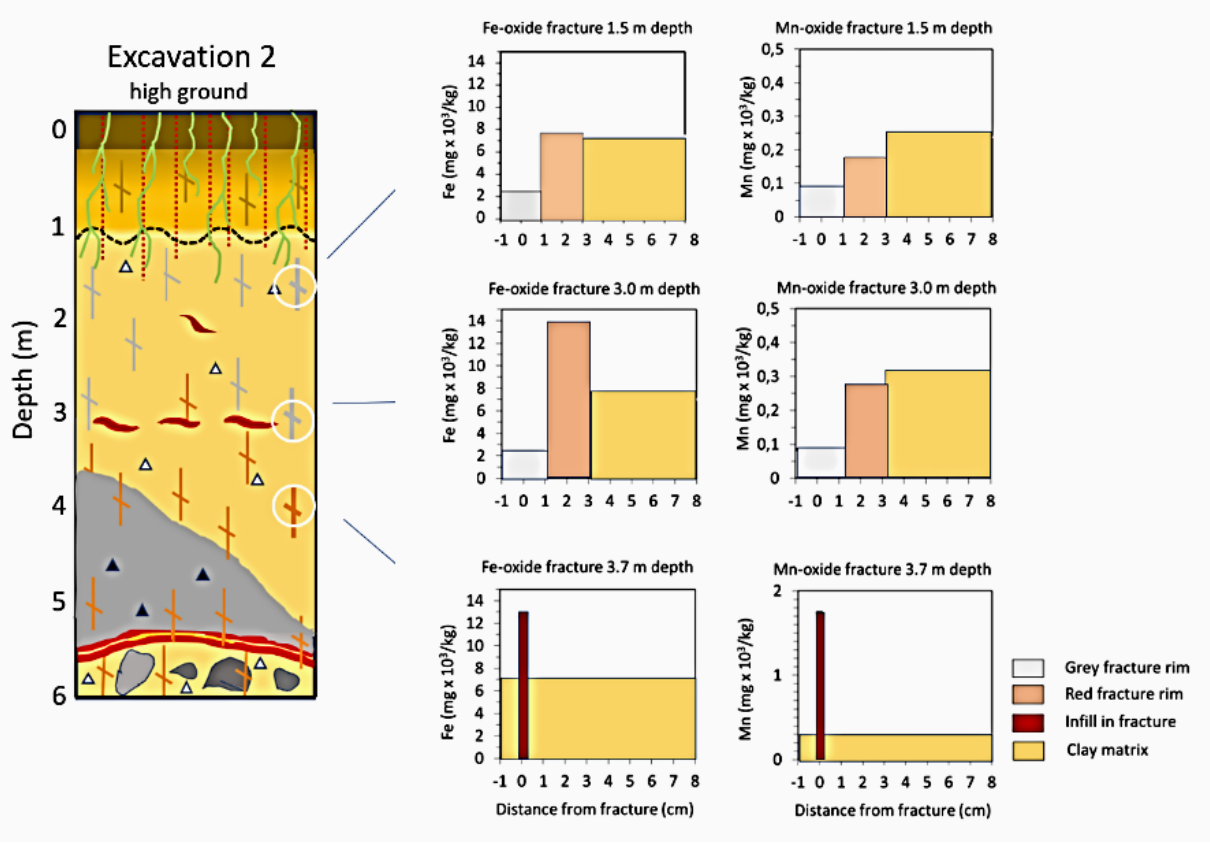

FIGURE 34. Concentration of Fe/Mn-oxides in rims along grey fractures (1.5 and 3 m depth) and fillings in red fractures (3.7 m depth).

Table 8 shows the mass balance estimate and the key-measures that it was based on. The estimate shows that Fe mass acummulated as filling in the red fractures correspeonds to 49% of the mass depleted from the grey fractures above. Hence, the estimate suggests that 51% of the Fe has been lost from the profile, which may be due to removal with interflow and flow into underlying ground water. Furthermore, Table 8 shows the minimum time estimated for accumulation of the Fe filling in the red fractures. The estimate was based on the measured maximum Fe concentrations in water samples from monitoring wells 1 and 2 (Appendix 2, Table A2.2), which were assumed to percolate the fractures with the maximum recharge (300 mm/yr). The minimum time required to build up the Fe-filling using this estimate was 2 to 21 kyr, which suggests that the fractures and root channels inside were likely at least several thousands years old. The same distribution of Fe/Mn-oxide concentrations as in Figure 34 along the fractures was shown in the previous Marebæk site by Jørgensen (1990).

The estimate was intented to indicate the span of time required for the observed redistributing the secondary Fe/Mn-oxides rather than provide accurate dating, which was not posssible due to significant variability of the parameters used for the estimation (e.g. Fe-concentrations in the

groundwater, variability of thichness of rims and fillings, etc). The rate of Fe-redistribution has most likely been decreasing over time, as the most reactive Fe-minerals have been degraded by weathering first and left behind the less reactive minerals, which define the current Fe-concentrations in the pore-water. Therefore, the estimate more likley indicate the time required if new channels were formed from live forest until the Fe/Mn fillings would be reestablished after a deforestation. However, despite uncertainties, the estimates support the geological interpetation that the fillings in red fractures and root channels are probably ancient features, which likely back-dates the Fe/Mn filled root channels to pre-historic time and hence with possible origin from the ancient forest covering most of Denmark.

TABLE 8. Estimated Fe-mass balance and time range for development of Fe/Mn-oxide fillings in red fractures in E2. Values used for estimation of the time required for building up the red fracture fillings are shown in **bold**.

Key-values of estimation	**Min**	**Max**
Total depth of soil column in calculation (m)	8	8
Frequency of fractures in geological profile (m^{-1}) (Figure 30)	0,07	4
Width of Fe/Mn-oxide rims along grey fractures (1-3 m depth) (m)	0.01	0.04
Width of Fe/Mn-oxide fill in red fractures (3-8 m depth) (m)	0.0025	0.0025
CBD-Fe in fracture rims and fracture fill (mg/kg) (Figure 34)	2347	13583
Depletion of Fe mass along grey fractures in 1-3 m depth (g/m^3)	1070	1070
Accumulation of Fe mass in red fractures in 3-8 m depth (g/m^3)	525	**525**
Total Fe in percolating porewater 1-3 m depth, Well 3.1 (mg/L)	0.002	**1,5**
Total Fe in percolating porewater 3-8 m depth, Well 3.2 (mg/L)	0,0002	**0.2**
Net recharge (percolation), ($m^{3/}m^2$)	0.05	**0.3**
RESULTS		
Mass-balance of Fe redistribution between grey and red fractures (above and below 3 m depth) (g/m^3)	545	545
Fe lost with interflow and into deeper groundwater (%)	51	51
Estimated min. time for accumulation of Fe-oxides in red fractures (3-8 m depth)	2,306 – 21,089 years	

Jørgensen and Fredericia, 1992; Ernstsen, 1998; Jørgensen et al., 2017 have described the distribution and chemical weathering of clay minerals along fractures in clayey till profiles. From those studies, it may be inferred that the orginal Fe source in the Fe-oxides were iron-rich chlorite minerals in the till, which caused the yellowish brown color of the oxidized till when weathered. This is corroberating with studies of similar tills by e.g. Quingly and Ogunbadejo (1976) and Cherry (1989). After and alongside with the weathering of the chlorite minerals, the bleached rims (grey fractures) and associated vertical Fe/Mn redistribution in the profile was developed by pseudogleing processes driven by decay of root organic matrial (Figure 27) and seasonal fluctuating ground water tables. The proces is described in further detail by Jørgensen & Frederica (1992); Westergaard & Hansen (1998); Jørgensen et al. (2004b, 2017).

3.4 Roots from crops and trees

Investigations in the PESTPORE study by Jørgensen et al., 2017 showed that live roots from fodder radish were reusing up 60% of pre-existing biopores to approximately 3.2 m depth. Figure 35 shows frequencies of live roots in pre-existing biopores in the current excavation sites. 10 – 80 % of the biopores were reused by live roots from the current crops (wheat, barley and rapeseed) with maximum depths of 2-3 m. Those represents a significant accessible biomass of reduced organic carbon for reductive Fe/Mn-oxide bleaching of the grey fractures and biopores during high-groundwater tables in winter (Figure 21). Figure 36 shows examples of live roots in the pre-existing root channels, which connected the deeper macropores as open flow paths to the soil surface.

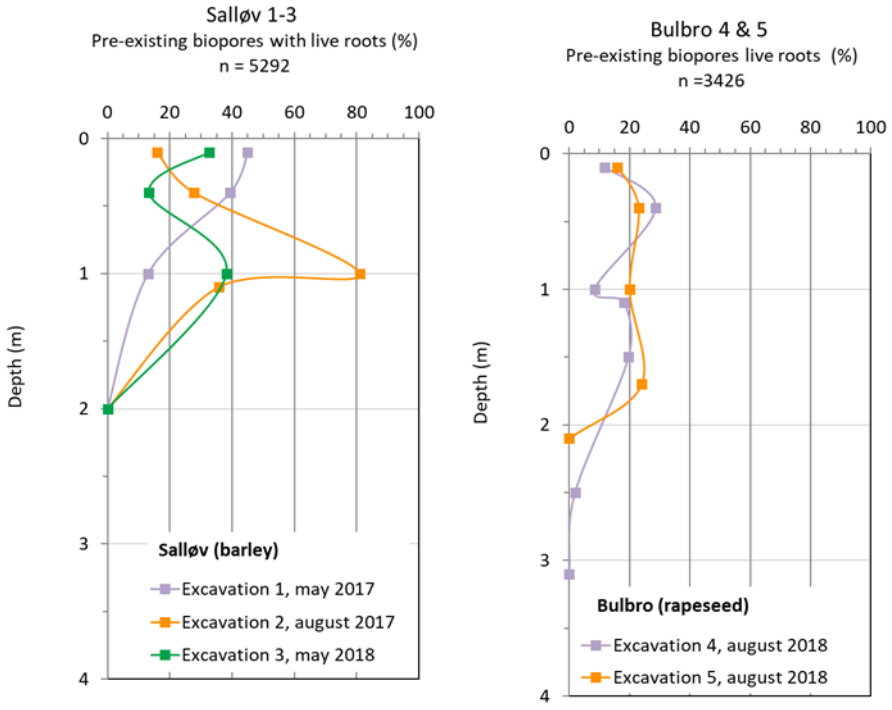

FIGURE 35. Live roots from current crops which were using pre-existing biopores for vertical growth in the high and low-ground excavations.

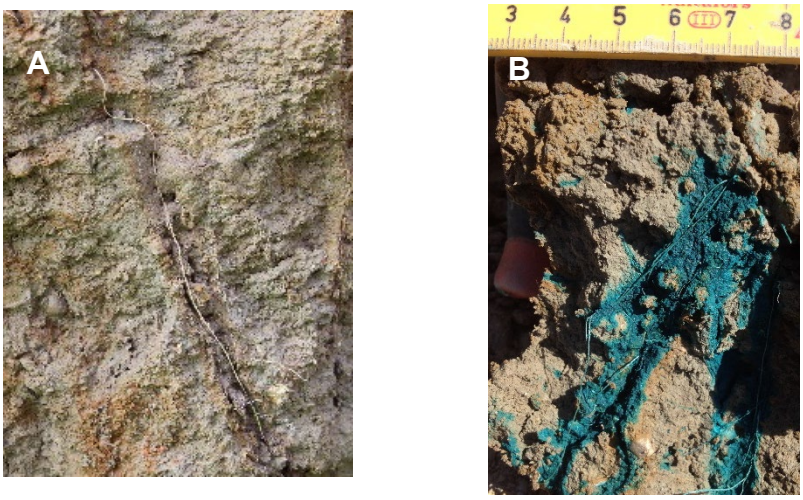

FIGURE 36. Examples of live roots from current crops in pre-existing biopores. (A) Rapeseed root in relic root channel in 1.3 m depth. (B) Worm burrow with live roots shown to be hydrological active by infiltrated dye tracer.

Additional to the live roots, 3 -7 kyr old roots from *A. Glutinosa* (common alder trees, Danish "Rødel", section 3.6) were found below the groundwater table in all three low-ground excavations (E4–E6), which suggests they represented ancient forest. Figure 37 shows a wide span of root sizes across E4 for those paleo or fossil roots, from very thin to several cm thick roots, which varied significantly across the excavations appearantly governed by the growth positions of individual trees or favorable local conditions for deep root penetration.

Figure 38 shows that above the groundwater table (Figure 38A and B), the fosiil roots had disappeared, leaving large pores, which were often partially filled with washed-down soil material, while below the groundwater table (Figure 38C to Figure 41), the roots were well-preserved. The preservation was likely unique due to the moist setting and upward anaerobic groundwater flow by foot of the hill slope. In the previous studies in the Marebæk site (Figure 1 and Figure 2), root channels were also found several meters below the groundwater table (Jørgensen et al. (2002a).

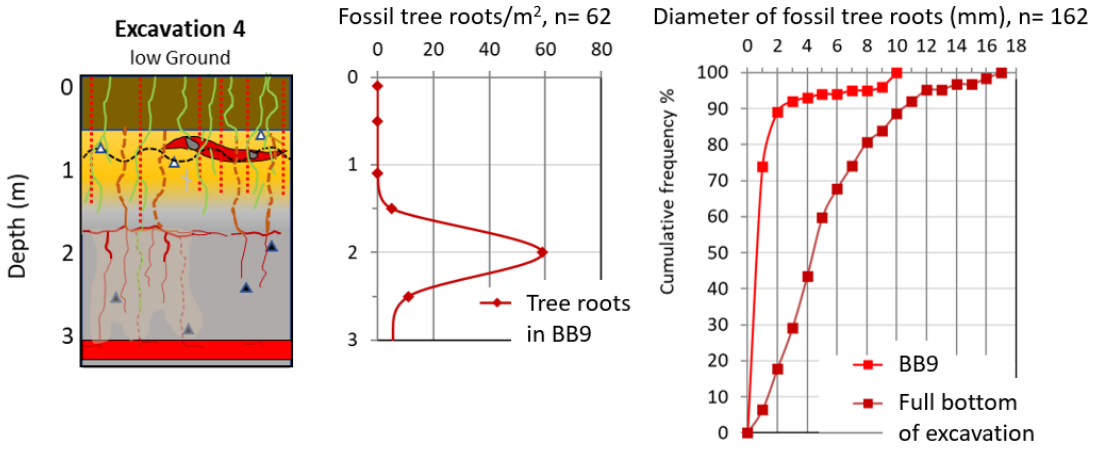

FIGURE 37. Frequency of ancient tree roots from *A. Glutinosa* (common alder trees) in low-ground excavation 4. Right diagram compares the root diameters underneath the BB9 infiltration field (1.8 m^2) and in the full bottom of the excavation in 2 m depth (13,5 m^2).

This suggests that those were likely also from ancient *A. glutionosa,* however, due to oxidation by downward groundwater flow in this site, the actual root fossils were not preserved.

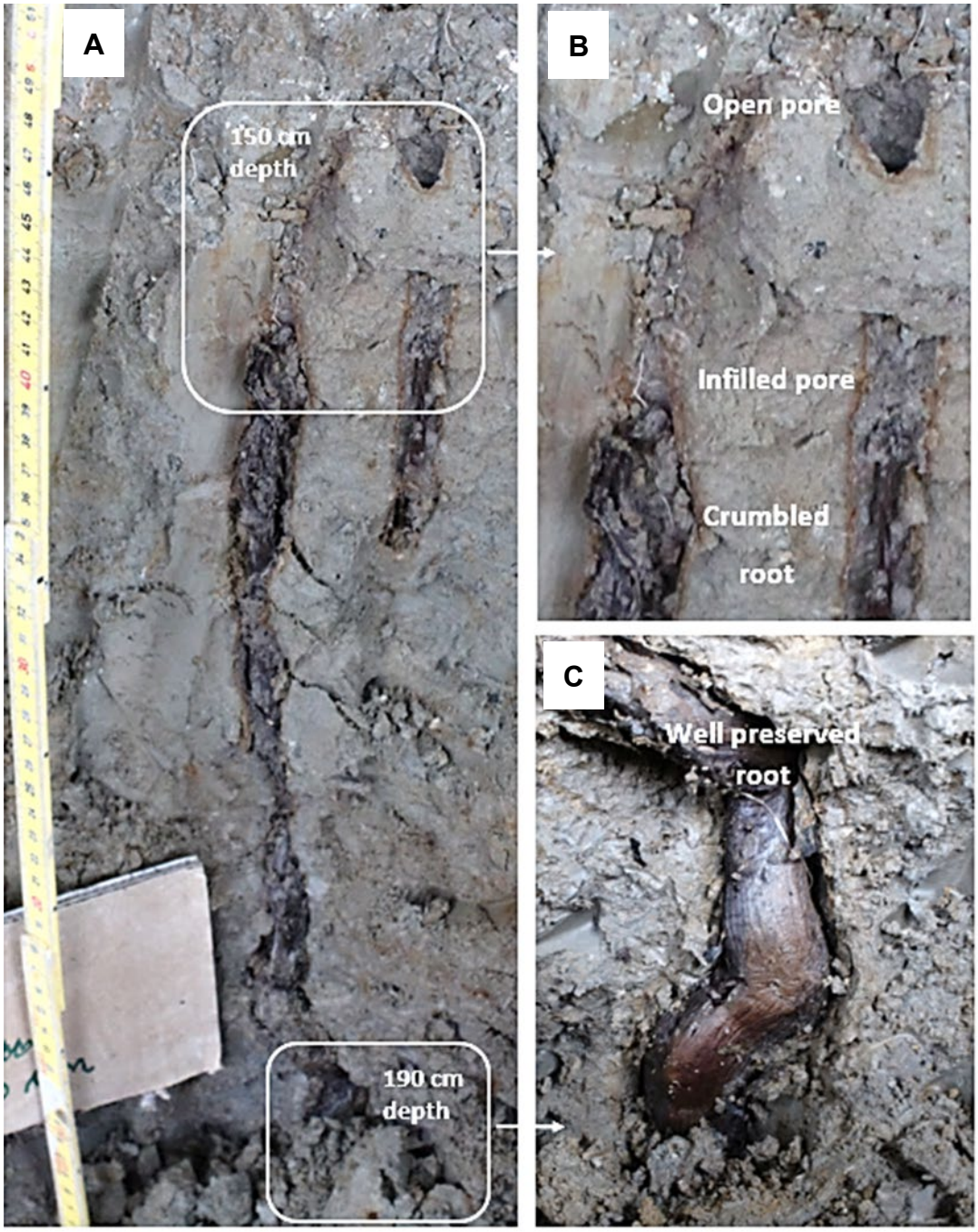

FIGURE 38. Excavation 4: Vertical sequence of fossil root weathering across groundwater table (approximately 1.6-1.7 m depth). (A-B) Above the groundwater table, the tree roots were weathered away leaving them large empty or partially filled with washed down soil material. (C) Below-groundwater table, the roots were well preserved. The roots were from A. glutinosa (common alder) dated to early Danish Bronze age 3,454 – 3,556 Cal BP (section 3.6.1 and 3.6.3).

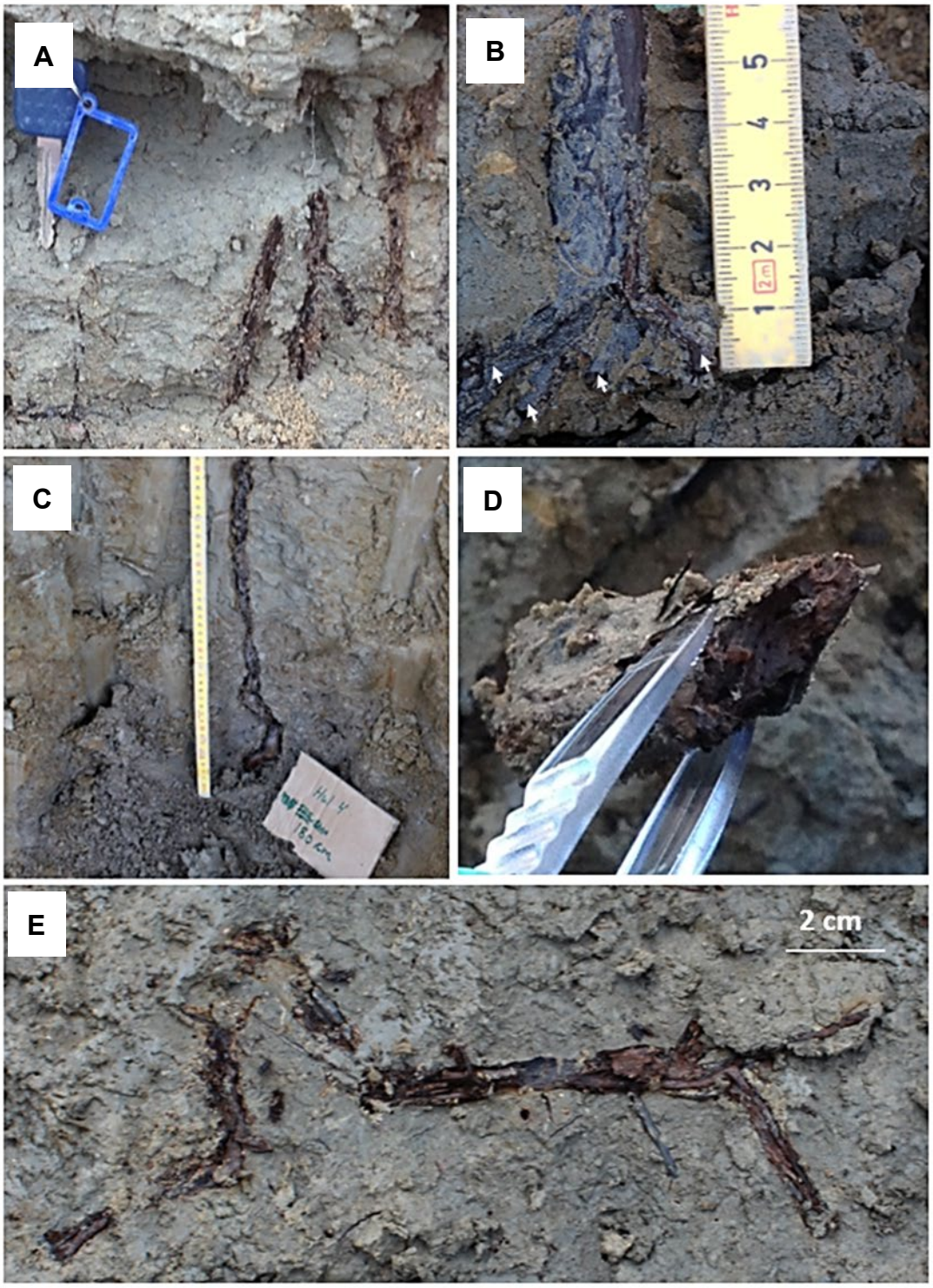

FIGURE 39. Excavation 4: Fossil tree roots in excavation 4, (A) Multiple roots in 2 m depth. (B) Single root branching out in 4 smaller roots (arrows) in 2 m depth. (C) Single vertical root in 1.5-1.9 m depth. (D) Flattened root in 2 m depth. (E) Horizonal root in 2 m depth. The roots were from A. glutinosa (common alder) dated to 7,254 – 3,389 Cal BP (section 3.6.1 and 3.6.3).

FIGURE 40. Excavation 5: Large fossil root from A. glutinosa (common alder) penetrating along a non-visible fracture (ghost fracture) in 2 m depth. The root branched in 8-10 smaller roots, some of which were followed to below 3 m depth. The root was dated to late Bronze age 2,833-2,797 Cal BP (section 3.6.1 and 3.6.3).

FIGURE 41. Excavation 6: Horisontal surface with large horizontal fossil root and many small vertical fossil roots in wash-drift sand in 1.3 m depth. The roots were from A. glutinosa (common alder) and dated to 6,894-6,496 Cal BP by the introduction of agriculture in the Stone Age (section 3.6.1 and 3.6.3).

Many of the fossil roots were flattened, which may be adapted during growth, or due to subsequent settling of the aperture's enhancement caused by the roots. Figure 42 shows comparison between horizontal directions of long-axis in flattened roots and the observed orientation of fractures in the excavations. The comparison reveals that the root long-axes were parallel with the overall directions of fracture strike in the area, which suggests that the roots had been following non-visible tectonic fractures (ghost fractures) in the unoxidized grey till.

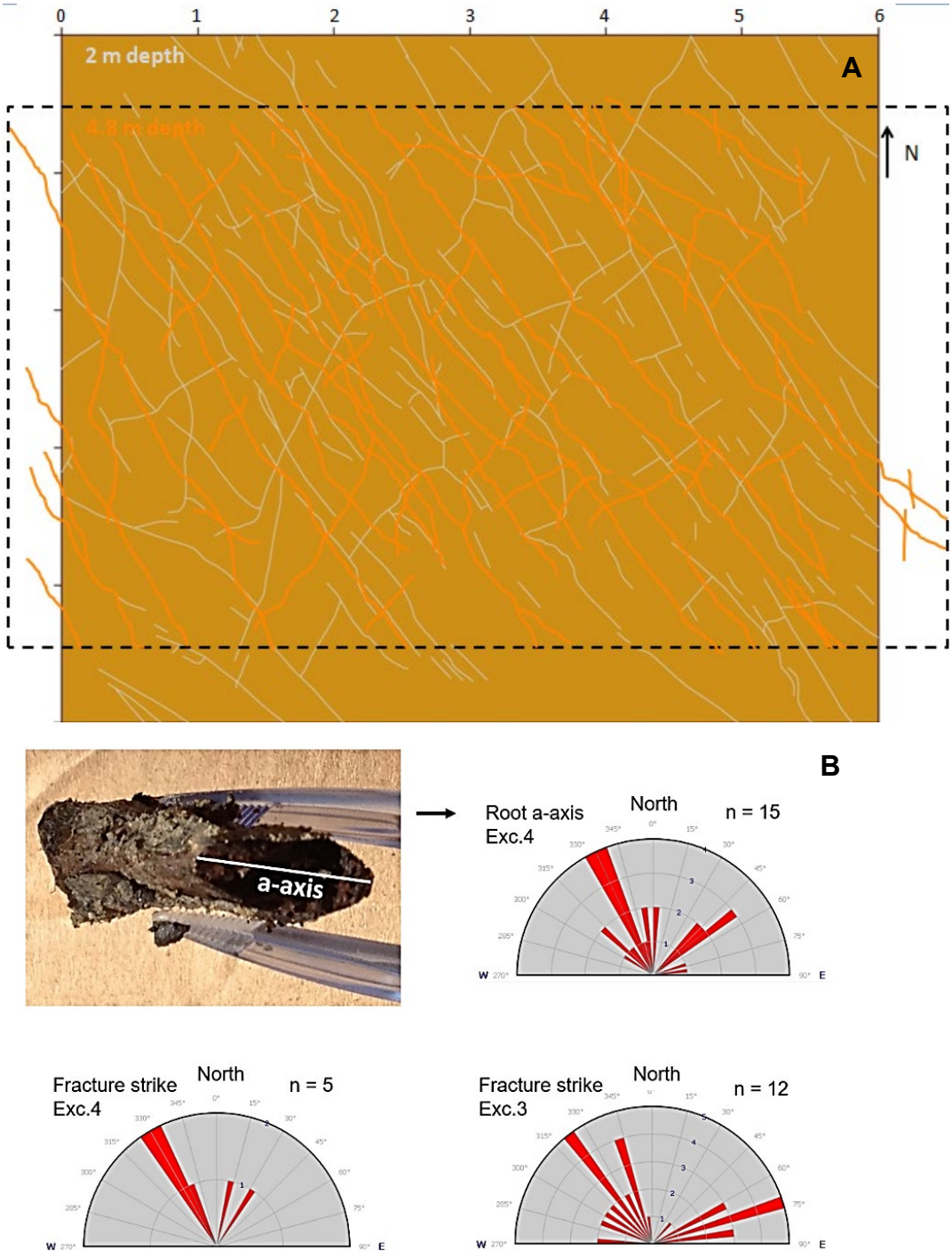

FIGURE 42. Indicated occurrence of non-visible fractures (ghost fractures) in the grey clay from analysis of fractures and root flattening directions in excavations (A). Direction of fractures in E2 (high-ground) on horizontal surfaces in 2 and 4.8 m depth. B: Same direction of flattened roots (a-axis in photo to the left) in the grey clay in excavation 4 (2m depth) with no visible coupling with fractures otherwise. Also shown strike of visible fractures above in E4 and E3, Figure 29 (approximately 450 m separation between the low and high-ground measurements).

In the high-ground, the contrasting environment with seasonally unsaturated and oxidizing conditions to great depth in the till had prevented preservation of fossil roots in the root channels. However, Figure 43 shows examples of large flattened root casts inside fractures, which may represent channels from root of similar size as the root fossils in the low-ground.

FIGURE 43. Large root casts (arrows) inside grey fracture at 2.8-3 m depth in E2 (high-ground). The root casts are flattened inside the fracture, which suggests that the size of the original roots resembled the tree roots found in the low-ground excavations (Figure 38 to Figure 41).

3.5 Dye tracer infiltration

Preferential flow was investigated by conducting 12 Brilliant Blue dye tracer infiltration experiments in excavations E1-E5 to maximum 6 m depth (BB0-BB11 in Figure 44). While previous field experiments by e.g., Rosenbom et al. (2005, 2008) and the predesssor PESTPORE study (Jørgensen et al., 2017) investigated vertical flow from the soil surface thoughout the till profiles, the main focus in this study was to investigate the connectivity of preferential flow paths in and across the vertical sequence of the till zones and structures shown in Figure 44A-D. The BB infiltration was combined with XRT/CT-scanning of intact samples, and pesticide migration lab studies using LUC samples (Aamand et al. in prep., 2020). The location of the dye experiments (and XRT/CT and LUC sampling) in the excavations is shown in Figure 4, the BB experimental conditions are shown in Table 2. In the following section, the dye tracer experiments are presented in the order of increasing depth from the high-ground to low-ground sites.

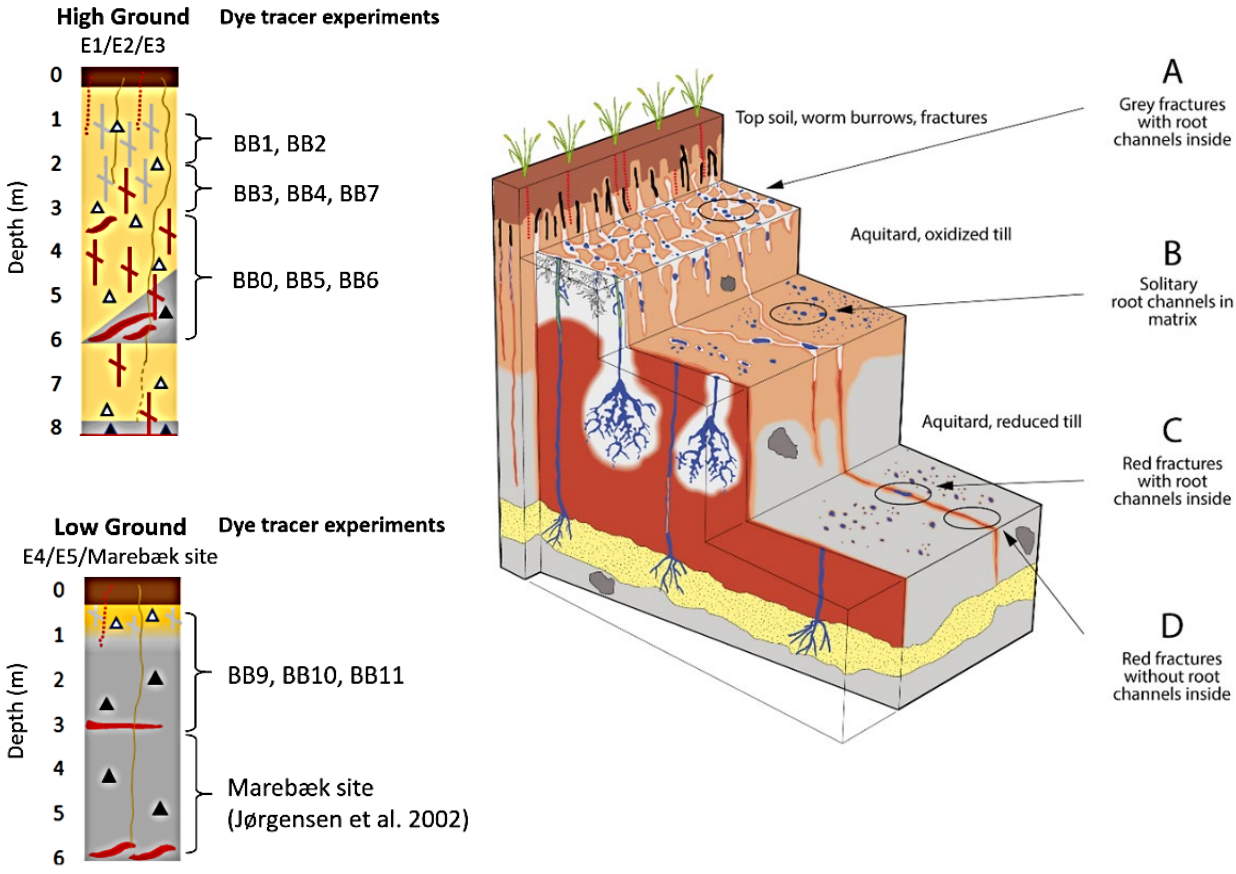

FIGURE 44. Vertical position of dye tracer experiments (BB0-BB11) in the high and low-ground geological profiles shown together with previous Marebæk site experiments in the low-ground area 1.5 km further south (see Figure 2). The conceptual diagram to the right shows the relation of the BB experiments to the occurrence of various structural and geochemical zones in clayey tills based on previous studies by Jørgensen et al. (1998a,b,c, 2002a,b, 2001, 2003, 2004a,b, 2017, 2020a,b); Jensen et al. (1999); Butzbach (2007); Rosenbom et al. (2005, 2008); Hansen et al. (2012b); Mosthaf et al. in review (2020).

3.5.1 High-ground experiments

1. Flow across the transition from soil to grey fractures in subsoil (Figure 44 A)

BB1 and BB2 dye tracer experiments, E2 (1-2 m depth)

Figure 45 to Figure 47 show the distribution of dye tracer in the BB1 and BB2 experiments after BB was infiltrated in 1 m depth (C-horizon of soil profile). Infiltration was maintained for 1 day, after which the BB field was excavated. After the mapping of flow paths, an intact column (XRT column 1, Figure 4) was collected from the BB1 infiltration field for further characterization of the macropore system with XRT.

The tracer arrived in the drain established underneath the infiltration basins 1 hour after application of the BB dye, corresponding to a migration rate above 20 m/day under free drainage, which is in agreement with observed flow and transport rates in grey fractures in previous field and lab experiments (e.g. Jørgensen et al., 1998a, 2017; Mosthaf et al. in review, 2020). In Figure 45, the excavated vertical profiles show that the BB dye had infiltrated worm burrows and closely spaced grey fractures.

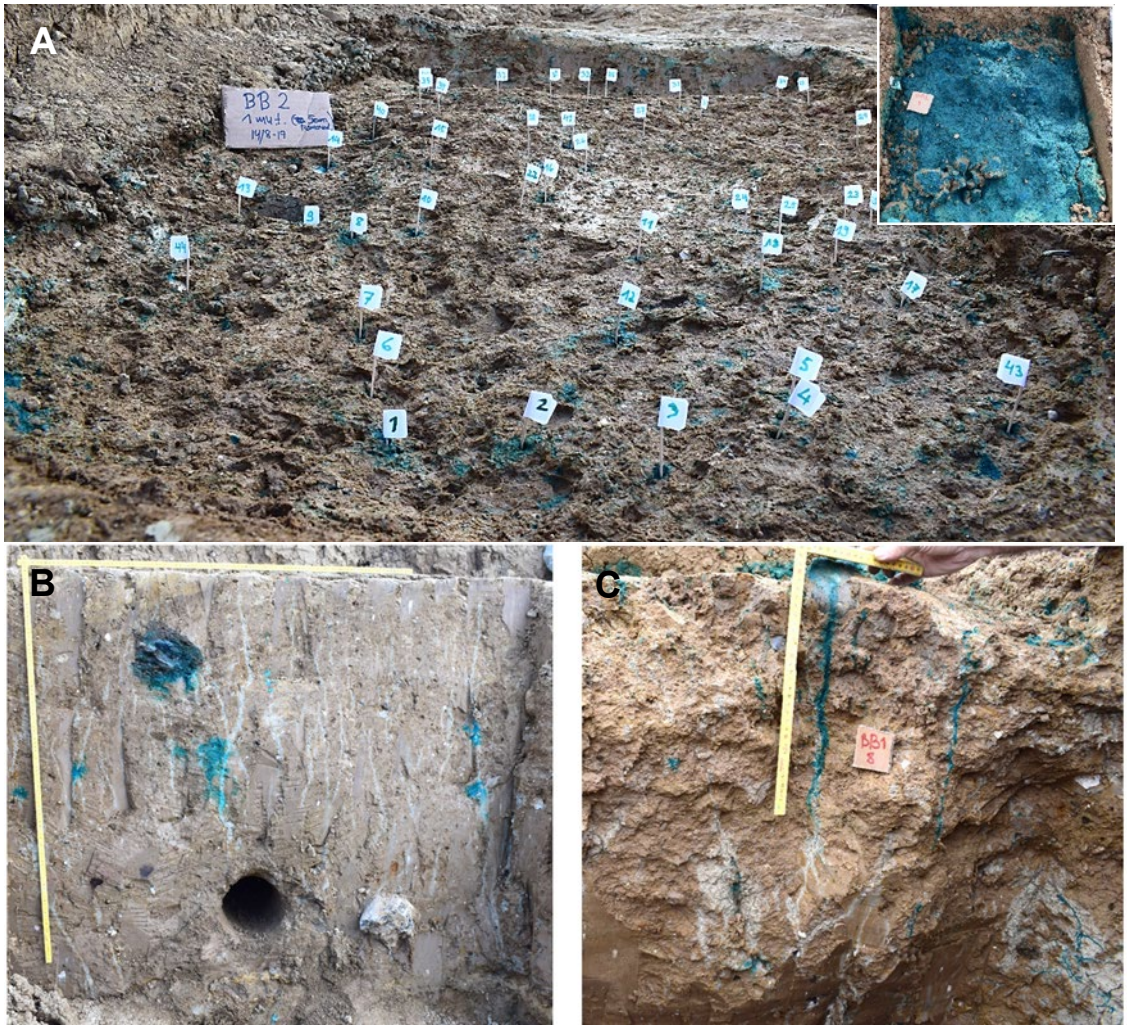

FIGURE 45. Brilliant Blue (BB) infiltration experiments BB1 and BB2 (1-2 m depth). (A) Dyed experimental field (insert) and numbered large macropores (d> 4mm). (B and C) Vertical sections in infiltration field. (B) Closely spaced grey fractures containing BB dye tracer, (C) large worm burrows connecting into narrow fracture domaines (lower right corner of photo). Arrival of BB into drain hole (arrow in B) occurred after 40 min. infiltration.

Figure 46 and Figure 47 show the details of BB flow paths and connections from solitary biopores to fracture flow paths in the experiments together with the size distribution of the biopores (worm burrows and root channels) in the surface of the experiments. 70-80 % of the biopores in the surface of the experiments were earthworm burrows, which terminated 20-40 cm below the surface of the infiltration fields (approximately 1.5 m depth below ground). Many of the worm burrows were infilled with drop-down topsoil material in the bottom. 50 % of the counted worm burrows continued vertically as dyed root channels (Figure 47 and Table 9) connecting into underlying grey fractures in which they formed dyed flow paths inside (Figure 47).

TABLE 9. Worm burrows continuing vertically as root channels in BB2 (selection of the burrows in Figure 46a).

Worm burrow	Depth (m)	Diameter (mm)	Extended vertically as root channel	Contained live root	Entered into fracture	Connected by BB flow
17	1.25	8	+	+	+	+
18	1.25	6	+	+	+	+
19	1,13	8	+	+	÷	+
20	1,18	5	÷	÷	÷	÷
23	1.12	6	÷	÷	÷	÷
24	1.20	6	÷	÷	÷	÷
25	1,20	5	÷	÷	÷	÷
29	1,25	8	+	+	+	+
30	1.40	8	÷	+	÷	÷
31	1.30	8	+	+	+	+
33	1.35	8	+	+	+	+
43	1.20	7	+	÷	÷	÷
44	1.20	7	+	÷	÷	÷
45	1.14	4	+	+	+	+

A high percentage of the dyed worm and root channels contained live roots from the current crops, showing that they were connected with the soil surface (see percentage of live roots in pre-existing macropores in Figure 37 and Jørgensen et al., 2017). Figure 46 furthermore shows that above 1-1.5 m depth, the BB dye tracer flow inside the fractures had occurred both in the root channels and in the fracture aperture space between the individual root channels, while in greater depth flow of the dye tracer was consistently absent in the fracture aperture spaces between the root channels suggesting the fractures were closed except for flow in the root channels. This was in agreement with observations in previous studies (e.g. Jørgensen et al., 2002a, 2004a,b, 2017; Butzbach, 2007; Aamand et al. in prep., 2020), which showed that below 1-2 m depth, flow is not active in the fractures if they are not enhanced by root channels.

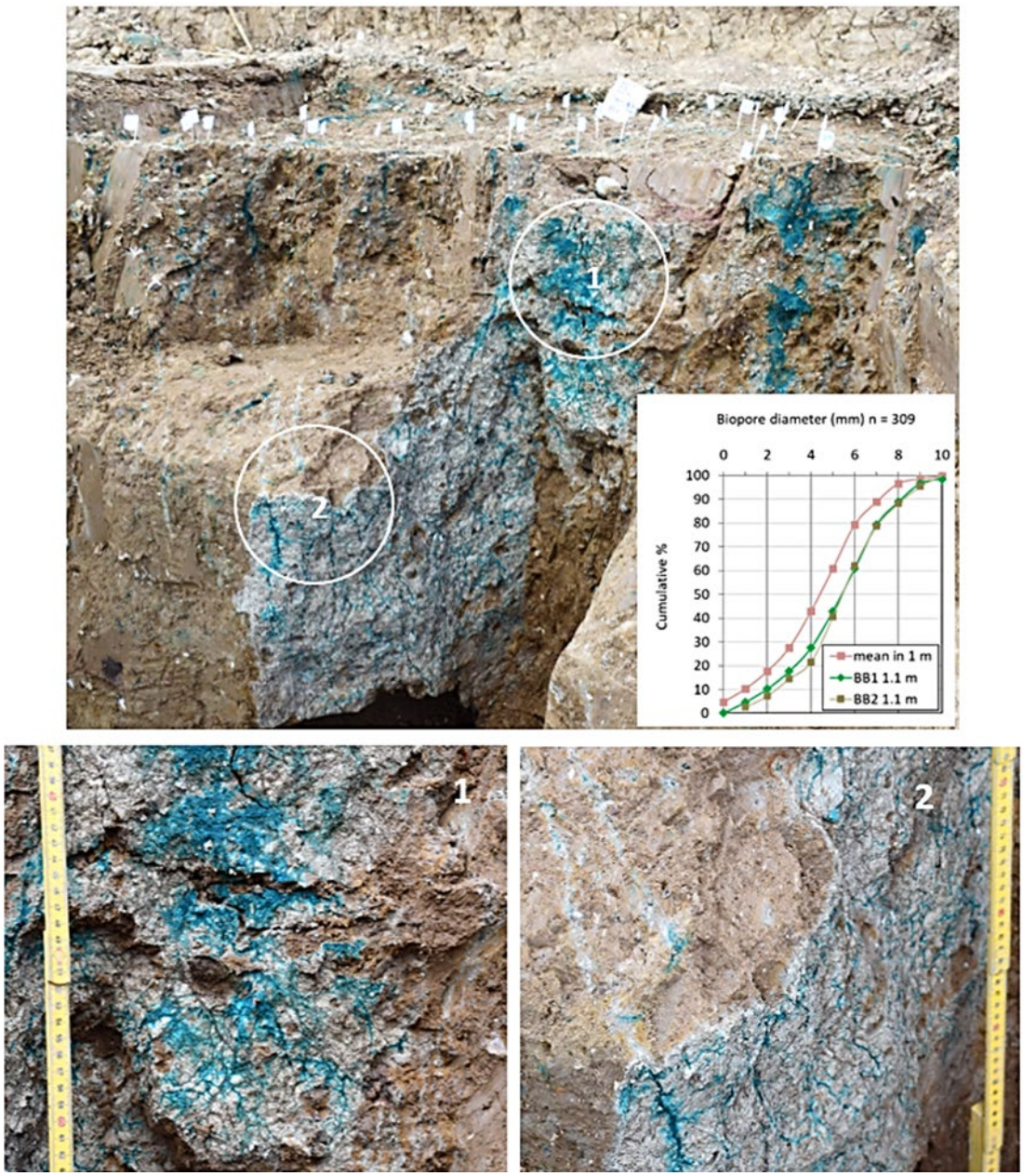

FIGURE 46. Excavation of BB2 infiltration field. (Top) Photo shows markings (white flags) of dyed worm burrows in surface of infiltration field (1 m depth) and, below, exposed grey fracture walls with dyed flow paths. Notice the occurrence of BB dye tracer along both the fracture wall and root casts in the uppermost exposed vertical fracture (1), whereas in the lower fracture (2) BB dyed flow paths occurred only in root casts and was absent along the fracture itself. Insert diagram compares distribution of biopore sizes in the surfaces of infiltration fields BB1 and BB2 with mean biopore diameter distribution determined in five other 1 m^2 fields in excavation 2.

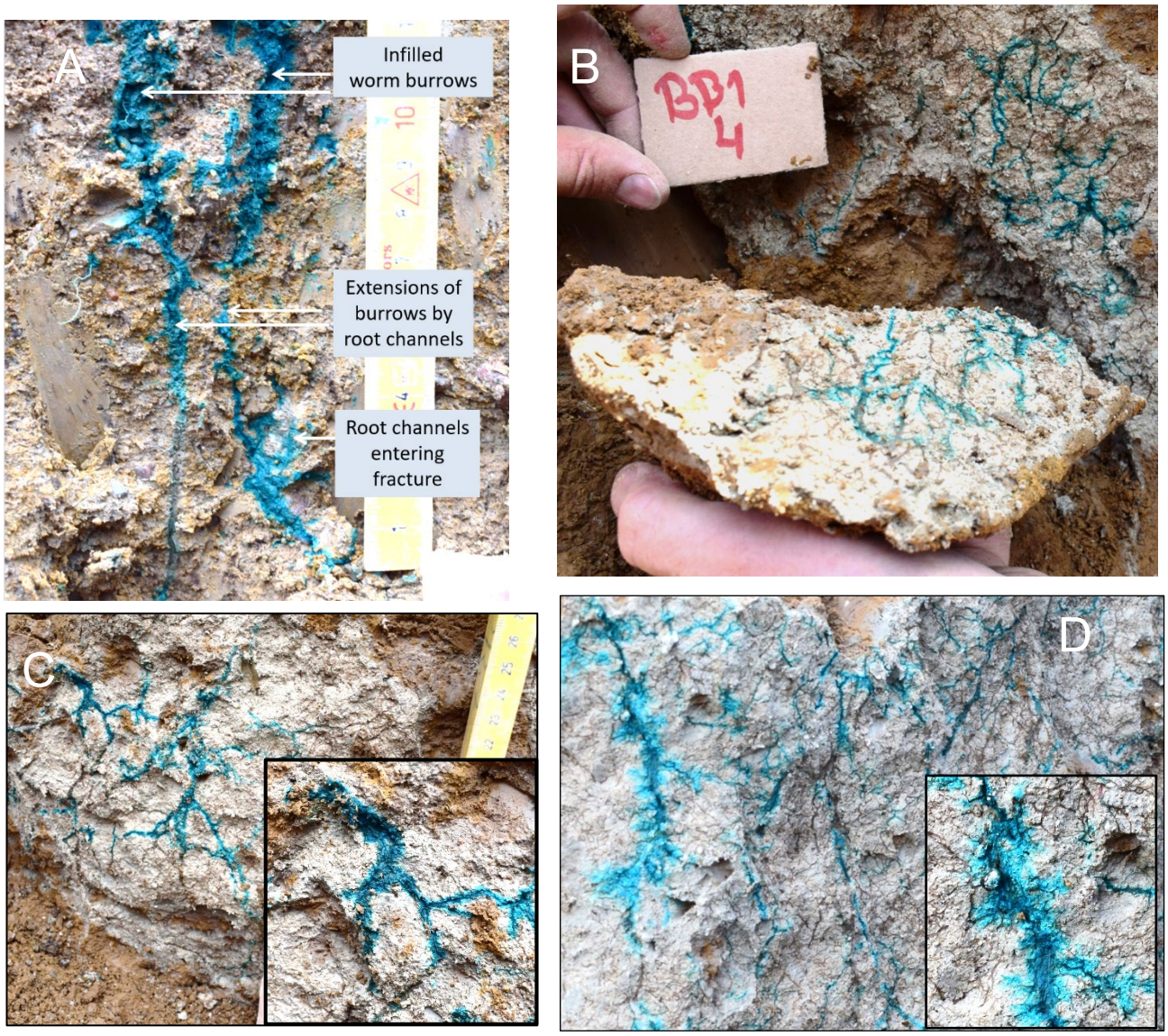

FIGURE 47. Dyed worm burrows and root channel flow in exposed grey fracture wall surfaces (BB1 and BB2 experiments). (A) Vertical section showing BB flow in worm burrows, which continue as root channels that enter a grey fracture in 1.4 m depth, (B) dyed root channel casts on the two opposite walls of a fracture in 1.3-1.4 m depth (BB1 experiment). Dyed root channels on fracture walls in (C) 1.8-2 m depth (BB1) and (D in 1.7-2 m depth (BB2).

XRT of BB1 intact column (Column 1) 1.1-1.6 m depth, E2

Figure 48 shows the sampling of the intact Column 1 for XRT investigation. The column was collected in the surface of the BB1 experiment from 1.1-1.6 m depth (C horizon of soil profile) (Figure 4). The top the column had two visible dyed worm burrows and one grey major fracture, which penetrated the column vertically. Figure 49 to Figure 52 show CT-scans of the column, which revealed that it contained 3 large worm burrows (> 4 mm) that were partially infilled with loose soil material from the topsoil in 1.2-1.4 m depth. After image pre-processing (Figure 50) and image segmentation with 430 µm resolution (Figure 51 and Figure 52), the column showed a structured macro-porosity of long, mainly vertical, root channels (< 4 mm) throughout the column. Many of the burrows and root channels were organized along the main fracture plain and smaller polygon fractures resembling soil ped interfaces in the clay. The

macropores resembled the BB dyed worm burrows and root channels observed in the dye experiments in Figure 45 and Figure 46, which were also observed when cutting up the column after the CT-scanning (Figure 49). Figure 53 shows the distribution of biopore diameters in the column, which revealed that the frequency of root channels (< 4 mm) was significantly higher than identified in the field investigation (90% against 20-30%), suggesting that many smaller biopores were overlooked in the field. The mean pore volume was 0.92 mm^3 (Table 10), and the larger pores (volume > 4 297 mm^3 in Figure 52) represented 0.70% of the macropore porosity. Pores had a mean diameter of 1.11 mm, with the large pores representing worm burrows distributed in the top part of the column (up to 9 mm in the 0-10 cm layer). Examples of worm burrows and root channels were extracted for detailed description in Figure 54 and Table 11. The worm burrow (pore 1) had diameters from 3.40 to 7.95 mm and the mean diameter 5.63 mm, while the root channels (pores 2, 3 and 4) had diameters up to 3.7 mm and mean diameters from 1.09 mm to 1.84 mm. The diameters are in overall agreement with the field measurements in Figure 30.

FIGURE 48. Sampling of XRT Column 1 from BB1 in 1.1-1.6 m depth (C-horizon) in E2. (A) Side view showing two large worm burrows dyed with infiltered Brilliant Blue (BB) tracer, and grey fractures penetrating the column vertically. (B) View of bottom of bottom of column showing grey fractures with BB dye tracer migrated along the fractures.

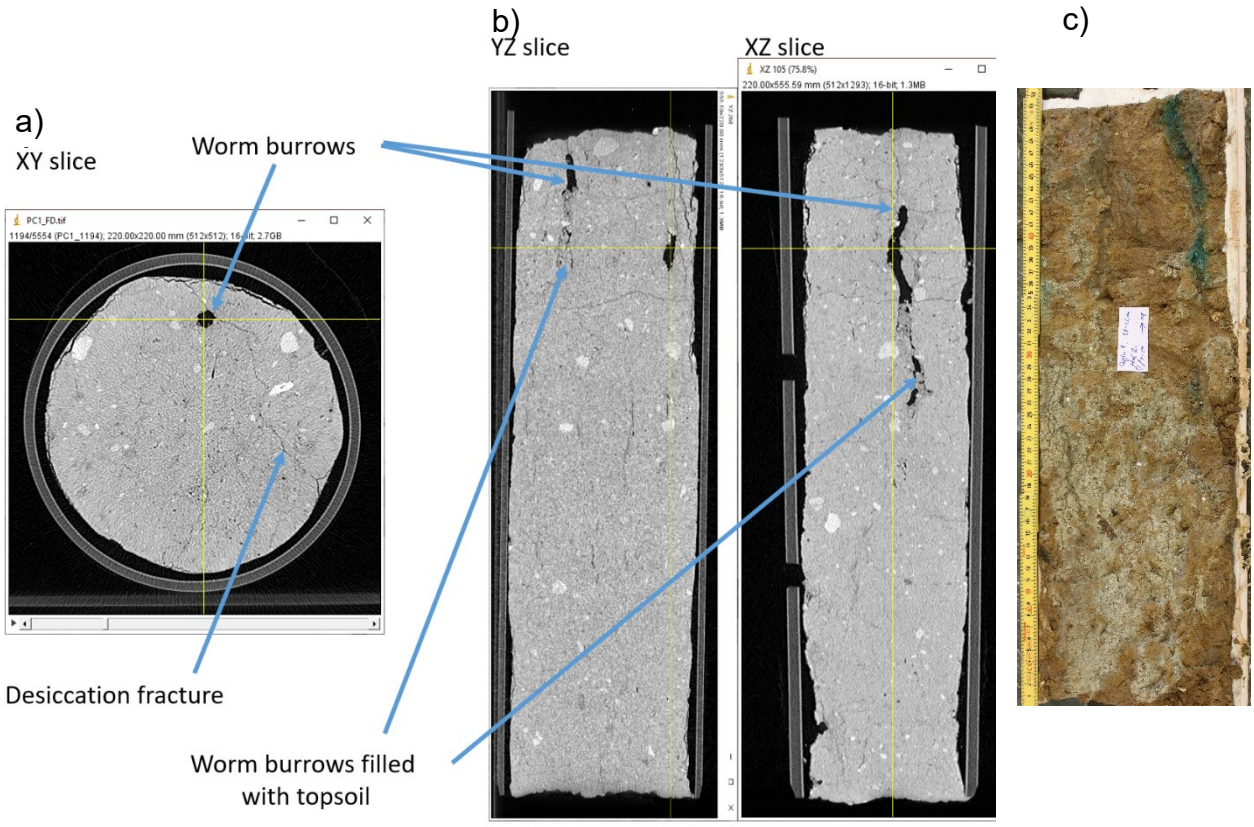

FIGURE 49. BB1 XRT Column 1 (image resolution: 430 µm). (a) XRT image of column showing worm burrow and open desiccation fractures. (b) XRT showing worm burrows with filling of washed down topsoil material. (c) Dismantling of BB1 column showing BB dye (BB1 exp.) in the deepest worm burrow (1.4 m depth). The washed-down topsoil in the burrow was radiocarbon dated to 3,420 ± 35 yr ^{14}C BP (section 3.6.1) and suggests that the burrow has probably been used by generations of earth worms.

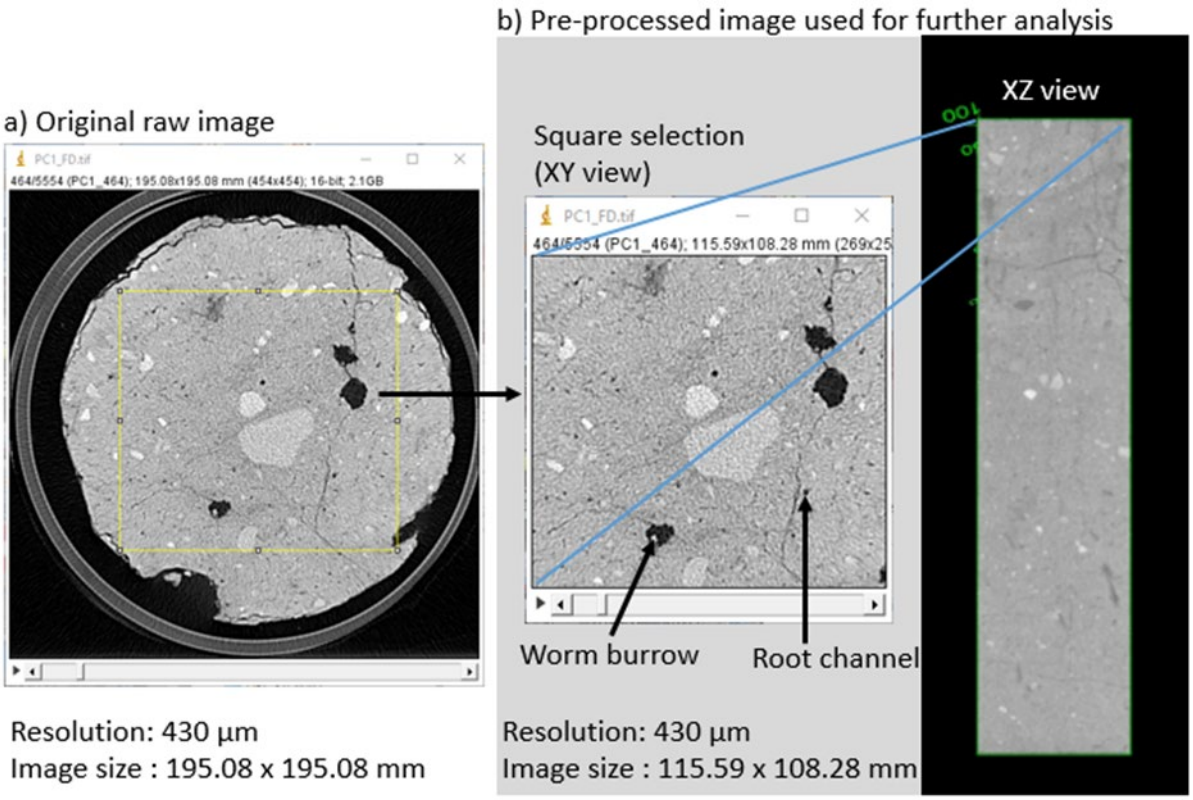

FIGURE 50. Image preprocessing of Column 1. (a) Raw image at 1.5 m belong ground, (b) ROI selection and 3D view of the column. Worm burrows (diameter ranging from 7 to 13 mm in this image) are located along desiccation fractures (aperture less than 1 mm). Some root channels are located in the soil matrix (diameter <2 mm in this image). Image resolution: 430 µm.

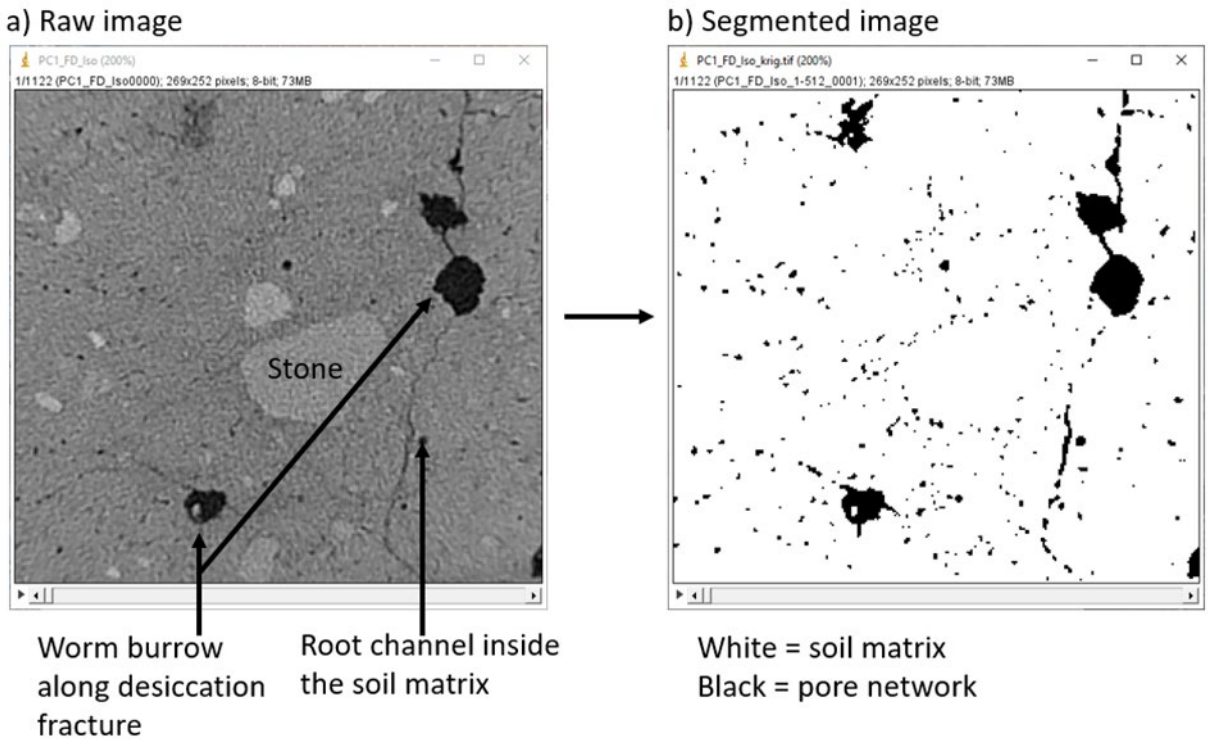

FIGURE 51. Image segmentation of horizontal section in Column 1 showing worm burrows and root channels following desiccation fractures in the clay (diameter ranging from 7 to 13 mm in this image). (a) Raw image, (b) image after segmentation. The small channel holes (diameter <2 mm in this example) are located around the stone and mostly follows the pattern of polygon desiccation fractures between soil peds in the clay. Image resolution: 430 µm.

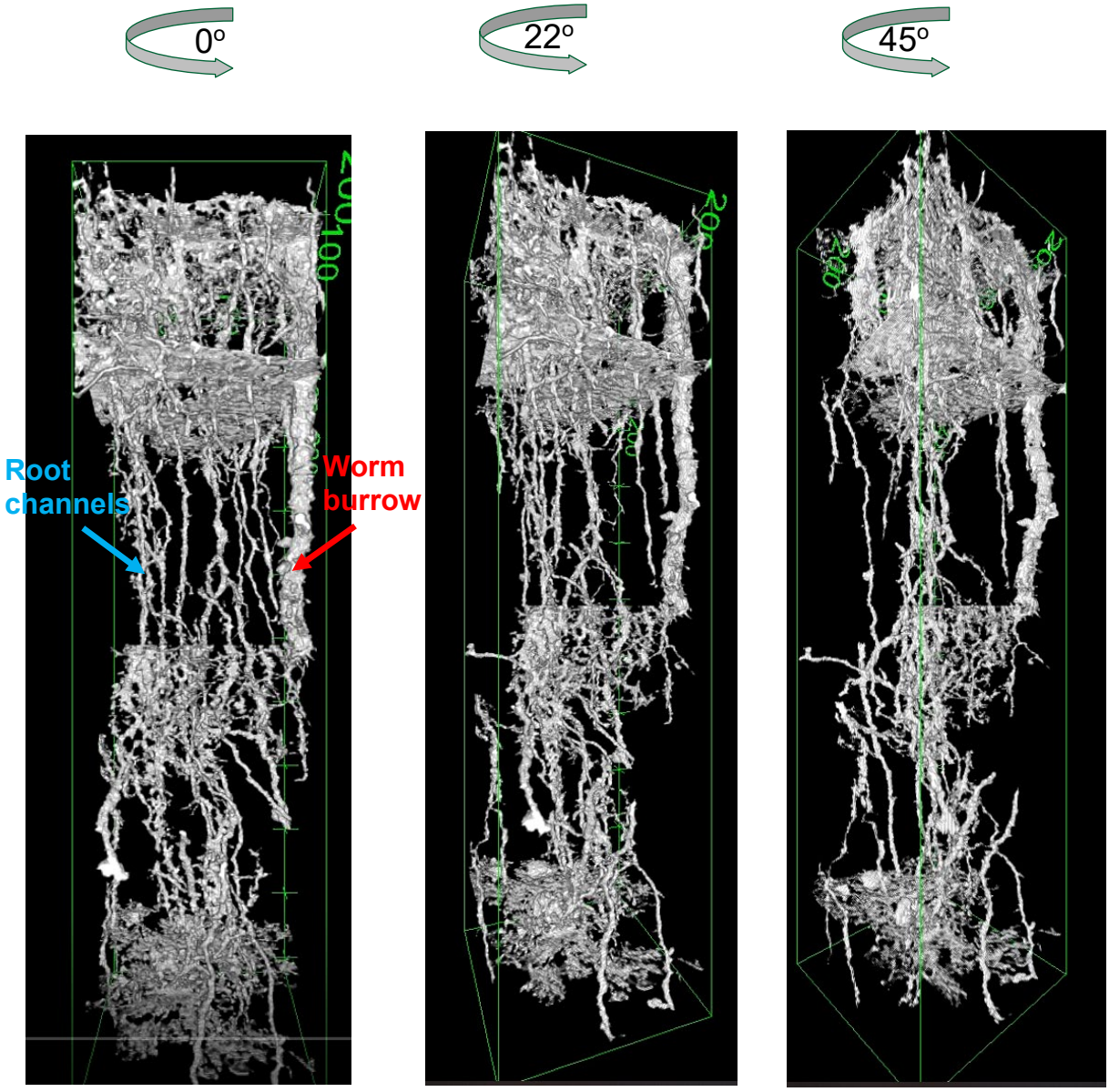

FIGURE 52. Column 1, visualisation of worm burrows and root channels located along vertical and horizontal fractures viewed from different angles from 1.2-1.6 m depth. From left: 45º view of main fracture showing density of root channels in the fracture, rotation to intermediate angle, and parallel view of fracture plane (green line) showing alignment of root channels along the fracture. Additional horizontal and sub-horizontal fractures with root channels are also visible. Worm burrows terminate at approximately 1.4 m depth, while the dense network of root channels penetrates past the maximum depth of the column. Image resolution: 430 µm (https://mst.dk/media/210348/pestpore2video1.mp4).

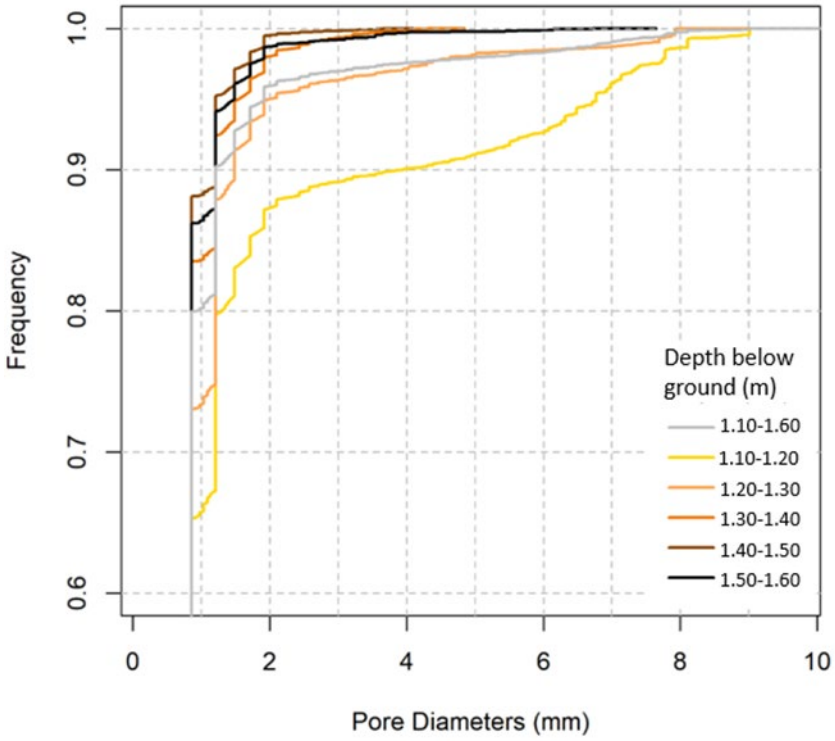

FIGURE 53. Pore size distribution in Column 1. The frequency of root channels (90% d < 4mm) is higher than observed in the field (Figure 30 and Figure 31), which suggests that the field counting underestimated the actual number.

TABLE 10. Pore diameter and porosity for Column 1.

Depth (m)	Pore diameter (mm)							Poro-sity (%)
	Min.	1st Qu.	Median	Mean	3rd Qu.	Max.	SD	
1-1.1	0.86	0.86	0.86	1.6	1.22	9.01	1.77	2.8
1.10--1.20	0.86	0.86	0.86	1.16	1.22	7.92	0.97	1.72
1.20-1.30	0.86	0.86	0.86	0.97	0.86	4.3	0.34	2.45
1.30-1.40	0.86	0.86	0.86	0.93	0.86	3.65	0.22	2.02
1.40-1.48	0.86	0.86	0.86	0.96	0.86	6.71	0.38	2.62
1-1.48	0.86	0.86	0.86	1.11	0.86	9.01	0.94	2.31

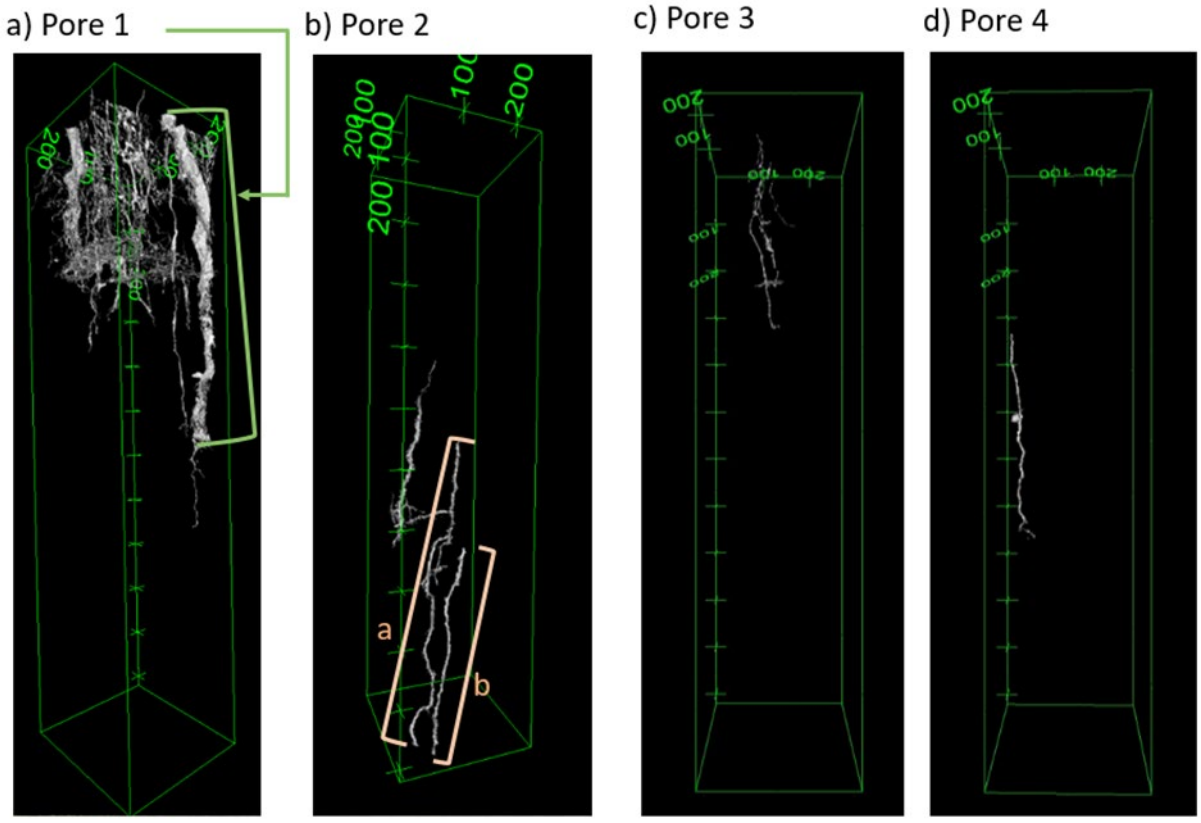

FIGURE 54. Visualisation of some selected pores for Column 1 (see Table 11 for quantitative description). (a) Worm burrow (diameter > 4mm) only in the upper part of the column (depth below-ground: 1.10-1.35), (b to d) Root channels (diameter < 2 mm) present throughout the column. Image resolution: 430.

TABLE 11. Detailed description of selected pores from the XRT-column 1. Resolution: 430 µm

Description in the analyzed section	Pore 1	Pore 2a	Pore2b	Pore 3	Pore 4
Length (cm)	25.16	29.98	16.23	15.59	17.24
Mean diameter (mm)	5.63	1.84	1.62	1.09	1.25
Min diameter (mm)	3.40	0.43	1.05	0.43	0.62
Max diameter (mm)	7.95	3.70	3.22	3.22	1.93

2. Flow across boundary from grey fractures to red fractures (Figure 44A-C)

BB3 and BB4 dye tracer experiments, E2 (2.4-3.4 m depth)

The BB3 and BB4 experiments were established in 2.4 m depth immediately underneath the BB1 and BB2 experiments (Figure 44). The BB infiltration was maintained for 1 day in BB3 and 5 days in BB4, after which the field was excavated. The tracer did not arrive in the drains established 1 m underneath each of the infiltration basins. After infiltration, XRT column 2 was collect from BB3 infiltration field for further characterization of the macropore system with XRT.

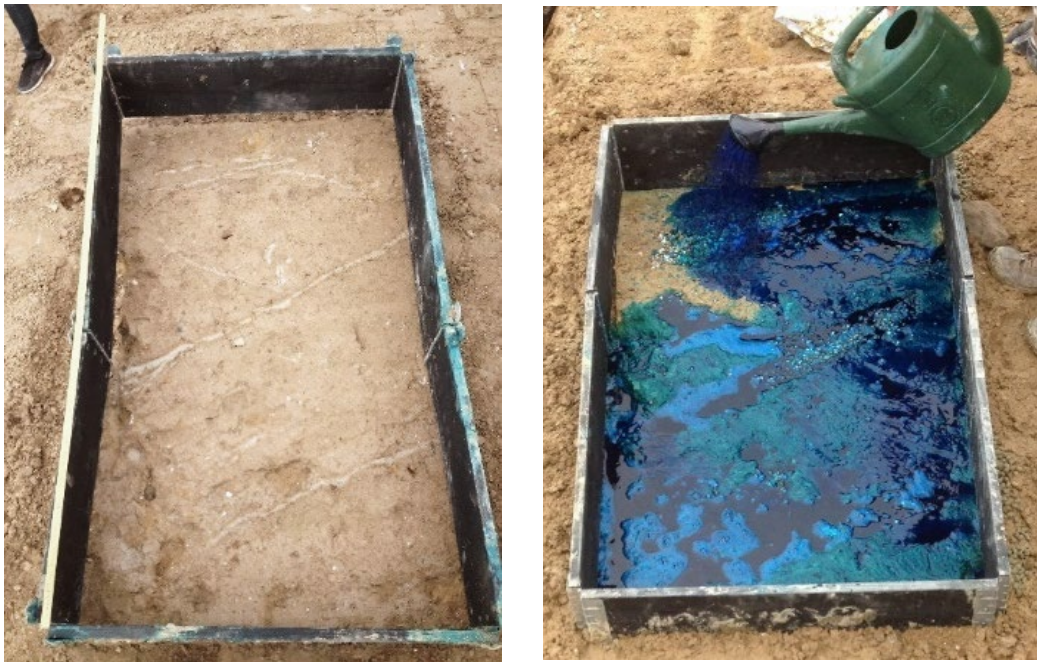

FIGURE 55. BB3 infiltration field and application of BB dye tracer.

Figure 56 and Figure 57 show the distribution of the BB tracer in the clay after the BB infiltration. In BB3, dye tracer occurred as 0.5-1 cm long segments along prominent sub-vertical grey fractures in the surface of the experiment in 2.4 m depth (Figure 56a), while in BB4 there was a higher occurrence of solitary root channels (Figure 56b). Figure 56c shows the transition from grey to red fractures infilled with Fe/Mn-oxides, which occurred 20-30 cm below the infiltration surfaces. In both BB3 and BB4, the dye tracer had only penetrated 2-15 cm into the fractures along root channels and 40 cm along solitary root channels in the clay matrix (Figure 56d). The shallow penetration of the BB flow, as compared with the BB1 and BB2 experiments, was likely caused by the water stewing in the macropore flow paths from saturation of the previous BB1 and BB2 experiments immediately above, which could not empty downwards due to underlying Fe/Mn-oxide infillings of the red fractures, Figure 56d. Generally, no BB penetration was observed in the red fractures, except for two examples, one of which is shown in Figure 57, where BB dye tracer infiltrated approximately 0.5 m below the grey/red fracture

boundary and maintained the braided shape of root casts observed in the grey fractures above.

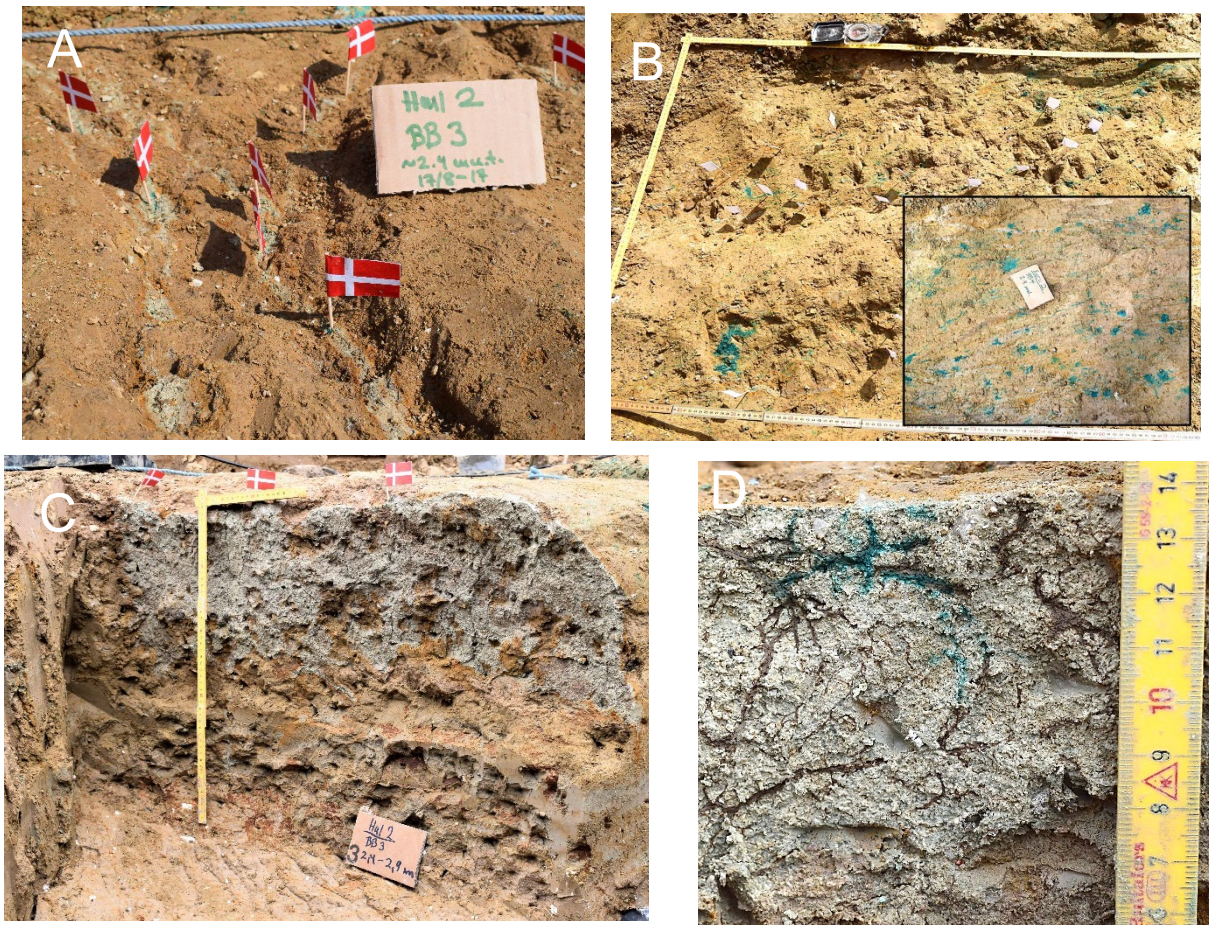

FIGURE 56. Excavation of BB3 and BB4 dye tracer infiltration experiment. (A-B) Horizontal surfaces of experimental fields showing dyed segments (flags) of grey fractures, (C) Vertical transition inside fracture from grey to red fracture by Fe/Mn-oxide infilling. (D) Halting of the BB dye tracer, probably due to water-saturation before the experiment, which could not drain vertically because of the Fe/Mn-oxide filling of underlying biopores and fractures.

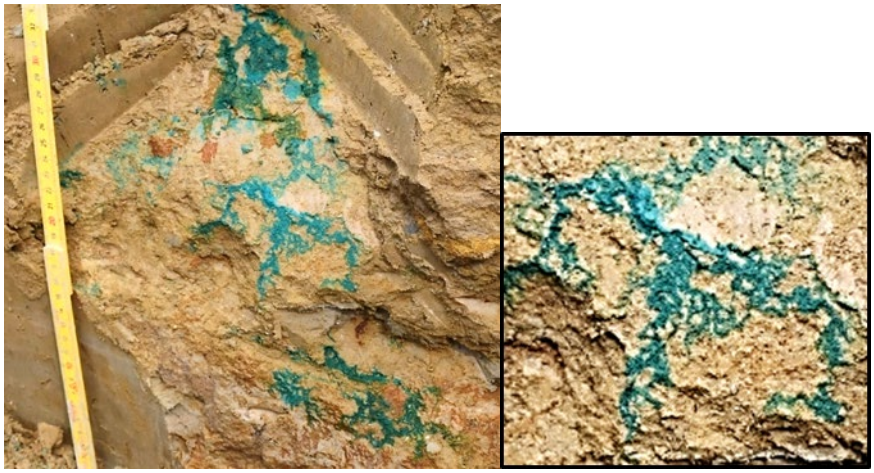

FIGURE 57. BB4 dye tracer experiment showing the only finding of significant preferential flow inside the red fractures in the BB experiments (magnification of channel pattern in frame).

XRT of BB3 intact column (Column 2) 2.4-2.9 m depth, E2

Figure 58 shows the column collected in the BB3 experiment from 2.4-2.9 m depth (Figure 44). The column was dominated by a sand lens and red fractures. No BB infiltration was observed in the column. The overall scan in Figure 58 shows fractures and the central sand lens together with further textural heterogeneity (sandy material) occurring in the lower part of the column.

Figure 59 and Figure 60 show the occurrence of circular pores along fractures, which represent root channels with diameters of 1-2 mm (see also Figure 57). The total column pores had a mean diameter of 1.19 mm, with the larger pores occurring closer to the bottom of the column (> 6 mm in the 30-50 cm layer). Selected root channel macropores are characterized in detail in Table 12. Pores 1 and 2 were from the upper part of the column, while pores 3 and 4 were from the bottom. They were developed in diagonal plans following the fractures (Figure 58). The four pores were relatively short (2.74 to 4.18 cm) The large pore (pore 4) had diameters from 1.07 mm to 2.05 mm (mean 1.50 mm). The other pores (pores 1, 2 and 3) had mean diameters ranging from 0.92 mm to 1.25 mm. The pores were not connected in the applied resolution (430 µm). The lack of connectivity was in agreement with the partial filling with Fe/Mn-oxides shown in section 3.4 and the observed absence of BB flow in the pores in the dye tracer experiments.

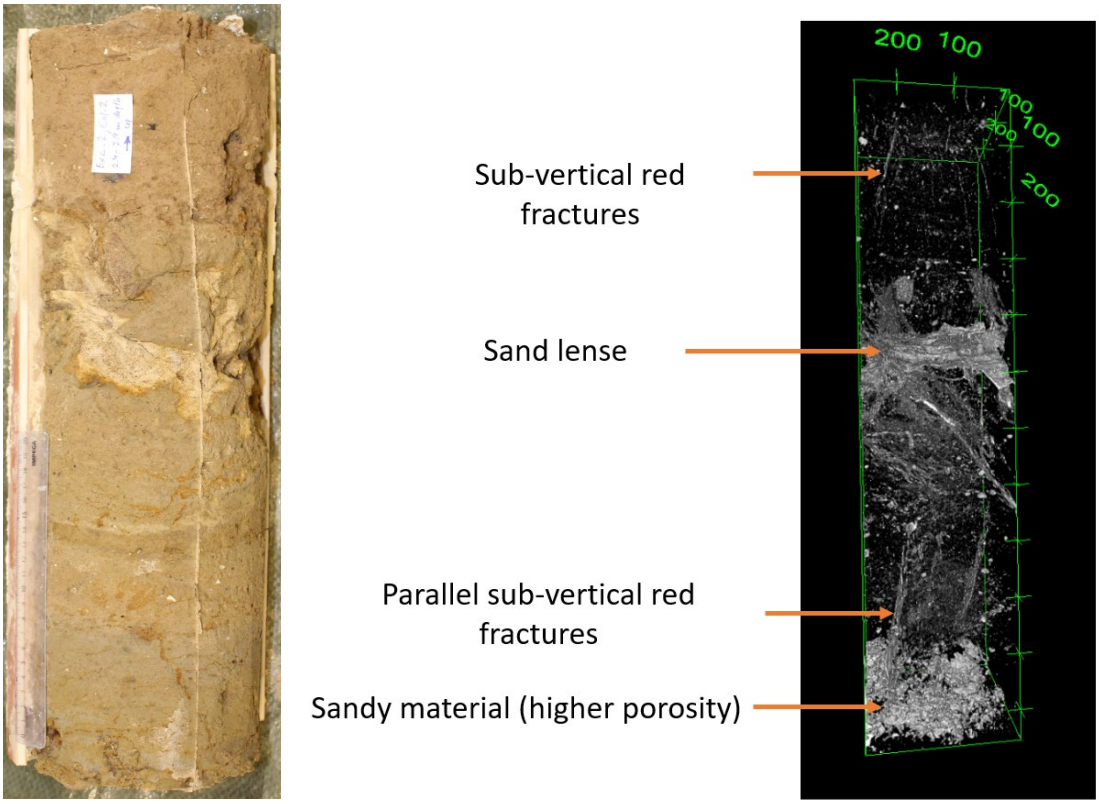

FIGURE 58. Column 2 from BB3 (a) full length with sand lens and in middle and example of red fracture with Fe/Mn infilling, (b) Full length CT-scan showing pore network in resolution 430 µm (porosity shown = 2.44%).

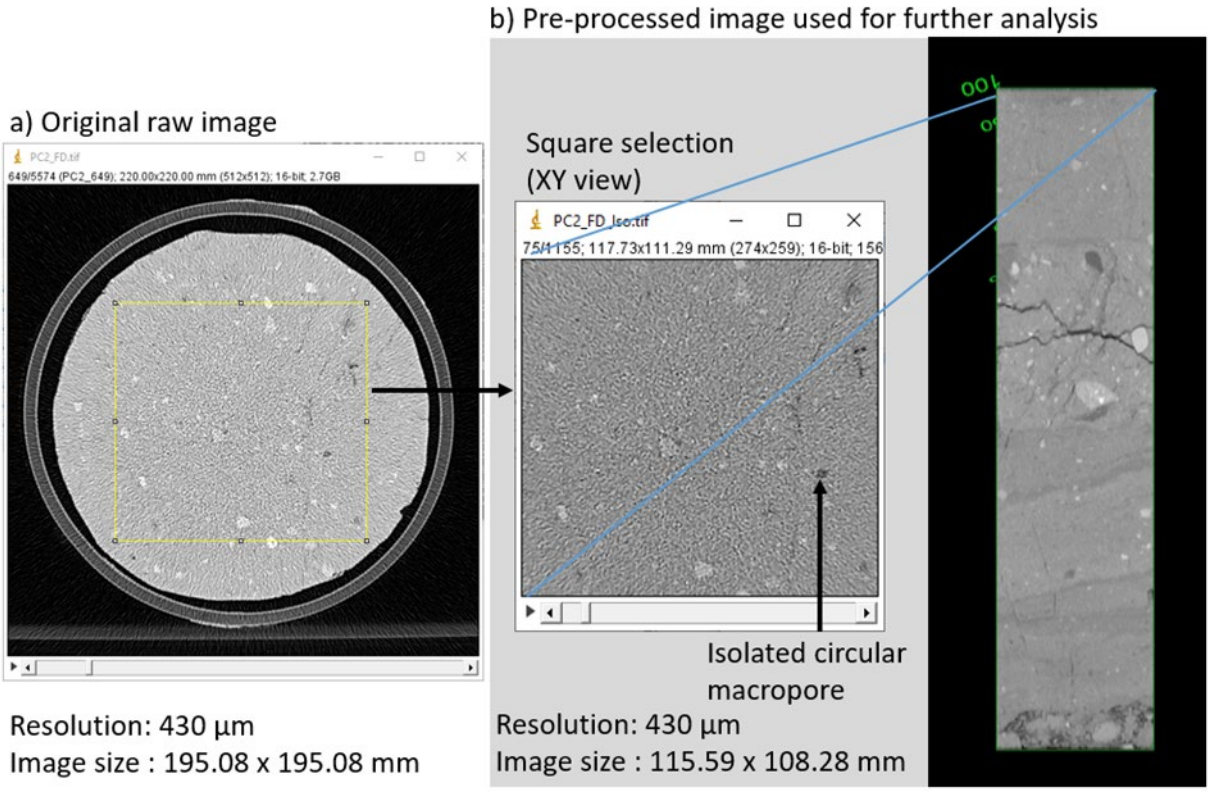

FIGURE 59. Image pre-processing for the Column 2. (a) Raw image, (b) ROI selection (2.40 m below ground) and 3D view of the column (2.40-2.90m below ground). Isolated circular macropores are visible in the soil matrix (diameter < 2 mm). Notice inherent sedimentary heterogeneity of the till matrix (vertical column image) which may provide heterogenous flow. Image resolution: 430 µm.

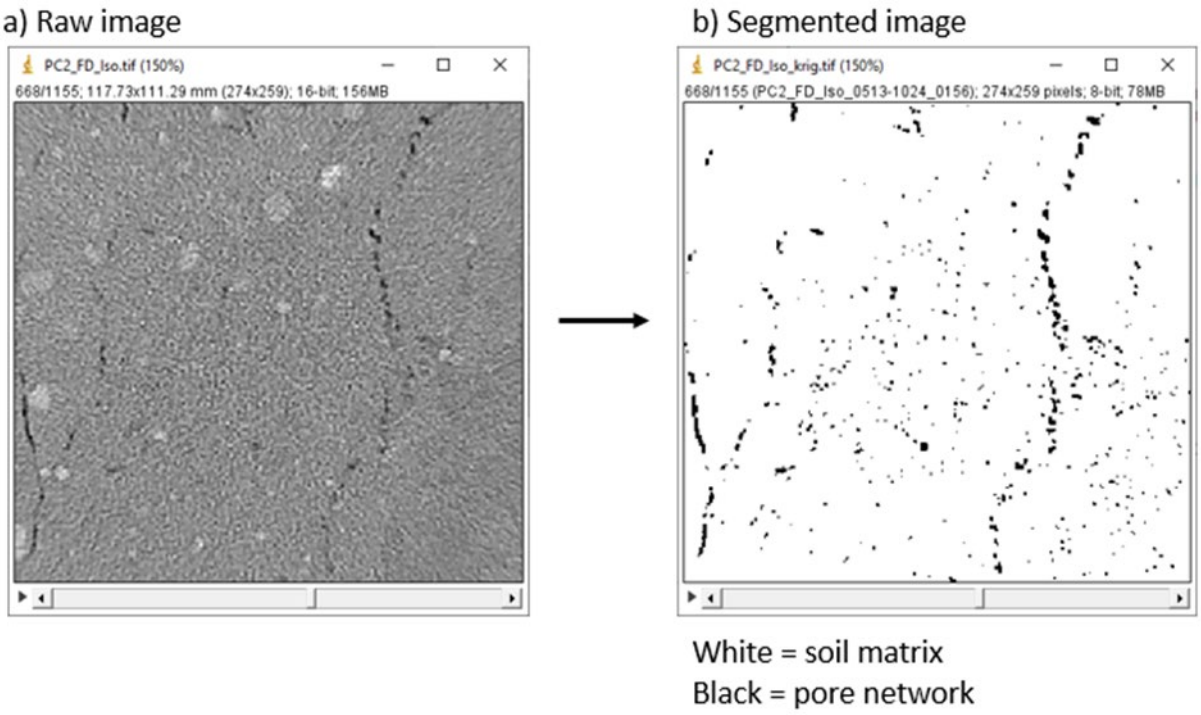

FIGURE 60. Image segmentation of the BB3 column 2 showing dense occurrence of macropores in matrix and in red fractures. The selection was at 2.70 m of depth below ground. The bigger biopores are organized along the fractures (diameter < 2 mm), while the smaller ones are visible inside the soil matrix (< 1 mm). Image resolution: 430 µm.

TABLE 12. Detailed description of selected pores for the BB3 column 2 (resolution: 430 µm).

Description in the analyzed section	Pore 1	Pore 2	Pore 3	Pore 4
Length (cm)	3.88	3.83	2.74	4.18
Mean diameter (mm)	1.25	0.92	1.19	1.50
Min diameter (mm)	0.43	0.64	0.43	1.07
Max diameter (mm)	1.93	1.29	2.35	2.05

BB7 dye tracer experiment E3 (2.05-3.75 m depth)

Figure 61 to Figure 63 show the BB7 dye tracer distribution in excavation 3 (Figure 44) after the dye tracer was infiltrated in 2.05 m depth. Infiltration was maintained for 12 days, after which the field was excavated. The tracer did not arrive in the drains established 1.7 m underneath the infiltration basin in the zone with only red fractures. Figure 61 shows the surface of the infiltration field in which the dye tracer was distributed in short segments along the fractures and in solitary root channels. Figure 62 shows the exposed inside of vertical fracture walls underneath with dyed root channels in the grey fractures from 2 m depth to the transition to red fractures in 2.8-3 m depth.

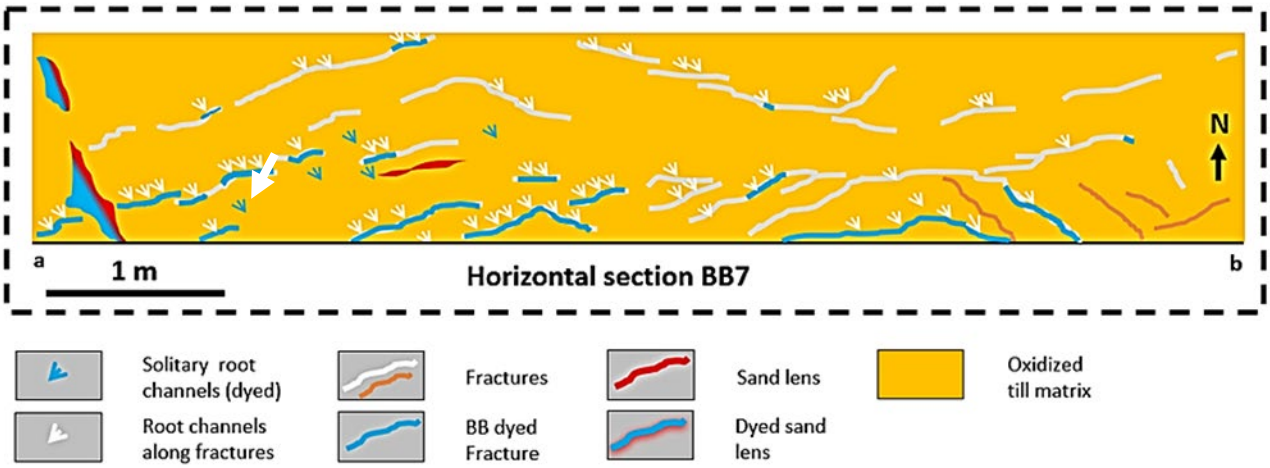

FIGURE 61. Distribution of dyed fractures and solitary root channels in BB7, 2.05 m depth. Line a-b (southern side of experimental field) shows the position of the excavated vertical profile in Figure 62.

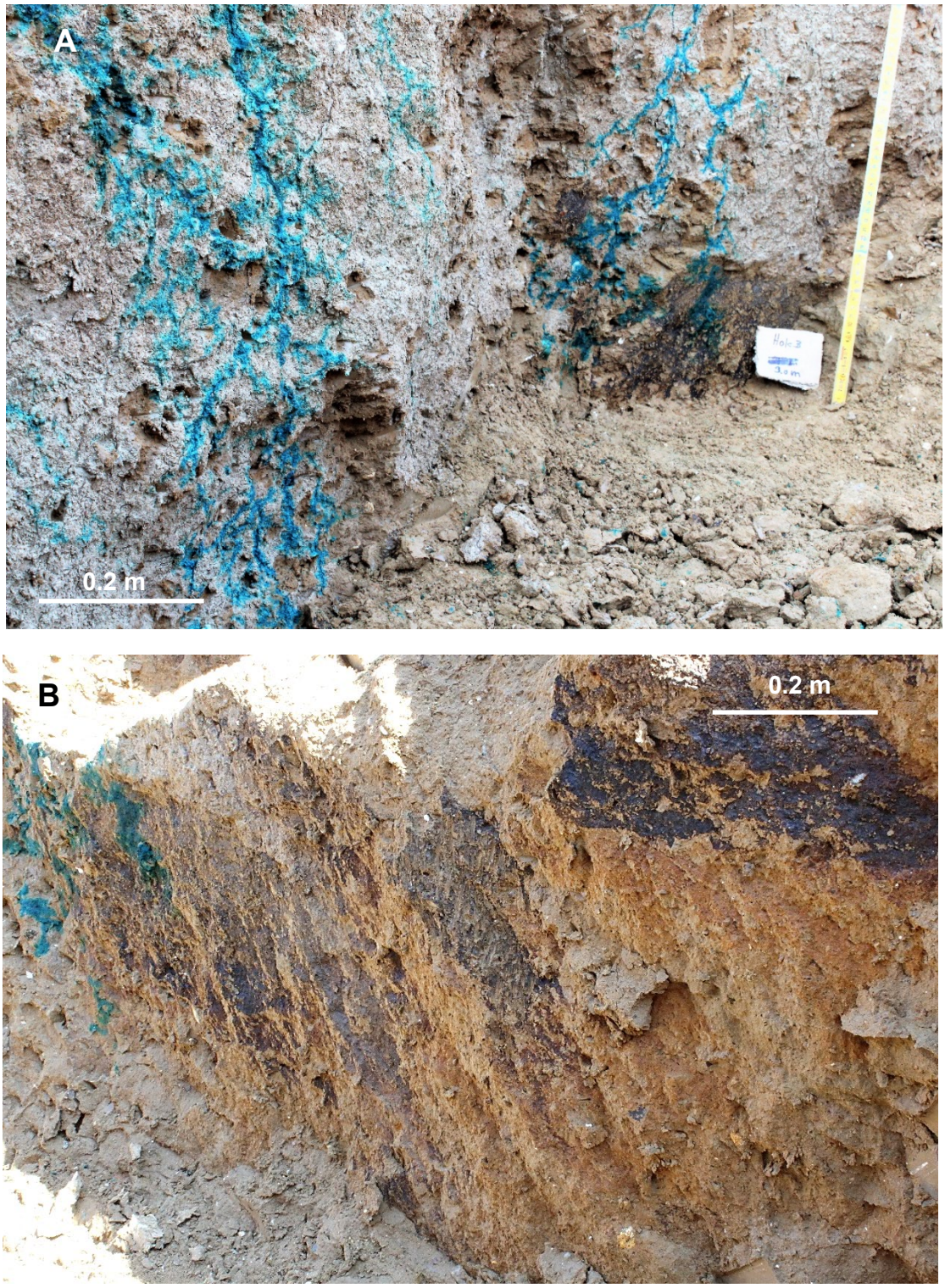

FIGURE 62. Vertical profile in 2-3 m depth underneath the BB7 experiment after dye tracer infiltration for 12 days. (a) Exposed inside of grey fractures with dyed root channels. (b) Dark brown and reddish Fe/Mn-oxide filled fractures (red fractures) with absence of BB dye tracer. The grey and red fractures occurred side by side in a transition zone between 2 and 3 m depth. They grey fractures always contained root channels inside with active flow, while no root channels were observed in the red fractures. Notice absence of BB flow internally in the factures between the root channels (https://mst.dk/media/210350/pestpore2video2.mp4).

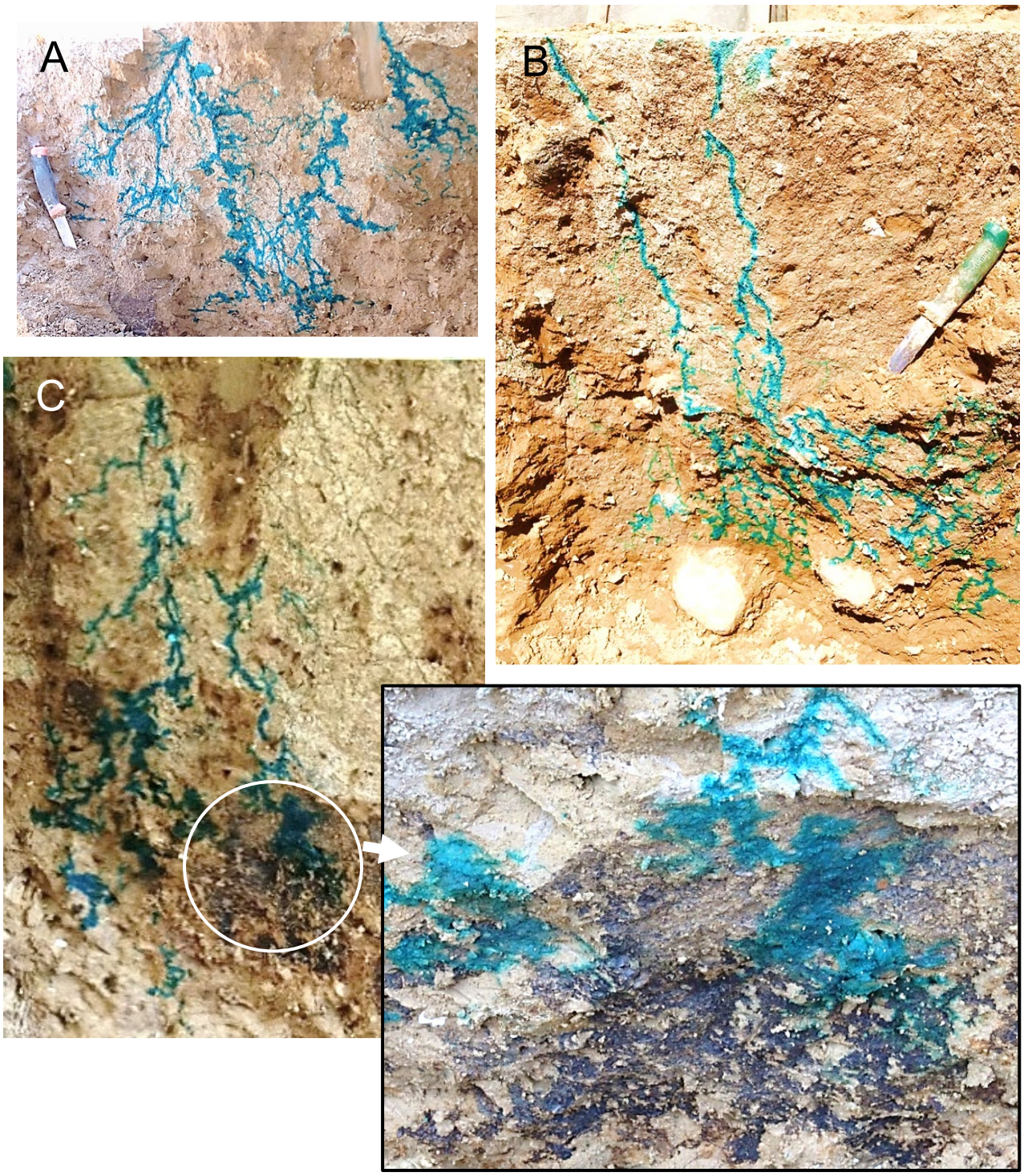

FIGURE 63. Dyed root channels on exposed grey fracture wall surfaces (BB7) in excavation 3. (A) BB flow in branching of root channels 2-3-2.8 m depth, (B) BB flow in dimorphic root channels (branching into dense root network when approaching capillary fringe or ground water table). (C) BB flow in root channels terminated by Fe/Mn-oxide filling of the root channels in transition from grey to red fractures (3 m depth). Notice absence of BB flow inside factures between the root channels.

The dyed pattern on the grey fracture walls shows the same overall pattern as in BB1 and BB2 (Figure 47) with no BB observed on the fracture walls between the dyed rot channels, which suggests that the fractures themselves were hydraulically very narrow or closed. Some of the

dyed root casts show dimorphic patterns (Figure 63b) expressed by intense branching of single deep roots when approached the capillary fringe or ground water table. In about 2.8-3 m depth, the fractures and root casts were infilled with Fe/Mn oxides, which terminated BB flow (Figure 63c-d). The root channel system continues into the red fractures as a blurred pattern of Fe/Mn-oxide precipitations, filling the porosity formed by the root channels along the fractures (Figure 63d). Hereby, the root channel macropore system appeared to have been established before the Fe/Mn-oxide infillings, which supports an early postglacial history and the estimated high age of the Fe/Mn fillings in the fractures in section 3.4.

XRT of BB7 intact column (Column 3) 2.3-2.8 m depth, E3

After the BB7 experiment, an intact column was collected from the corner of the BB7 experiment in 2.3-2.8 m depth (Figure 4). The upper half of the column was disturbed in the sampling process and is omitted in the following. The XRT scan in Figure 58 showed distinct branches of vertical pores in the relatively undisturbed lower half of the column. Most large pores occurred inside the main fracture in the column (Figure 64b), which resembled the dyed root channels observed inside the grey fractures in the BB1, BB2, and BB7 experiments (Figure 46, Figure 47, Figure 62, and Figure 63). The scan revealed that widened lenticular fracture aperture zones were developed along the largest root channels (Figure 65b). Those zones resembled the few cm wide BB dyed segments observed along fractures in the BB field experiments (Figure 65c) and were also observed in the fractures in the Marebæk site by Jørgensen et al. (2002a). In the Marebæk site, those overlapped to produce 10-30 cm wide dyed fracture segments along deep tectonic fractures, which were otherwise Fe/Mn-oxide filled. The lenticular aperture shape also resembles the Fe/Mn-oxide infilled pore spaces in deep red fractures in the current study (Figure 28b and Figure 67), suggesting that those fillings are also related to aperture enhancements by original roots. The fracture aperture enhancement related to the root casts may be due to desiccation and shrinking from high tension water uptake by the original roots, or may be due to healing of originally large root holes (Figure 43). Shrinkage implies that the concept of fracture desiccation may be extended to include tectonic fractures in the rooting zone. Enhanced flow channels due to desiccation along the observed fossil roots were not observed in the ghost fractures below the water table in the low Bulbro ground site (section 3.4 and below), which suggests that the shrinkage may be indicative of unsaturated condition in the fractures when the roots were active. Fingering flow similar to the flow pattern in the fractures has been described in soils due to viscosity and/or gravity-driven instabilities by e.g., Chuoke et al. (1959) and Homsy (1987). The field observations and XRT results, showed that the observed flow patterns were controlled by physical macropores from actual root channels and hence could not be explained as from viscosity/gravity-controlled instabilities.

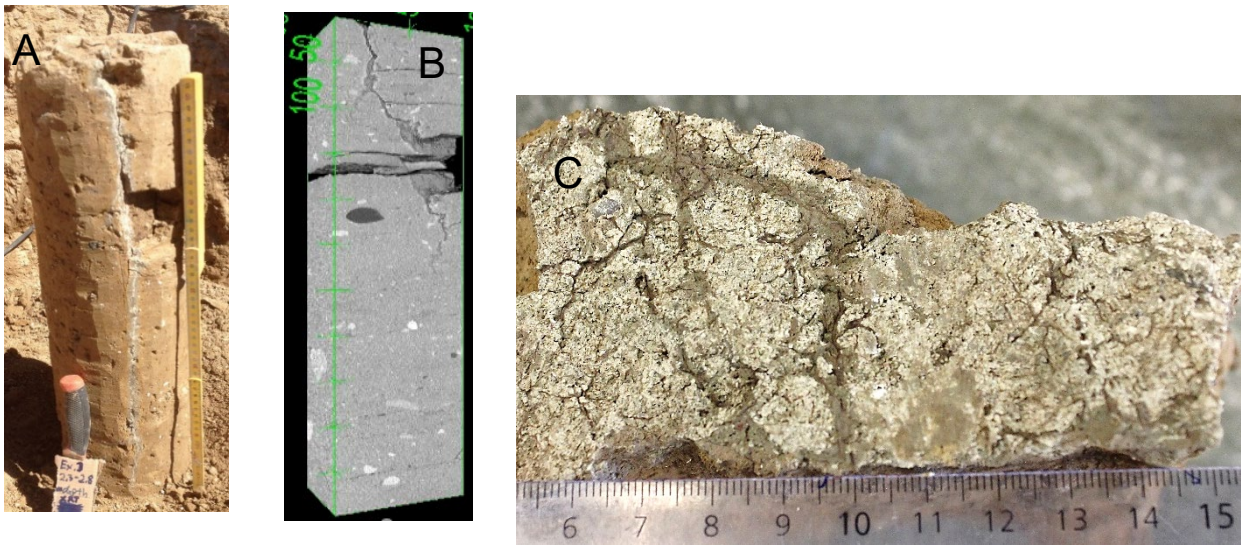

FIGURE 64. XRT column from BB7 (2.3-2.8 m depth) with prominent grey fracture penetrating the top of the column vertically. (A) Sampling of column in excavation, (B) CT-scan of the column at 369 µm resolution, (C) root casts along the grey main fracture from the lower half of the column. Notice disturbance and artificial fracture enhancement in upper half of the column.

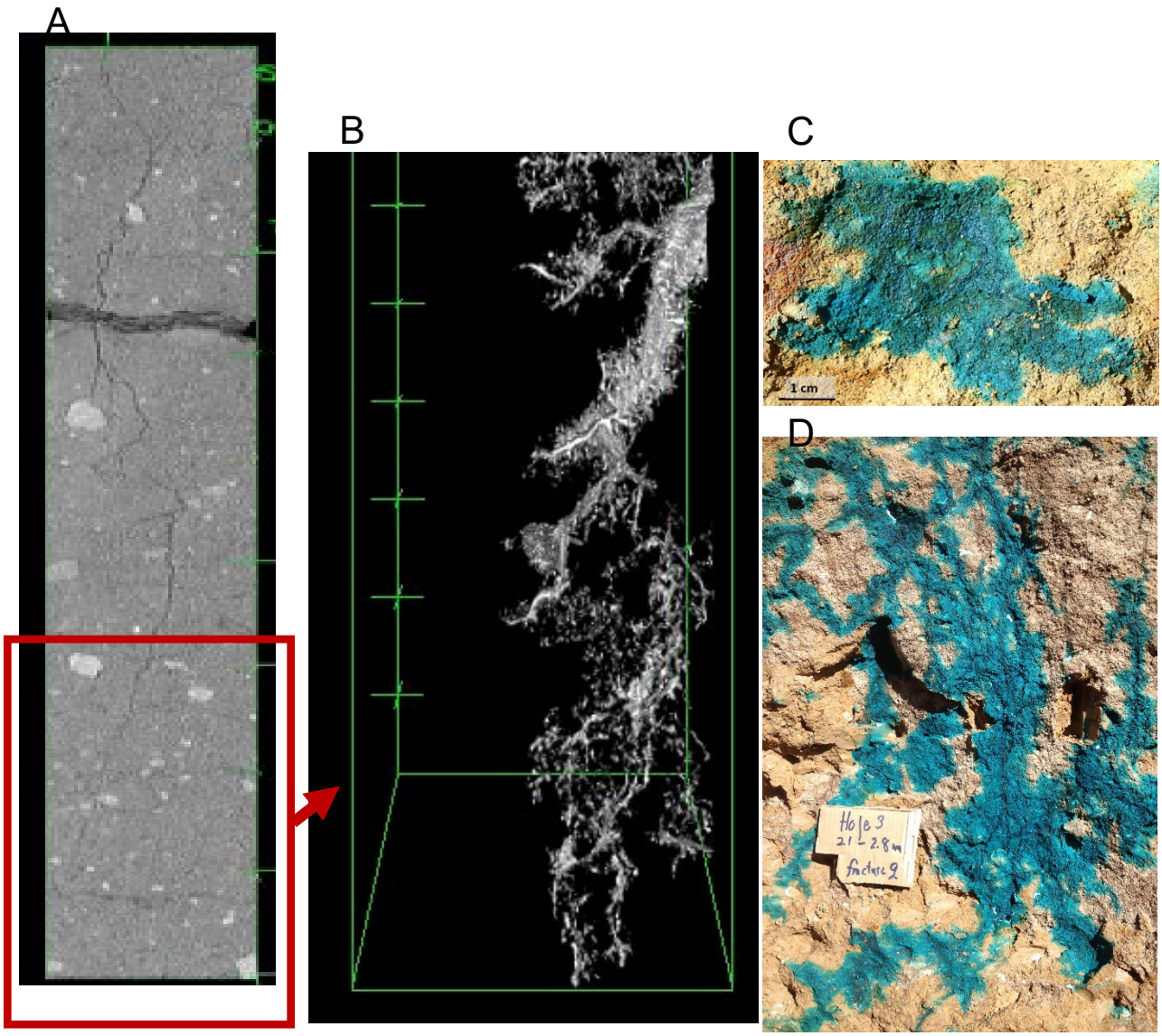

FIGURE 65. XRT scan of Column 3 and root channels along fractures in BB7 (2.1-2.8 m depth). (A) Overall column (frame shows relatively undisturbed part of column in B), (B) XRD 369 µm resolution of enhanced porosity area (grey) along discrete root channels (white) inside fracture in framed section of column, (C) and (D) BB dyed fracture channel areas inside fractures related to discrete root channels in the field experiment.

Table 13 shows the mean diameters and porosities of the root channel macropores in the undisturbed lower section of the column, which compares to the diameters observed in the field excavation (Figure 30).

TABLE 13. Pore diameter and porosity of pores > 369 µm in the relatively undisturbed lower half of XRT column BB7.

Depth (m)	Pore diameter (mm)							Porosity (%)
	Min.	1st Qu.	Median	Mean	3rd Qu.	Max.	SD	
2.30-2.40	0.74	0.74	0.74	0.82	0.74	3.39	0.23	2.2
2.40-2.50	0.74	0.74	0.74	0.81	0.74	2.76	0.19	2.38

3. Flow in deep red fractures (Figure 44 D)

BB5 and BB6 dye tracer experiments, E2 (5.1-6 m depth)

The BB5 and BB6 experiments were established in 5.1 m depth in E2 (Figure 44) and included the deepest relic root channels observed in the high-ground site, and both oxidized and reduced clayey till (Figure 66). In the western end, both experimental fields were tectonically disturbed by lateral glacial forces along the boundary of till TC and till TD, which had pushed rock cobbles, boulders, sheared sand lenses, and Paleocene slabs (Figure 66) from the underlying limestone aquifer into the till. Due to the rock obstacles, no drainage tubes were established underneath the experimental fields and they were not water saturated prior to the BB infiltration (to avoid water stewing in fractures and biopores as was observed in BB3 and BB4). The BB infiltration was maintained for 15 days, after which the fields were excavated. Figure 66 shows the distribution of the dye tracer in the experimental fields after 2-3 cm of the surface of the experiments were removed.

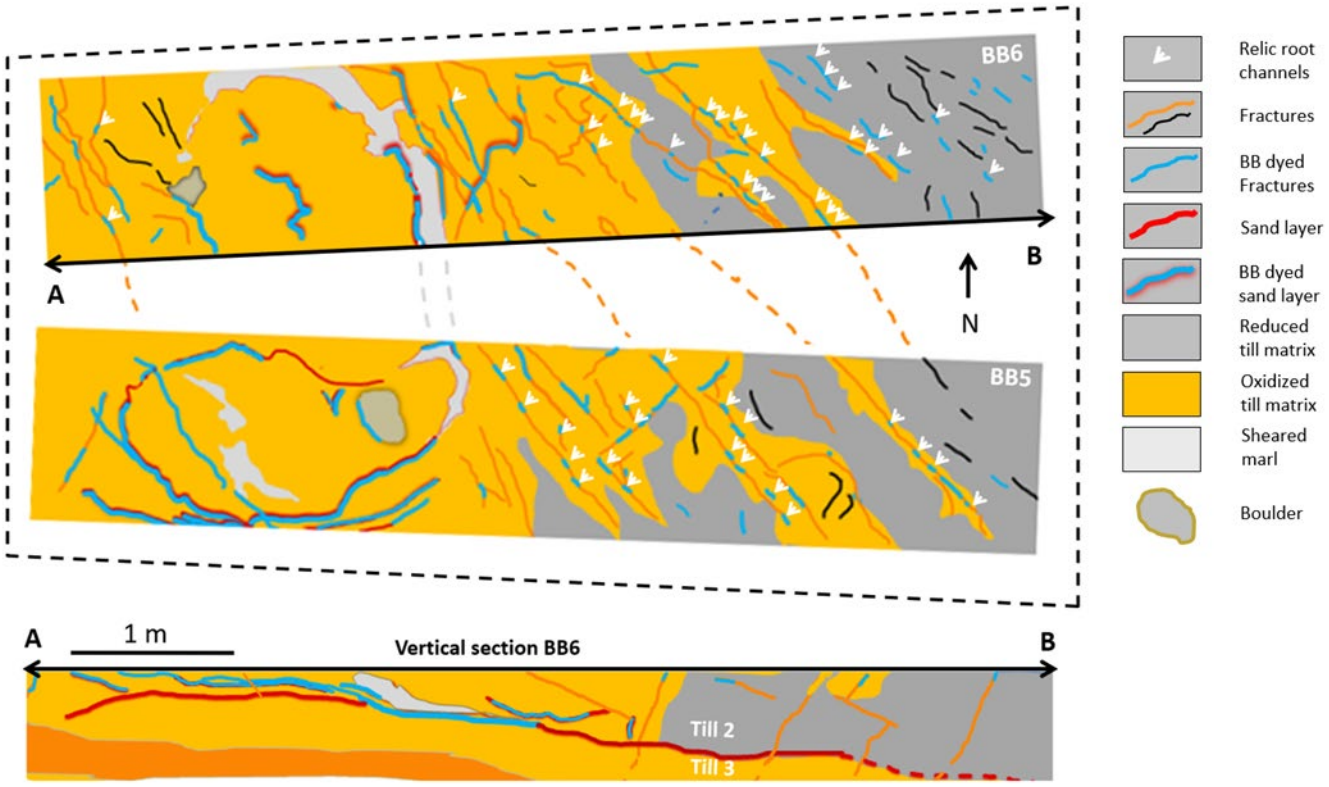

FIGURE 66. Horizontal and vertical sections of BB5 and BB6 dye tracer infiltration experiments showing the distribution of BB dye tracer in fractures, biopores and sand layers (horizontal surfaces are shown after removal of upper 2-3 cm of infiltration fields). Indicated root channels represents minimum frequencies because of rainstorm conditions during mapping of the experiments made identification difficult. Notice very shallow penetration of BB dye in the fractures, while extensive flow of BB occured in sheared sand layers (Figure 68D).

The dye tracer was distributed along the sheared sand lenses (Figure 66 and Figure 68) and along 2-40 cm wide fracture segments, which were related to the partially Fe/Mn-oxide clogged macropore channels along the fractures (Figure 67). BB flow clearly dominated in the sand lenses and was, in general, small along the fractures. In the reduced clay, the vertical penetration of the dye tracer in the fractures was 2-4 cm, while it was 2-40 cm in the oxidized till. The deepest penetration of the dye along the fractures was related to the macropores inside the fractures, which resembled the patterns of root channels observed inside the grey fractures above (BB1-BB7 experiments, e.g., Figure 63), except for preferential flow was strongly inhibited by the Fe/Mn-oxide fillings in the channels (Figure 67). The origin as root channels was supported by finding of ancient aDNA from the willow tree/scrub family (section 3.6.3) in the channels and in the matrix along those, where small root holes with oxidized haloes were also observed (Aamand et al. in prep., 2020). Well-defined hydraulic experiments with saturated large undisturbed columns (LUC) collected from the E2 vertical profile and the BB5 experiment showed similar lack of penetration of the dye tracer in fractures as observed in the field experiments (Aamand et al. in prep., 2020, and Mosthaf et al. in review, 2020).

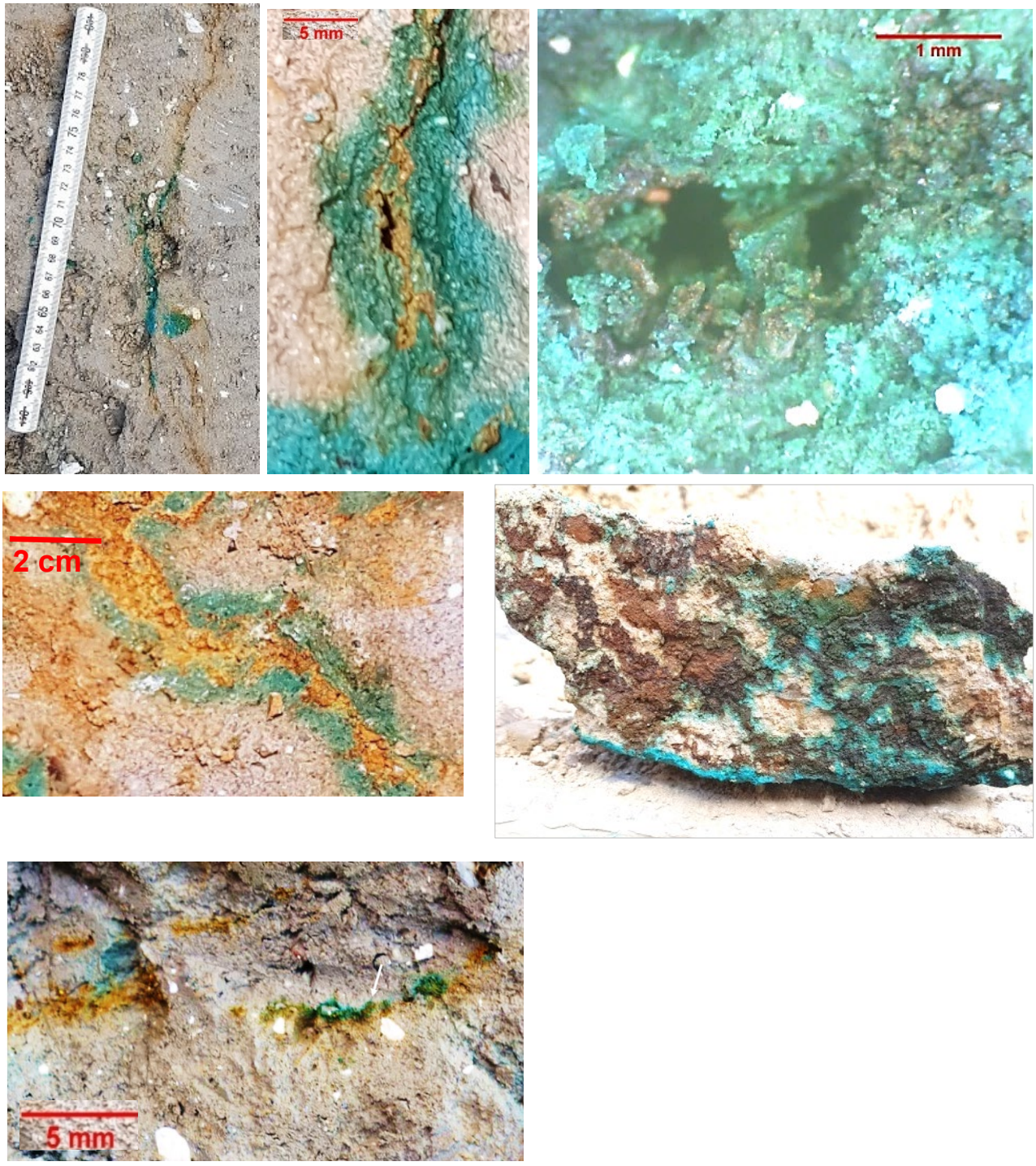

FIGURE 67. BB dye along fractures and relic root channels inside fractures. (top) Relic root channels in the surfaces of BB5 and BB6 infiltration fields (middle and bottom). Fe/Mn-oxide filled root channels macropores inside fractures resembling the root patterns observed inside the grey fractures (e.g., Figure 63 and Figure 65). The origin of the channels from tree roots was supported by findings of ancient aDNA inside and along the from willow tress/scrub along the channels in all examples shown (section 3.6.3).

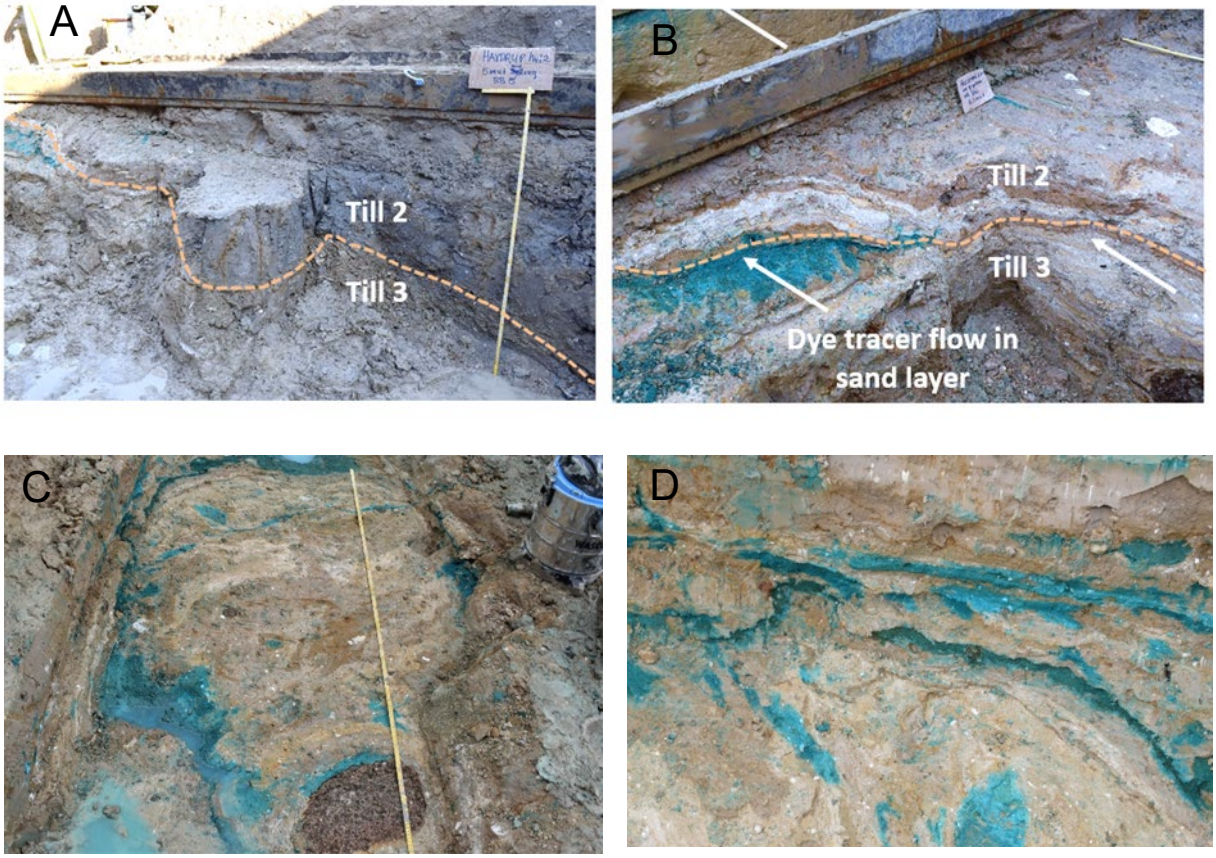

FIGURE 68. Excavation of BB5 and BB6 dye tracer experiment showing BB flow in the sheared sand layers along the boundary between till unit TC and till unit D. (A) South-east inclining boundary between reduced clayey till unit D (Baltic ice advance) overriding oxidized clayey till unit C (late Weichsel main ice advance) marked with dashed line (see Figure 2 about till units and sand layers in the tills). (B) BB transport along the inclined sheared sand layers, which dominated flow in BB5 and BB6. (C) Horizontal surface showing BB transport along the sand layers, yard stick 2 m. (D) Vertical section showing the dyed sand layers in closer view (photo 0.5 m across).

XRT of BB6 intact samples (Columns 3 and 4) 3.5-4.5 m depth, E2

After the BB5 and BB6 experiments, 2 intact blocks for XRT analyses were collected from 3.5 to 4,5 m depth adjacent to BB6 in E2 (Figure 4 and Figure 69). The two blocks were similar with respect to occurrence of red fractures in the oxidized clayey till and resemble the LUC experiments from the same depths by Aamand et al. in prep. (2020). The overall XRT images of the blocks in Figure 70 show the occurrence of linear structures with high porosity, which resembles the larger aperture segments observed along the red fractures in the field (e.g., Figure 28).

FIGURE 69. Intact block containing red fractures in oxidized till collected from 4-4.5 m depth in E2 for XRT analyses.

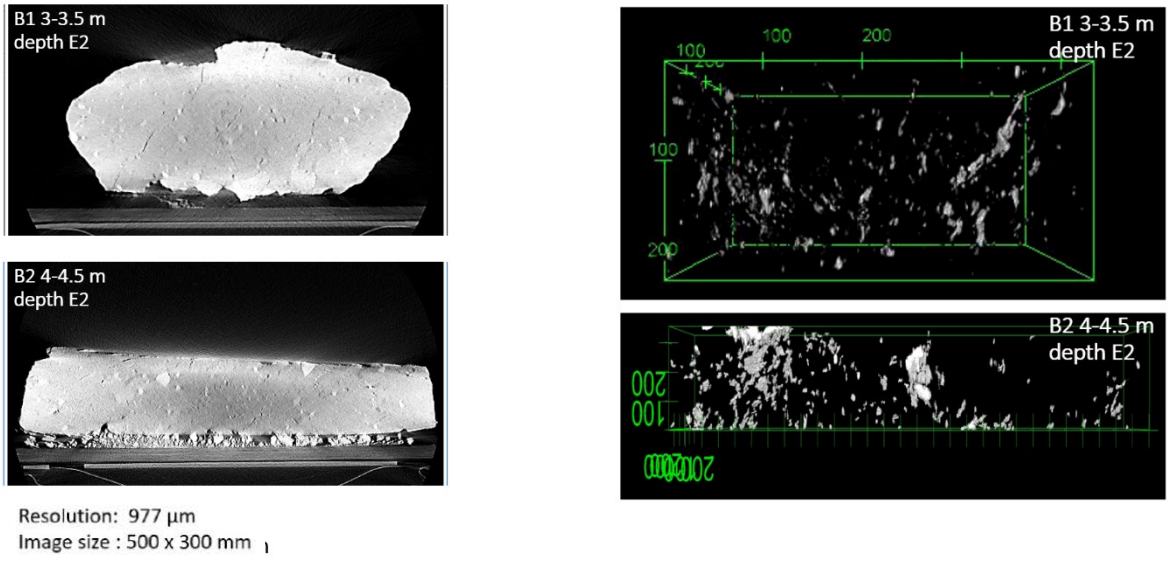

FIGURE 70. XRT scanning of Intact blocks 1 (top) and 2 (bottom). (left) Overall image showing linear segments of large fracture aperture sections along fractures (resolution 977µm). (right) 3D scans showing porosities related to the fractures in the blocks, which constitute 0.45% and 0.43%, respectively, in the two blocks. The large aperture segments are shown to be poorly connected in the applied resolution (146 µm).

The XRT scan images, also in Figure 70, show that the segments were parallel tabular pore organized along the fractures. They appeared disconnected or poorly connected in the 977 µm resolution of the scan, which was in agreement with the partial infilling with Fe/Mn-oxides (section 3.3) and observed absence of BB flow in the pores in the BB5 and BB6 infiltration experiments.

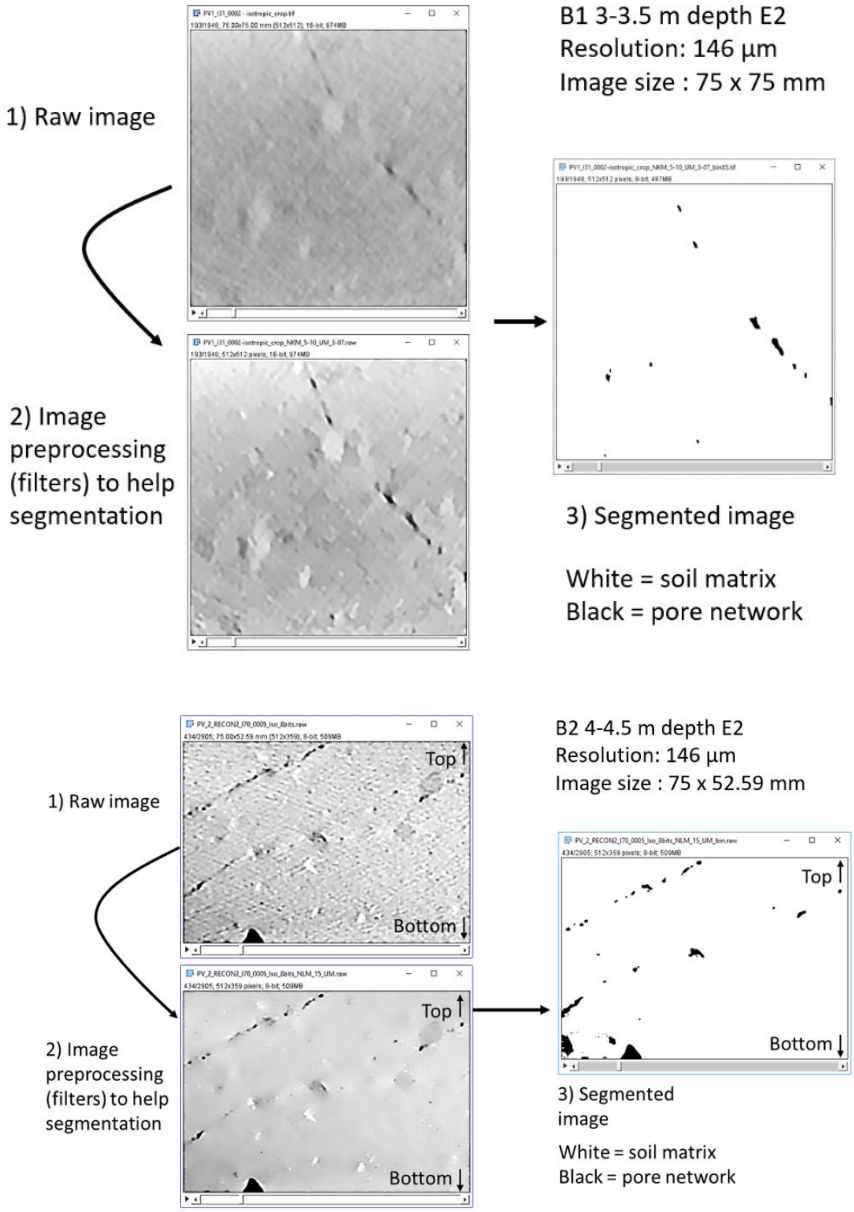

FIGURE 71. Detailed XRT images of pore structure along the fractures in Block 1 (top) and Block 2 (bottom). The images show many circular and elongated macropores along the fractures (diameter < 2 mm), which resemble the root channels observed elsewere along the fractures in the excavations (image resolution 146 µm).

Figure 71 shows the occurrence of isolated circular or elongated pores resembling root channels, which represent the inside of the large aperture fracture segments. The 3D images in Figure 72 show that they formed tabular, apparently disconnected, pore spaces organized

along the fractures, which resembled the Fe/Mn-oxide fillings of pore spaces related to the root channels shown in Figure 28B. As mentioned, the lack of connectivity was in agreement with the very small penetration of the BB dye tracer into the fractures in the BB5 and BB6 infiltration experiments, which was due to filling of the pores with Fe/Mn-oxides (section 3.4).

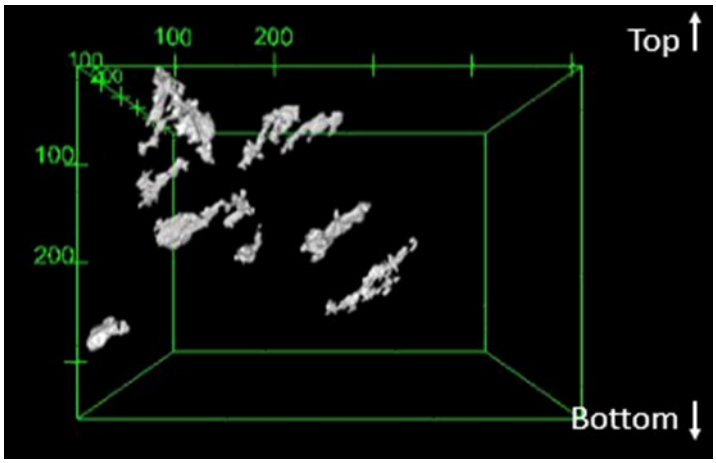

FIGURE 72. Example of the largest continuous pores in Block 2 (146 µm resolution). At the given resolution, the hydraulic connectivity between the pores could not be concluded.

Some planar pores were extracted for detailed description in Table 14. They were representative for both blocks and constituted short isolated segments (1.71 and 1.39 cm) with a maximum diameter of 2.67 and 1.88 mm developed in diagonal plans along the fractures in the till. For the entire blocks, the macropores had a mean diameter of 0.71 and 1.27 mm (Figure 73). Notice that the XRT macropore diameters were estimated as the diameter of the greatest sphere that fits within the open tabular structures, and thus are not representing diameters of tubular channels such as the root holes.

TABLE 14. Detailed description of selected pores for the BB6 XRT Block 2 (4.0-4.5 m) (pores extracted from the 146 µm image).

Description in the analyzed section	Pore 1	Pore 2
Length (cm)	1.71	1.39
Mean diameter (mm)	1.26	1.12
Min diameter (mm)	0.29	0.29
Max diameter (mm)	2.67	1.88

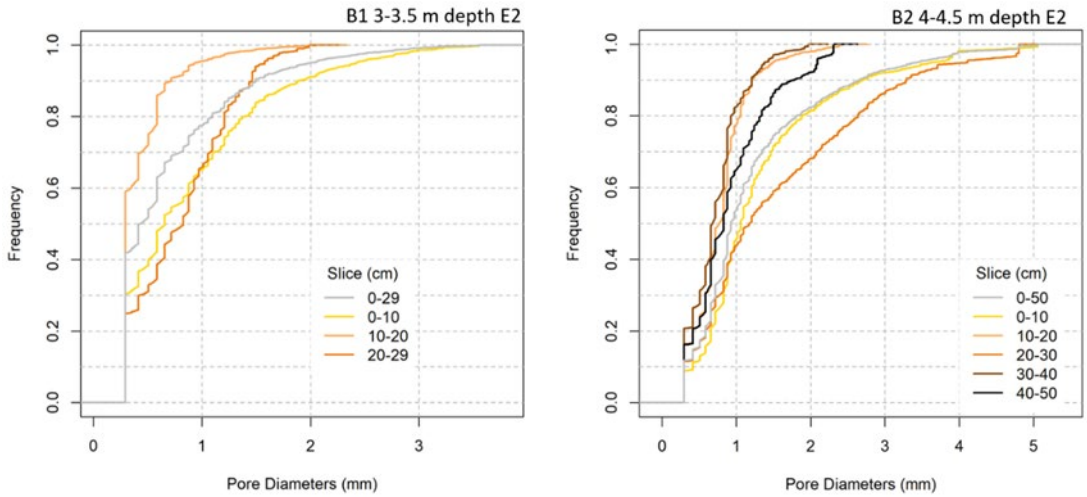

FIGURE 73. Macropore size distributions in vertical slices along Block1 (3.0-3.5 m) and Block 2 (4.0-4.5 m) (resolution: 146 µm).

BB8 dye tracer experiment E3 (3.1-3,75 m depth)

The BB8 infiltration experiment was established in the zone with only red fractures in 3.1 m depth immediately below the BB7 experiment and the transition from the grey to red fractures (Figure 44). The experiment was water saturated before the BB infiltration and maintained for 10 days, after which the experimental field was excavated. Figure 75 shows the distribution the dye tracer along fractures after 2-3 cm of the surface of the infiltration field was removed. The experiment revealed that BB flow had locally penetrated 2-10 cm into the red fractures or biopores, confirming that the transition from grey to red fractures and biopores marked the lower boundary of rapid preferential flow in the fractures and root channels. The tracer did not arrive in the drain established 0.7 m below the infiltration basin, however, it was transported approximately 1 m downward along a sub-vertical sand lens embedded in the till (Figure 75c).

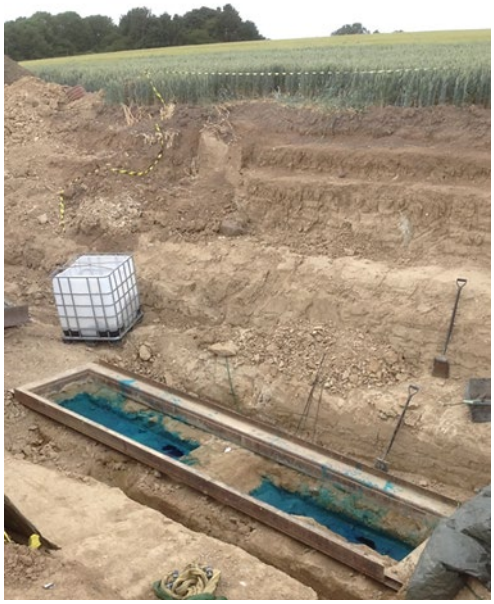

FIGURE 74. BB8 dye tracer experiment in 3.5 m depth in E3. The infiltration field had to be separated in two because fractures were accidently disturbed by the excavator in the middle section.

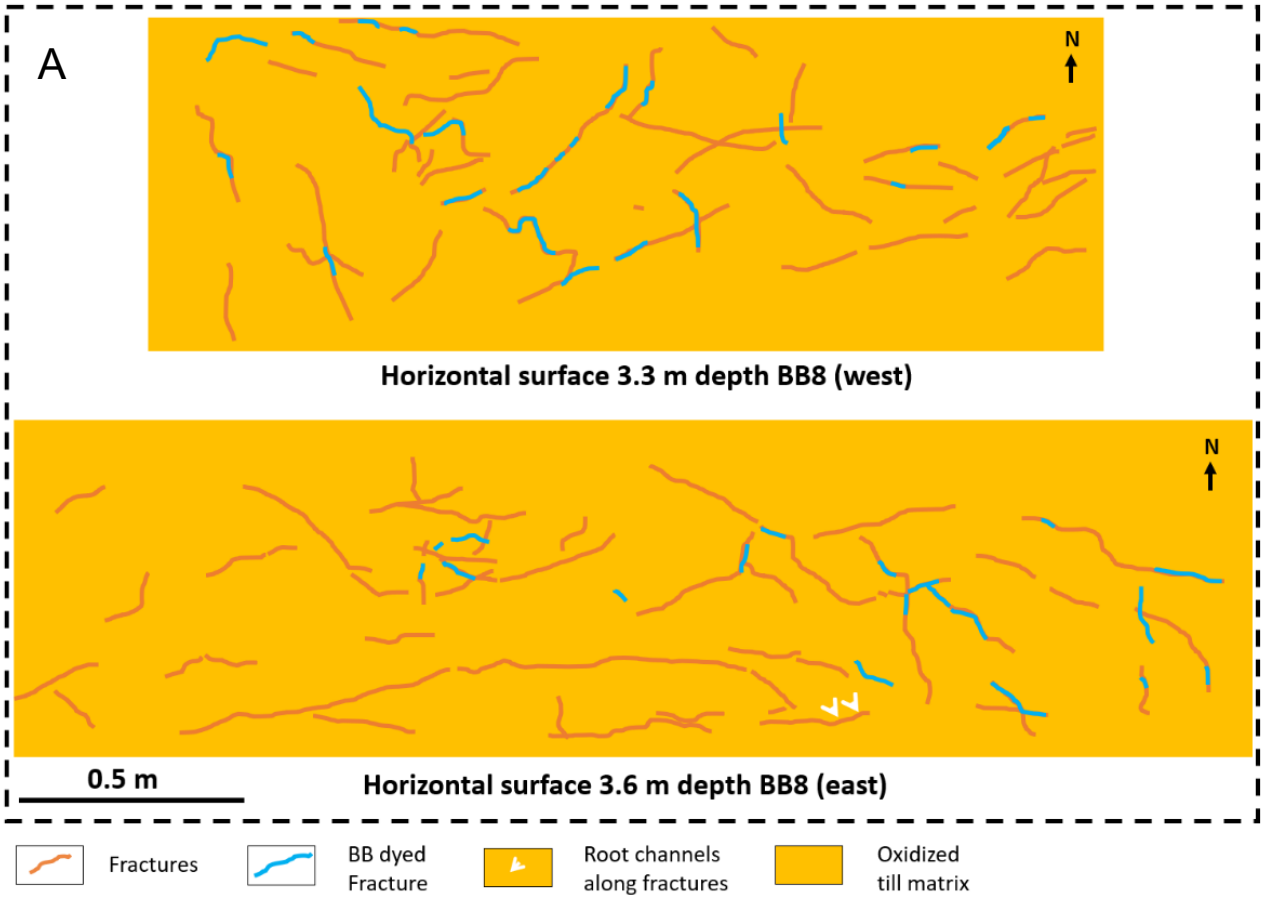

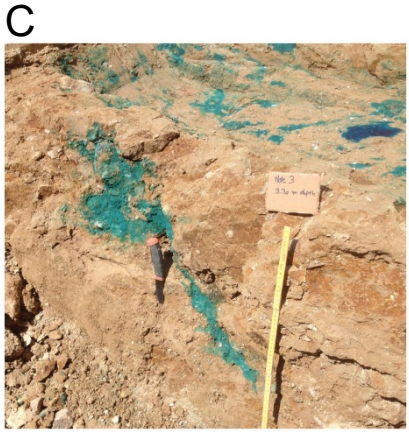

FIGURE 75. BB8 infiltration field after dye tracer infiltration. (A) Horizontal surface of experiment with BB along fractures (ca. 2-3 cm below excavated surfaces), (B) Surface of exposed vertical fracture wall showing massive Fe/Mn-oxide filling of fracture and absence of BB dye tracer, (C) Dye tracer flow along inclined sand lens.

BB0 dye tracer infiltration experiment, E1

Initially, a 6 m x 1 m infiltration basin was prepared with the surface in 3.55 m depth near the vertical transition from oxidized brown to reduced grey clay. Unfortunately, this field had to be given up because the fractures were accidently disturbed when establishing the drain tube underneath the field. A substitute field 2.5m x 0.5 m was then established in 5.0 m depth in TD till unit (Figure 76). The TD till unit was initially saturated and reduced, while the till TC below was

oxidized and unsaturated. Most vertical fractures in the till terminated just above the surface of the infiltration field, where only 3 red fractures occurred. After 8 days BB infiltration, the experimental field was excavated, which revealed that no visible penetration of BB had occurred in the fractures or clay matrix (in agreement with the perched groundwater conditions in this high-ground location (Figure 21 and Figure 22). It was further revealed that TC unit and its related glacial pavement was reached 25 cm below the surface of the infiltration field (Figure 78). More red fractures occurred in the TD till just above the boundary to this, apparently due to upward oxidation from the unsaturated underlying oxidized TC till (Figure 77 and Figure 78).

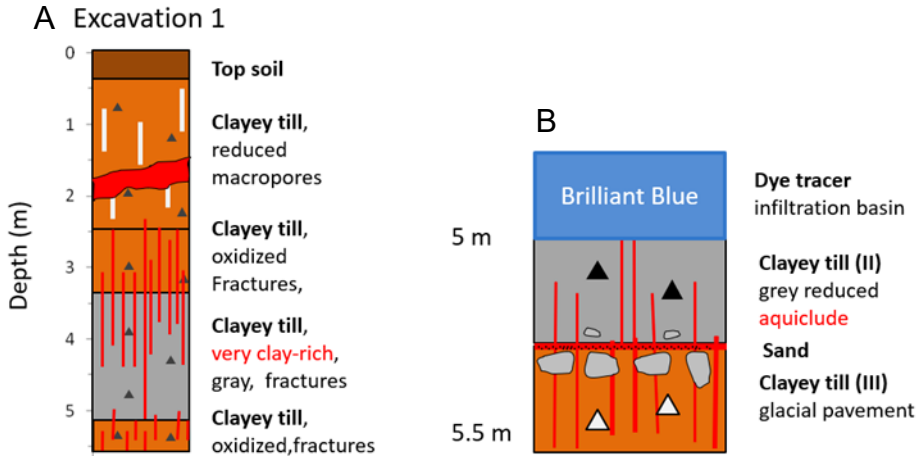

FIGURE 76. Brilliant Blue dye tracer experiment in excavation 1. (A) Geological profile showing a very clay rich layer (aquiclude, see Figure 22) in the experiment, (B) Details of BB infiltration field. No dye tracer infiltration into the fractures was observed after 8 days of infiltration.

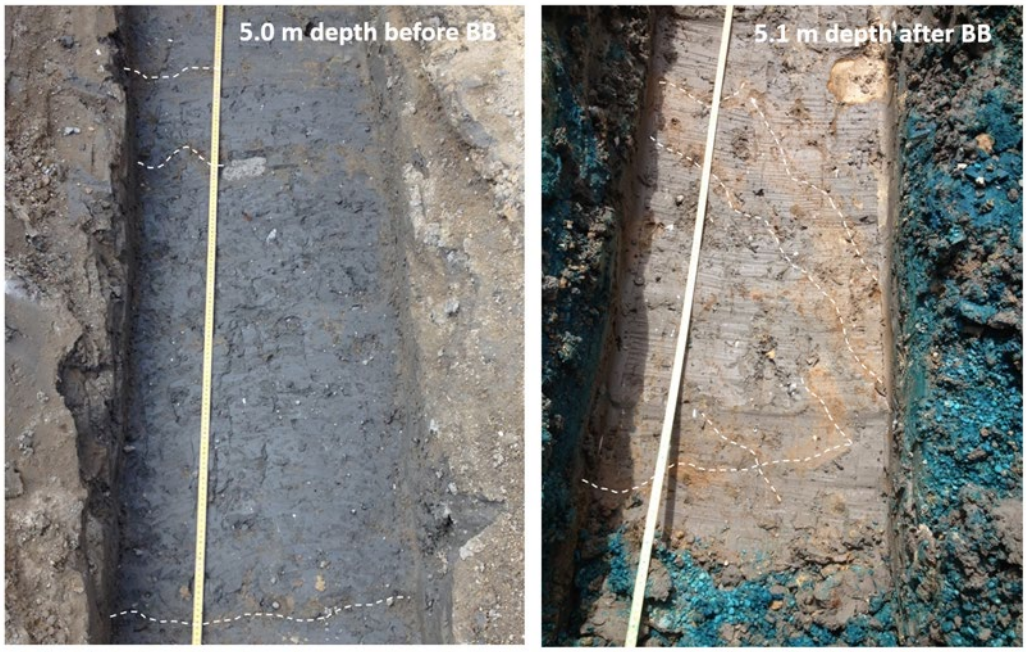

FIGURE 77. Surface of BB0 infiltration basin before and after BB infiltration (yard stick 1.2 m long). No BB transport along fractures was observed. Notice increasing oxidation of fractures with depth, indicating upward oxidation of non-visible fractures in the grey clay from oxidizing conditions below (Figure 76).

The absence of BB transport in the fractures showed they were largely closed, which indicated that the lower boundary of Till D constituted an aquiclude (Figure 76A), which is in agreement

with the observed permanent high and perched water table shown for this excavation site (Figure 21 and Figure 22). The local nature of the perched water table and hence heterogeneity of the aquitard was indicated by observed absence of the water table and the very clay-rich reduced till (aquiclude) throughout a 6 m deep borehole made 50 m west from the excavation (H2 in Figure 3).

FIGURE 78. Boundary between oxidized clayey till unit TC (late Weichselian main ice advance) and reduced till unit TD (Baltic ice advance) separated by thin SC sand layer (dashed line). Identification TC is made from glacial pavement present in top of TC and in much of the area (see Figure 2).

3.5.2 Low-ground experiments

The low-ground BB experiments investigated infiltration from the bottom of soil zone into the clay and embedded sand layers to 3.5 m depth (Figure 44A-D). Due to the dominating upward flow in the Bulbro low-ground site (Figure 23), downward flow was created artificially by pumping groundwater from the drain tubes established underneath the infiltration experiments (section 2.4).

BB9 dye tracer infiltration experiment, E4 (1-3.2 m depth)

Figure 79 shows the observed distribution of dye tracer in the BB9 experiment after BB was infiltrated in 1 m depth in excavation 4. The tracer arrived in the SC sand layer (see Figure 2) in 3.2 m depth underneath the infiltration field in less than 1 hour after application of the tracer. Hereafter, the infiltration field was excavated and characterized.

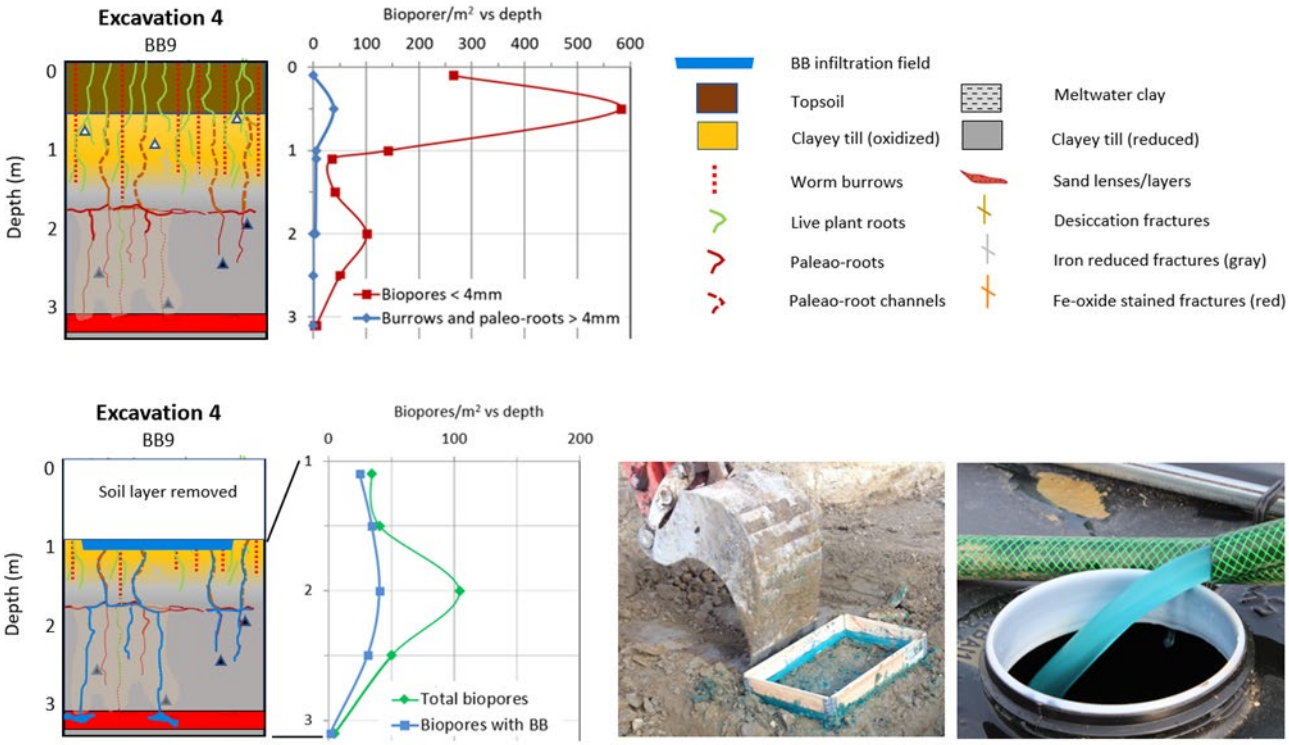

FIGURE 79. BB9 dye tracer infiltration experiment in excavation 4. (Top) Frequency of biopores in geological profile. Photos: Excavation after BB infiltration field and first arrival of the dye tracer in ground water pumped from the SC sand layer in 3.2 m depth.

The excavation showed that the tracer had migrated into the sand layer along mainly 1-2 mm root channels, decreasing from 48 channels/m^2 in 2 m depth to 2-5 channels/m^2 in 3.2 m depth (Figure 79). Figure 80 shows that in the shallow oxidized zone some of the root channels occurred inside grey fractures, resembling the observed flow channels in the grey fractures in the high-ground excavations (e.g., Figure 45 and Figure 63). In the underlying reduced clay (grey) some of the dyed root channels and fossil roots were apparently continuing along the non-visible ghost fractures described in Figure 42. However, most of the channels were solitary features in the clay and had Fe/Mn precipitated rims and haloes. The oxidized haloes persisted in the reduced clay below groundwater table, and the clay matrix was slightly oxidized adjacent to the channels (Figure 80). In other channels, fossil root residuals were still preserved below the water table, while the fossil roots were generally absent above and instead partially filled with loose soil material.

The dyed root channels with oxidized halos were connecting to the local sand layer in 3.2 m depth, which provided evidence that downward flow had been occurring prior to the experiment (despite the mostly upward hydraulic gradients observed in the low-ground monitoring wells, Figure 23). It is, however, unclear if downward flow in the root channels had only occurred in present time (induced by the water abstraction from the nearby Thorsbro water wells (*Figure 2*), or was related to the long-term history of changing climate and flow. As mentioned, the water abstraction has lowered hydraulic heads 5-7 m in the main aquifer since 1951, (Kruger A/S, 1989).

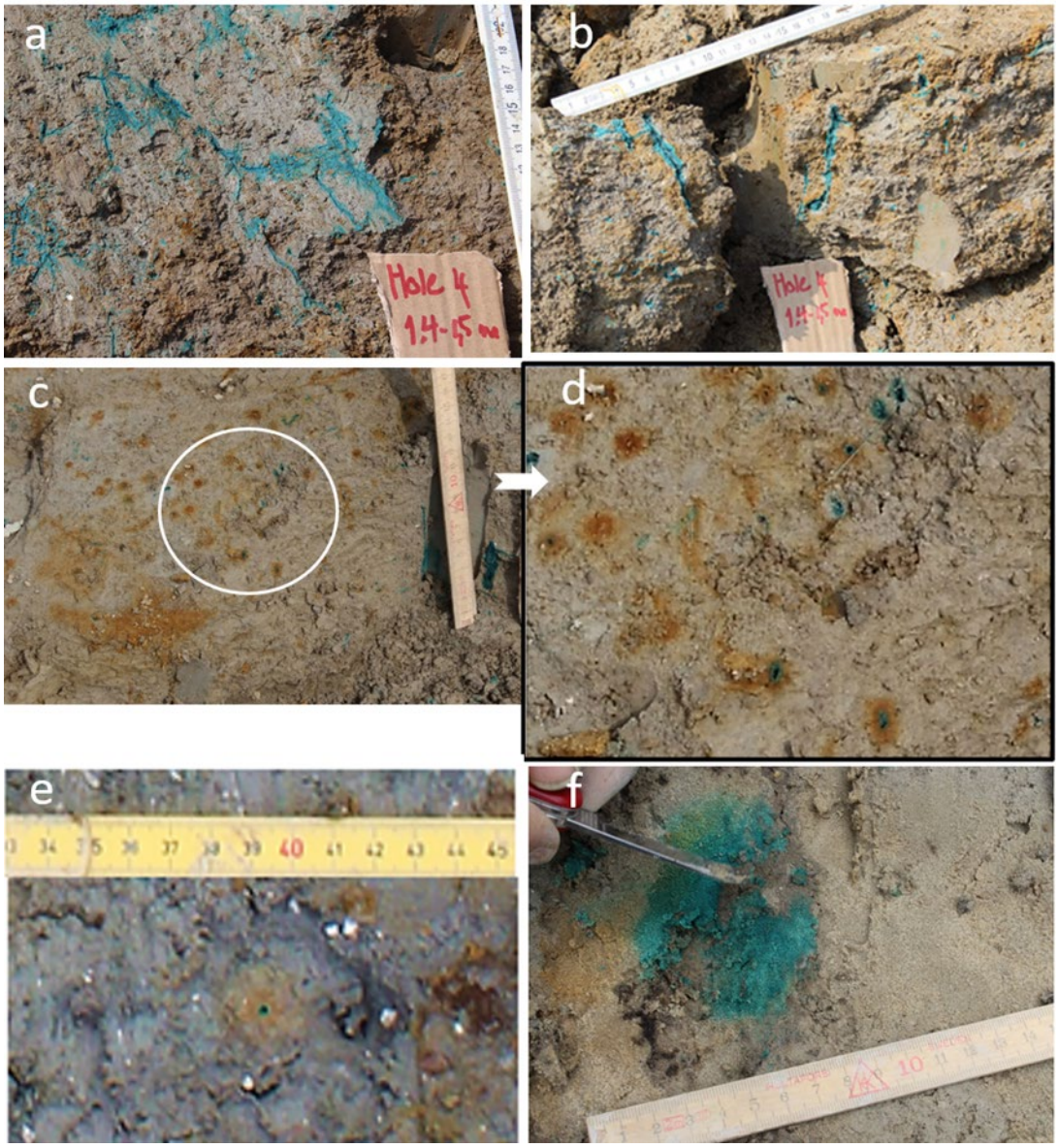

FIGURE 80. BB dye tracer migration in open root channels in BB9 infiltration field. (a) Dyed root channels inside sub-horizontal grey fracture, (b) Dye tracer in solitary root channels, (c and d) Horizontal surface in oxidized zone in 1.7 m depth showing high frequency of dyed root channels with Fe/Mn-oxide halos, (e) Horizontal surface in reduced clay in 2.5 m depth showing dyed root channels with Fe/Mn-oxide halos, (f) Surface of SC sand layer in 3.2 m depth showing the arrived dye tracer, which occurred less than 1 hour after start of infiltration of the tracer in 1 m depth.

Figure 80f shows the appearance of dye tracer spots in the surface of the SC sand layer, which closely resembled the appearance of previous infiltrated dye along root channels into the SC sand layer in the low-ground Marebæk site (*Figure 2*) described by Jørgensen et al. (2002a). Figure 81 shows how transport of the BB tracer also occurred along and inside large fossil roots in the BB9 field. As mentioned, some of these roots appeared to follow non-visible ghost-fractures in the till, however, none of these fractures were dyed and hence appeared to be hydraulically inactive.

FIGURE 81. BB dye tracer migration in fossil roots BB9 infiltration field. (a) Dyed root in 2-2.5 m depth extending from oxidized clay into underlying reduced clay. (b) Dyed root in oxidized clay in 1.5 m depth, and (c) in reduced clay in 2 m depth, (d) Horizontal surface in reduced clay in 2 m depth with dyed root.

BB10 and BB11 dye tracer infiltration experiment, E5 (0.6-3m depth)

Figure 82 shows the distribution of dye tracer in the BB10 and BB11 experiments after the tracer was infiltrated in 0.6 m depth in excavation 5. Infiltration was maintained for 10 days, during which the dye tracer did not arrive in the drain established in 3.5 m depth underneath the experimental fields. Hereafter, the experimental fields were excavated.

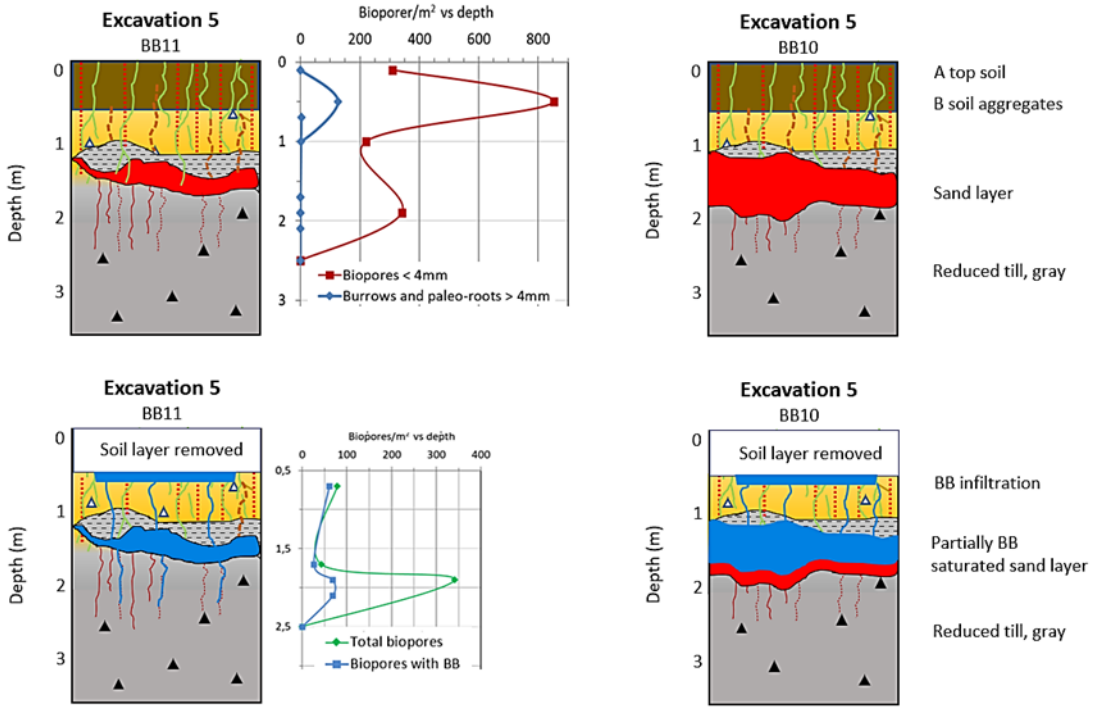

FIGURE 82. BB10 and BB11 dye tracer infiltration experiments in E5. (Top) Frequency of biopores in geological profile. (bottom) Distribution of BB dye tracer in biopores after infiltration (legend in Figure 79).

The excavations showed that a local 0.1-1 m thick sand lens occurred 0.5 m below the experimental surfaces. In both profiles, root channels were penetrating through the sand layer into the underlying clay to approximately 2.5 m depth (Figure 82). In BB11, the dye tracer had infiltrated through the sand layer and into the underlying root channels, while in BB10 the dye tracer did not reach the underlying root channels (limited by applied amount of dye tracer). As with BB9, the BB10 had a maximum of dyed root channels in 2 m depth, while maximum rooting depth was 2.5 m. Elsewhere in the E5, the maximum observed rooting depth was more than 3 m (see Figure 40). Notice that there was no sand layer observed deeper in the E5 geological profile for the roots to reach.

At the end of the excavation work, the pressure head in the drain tube (3.5 m depth) underneath the infiltration fields was 1 m above the bottom floor of the excavation (3 m depth) and hence the upward hydraulic gradient was 3. No root channels, fractures or up-ward waterflow were visible in the floor, however, to reveal any upward flow along possible non-visible flow paths, the excavation floor was monitored for 3 days during which it was covered with plastic tarpaulins to minimize evaporation. During this period, only few liters of upward flow accumulated, which suggests that no active preferential flow paths were present in the clay.

XRT of BB10 intact column (Column 4) 1.8-2.3 m depth, E5

After the BB10 and BB11 experiments, the intact XRT Column 4 was collected from the corner of the BB10 experiment in 1.8-2.3 m depth in E5 (Figure 83). The upper surface of the column contained ancient horizontal fossil roots of *A. glutinosa*, with thin vertical extensions. Most of these had diameters of 0.5-2 mm and resembled the dense occurrence of root holes observed in 5-10 m^2 oxidized areas in 2-3 m depth in the low-ground excavations. The mean pore volume was 0.47 mm^3 (Table 15) and the larger pores (volume > 4297mm^3) represent 0.38% of the porosity. Pore size distributions are presented in Figure 86 and show a mean diameter of 0.97 mm. Pore diameters appears rather stable along the column except for the larger fossil roots and channels in the 0-10 cm layer.

FIGURE 83. XRT Column 4 from 1.8-2.3 m depth in E5. (left) Transition from oxidized to reduced till in upper 10-20 cm of column with sub-horizontal fossil roots in top of column. (right) The top of the column shows horizontal and vertical fossil roots from A. glutinosa (Red alder) dated 2,984 -2,880 Cal BP.

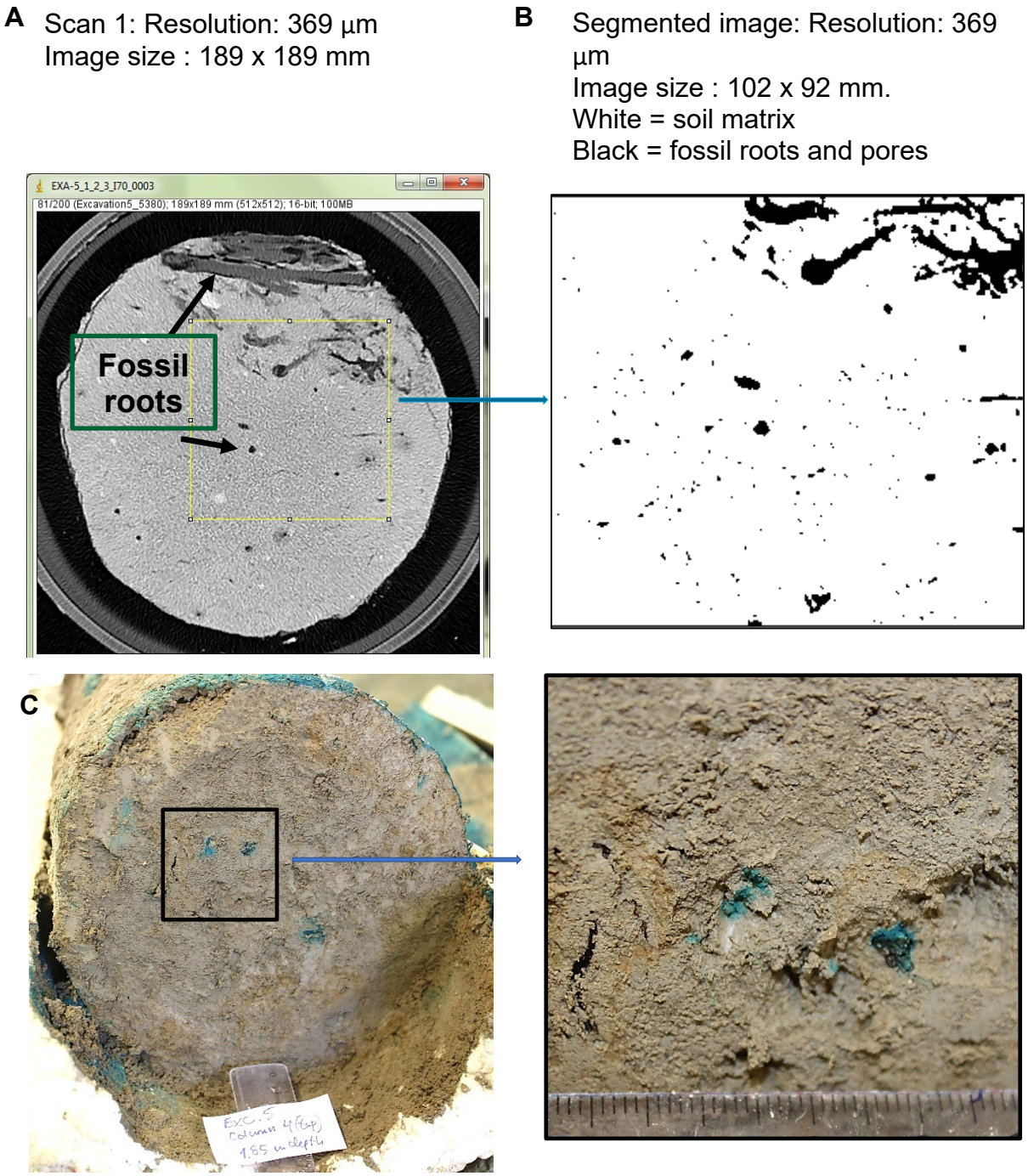

FIGURE 84. Horizontal XRT image of XRT Column 4. (A) The top of the column contains horizontal and vertical fossil roots. Selected area for further analysis is shown with a square. (B) Segmented image of selected area showing the large fossil roots and high density of small roots and pores. (C) Dismantled column after XRT showing dyed fossil roots in top end of column. The horizontal root in the top of the column was A. glutinosa (Red alder) from 2,984 ±28 Cal BP.

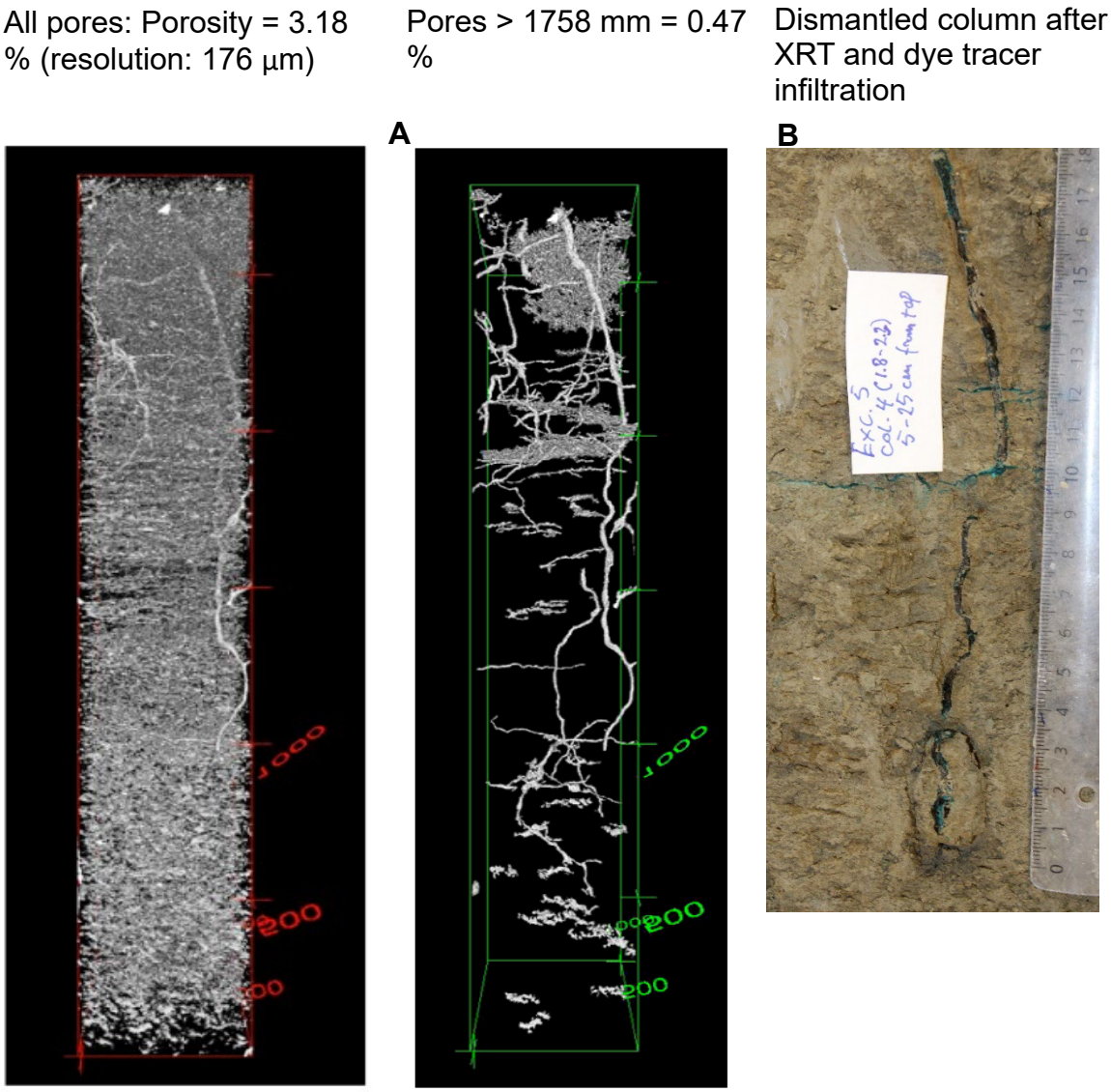

FIGURE 85. Images and photo of Column 4. (A) Pore network extraction: the left image shows high abundancy of small disconnected pores and the right image shows vertical penetration of fossil roots. (B) One of the roots exposed by dismantling the columns after XRT and infiltration of dye tracer. The dyed root was A. glutinosa (common alder) from 2,880 ± 33 Cal BP (section 3.6.1 and 3.6.3).

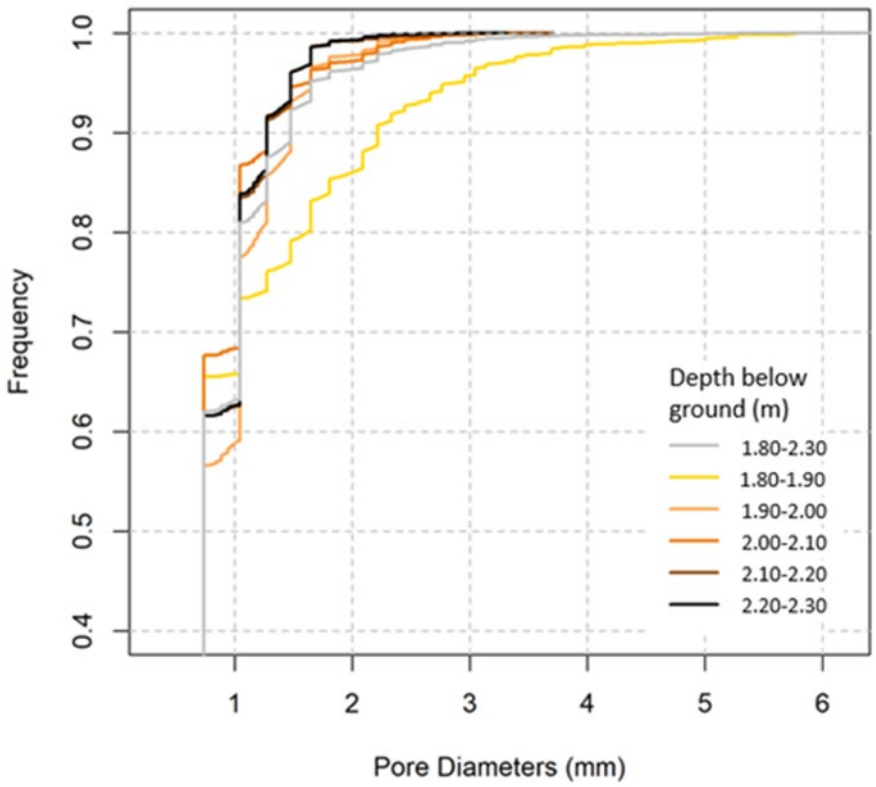

FIGURE 86. Pore-size distribution in XRT Column 4 (resolution 369 µm). The larger pores are mostly observed at the top of the column (1.80-1.90 m), where about 15% of the pores have a diameter > 2 mm. Pore size with a diameter > 4 mm are found only found between 1.80 and 1.90 m below ground, while pores with a diameter of 1-2 mm are present throughout the column.

TABLE 15. Pore diameter and porosity of pores > 369 µm in XRT column 4.

Depth (cm)	Min.	1st Qu.	Median	Mean	3rd Qu.	Max.	SD	Porosity (%)
1.8-1.9	0.35	0.35	0.7	0.71	0.95	4.35	0.35	1.9
1.9-2.0	0.35	0.61	0.79	0.81	0.99	3.08	0.34	2.14
2.0-2.1	0.35	0.35	0.7	0.71	0.86	2.86	0.37	2.06
2.1-2.2	0.35	0.35	0.7	0.72	0.96	2.92	0.38	3.86
2.2-2.3	0.35	0.35	0.5	0.6	0.7	4.28	0.39	6.04
1.8-2.3	0.35	0.35	0.61	0.68	0.82	4.35	0.38	3.18

3.5.3 Summary and evaluation of flow paths in the dye tracer experiments

The BB infiltration experiments were carried out in a vertical series of individual experiments from the soil C horizon into the underlying aquitard to investigate vertical flow and connectivity of the macropore flow system. Flow and transport in the C-horizon were controlled by worm burrows and root channels, which occurred as solitary macropores in the clay, while many formed macropore flow channels inside desiccation fractures and continued into the grey tectonic fractures in the underlying clay.

In the high-ground site, the fractures were open to approximately 1-1.5 m depth. Below this depth flow in the grey fractures only occurred along the root channel macropores, which provided prominent fingering patterns inside the fractures with tested dye tracer flow velocities of > 20 meter/day under free drainage. The almost complete depletion and leaching of Fe/Mn-oxides inside the grey fractures between the dyed root macropores (Figure 47), suggested the fractures were originally open when the depletion and leaching occurred (probably due to past dryer climates and water up-take by the original forest), while the fractures had healed afterwards by long-term settling of the fracture apertures, which had not yet fully occluded the root channels. Such healing was indicated to have actually occurred by the observed flattening of larger residual root channels (e.g., Figure 43).

In 2-3 m depth the fractures transformed from grey to red fractures, which marked the lower boundary of rapid preferential flow in the tills because the red fractures and root channels were clogged by precipitated Fe/Mn-oxides (which had been depleted and redistributed from above in the profiles as described in section 3.3). This created a hydrological barrier in the till profiles which controlled the perched water table conditions observed in E1 and E3 (Figure 21 and Figure 22). Only one example was observed where root channels along fractures in the Fe/Mn-oxide barrier had provided rapid dye tracer flow paths to 0.5 m depth in the barrier. Instead, inclined sand lenses, and sheared micro sand layers (from a few cm to many meters in length) were common random features in the tills. Those were observed to be conducting flow through the hydrologic barrier into underlying groundwater.

In the low-ground site, high frequencies of similar root channels, and in addition, fossil roots were connecting into the groundwater zone as rapid flow paths to 3.2 m depth. Those were not clogged by Fe/Mn precipitation, which was due to permanent the high-groundwater table (Figure 23) and low intensity of chemical weathering in the low-ground.

Table 16 shows estimated hydraulic apertures of the Fe/Mn filled fractures in the hydrologic barrier in the high-ground E1-E3 excavations. The estimation was carried out by model calculations, which utilized the observed infiltration depth of dye tracer in the fractures in the BB experiments (calculations described in section 2.4).

TABLE 16. Estimated fracture hydraulic apertures (2b) of Fe/Mn-oxide filled fractures (red fractures) in BBO, BB5, BB6 and BB8 dye tracer infiltration experiments in the high-ground hydrologic barrier. Fracture apertures > 6 µm were all related to flow along the partially Fe/Mn-oxide filled root channels inside the fractures in the barrier. Notice that flow (volume/time) in the fractures varies with the 3. power of the aperture (Snow 1969) meaning that flow is increasing 8 times when doubling the aperture. Estimation of the apertures was based on modeling by Thalund-Hansen (2018) which is described in 2.4.

Depth	**Excavation**	**Experiments**	**Number of fractures or fracture segments**			
			Without root channels inside		With Fe/Mn-oxide infilled root channels inside	
			2b = 0-3µm (0-5 cm infiltration)	2b = 3-6µm (10-20 cm infiltration)	2b = 6-8 µm (20-25 cm infiltration)	2b = 8-10 µm (25-40 cm infiltration)
3.5	E3	BB8 (red fractures)	6	2	0	0
5.0	E1	BB0 (red fractures)	3	0	0	0
5.2	E1	BB0 (red fractures)	5	0	0	0
5.2	E2	BB5 (red fractures)	19	5	1	0
5.2	E2	BB6 (red fractures)	2	5	1	1

The estimations show that the fractures in BB0 and BB8 without root channels inside the fractures (in E1 and E3, respectively) had very small hydraulic apertures (0 - 6 µm), while the fractures or fracture segments in BB5 and BB6, which contained the Fe/Mn filled root channels had apertures up to approximately 10 µm.

Based on the fracture hydraulic apertures in Table 16, Table 17 shows calculated bulk-hydraulic conductivities of the tills together with the increase of hydraulic conductivity over the unfractured matrix caused by the fractures. The calculations show that the red fractures without root channels only caused a marginal increase (<11%) of the hydraulic conductivity over the matrix. The deep infilled root channels in the red fractures in E2 caused a further marginal increase (7-37%). This confirms that the clayey till below the grey fractures in all tree high-ground excavations (when excluding influence of intercepting sand lenses) provided a hydrological barrier with bulk flow properties similar to the uncompromised clay (Table 1), despite the fact that there was a high frequency of prominent red fractures in the clay.

TABLE 17. Calculated hydraulic conductivities of flow paths in the BB experiments in the hydrologic barrier and the increase of hydraulic conductivity (Ks) in the barrier over the unfractured matrix caused by red fractures with and without root channels inside (using the approach described by Jørgensen et al., 2002a). The calculations are based on the fracture apertures in Table 16, observed fracture spacings in Figure 66, and the measured hydraulic conductivity of the matrix in Table 1.

Depth (m)	**Excava-tion**	**Experiment**	**Hydraulic conductivity (m/s)**			**Increase of hydraulic conductivity**
			Clayey till with red fracture without root channel (2b < 6 µm)	**Clayey till with red fractures containing infilled or partially infilled root channels (2b = 6-10 µm)**	**Unfractured clay matrix**	**Caused by fractures (%)**
3.5	E3	BB8	< $5.8*10^{-9}$	-	$5.3*10^{-9}$	< 12
5.0	E1	BB0	< $1.9*10^{-9}$	-	$1.7*10^{-9}$	< 13
5.2	E2	BB5	-	2.5-3.2 $*10^{-9}$	$2.3*10^{-9}$	7-37
5.2	E2	BB5	< $2,5*10^{-9}$	-	$2.3*10^{-9}$	< 11

In E2, multiple sand lenses in the BB5 and BB6 experiments provided active preferential flow paths connecting through the hydrological barrier and into the underlying aquitard (Figure 68). The leakage along the sand lenses was evaluated by estimating the distribution of water fluxes between the fractures, clay matrix and sand lenses in BB5. The estimation shows that < 1 - 17 % of flow occurred in the fractures (high-end percentage caused by the infilled root channels along fractures), 53-59 % in the sand lenses, and 30 % in the matrix. The estimation was based on the hydraulic conductivity (Ks) of the aquitard in BB5 (Ksat = $8*10^{-9}$ m/s), total length of fractures (13,9 m, Figure 66), fracture apertures (3-10 µm in Table 16), and hydraulic conductivity of the matrix (Table 1) by using the approach of Jørgensen et al. (2002a). Hence the leakage in E2 was dominated by flow in the sand lenses, while above the sand lenses (from 3-5 m depth) vertical flow was significantly inhibited by hydrological barrier (see water table in upper screen in Well 2, Figure 21). Notice, that the calculated leakage along the sand lenses is corroborating with the observed deep seasonal decline of the water tables in the E2 wells as opposed to the perched water table conditions in E1 and E3 (Figure 21). The hydrogeological role of the embedded sand lenses or continuous sand layers in the till is in agreement with hydrogeological studies by Haldorson and Krüger (1990), who explained large differences in measured Ksat from observed differences in lithofacies represented by sand lenses in contemporary clayey tills.

Limitations and uncertainties

As mentioned, the BB5 and BB6 infiltration fields were not fully saturated before the start of the experiments, which may have reduced infiltration and caused underestimation of the fracture hydraulic aperture values in those experiments. The hydraulic apertures determined from the BB5 and BB6 experiments were, however, in agreement with the hydraulic apertures of the red factures in the BB0 and BB8 experiments (which were fully water saturated before experiments) and with hydraulic apertures determined in the three LUC samples (hydraulic apertures = < 10 µm), which were collected from or nearby to the BB5 and BB6 fields (Figure 4) in Aamand et al. in prep. (2020).

Despite chipping of the clay from the upper few cm of the fractures with knifes in the surface of the BB infiltration fields (Figure *6* C), fractures may have been surficially opened by the excavator shovel (Figure *6* A,B). This may have caused BB penetration into fractures, which would otherwise not have occurred and consequently may have resulted in larger calculated apertures than was actually occurring in the undisturbed clay, especially for the small aperture fractures (2b = 0-3 µm in Table 16).

The preservation of the fossil roots and absence of Fe/Mn-oxide clogging of root channels in the Bulbro site may be considered unique due to the location of the site by the foot of the hill, which had provided local upward flow and permanent water saturation below approximately 1.5 m depth. As mentioned, the observed very rapid downward migration of the dye tracer along the root channels was created by pumping groundwater from the drain tubes established underneath the infiltration experiments. Consequently, the Bulbro site cannot be considered fully representative for the overall low-ground area. However, in the low-ground Marebæk site 1.5 km further south, the groundwater flow was naturally downward and similar open root channels were abundant and controlled groundwater recharge and rapid pesticide migration to 5 m depth into the SC local aquifer (Figure 3) in the previous studies by Jørgensen et al. (2002a, 2004c), and Stenemo et al. (2005).

3.6 Origin and age of relic roots and biopore channels

Radiocarbon ages, $\delta^{13}C$ values and aDNA were determined in parallel sub-samples of the top-soils, fossil roots, worm burrown, organo-mineral fillings in root channels and clay matrix from excavations E2-E6, Figure 87. Additional eDNA was determined in worm burrown to evaluate current worm activity.

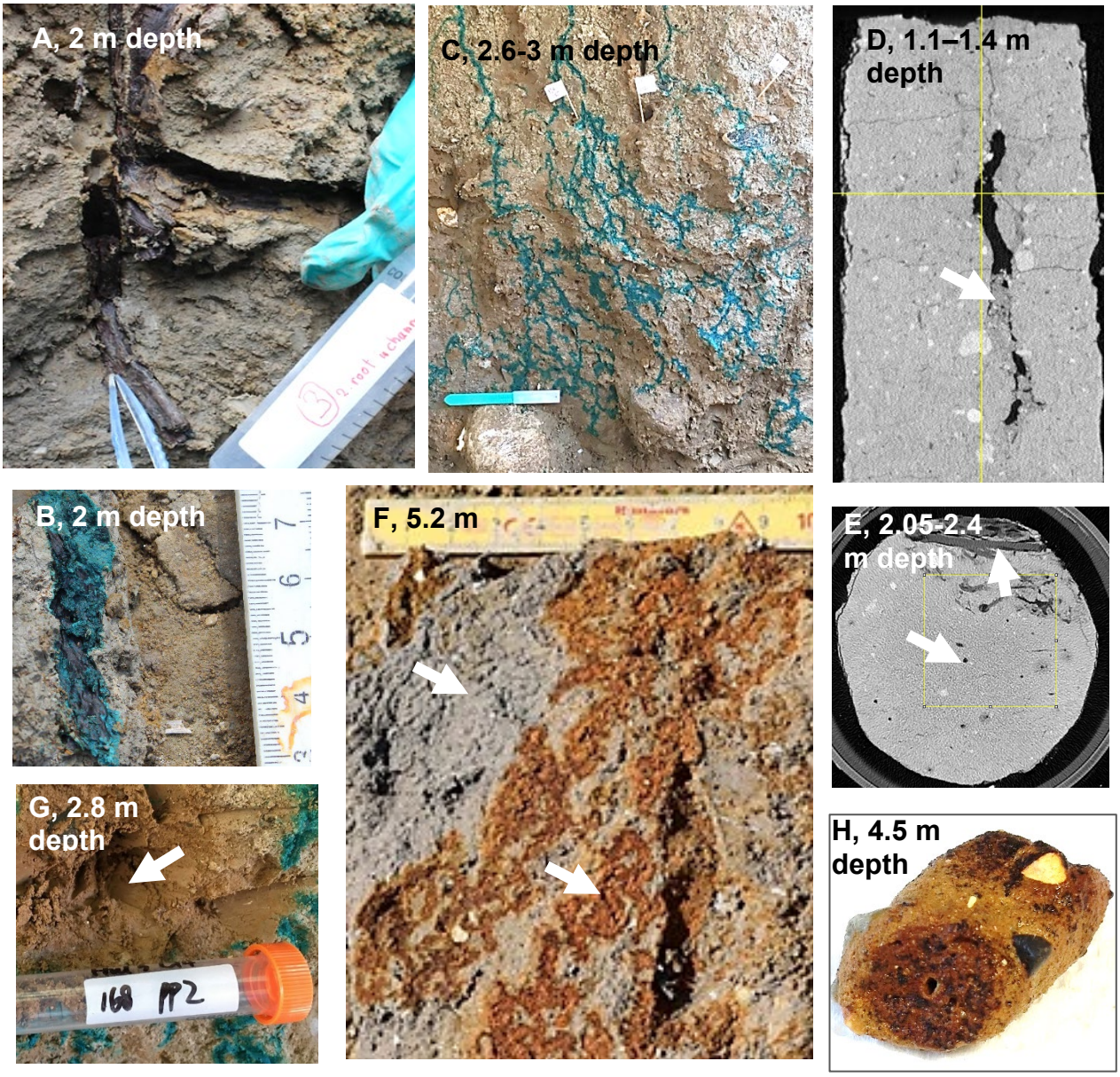

FIGURE 87. Examples of sample types that were determined by radiocarbon dating and DNA analysis. (A, B) fossil roots from E4, (C) sediment fillings of root channels from E3, (D) Worm borrow topsoil filling from XRT-column 1 in E2, (E) Dyed fossil roots from XRT-column 4 in E5, (F) Channels along Fe/Mn-oxide filled red fracture and adjacent unoxidized matrix in E2. (G) Matrix from E3, (H) Fe/Mn-oxide concretion from previous Flakkebjerg site (Jørgensen et al., 2017). Complete photo-documentation of samples and results is shown in Appendix 3.

The analysis includes both dyed and non-dyed samples in order to identify the possible influence of the BB dye tracer on the result (see section 2.6). To bridge the current study with the predecessor PESTPORE study with similar deep root channels in Flakkebjerg, Sjælland,

(Jørgensen et al. 2017), a series of samples from this site was also included. We hypothesize that possible ancient root remains might be captured inside Fe/Mn-concretions with root holes, found at this site (Figure 87H). Complete photo documentation of the samples with radiocarbon and aDNA results are shown in Appendix 3, Table A3.4.

3.6.1 Radiocarbon ages and C-isotopes

Table 18 shows the radiocarbon ages and $\delta^{13}C$ values for topsoil's, subsoil clay matrix and organo-mineral fillings in the biogenic macropores in E2-E5. Table 19 shows radiocarbon ages and $\delta^{13}C$ values for the fossil root samples, and Table 20 and Figure 88 show calibrated age results and $\delta^{13}C$ values for these samples. Figure 90 and Table 21 show radiocarbon ages from ramped pyroxidation of Fe/Mn-filled channels inside the red fractures from E2, and the Fe/Mn-concretions with root holes (Figure 87H) from the Flakkebjerg site. Table 22 show radiocarbon ages of additional Flakkebjerg samples.

The radiocarbon ages in Table 18 and Table 22 are derived from bulk sediment samples as either humic (base solvable) or humin (base insolvable) fractions. The carbon contained in bulk sedimentary samples is generally assumed to represent an open system where there is a continuous uptake and release of carbon. Thus, the ^{14}C ages likely represent the mean residence time of carbon, which has not been mineralized and emitted as CO_2 to the atmosphere. The humic substance are mobile and are derived from decomposing organic matter. The results show that the humic substances are younger than the humin fractions, indicating that a larger proportion of their carbon originates from carbon reservoirs with higher ^{14}C concentration, i.e., from carbon reservoirs with younger ages. Because of the high mobility of the humic substances, they are difficult to use for inferred ages of the sediment. However, the humin substance is the insoluble organic matter fraction and usually makes up a substantial part of the total organic matter content in sediment samples. The carbon of the humin fractions can be assumed to be immobile and more resistant to chemical reactions and decomposition. Hence, we assume the humin fraction to be closed systems from which we can infer the age since the last deposition of organic matter, e.g., residual root material preserved in the soil. However, the organic matter may also have an earlier history by redeposition with the till. This complicates interpretations further, especially for the deep samples with low content of recent organic material.

TABLE 18. Radiocarbon ages and $\delta^{13}C$ values for bulk-sediment samples collected in high-ground (HG) E2-E3 and low-ground (LG) E4-E5 form fillings in the biogenic macropores and samples of topsoil's and subsoil clay matrix. High-ground samples of macropores were prioritized due to absence of fossil root remains in this setting.

Sample Number	Site/Excavation	Sample Origin	Depth (m)	Sediment			
				Humic		Humin	
				δ13C (‰ VPDB)	^{14}C age (BP)	δ13C (‰ VPDB)	^{14}C age (BP)
PP2-247	Salløv E2 (HG)	Topsoil	0.1	-30.4			256 ±19
PP2-249	Salløv E2 (HG)	Topsoil	0.1	-29.8		-26.7	431 ±19
PP2-292	Bulbro E4 (LG)	Topsoil	0,1	-30.0	170 ±20		1046 ±20
PP2-351	Salløv E2 (HG)	Worm burrow infill XRT1	1.1			-22.8	Failed
PP2-352,	Salløv E2 (HG)	Worm burrow infill XRT1	1.3		1307 ±42	-23.4	3420 ±35
PP2-34	Salløv E2 (HG)	Worm burrow infill	1.3		1424 ±29		4082 ±31
PP2-293	Salløv E2 (HG)	Worm burrow infill	1.2				3851 ±34
PP2-36	Salløv E2 (HG)	Worm burrow infill	1.2		2069 ±27		5172 ±36
PP2-296	Salløv E2 (HG)	Clay matrix 3 cm from burrow	1.2		8209 ±36		8642 ±32
PP2-159	Salløv E3 (HG)	Root channel infill (grey fracture)	2.8			-23.3	15377 ±74
PP2-180	Salløv E3 (HG)	Root channel infill (grey fracture)	2.5				6656 ±37
PP2-161	Salløv E3 (HG)	Root channel infill (grey fracture)	2.5			-24.0	10016 ±53
PP2-182	Salløv E3 (HG)	Root channel infill (grey fracture)	2.5				5474 ±49
PP2-200	Salløv E3 (HG)	Root channel infill (grey fractures)	2.5				14412 ±70
PP2-227	Salløv E3 (HG)	Root channel infill (grey fractures)	2.0	-40.5			15539 ±147
PP2-194	Salløv E3 (HG)	Root channel infill (grey fracture)	2.5			-18.3	Failed
PP2-158	Salløv E3 (HG)	Root channel infill (grey fracture)	2.8			-20.9	Failed
PP2-198	Salløv E3 (HG)	Root channel infill (grey fracture)	2.5				5526 ±37
PP2-185	Salløv E3 (HG)	Root channels (grey fracture)	2.1				9191 ±56
PP2-160	Salløv E3 (HG)	Root channel infill (grey fracture)	2.5			-22.2	12899 ±95
PP2-229	Salløv E3 (HG)	Clay matrix (oxidized)	2.3				25950 ±121
PP2-193	Salløv E3 (HG)	Clay matrix (oxidized)	2.4				19629 ±59
PP2-202	Salløv E3 (HG)	Clay matrix (oxidized)	2.5				22014 ±91
PP2-168	Salløv E3 (HG)	Clay matrix (oxidized)	2.8			-26.8	22412 ±117
PP2 174	Salløv E3 (HG)	Clay matrix (oxidized)	3			-24.0	17346 ±99
PP2-82b	Salløv E2 (HG)	Clay matrix (reduced)	5.2		19375 ±104		27952 ±148
PP2-37b	Salløv E2 (HG)	Clay matrix (reduced)	5.4				25862 ±115

Table 19 shows the results for the fossil roots from the low-ground site excavations 4-6. The roots are considered closed systems and contain carbon from the contemporaneous prehistoric atmosphere. Hence these samples may be calibrated to calendar years using the international calibration curve, IntCal13, and the online calibration program, OxCal 4.1 (Bronk Ramsey, 2009; Reimer et al., 2013). Figure 88 and Table 20 show the calibrated ages, which fall in

two ranges: 1) between 7,200 to 6,200 calBP and 2) 3,500 to 3,000 calBP. The samples PP2-312 and PP2-307 as well as PP2-337 and PP2-332 are taken from the same two roots at different depths. Both pairs of samples are statistically in agreement within measurement error (Table 19).

TABLE 19. Radiocarbon ages and $\delta^{13}C$ values for fossil roots from the low-ground (LG) sites E4-E6.

Sample number	Site/Excavation	Sample Origin	Depth (m)	Relic roots	
				δ13C (‰ VPDB)	^{14}C age (BP)
PP2-263	Bulbro E4 (LG)	Fossil root	2	-28	6240 ±25
PP2-270	Bulbro E4 (LG)	Fossil root	2	-27.5	3119 ±23
PP2-307	Bulbro E4 (LG)	Fossil root	2.1	-29	3215 ±23
PP2-312	Bulbro E4 (LG)	Fossil root	2.1	-28.9	3192 ±25
PP2-302	Bulbro E4 (LG)	Fossil root	2.2	-30.3	3237 ±24
PP2-262	Bulbro E4 (LG)	Fossil root	2.0	-29.5	6176 ±33
PP2-358	Bulbro E5 (LG)	Fossil root	1.8		2984 ±28
PP2-359	Bulbro E5 (LG)	Fossil root	2.3		2880 ±33
PP2-332	Bulbro E5 (LG)	Fossil root	3.0	-29.4	2797 ±26
PP2-337	Bulbro E5 (LG)	Fossil root	2.0	-30	2833 ±22
PP2-255	Bulbro E6 (LG)	Fossil root	1.3	-27.2	5651 ±31
PP2-256	Bulbro E6 (LG)	Fossil root	0.9	-28.6	5969 ±33

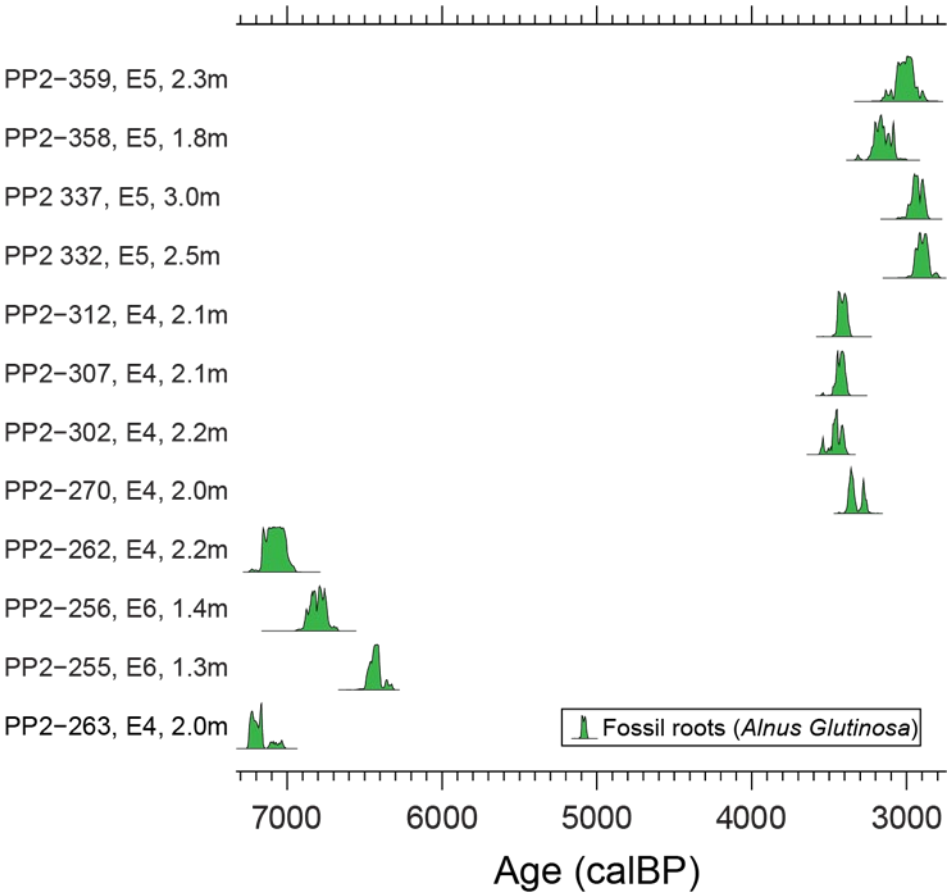

FIGURE 88. Calibrated age probability distributions of the fossil roots found in the low-ground excavations 4-6.

TABLE 20. Calibrated age ranges of fossil roots in calBP where BP is before present, and present is defined as 1950CE.

Sample number	Lab ID	Calibrated age (calBP) 68.2% confidence range	Calibrated age (calBP) 95.4% confidence range
PP2-312, E4, 2.1m	AAR-29096	3445 – 3386	3454 – 3368
PP2-307, E4, 2.1m	AAR-29095	3452 – 3399	3475 – 3382
PP2-270, E4, 2.0m	AAR-29081	3376 – 3271	3389 – 3250
PP2-263, E4, 2.0m	AAR-29077	7244 –7160	7254 – 7026
PP2-302, E4, 2.2m	AAR-29094	3479 – 3403	3556 – 3388
PP2-262, E4, 2.0m	AAR-30429	7156 – 7019	7169 – 6973
PP2-358, E5, 1.8m	AAR-31347	3210 – 3080	3318 – 3065
PP2-359, E5, 2.3m	AAR-31348	3060 – 2960	3142 – 2886
PP2-332, E5, 3.0m	AAR-29141	2941 – 2860	2963 – 2802
PP2-337, E5, 2.0m	AAR-29150	2963 – 2885	2998 – 2869
PP2-255, E6, 1.3m	AAR-30427	6467 – 6404	6496 – 6322
PP2-256, E6, 0.9m	AAR-30428	6850 – 6745	6894 – 6695

Figure 89 shows the $\delta^{13}C$ values for the samples in Table 18 and Table 19. $\delta^{13}C$ are commonly used for identifying carbon sources or chemical processes (fractionation). Reference $\delta^{13}C$ values for bulk-till are found to range between 0 ‰ and 2 ‰ (Kolstrup and Buchardt, 1982; Noe-Nygaard et al., 1998), which is also indicated in Figure 89. The three clay matrix samples from the current study in Table 18 were measured with a mean $\delta^{13}C$ value of 1.2 ± 0.1 ‰. Thus, the clay matrix is in agreement with the reference bulk till $\delta^{13}C$ values, which is due to the high limestone carbonate content of till.

The mean $\delta^{13}C$ values of the fossil roots were -28.7 ±1.1‰ (n=12), which is in agreement with typical organic matter $\delta^{13}C$ values ranging between -25 ‰ and -30 ‰ (Meyers and Teranes, 2001; Philippsen et al., 2019). Thus, there is no evidence of fractionation, e.g., due to microbiological decomposition of the roots. Hence the fossil roots represent a closed carbon system and the radiocarbon age therefore provides an accurate age.

The humin fraction (base insolvable) of fillings from the root channels in grey fractures show a broad range of $\delta^{13}C$ values ranging from -29.1 ‰ to -4.1 ‰, with a mean value of -22.4 ±5.4 ‰ (n=23) in Figure 89. The elevated $\delta^{13}C$ values of the humin fraction indicate that a fraction of the carbon source for humin organic matter originates from dissolved limestone carbonate. A simple mixing model assuming a limestone $\delta^{13}C$ endpoint of +1.0‰ and an organic matter $\delta^{13}C$ endpoint if -27.5 ‰ suggests the average limestone derived carbon in the humin fraction to be about 19%. The extreme single value of -4.1 ‰ suggests a limestone derived carbon fraction of 82 %. The limestone in till is of Cretaceous age and hence contains no ^{14}C atoms. In terms of radiocarbon ages, this corresponds to an infinite ^{14}C age. Thus, if organic matter contains even a small amount of limestone derived carbon, this would cause the radiocarbon age to be older than its true ^{14}C age, as the ^{14}C concentration would be lower than expected. Therefore, general caution should be taken when interpreting the ^{14}C age of the humin fraction if the $\delta^{13}C$ values are higher than -25 ‰. It is, however, likely that $\delta^{13}C$ values up to about -20

‰ are due to natural fractionation and, thus, without the influence of limestone derived carbon (Lichtfouse et al., 1995; Nissenbaum and Schallinger, 1974). A further complicating factor is the fact that the humin fraction $\delta^{13}C$ values are indistinguishable from the Brilliant Blue $\delta^{13}C$ value of -25.4 ‰. Hence a possible Brilliant Blue contamination cannot be differentiated using the $\delta^{13}C$ values alone, however, the FTIR analysis presented above (method section 2.6) indicates the influence of Brilliant Blue to be very low. The mean $\delta^{13}C$ values of the humic acid (base solvable) fraction is -30.0 ±0.5 ‰ (n=5, one extreme value of -40.5 ‰ removed). Humic acids are derived from decomposing organic matter, and the slightly lower $\delta^{13}C$ values likely reflect the natural fractionation occurring when organic matter is transformed into humic acids (Lichtfouse et al., 1995; Nissenbaum and Schallinger, 1974). Further, the significantly lower $\delta^{13}C$ values relative to the Brilliant Blue value of -25.4 ‰ suggest that the humic acid fraction is not influenced by Brilliant Blue, as is furthermore confirmed by the FTIR analysis (section 2.6, Figure 11).

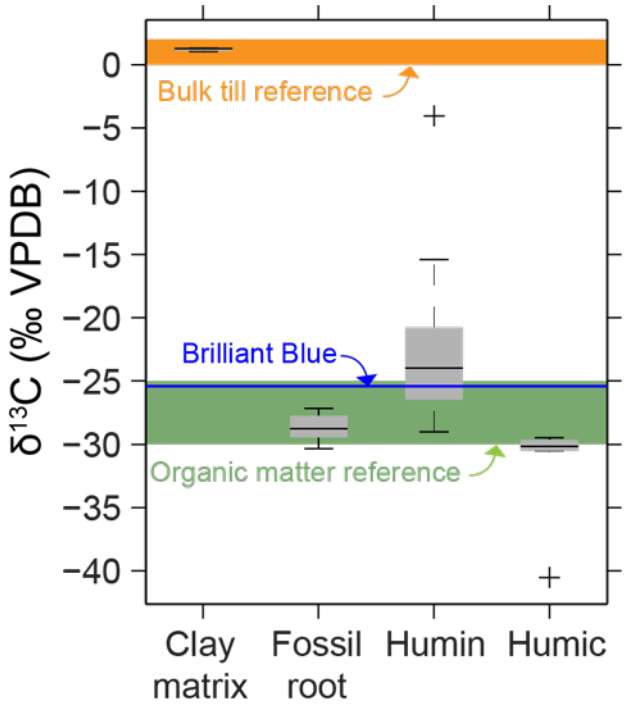

FIGURE 89. $\delta^{13}C$ values of the fossil roots and bulk sedimentary humic and humin organic fractions derived from topsoil, organo-mineral fillings in worm burrows, root channels, and clay matrix samples. The diagram also shows reference $\delta^{13}C$ range for bulk till and organic matter (mostly terrestrial plants) (green shaded) together with the $\delta^{13}C$ value of Brilliant Blue ($\delta^{13}C$ = -25.4‰).

Ramped pyroxidation

The samples of Fe/Mn infillings from the red fractures and the concretions included from the Flakkebjerg site exhibit a challenge in terms of pre-treatment because the organic carbon of interest in this study is assumed to be absorbed or captured inside the Fe/Mn oxides. Prior to any ^{14}C analysis, the high $CaCO_3$ content needs to be removed from the samples using 1M HCl. However, the low pH will dissolve the iron and manganese and thus mobilize the organic matter of interest, which is then lost by washing. The normal pre-treatment procedure is therefore likely to fail. To overcome this problem, the Fe/Mn-oxide samples were analysed using the ramped pyroxidation method at Queen's University Belfast (Keaveney et al., 2020).

During the thermal decomposition of organic carbon as temperature increases, the most labile carbon compounds are oxidized to CO_2 first followed by more stable carbon compounds.

Thus, the method provides a range of different ages for the different compounds derived at different temperatures. The decomposition of calcite (the limestone in the samples) onset from c. 600 °C, however, a steep rise in the CO_2 flow at 500 °C is suggested to reflect the decomposition of $CaCO_3$. This can be verified by the ^{14}C ages around 40,000 ^{14}C years for CO_2 collected above 500 °C (Figure 90 and Table 21). For the ramped pyroxidation system, a ^{14}C age of c. 40,000 corresponds to an infinite ^{14}C age and thus represents the limit of this method. Therefore, only temperature fractions lower than 500 °C are considered to have an organic matter origin.

The matrix sample PP2-82b provides organic matter ages from c. 14,000 to 22,500 ^{14}C years BP. The humic acid fraction of the sample yielded a ^{14}C age of 19,375 ±104 ^{14}C years BP in Table 18. This represents the complexity of bulk organic matter ^{14}C analysis because each of the temperature fractions are likely to represent carbon reservoirs with different mean residence times. In turn, each of these carbon reservoirs are expected to be open systems, where carbon is continuously being replaced through time.

To combine all organic matter fractions (<500 °C) to a single value for comparison, the size weighted average is calculated:

$$\langle F^{14}C \rangle = \frac{\sum w \cdot F^{14}C}{\sum w}, w = \frac{m}{\sigma^2_{F^{14}C}}$$

$F^{14}C$ is the ^{14}C concentration expressed as a dimensionless number ranging between 0 (infinite) and 1 (1950 CE), m is the integrated CO_2 fraction in mg C and σ is $F^{14}C$ analytical error of the individual temperature fractions. The size weighted average of sample PP2-82b is 19,066 ±48 ^{14}C years BP and is thus comparable to the humic acid fraction, despite the fact that the two methods may not be directly comparable. Table 21 provides the size weighted averages of all ramped pyroxidation samples, which show ages between 15,038 and 25,269 ^{14}C years BP.

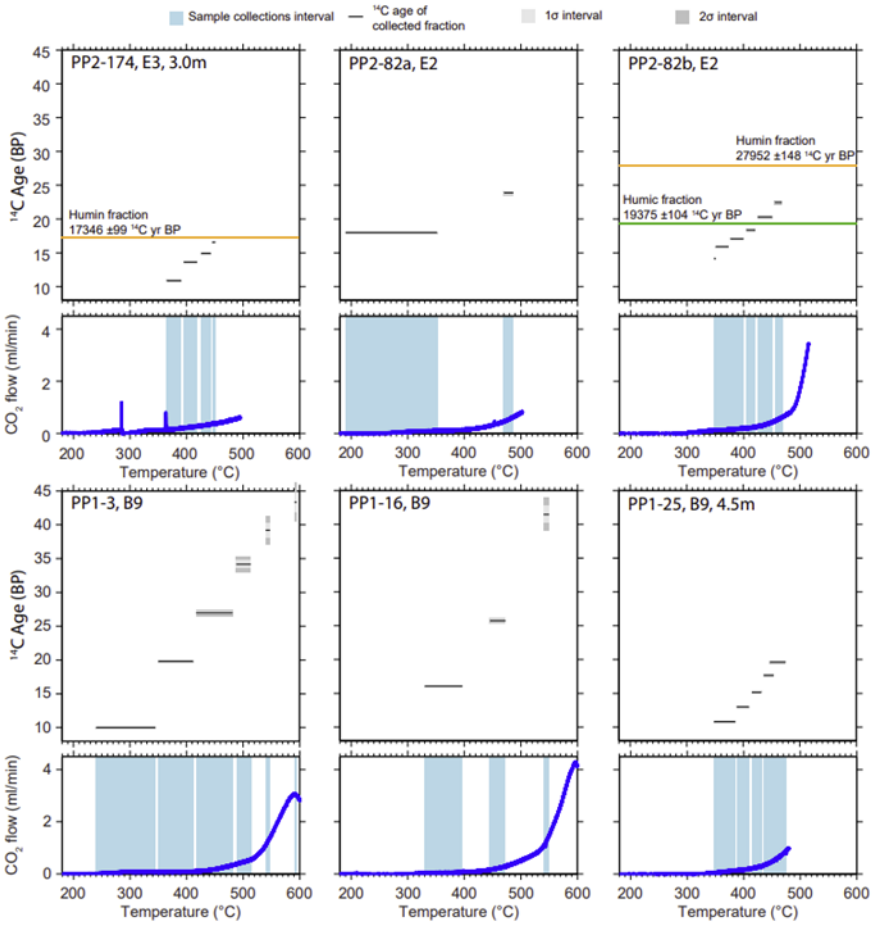

FIGURE 90. CO_2 flow profiles, collected sample temperature ranges (shaded) and ^{14}C ages (in thousands of years) determined with ramped pyroxidation method.

TABLE 21. Combined ^{14}C organic matter ages for ramped pyroxidation temperature intervals below 500°C.

Name, excavation, depth	Sample origin	Temperature interval (°C)	^{14}C age (^{14}C yr BP)
PP2-174, E3, 3.0m	Clay matrix (oxidized)	<500 °C	15038 ±40
PP2-82a, E2, 5.2m	Root channel (oxidized)	<500 °C	21924 ±100
PP2-82b, E2, 5.2m	Clay matrix (reduced)	<500 °C	19066 ±48
PP2-174, E3, 3.0m	Clay matrix (oxidized)	<500 °C	15038 ±40
PP1-3, B9, 4.5 m	Concretion (oxidized)	<500 °C	21342 ±96
PP1-16, B9, 4.5 m	Concretion (oxidized)	<500 °C	25269 ±169
PP1-25, B9, 4.5m	Clay matrix (oxidized)	<500 °C	15304 ±34

As mentioned, the radiocarbon ages for the Flakkebjerg high-ground (HG) samples in Table 21 and Table 22 were included for comparison with this study site where water flow and pesticide transport were dominated by rapid preferential flow in deep root channels as in the current study sites (Jørgensen et al., 2017). The Flakkebjerg samples show similar distribution of ages for the groups of samples as in the current study.

TABLE 22. Radiocarbon ages from the Flakkebjerg site (Jørgensen et al. 2017). The table shows bulk-sediment samples collected from fillings in biogenic macropores and samples of top soil and subsoil clay matrix samples.

Sample Number	Site/Excavation	Sample Origin	Depth (m)	Sediment	
				Humic	Humin
				^{14}C age (BP)	^{14}C age (BP)
PP1-13, B5	Flakkebjerg (HG)	Topsoil	0.1	13 ±27	294 ±21
PP1-11, B5	Flakkebjerg (HG)	Worm burrow infill	1.3	1164 ±31	3205 ±37
PP1-10, B5	Flakkebjerg (HG)	Wall of worm burrow	1.3	2597 ±36	10197 ±71
PP1-12, B5	Flakkebjerg (HG)	Clay matrix 3 cm from burrow	1.3	3372 ±39	8703 ±48
PP1-22, B9	Flakkebjerg (HG)	Root channel Fe/Mn concretion	4.5		18184 ±124
PP1-23, B9	Flakkebjerg (HG)	Root channel Fe/Mn concretion	4.5		20520 ±82
PP1-24, B9,	Flakkebjerg (HG)	Root channel Fe/Mn concretion	4.5		18685 ±81
PP1-15, B5	Flakkebjerg (HG)	Grey halo of root channel	2.75	3805 ±66	16478 ±126
PP1-17, B5	Flakkebjerg (HG)	Fe/Mn halo of root channel	2.75	4734 ±120	21097 ±163
PP1-18	Flakkebjerg (HG)	Clay matrix (oxidized)	2.75	12011 ±84	28486 ±159
PP1-14, B5	Flakkebjerg (HG)	Clay matrix (oxidized)	3.5	9157 ±89	21325 ±101
PP1-19, B9	Flakkebjerg (HG)	Clay matrix (reduced)	4.5		20502 ±79
PP1-20, B9	Flakkebjerg (HG)	Clay matrix (reduced)	4.5		20824 ±82
PP1-21, B9	Flakkebjerg (HG)	Clay matrix (reduced)	4.5		20906 ±194
PP1-25, B9	Flakkebjerg (HG)	Clay matrix (reduced)	4.5		21822 ±110

The pyroxidation method at QUB is still an experimental method and the data obtained using this method is not as complete as one could have wished for. The organic component of samples was low and it was necessary to collect over a long period with a broad temperature range to obtain a sufficient quantity (0.3 mg) for ^{14}C analysis. Due to the clay content in the samples a large quantity of water was produced as a by-product of the pyroxidation reaction. This resulted in ice trap blockages and pressure build-ups further down the line and necessitated interruption/abandonment of the run. For example, not all samples have dated ^{14}C fractions over the complete temperature range and some temperature profiles are detailed whereas others are very broad and only one sample, PP2-82, E2, yielded results from all methods (Figure 5, Table 3). Hence these data are difficult to interpret. However, all ^{14}C temperature profiles range from younger ^{14}C ages at low temperatures and older ^{14}C ages at higher temperatures. This likely reflects the fact that labile carbon combusting at low temperatures is of an age of approximately 10 to 14 kyr ^{14}C BP and that refractory carbon combusting at higher temperatures shows an age of 17 to 27 kyr ^{14}C BP. For the clay matrix samples, the latter is consistent with the humin ^{14}C age fractions.

The pyroxidation method reveals that even the clay matrix samples have labile organic matter of younger ages up to about 10 kyr ^{14}C BP. This is also consistent with the few humic ^{14}C age

fractions obtained on the clay matrix samples (Table 1, Table 3). Unfortunately, no conclusion can be drawn regarding the root channels using the pyroxidation method, as the one measured shows a very large temperature range and hence integrates both labile and refractory carbon (Figure 5, Table 3). The two concretion pyroxidation samples from the Flakkebjerg site (PP1) show ^{14}C ages, which are indistinguishable from clay matrix ^{14}C ages. This suggests that carbon trapped in the concretions is either of an age of 10 to 16 kyr ^{14}C BP or that the amount carbon trapped in the concretions is much less than the carbon content of the matrix.

3.6.2 eDNA of worms and burrows

To support the identification of organisms in the biopores, we barcoded a selection of earthworms to support the metabarcoding and aDNA analyses. Three 25×25×30 cm^3 soil blocks were hand sorted at E2 October 2., 2017. The average density was 427 indv. m^{-2} (n=3). Characterization of earthworm populations are shown in Table 23.

TABLE 23. Earthworm species composition and abundances per soil block of 25×25×30 cm^3 at E2.

***Latin* scientific name, Danish *common* name**	**Adults**	**Juvenile**
A. rosea, Rosa orm	2.3	4.3
A. caliginosa, Lille grå orm	4.0	8.4
A. longa, Lang orm	0.7	0
A. chlorotica, Grøn orm	0.3	2.3
Lumbricus herculeus	0	4.3

Twenty-nine earthworms were collected for COI barcoding on the Sept. 11th and Oct. 2nd, 2017, of which 23 were sequenced. Of 14 *Lumbricus* sp. individuals, all 14 specimens were verified *Lumbricus herculeus*. *L. herculeus* is a cryptic species not distinguishable morphologically from *Lumbricus terrestris*, with a body weight roughly half of *L. terrestris* (James *et al.*, 2010). Five individuals of *Aporrectodea* sp. turned out to be *A. caliginosa,* although they were wrongly expected to be *A. tuberculata* (Stor grå orm), and three individuals identified morphologically to be *A. caliginosa* were confirmed to be so. Thus, the location is inhabited by *A. caliginosa* and, as expected, not *A. tuberculata*.

qPCR of the soil materials from the worm burrow walls and adjacent matrix (Table 23) was performed to screen for the presence of earthworm DNA fragments and assess their relative abundance. The hypothesis was: if the long 383 bp DNA ewA/ewE amplicon of earthworms inhabiting the soil at the time of sampling could be detected, then this would indicate their presence, as opposed to detection only of the short 30 bp DNA sequence, which would merely indicate past presence of earthworms in the sample soil.

According to the *in silico* testing (section 2.7), the primer sets ewA/ewE (forward: ewA 5'-CGACTGTTTAACAAAAACAT-3' and reverse ewE 5'-CTGTTATCCCTAAGGTAGCTT-3') and ewB/ewC (forward: ewB 5'-CAAGAAGACCCTATAGAGCTT-3' and reverse ewC 5'-GGTCGCCCCAACCGAAT-3') targeting the mitochondrial 16S region were selected for qPCR. Table 24 shows the resulting outcome of the qPCR in terms of relative amplicon abundance. In Table 24, "÷" indicates no amplification, "+" indicates weak amplification and "++" indicates strong amplification. Of 18 samples, 15 contained amplifiable templates. Samples from about three meters depth contained the lowest level of DNA and amplicons and the same was found for matrix soil from one-meter depth, but it was amplifiable. All samples with a detectable content of DNA had amplifiable ewA/ewE 380 bp templates in the qPCR, and even one sample (EW21) without detectable DNA had ewA/ewE amplicons (Table 24). The abundances of the long and short amplicons were of identical order in ten cases, while they differed

TABLE 24. Results of qPCR amplification creating a long and a short barcode. Sample information in 0. Level of amplification: ⁒: none; + : weak; ++ : strong. Neg. con.: Negative control.

Sample	Site/excavation/depth (m)	Sample type/origin	DNA conc. Qubit ng/µL	ewA/ ewE 380 bp	ewB/ ewC 30 bp
PP2-1	Salløv (HG)/2/2.8	Matrix soil	Too low	⁒	⁒
PP2-1	Salløv (HG)/2/2.8	Fracture pore lining	0.26	+	+
PP2-1	Salløv (HG)/2/2.8	Pseudogley	Too low	⁒	⁒
PP2-1	Salløv (HG)/2/2.8	Fracture lining	0.13	⁒	⁒
PP2-1	Salløv (HG)/2/2.8	PP2-1 Neg. con.	Too low	⁒	⁒
PP2-1	Salløv (HG)/2/2.8	PP2-1 Neg. con.	Too low	⁒	⁒
Blanks		Blank	Too low	⁒	⁒
Blanks		Blank	Too low	⁒	⁒
PP2-10	Salløv (HG)/2/1.2	Infilling	3.14	+	+
PP2-11	Salløv (HG)/2/1.2	Infilling	3.98	++	+
PP2-12	Salløv (HG)/2/1.2	Infilling	3.05	+	++
PP2-13	Salløv (HG)/2/1.2	Infilling	0.449	+	+
PP2-14	Salløv (HG)/2/1.2	Matrix soil	0.277	+	+
PP2-15	Salløv (HG)/2/1.2	Burrow lining	3.67	+	++
PP2-16	Salløv (HG)/2/1.2	Matrix soil	0.4	+	+
PP2-17	Salløv (HG)/2/1.2	Burrow lining	0.703	++	+
PP2-18	Salløv (HG)/2/1.2	Burrow lining	2.89	++	++
PP2-21	Salløv (HG)/2/0.1	Topsoil	14.1	++	++
PP2-21	Salløv (HG)/2/0.1	Topsoil	15.9	++	++
PP2-21	Salløv (HG)/2/0.1	Topsoil	11.8	++	++
PP2-21	Salløv (HG)/2/0.1	Topsoil	8.14	++	++
Neg. con.		PP2-21 Neg. con.	Too low	⁒	⁒
Neg. con.		PP2-21 Neg. con.	Too low	⁒	⁒
PP2-1	Salløv (HG)/2/2.8	Matrix soil	Too low	+	⁒
		Extraction negativ0109	Too low	⁒	⁒
		Extraction negativ0105	Too low	⁒	⁒

Negative Control	Matrix soil	Topsoil	Burrow lining and other sample types

inconsistently in 4 cases, i.e., the expectation that the short barcodes were more likely to amplify more abundantly than the long amplicon was not confirmed, nor was the short barcode found while the long barcode was absent. Thus, we have no indication of absence of current worms in the selected burrows. In three samples, the ewB/ewC amplicons were less abundant

than the ewA/ewE amplicons (one undetectable ewB/ewC), and in two samples the ewB/ewC amplicons were more abundant than the long ewA/ewE.

3.6.3 aDNA of fossil roots and root channel macropores

Three sample types were sequenced: root fossil samples (n=11;), sediment samples (n=25) and control samples (n=7). There is a striking difference in the size distribution of reads when comparing root fossils and sediment samples (Figure 91). The sediment samples have a low average length and appear more degraded, while a higher preservation level is observed for the root samples. In addition, in sample PP2-34 and PP2-76a, a ~10bp periodicity is discernible in the size distribution, indicating the size of a full turn of the DNA-helix when wrapped around a histone. These patterns suggest that the sediment DNA is extremely degraded compared to the root fossil DNA.

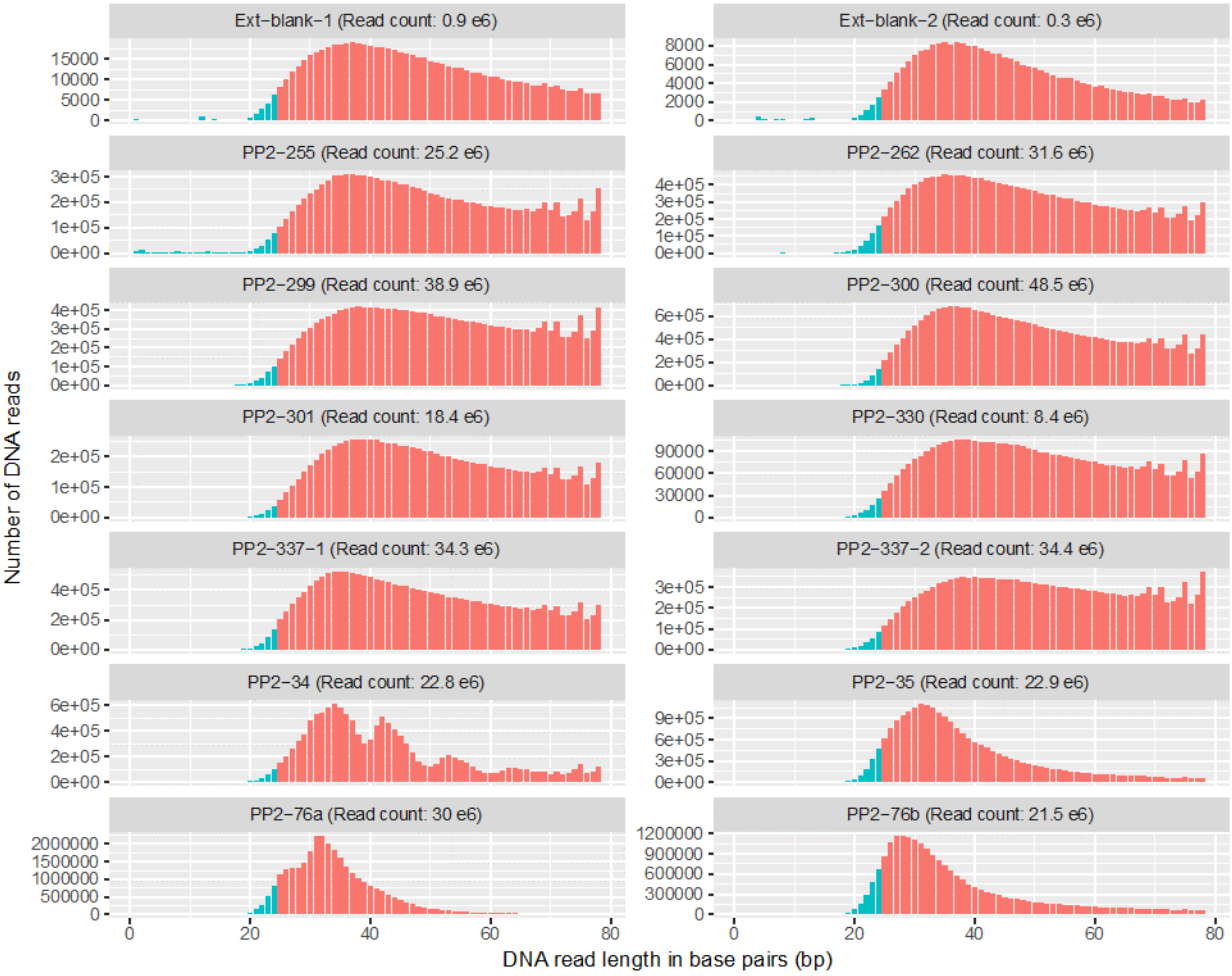

FIGURE 91. DNA read length distribution for a select subset of samples. Blue colour represents reads that were discarded due to their short length (<25bp). Red bars represent reads that were retained for downstream analysis. Samples PP2-34, 35 and 76a,b are sediments (root channel organo-mineral fill and matrix). All other samples are fossil roots.

Figure 92 shows results of aDNA shot-gun identification of plant DNA families represented in the complete array of samples (Appendix 3, Table A3.1). In Table 25 is show the aDNA results paired with the radiocarbon dating in sub-samples (photo documentation in Appendix 3,Table A3.4). Figure 92 show that the fossil root samples are readily discernible from the other samples due to their high abundance in DNA from the birch family (*Betulaceae*). Furthermore, seven samples stand out with relatively high amounts of DNA from the willow family (*Salicacae*). However, the remainder of the sediment samples and control samples cannot be distinguished based on plant composition. This pattern is also apparent in an ordination analysis

based on identified plant families (Figure 96). While root fossil samples and samples with *Salicaceae* present form two separate clusters, the remainder of sediment and control samples cluster together.

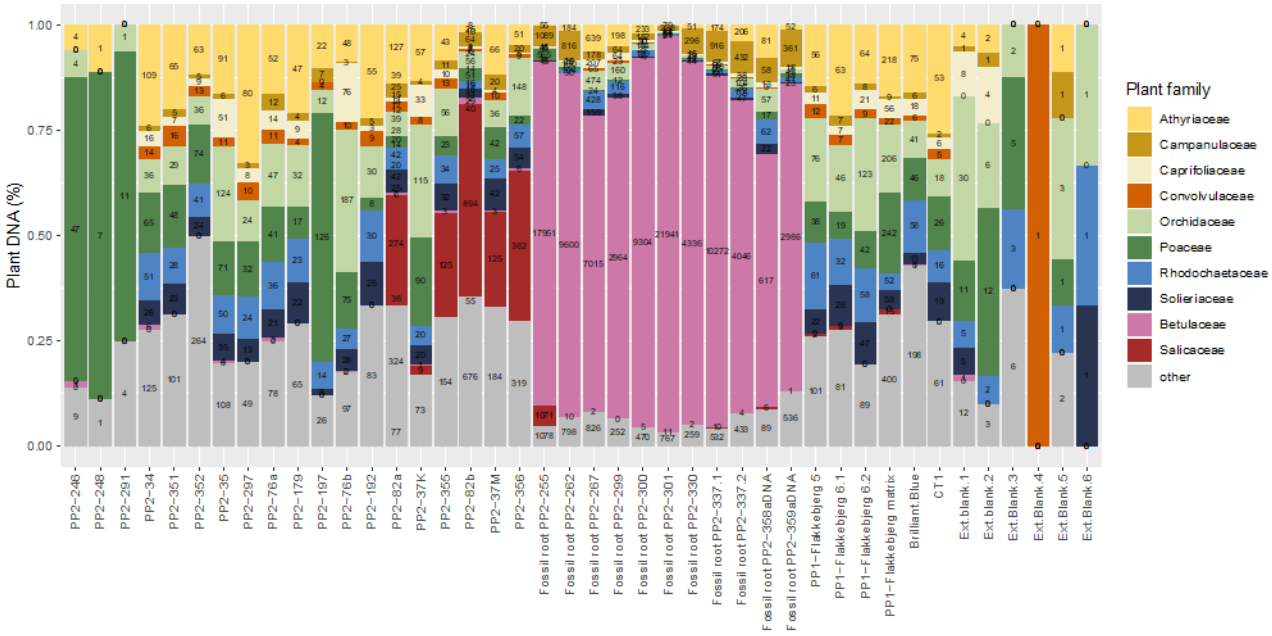

FIGURE 92. Barplot showing shot-gun aDNA abundance of plant families for a complete array of samples. Counts represent number of DNA reads assigned to each family.

Based on these observations, we hypothesize that DNA from *Betulaceae* and *Salicaceae* represents endogenous DNA, while all other plant reads represent background noise. To test this, we compared ancient DNA damage patterns with plastome depth of coverage plots of the most abundant family in each sample (Appendix 3). We found that most samples had two or four peaks, representing conserved regions in the 16S and 23S rRNA genes. However, only reads mapped to either *Betulaceae*, *Salicaceae* or *Poaceae* had any noticeable coverage outside of these regions. This suggests that the background noise detected here represents false positives mapped to very conserved regions in the 23S and 16S rRNA genes that are ubiquitous in plants. This observation is further supported by the associated ancient DNA damage patterns, which only display 5' C to T and 3' G to A misincorporations in *Betulaceae* and *Salicaceae*. The absence of ancient DNA damage patterns in DNA from the grass family (*Poaceae*) is expected because of the young age of most of these samples (PP2-246 and PP2-248 in Table 25). However, at a radiocarbon age of 5526 ±37 it is surprising that PP2-197 does not exhibit ancient DNA damage patterns. This could suggest that DNA from grass should also be classified as contamination, although it is equally possible that this DNA is endogenous. Thus, we conclude that reads mapped to the birch and willow families represent endogenous ancient DNA from the past environment while grass could be endogenous DNA. All other plant assignments represent background contamination.

The relatively low amount of plant DNA identified in the sediment samples, and in particular the young sediment samples, is most likely due to high concentrations of bacterial DNA diluting the plant DNA in the samples. Sediment is known to host vast quantities of bacteria, which would cause the majority of sequenced DNA to be of bacterial origin. This is supported by the relatively high amounts of plant DNA in root fossil samples, where the quantity of bacterial DNA is expected to be comparatively low.

TABLE 25. Paired results of aDNA and radiocarbon dating in sub-samples.

aDNA sub-sample	^{14}C sub-sample	Site/Excavation /depth (m)	Sample type/origine	Origine of aDNA	Age of sediments YrBP	Age of fossil roots CalBP
PP2-246	PP2-247	Salløv (HG)/E2/0.1	Topsoil	(*Poaceae*, Grass fam.)	256 ±19	
PP2-248	PP2-249	Salløv (HG)/E3/0.1	Topsoil	(*Poaceae*, Grass fam.)	431 ±19	
PP2-291	PP2-292	Bulbro (LG)/E4/0.1	Topsoil	No plant DNA	1046 ±20	
PP2-34	PP2-34	Salløv (HG)/E2/1.3	Worm burrow (soil fill)	No plant DNA	4082 ±31	
PP2-351	PP2-351	Salløv (HG)/E2/1.1	Worm burrow XRT1 (soil fill)	No plant DNA	failed	
PP2-352	PP2-352	Salløv (HG)/E2/1.3	Worm burrow XRT1 (soil fill)	No plant DNA	3420 ±35	
PP2-CT1	PP2-CT1	Salløv (HG)/E2/1.5	Root channel XRT1 (fill in grey fracture	No plant DNA	NA	
PP2-35	PP2-296	Salløv (HG)/E2/1.2	Clay matrix, oxidized (next to Worm burrows)	No plant DNA	8642 ±32	
PP2-297	PP2-296	Salløv (HG)/E2/1.2	Clay matrix, oxidized (next to Worm burrows)	No plant DNA	8642 ±32	
PP2-76a	PP2-76a	Salløv (HG)/E2/2.8	Root channel-fill (in grey fracture)	No plant DNA	NA	
PP2-179	PP2-180	Salløv (HG)/E3/2.4	Root channel fill (grey fracture)	No plant DNA	6656 ±37	
PP2-197	PP2-198	Salløv (HG)/E3/2.6	Root channel fill (grey fracture)	(*Poaceae*, Grass fam.)	5526 ±37	
PP2-76b	PP2-76b	Salløv (HG)/E2/2.8	Clay matrix, oxidized (next to 179 and 197)	No plant DNA	NA	

TABLE 25 continued

aDNA sub-sample	^{14}C sub-sample	Site/Excavation /depth (m)	Sample type/origin	Origin of aDNA	Age of sediments YrBP	Age of fossil roots CalBP
PP2-192	PP2-193	Salløv (HG)/E3/2.4	Clay matrix, oxidized (next to 179 and 197)	No plant DNA		
PP2-82a	PP2-82a	Salløv (HG)/E2/5.2	Root channel fill (red fracture)	*S. chamaetia /vetrix* (Willow fam.)	21924 ±100 (pyroxidation)	
PP2-37K	PP2-37a	Salløv (HG)/E2/5.2	Root channel fill (red fracture)	*S. chamaetia /vetrix* (Willow fam.)	NA	
PP2-355	PP2-355	Salløv (HG)/E2/5.5	Root channel fill (red fracture)	*S. chamaetia /vetrix* (Willow fam.)	NA	
PP2-82b	PP2-82b	Salløv (HG)/E2/5.2	Clay matrix, reduced (next to 82a)	*S. chamaetia /vetrix* (Willow fam.)	19066 ±48 (pyroxidation)	
PP2-37M	PP2-37M	Salløv (HG)/E2/5.2	Clay matrix, reduced (next to 37F)	*S. chamaetia /vetrix* (Willow)	NA	
PP2-356	PP2-356	Salløv (HG)/E2/5.5	Clay matrix, reduced (next to 355)	*S. chamaetia /vetrix* (Willow fam.)	NA	

TABLE 25 continued

aDNA sub-sample	^{14}C sub-sample	Site/Excavation /depth (m)	Sample type/origin	Origin of aDNA	Age of sediments YrBP	Age of fossil roots CalBP
PP2-255	PP2-255	Bulbro (LG)/E6/1.3	Root fossil	*A. glutinosa* (Common alder)		
PP2-262	PP2-262	Bulbro/E4/2.2	Root fossil	*A. glutinosa* (Common alder)		6894 – 6695
PP2-267	PP2-263	Bulbro/E4/2	Root fossil	*A. glutinosa* (Common alder)		7169 – 6973
PP2-299	PP2-302	Bulbro/E4/ 2.2	Root fossil	*A. glutinosa* (Common alder)		7254 – 7026
PP2-300	PP2-307	Bulbro/E4/2.1	Root fossil (twin1)	*A. glutinosa* (Common alder)		3556 – 3388
PP2-301	PP2-312	Bulbro/E4/2.1	Root fossil (twin2 of 300/307)	*A. glutinosa* (Common alder)		3475 – 3382
PP2-330	(same root as 337)	Bulbro/E5/3	Root fossil	*A. glutinosa* (Common alder)		3454 – 3368

TABLE 25 continued

aDNA sub-sample	^{14}C sub-sample	Site/Excavation /depth (m)	Sample type/origin	Origin of aDNA	Age of sediments YrBP	Age of fossil roots CalBP
PP2-337.1	PP2-337	Bulbro/E5/2	Root fossil	*A. glutinosa* (Common alder)		ND (same root as 337 and 332)
PP2-337.2	PP2-332	Bulbro/E5/2.5-3	Root fossil (thin vert. extention of 337.1)	*A. glutinosa* (Common alder)		2998 – 2869
PP2-358aDNA	PP2-358	Bulbro/E5/1.8	Root fossil XRT4	*A. glutinosa* (Common alder)		2963 – 2802
PP2-359aDNA	PP2-359	Bulbro/E5/2.3	Root fossil XRT4 (thin vertcal extension)	*A. glutinosa* (Common alder)		3318 – 3065
Flakkebj. PP1-5	PP1-3	Flakkebjerg (HG)/B9/4.5	Concretion (oxidized)	No plant DNA	21342 ±96 (pyroxidation)	
Flakkebj. PP1-6.1	PP1-16	Flakkebjerg (HG)/B9/4.5	Concretion (oxidized)	No plant DNA	25269 ±169 (pyroxidation)	
Flakkebj. PP1-6.2	-	Flakkebjerg (HG)/B9/4.5	Concretion (oxidized)	No plant DNA		
Flakkebj. PP1-matrix	PP1-25	Flakkebjerg (HG)/B9/4.5	Clay matrix (reduced)	No plant DNA	15304 ±34 (pyroxidation)	

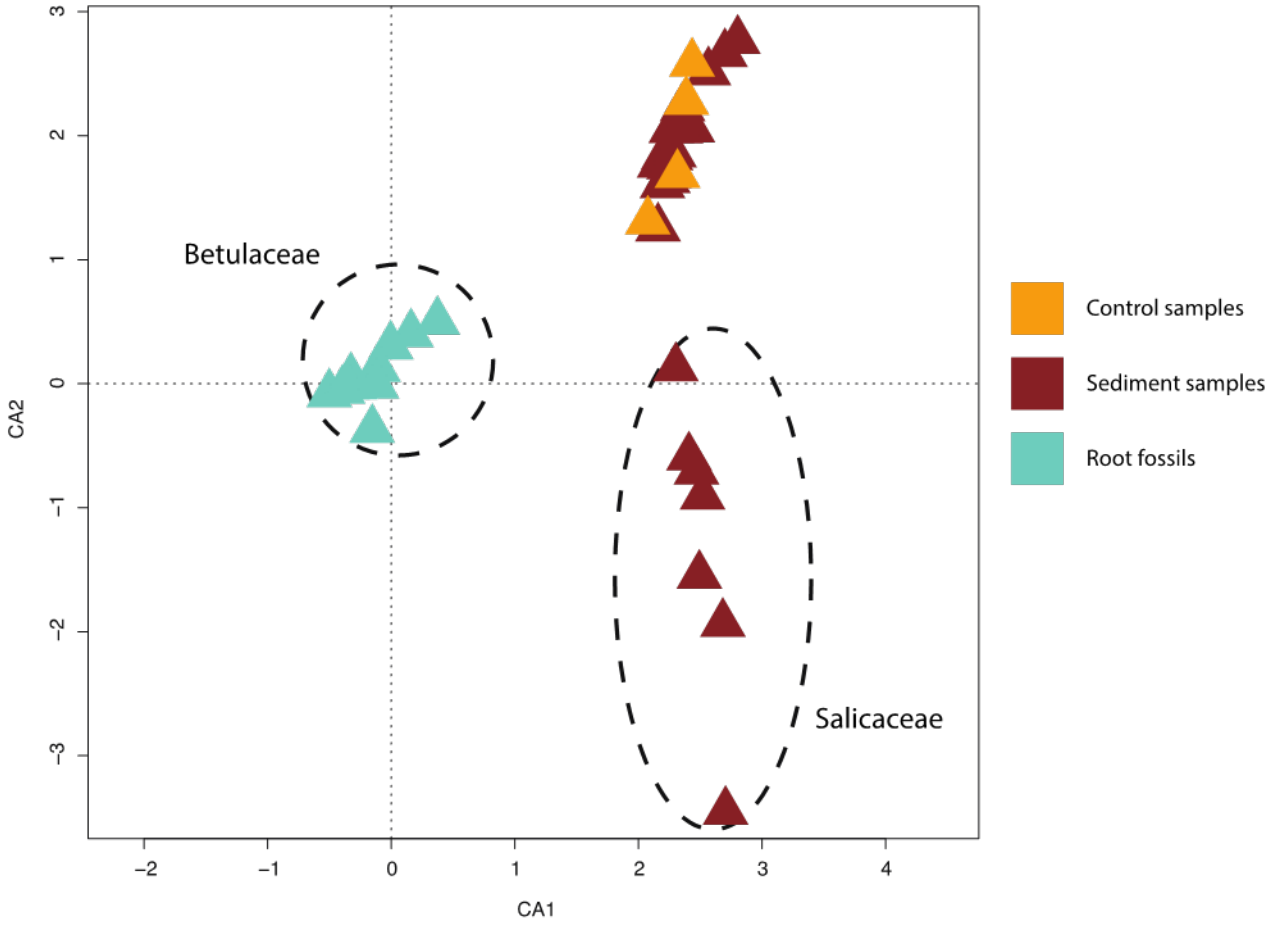

FIGURE 93. Cluster analysis (CA) showing comparison of plant DNA composition in root, sediment and blank control samples.

To further assess the origin of the birch family DNA in the root fossil samples, we assessed the most abundant genera identified among the Betulaceae reads. We found the Alder (*Alnus*) was the only genera identified within the family. This is in agreement with morphological characterizations of some of the root fossils, which tentatively identified them as common Black Alder (*A. glutinosa*). To further assess the origin and age of the root fossil samples, we mapped reads to the reference genome for common alder (*A. glutinosa*). The presence of distinct ancient DNA damage patterns for most root samples (Figure 94) strongly suggests that the *Alnus* DNA identified in these samples is ancient in nature. To confirm the species for each fossil root sample, we generated phylogenies based on full chloroplast genomes from each sample and all available chloroplast genomes of *Alnus* sp. in genbank (Appendix 3 Figure A3.1). We found that all ancient samples clustered together in a group with reference sequences from both *A. incana* and *A. glutinosa*. We also generated a phylogenetic tree based on ribosomal RNA (Appendix 3, Figure A3.2). Using this approach, the ancient samples clustered exclusively with *A. glutinosa* species, while *A. incana* formed a sister clade. Hence based on the results from both of these phylogenies, we conclude that the ancient root fossils analysed are from *A. glutinosa*.

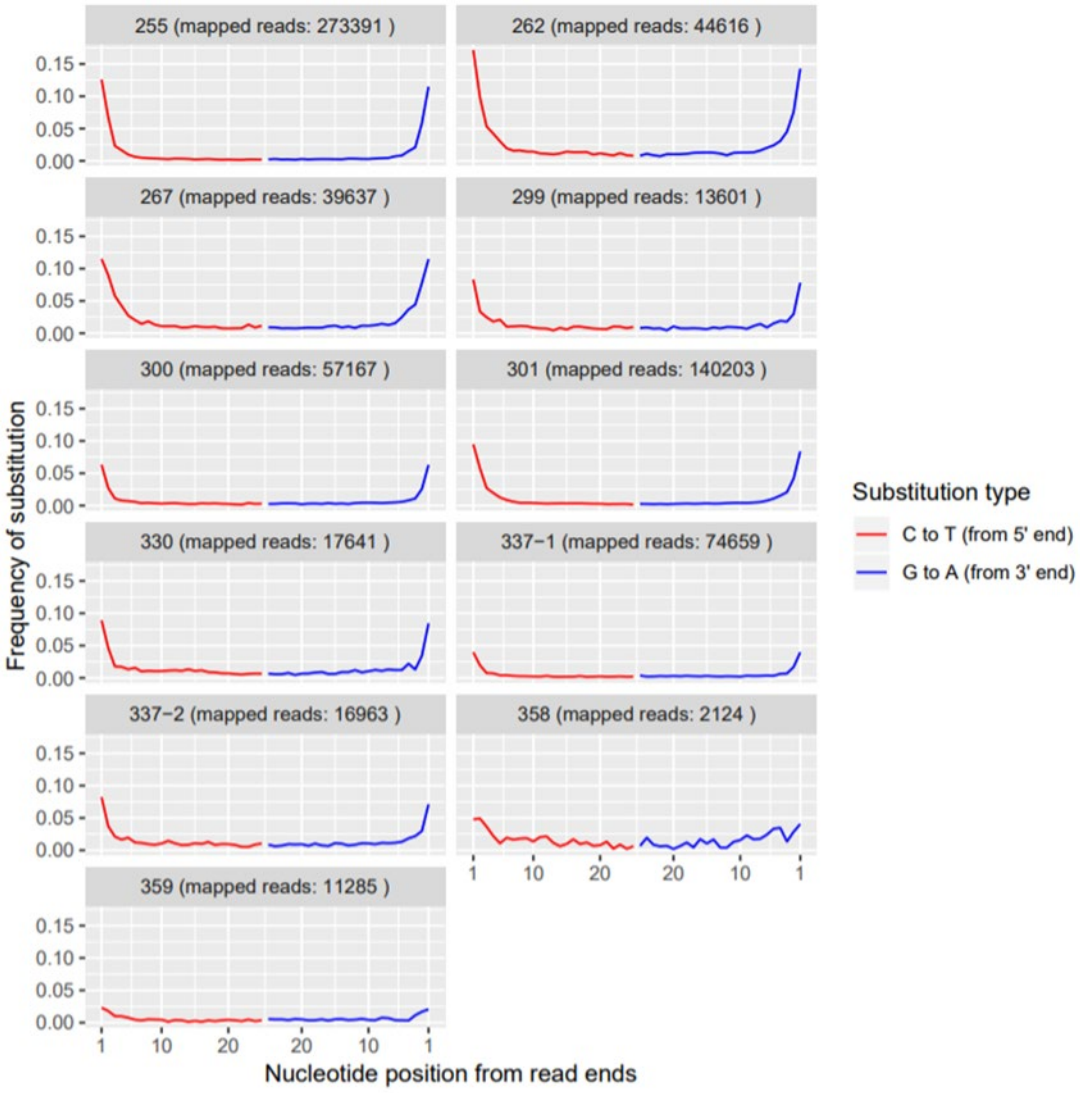

FIGURE 94. Ancient DNA damage patterns in reads mapped to A. glutinosa. Two types of base substitutions are plotted: C to T substitutions towards the 3' prime end of the read (red) and A to G substitutions towards the 5' prime end of the read (red). The number of mapped reads is shown in parenthesis after sample names.

To analyze how the ancient root fossils compare with the general population of *A. glutinosa* across Europe, we compared our samples with DNA data from Havrdova et al. (2015)[1]. We analysed the same ~2,800 bp composite sequence, based on three concatenated regions as described in Havrdova et al. (2015). We found that our samples were different from all other specimens described. Our samples are, however, closely related (1 mismatch) to haplotypes 1,2 and 4 from Havrdova et al. (2015). These haplotypes belong to a group of haplotypes that spread quickly after the Last Glacial Maximum (LGM) and are widely distributed across Northern Europe, including Denmark. A. glutinous (Rødel) is a tree up to 25 m high (Figure 96) and was one of the four most common trees in the forest 7,000-3,000 yr BP in Denmark.

The identification of willow DNA in seven sediment samples without the presence of any root fossil remains demonstrates one of the advantages of DNA-based methods. However, due to the highly degraded nature of the sediment samples analyzed in this study, the amount of willow reads identified is generally low (<500 reads). Nevertheless, in one sample (sample PP2-82b) the concentration of willow DNA is slightly higher at 894 reads assigned to Salicaecae when compared to all chloroplast genomes available. On the other hand, when all reads from this sample were mapped directly to the *Salix suchowensis* reference genome, around 5,000

reads could be mapped to the reference. In order to assess the phylogenetic origin of willow DNA in sample 82b, we generated a consensus plastome and compared it to other *Salix* plastomes. The partial plastome alignment of 27+1 species contained 99,096 bp, including coding and non-coding regions. Of this, 755 sites were variable (0.76%) and 1.09% were missing data.

The resulting phylogeny shows a clear separation of subgenus *Salix* and the *Chamaetia/Vetrix* clade (Figure 95). The ancient sample falls within the latter. It groups within an unsupported clade of European species (Wagner et al. 2018a,b, 2020). However, the low number of informative characters resulted in low statistical support and very short branches within the *Chamaetia/Vetrix* clade. On the contrary, the long branch of the ancestral sample most likely results from the number of ambiguous sites in the ancient partial plastome. Thus, clear sister relationships of the ancestral sample cannot be inferred.

The positive identified subg. *Chamaetia/Vetrix* is usually referred to as “shrub willows”. Some of them are up several m high scrubs and trees, such as the European species *S. caprea, S. eleagnos, S. cinereal, and S. myrsinifolia*. The species *S. caprea* (Seljepil), *S. cinerea* (Gråpil), and *S. myrsinifolia (Sort pil)* are common species in Denmark in both high and low-ground. *S. caprea* are scrubs and up to 10-15 m high trees with robust stems (Figure 96), which preferably grows on clayey till soils. They were among the first shrubs and trees to spread widely in the open post glacial landscape 11,000 – 10,000 yr BP (Naturstyrelsen, 2010: GEUS, 2017).
Lastly, we tested whether vertebrate DNA could be amplified from the samples to better characterize the paleo-environment. We used two short metabarcoding assays targeting the *16S* and *12S* mitochondrial genes, and sequenced the resulting metabarcoding amplicons on the Illumina MiSeq system. We found that no endogenous vertebrate DNA was amplified in any of the samples analyzed. The only vertebrate species detected using this approach were the common contaminants human (*Homo sapiens*), pig (*Sus scrofa*) and cat (*Felis* sp.). These taxa most likely represent background contamination from the sampling or from the laboratory.

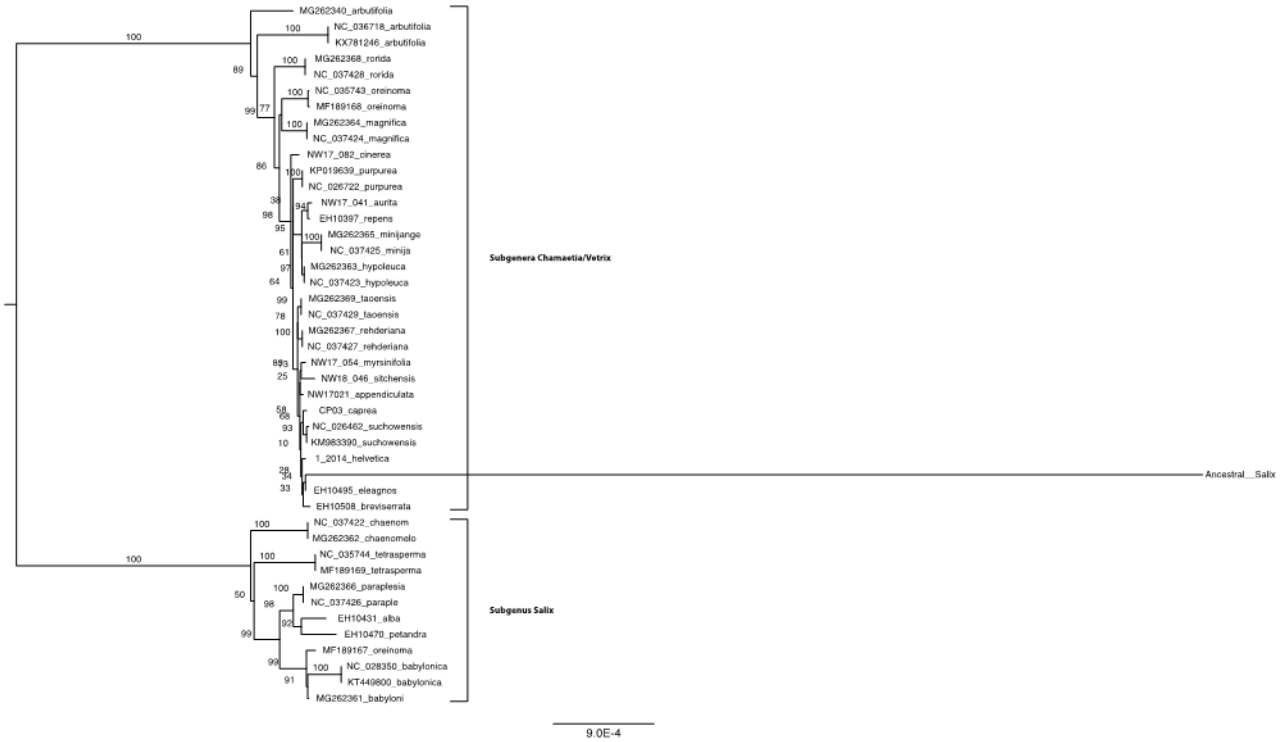

FIGURE 95. Maximum likelihood phylogeny of the partial plastome alignment of 44 samples (27 species). A clear separation of the subgenus Salix and the Chamaetia/Vetrix clade can be observed. The ancestral sample groups within the Chamaetia/Vetrix clade in an unsupported group of European species (Wagner et al. 2018a,b, 2020).

FIGURE 96. (left) A. glutinosa (Rødel) was one of the four most abundant trees in the forest 7,000-3,000 years BP. (Right) Salix caprea (Seljepil) was widespread pioneer scrubs and trees on clayey till soils 11,000 -10,000 yr BP.

3.6.4 Summary and evaluation of radiocarbon and DNA results

Figure 97 summarizes the radiocarbon ages and aDNA determination carried out for the fossil roots and sediment samples related to root channels in the geological profiles.

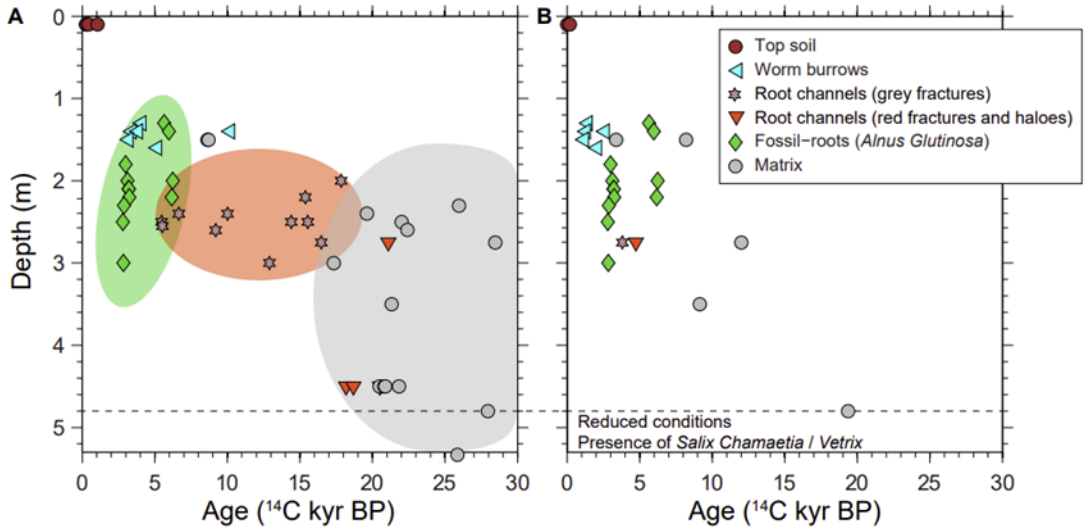

FIGURE 97. Summary of radiocarbon ages and aDNA analyses from Salløv and Bulbro, and the Flakkebjerg concretions A: Humin ages for all samples other than fossil roots. B: Humic ages for all samples other than fossil roots. The fossil roots represent correct results for radiocarbon age and origin of aDNA. The radiocarbon ages for root channels (organo-mineral fillings) and till matrix samples are predominantly overestimated due to heterogeneity of the carbon source and open system weathering processes.

It shows the topsoil humin ages are modern in the high-ground to more than 1,000 years old in the low-ground. The difference reflects degradation of topsoil organic matter by intensive oxidation in high-ground, while high soil moisture in the low-ground had preserved soil organic matter and resulted in older ages. The older ages of the topsoil fillings in the worm burrows (only collected in the high-ground) suggest that the infillings were not modern top soil. Hence the burrows appear to old features being reused by younger generations of worms. The apparent lack of plant DNA in the top soil and worm burrow fillings is likely due to overshadowing by high concentrations of DNA from soil bacteria in those samples.

The calibrated ages of the fossil roots from *A. glutinosa* falls in two periods; from 7.2 – 6.3 kcal BP and 3.5 - 2.8 kcal BP. The older period marks the end of Mesolithic stone age, and the younger period the Bronze Age. The old radiocarbon ages and the finding of the fossil roots in all 3 low-ground excavations imply that the study site was covered by widespread mid-Holocene original forest. Major changes in the Danish landscape and biogeography, however, took place in both periods; first the beginning clearance of the dense native forest for farming, and secondly the final great expansion of the cultural landscape (Jensen 2013). The latter is visible in the local landscape by the occurrence of several Bronze Age burial mounds within the Havdrup project area. The age and aDNA results for the fossil roots can be considered to be accurate as they represent closed systems and have $\delta^{13}C$ values, which falls within reference values for recent organic material. Also, there is a high number of aDNA reads from *A. glutionosa*, which provides a high certainty with respect to the aDNA identification.

In the high-ground, long-term deep weathering and oxidation (governed by the elevation in the landscape) likely explains the lack of preserved fossil plant roots and the lack of plant aDNA in the oxidized till in this setting. The organo-mineral fillings of root channel in the grey fractures had humin radiocarbon ages from about 5,500 to17,000 years. Corresponding matrix ages were about 17,000 to 28,000 years, which were similar to the matrix samples deeper in the

profiles. The wide range and very high ages probably reflect that the root channels represent an open system and differences in source of the organic carbon. Influence of the latter is indicated by the less negative $\delta^{13}C$ values (Figure 89) for the samples, which reflects influence of C derived from much older Tertiary or Palaeocene marine limestone carbonate in the till material by microbial degradation of the organics. Additionally, organic carbon from embedded glacial organic material in the till may also be present as indicated by organic fragments collected from the tills and dated to approximately 35,000 to 39,000 ^{14}C yr BP (PP2-338 OM and PP2-452 in Appendix 3, Table A3.3). This is a likely explanation why both the conventional ^{14}C method and the pryoxidation method are providing glacial ages.

As a consequence of those factors, the radiocarbon ages of the organo-mineral fillings in the root channels and the clayey matrix samples must be considered uncertain and predominantly too high. Actual high ages of the root channels, however, is indicated by absence of ^{14}C from modern organic material and absence of bomb induced ^{14}C. The probable origin from of the channels from ancient roots is also evident from the abundant findings of the deep fossil roots and similar root channels in the nearby low-ground Bulbro site and from the Fe-oxide mass balance calculations in section 3.3, which estimated an age of 2,000 to 21,000 yr BP for clogging of the root channels by Fe/Mn-oxide precipitation.

As mentioned, the root channels in the red fractures and the matrix had very high and similar ^{14}C ages. In the former case, this was likely due to a combination of the organic matter being decomposed by oxidizing conditions and leaving behind only the less reactive organics (refractory carbon) similar to the results for the channels in the grey fractures. In the unweathered grey (anaerobic) clay matrix samples organic matter would be better preserved (samples from 5.2-5.4 m depth, Table 18 and Table 21), which may explain the finding of the aDNA from the willow fam. (*S. chamaetia/vetrix*) along the root channels and adjacent clay in those samples (Figure 97). Also, in this case the ancient origin of the material was evident from the extreme degradation of the DNA in the samples. Those indicators together with the extensive filling of the root channels with Fe/Mn-oxides (*Figure 67*) corroborates with the biogeography evidence showing maximum spread of willows in clayey till landscapes in early post glacial time 11,000-10,000 yr BP. However, because only the family or clade of willow could be determined with the aDNA analysis, a possible alternative explanation to the origin of this aDNA may be willow scrubs (members of the *S. chamaetia/vetrix* clade) from the tundra taken up by glaciers and redeposition with the till material. The attempts to follow this track by including vertebrate aDNA sequencing for the till material to characterize the paleo-fauna was unsuccessful.
The Flakkebjerg samples showed the same ^{14}C values and pattern over depth as the samples in the current study and would be subjected to the same factors of uncertainty and error as discussed above. We identified traces of willow scrubs (*Salix Chamaetia/Vetrix)* in the Flakkebjerg concretions, however, the number of reads did not separate those from the background noise and hence could not be confirmed to be endogenous DNA.

3.7 Numerical modeling

3.7.1 Hydraulic data

The Daisy modeling was based on LUC hydraulic data from previous LUC studies, which are shown in Figure 103 (section 4). The LUC data represent 8 clayey till sites with a wide range of fracture and biopore occurrences, which represented individual model scenarios. The LUC samples (subjected to *in situ* effective soil stress in the flexible wall LUC permeameter by Jørgensen et al., 2019) represents undisturbed clayey till (O´Hara et al., 2000) with maximum fracture frequencies observed in field studies of clayey tills (Aamand et al. in pres., 2020). Additionally, the LUC provides tracer and pesticide transport data in a number of the LUC studies, which were utilized to calibrate and evaluate the performance the Daisy model (Appendix 4). Table 26 shows key hydraulic parameters for the LUC samples (Jørgensen et al., 2017).

TABLE 26. LUC hydraulic parameters applied in the modeling (from Figure 103 and Figure 104). Columns controlled by root channels in fractures or solitary in matrix are shown in green.

Study Site	Column sampling depth* [m]	LUC hydraulic conductivity of columns, K_{sat} [m/s]	LUC hydraulic conductivity of columns, K_{sat} [mm/yr]	Matrix hydraulic conductivity, K_{matrix} [mm/yr]	Cumulative fracture spacing, 2B [m], (Fracture hydraulic conductivity [mm/yr])
Marebæk1	1.0-1.5 (grey)	1.2E-05	378432	16	0.03, (37,8416)
Marebæk2	2.0-2.5 (grey)	6.9E-06	217598	16	0.05. (21,7522)
Marebæk3	4.0-4.5 (red)	6.1E-07	19237	16	0.08, (19,221)
Marebæk4	4.5-5.0 (red)	4.4E-09	139	10	0.5, (129)
Marebæk5	4.5-5.0 (red)	3.0E-09	95	10	0.5, (85)
Marebæk6	4.5-5.0 (red)	1.2E-07	3784	10	0.5, (3.774)
Skælskør1.1	2.0-2.5 (grey)	1.2E-06	37843	63	0.5, (37,780)
Skælskør1.2	2.0-2.5 (gey)	1.4E-06	44150	63	0.03, (44,087)
Skælskør1.3	4.0-4.5 (red)	7.2E-09	227	63	0.04, (164)
Skælskør1.4	5.5-6.0 (red)	8.6E-09	270	63	0.075, (207)
Skælskør 2.1	3.3-3.8 (red)	1.2E-08	378	63	0.17, (315)
Skælskør 2.2	4.1-4.6 (red)	2.0E-08	631	32	-, (599)
Skælskør 2.3	4.7-5.2 (red)	8.4E-09	265	252	0.25, (13)
Skælskør 2.4	2.7-3.2 (grey)	1.2E-07	3784	63	0.5, (3,721)
Ringe1*	1.0-1.5	2.8E-06	86724	16	- (86,718)
Ringe2	2.5-3.0 (grey)	2.8E-06	89562	16	0.09, (89,546)
Grundfør1*	1.0-1.5	3.0E-06	95239	16	-, (95,223)
Grundfør2*	2.5-3.0	2.0E-08	631	16	-, (615)
Hinnerup1	1.0-1.5 (grey)	2.6E-06	81678	16	0.17, (81,662)
Hinnerup2	2.5-3.0 (red)	3.1E-06	99023	16	0.1, (99,007)
Farre1	0-1.0 (grey)	1.5E-05	473040	22075	-, (450,965)
Flakkebjerg1	3.4-3.9 (grey)	6.9E-08	2176	410	0.13, (1.766)
Flakkebjerg2	4.3-4.8 (grey)	3.1E-07	9776	303	0.13, (9,473)
Flakkebjerg3	5.2-5.7 (red)	2.9E-09	93	35	0.5, (-)

** only solitary root channels*

Flow (volumetric flow pr. time unit) is proportional to the hydraulic aperture of fractures in 3. power and the diameter for solitary channels in 4. power (section 2.9, and Jørgensen et al. 1998b). Therefore, the LUCs that contain root macropores in fractures or solitary in the matrix have a great potential to dominate groundwater flow. This is, however, provided that they are

not limited by water supply from precipitation and that they are sufficiently drained into underlying ground water flow regimes with high hydraulic conductivity, such as coarse textured till, embedded sand/gravel layers, or directly into aquifers (e.g., Jørgensen et al, 2002a).

3.7.2 Scenario modeling

Scenario modeling uses a very simple model-setup of 1 m of sand representing the root zone followed by 4 m of moraine till (Figure 98). A drain is located at a depth of 0.9 m in the upper sand layer. The Daisy model uses a simple model to calculate drain flow based on the soil properties and the distance between the drains (Hansen et al., 2012a). The sand layer had a hydraulic conductivity of 3.2 * 10^{-5}m/s. To calculate unsaturated hydraulic conductivities, we used the same Van Genuchten properties (n=1.128 and α=0.02 cm^{-1}) for the sand and moraine layer to keep it as simple as possible. The lower boundary is in one case a 2 m thick clay aquitard without macropores with a fixed water table at 5 m.b.g.s. and low hydraulic conductivity of 1.0 * 10^{-9}m/s or 32 mm/year. This case corresponds to a field situation where fractures and biopores terminate as dead-end flow paths in clay matrix. In the second case, the lower boundary is free drainage. This case corresponds to a field situation where fractures and biopores have unlimited discharge into an underlying aquifer or embedded sand layers with free discharge into deeper groundwater. Weather data are from DMI's climate grid for Roskilde and we have run the model from 1990 to 2000 using the first year as a warm-up period. We used a standard management with spring barley every year. Discretization ranges from 0.5 cm in the top layer to 10 cm in the lower layers. We ran the two cases with all the hydraulic conductivities of the LUC columns in Table 26 and used the secondary domain model to represent the fractures (described in section 2.9 and Appendix 4).

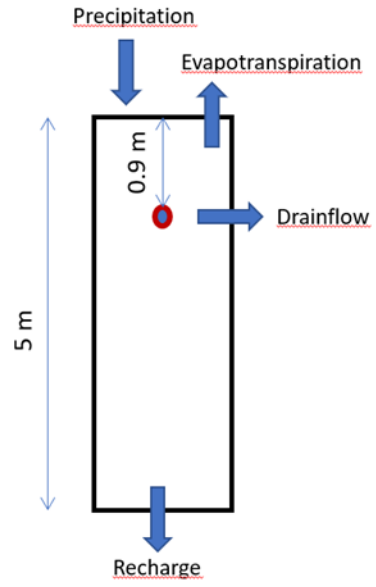

FIGURE 98. Schematic of model setup with arrows showing the components in the water balance of the scenario modeling.

Groundwater recharge

Table 27 and Table 28 shows the average yearly water balances calculated with for all the scenarios represented by the LUC samples. The yearly precipitation is 718 mm and the evapotranspiration is around 420 mm, resulting in around 300 mm of net precipitation, which either drains or recharges the ground water. For the case with free outflow as the lower boundary, Table 27 shows that all the net precipitation recharged for the scenarios with LUCs that contained macropores (root channels inside the fractures or solitary root channels in the matrix). The lowest groundwater recharge was 31 mm/year for the Flakkebjerg3 column with red fracturs without root channels inside. For this column, the hydraulic conductivity was 93 mm/year.

The recharge was lower than the hydraulic conductivity because it was only a part of the year that net precipitation was positive, leading to considerable drain flow.
For the case with the unfractured clay aquitard without macropore flow as lower boundary (Table 28), there was much lower variation in the groundwater recharge. This is because it was the low permeability aquitard that limited the groundwater recharge and not the macropores in the till. Most of the water left the column through the drain.

TABLE 27. **Water balance for the column simulations (fracture without root channels inside in red). Free outflow as lower boundary.**

Site	Hydraulic conductivity [mm/y]	Precipitation [mm/y]	Evapo-transpiration [mm/y]	Groundwater recharge [mm/y]	Drain flow [mm/y]
Marebæk1	378432	718	418	305	0
Marebæk2	217598	718	418	305	0
Marebæk3	19237	718	418	303	2
Marebæk4	139	718	417	55	249
Marebæk5	95	718	417	43	261
Marebæk6	3784	718	419	286	18
Skælskør1.1	37843	718	420	303	0
Skælskør1.2	44150	718	420	303	0
Skælskør1.3	227	718	420	68	234
Skælskør1.4	270	718	422	89	211
Skælskør 2.1	378	718	421	116	184
Skælskør 2.2	631	718	421	178	122
Skælskør 2.3	265	718	424	81	216
Skælskør 2.4	3784	718	420	288	15
Ringe1*	86724	718	419	305	0
Ringe2	89562	718	419	305	0
Grundfør1*	95239	718	418	305	0
Grundfør2*	631	718	420	178	124
Hinnerup1	81678	718	419	305	0
Hinnerup2	99023	718	419	305	0
Farre1	473040	718	428	297	0
Flakkebjerg1	2176	718	423	273	26
Flakkebjerg2	9776	718	422	300	2
Flakkebjerg3	93	718	416	31	266

** solitary root channels*

TABLE 28. Water balances for the column simulations. Aquitard as lower boundary with hydraulic conductivity of $1.0*10^{-9}$m/s or 32 mm/year.

Site	Hydraulic conductivity [mm/y]	Precipitation [mm/y]	Evapo-transpiration [mm/y]	Groundwater recharge [mm/y]	Drain flow [mm/y]
Marebæk1	378432	718	421	50	251
Marebæk2	217598	718	421	50	250
Marebæk3	19237	718	422	49	250
Marebæk4	139	718	422	28	271
Marebæk5	95	718	422	25	274
Marebæk6	3784	718	422	46	253
Skælskør1.1	37843	718	423	51	248
Skælskør1.2	44150	718	423	51	248
Skælskør1.3	227	718	424	32	266
Skælskør1.4	270	718	424	35	262
Skælskør 2.1	378	718	423	38	259
Skælskør 2.2	631	718	423	42	256
Skælskør 2.3	265	718	425	36	260
Skælskør 2.4	3784	718	423	48	249
Ringe1*	86724	718	422	50	249
Ringe2	89562	718	422	50	249
Grundfør1*	95239	718	421	50	250
Grundfør2*	631	718	422	40	258
Hinnerup1	81678	718	422	50	249
Hinnerup2	99023	718	422	50	249
Farre1	473040	718	436	52	233
Flakkebjerg1	2176	718	425	49	246
Flakkebjerg2	9776	718	425	51	245
Flakkebjerg3	93	718	424	21	276

** solitary root channels*

Figure 99 and Figure 100 show the results from the Havdrup soils as column diagrams. These illustrate that when the hydraulic conductivity is lower than the net precipitation, the surplus water will leave the column through the drain.

These show that despite the fact that the hydraulic conductivity varies with orders of magnitude, we do not see orders of magnitude difference in groundwater recharge in Figure 100. This is not surprising, since only the calculated surplus of precipitation will infiltrate the fractures in the simple 1D model. However, in field situations the water supply to individual preferential flow paths will not be equal to the net precipitation suggested in Table 27 and Table 28 because groundwater may be supplied by lateral flow (Section 3.5.3) from a larger area than assumed in the 1D calculations (e.g., Jørgensen et al., 2017).

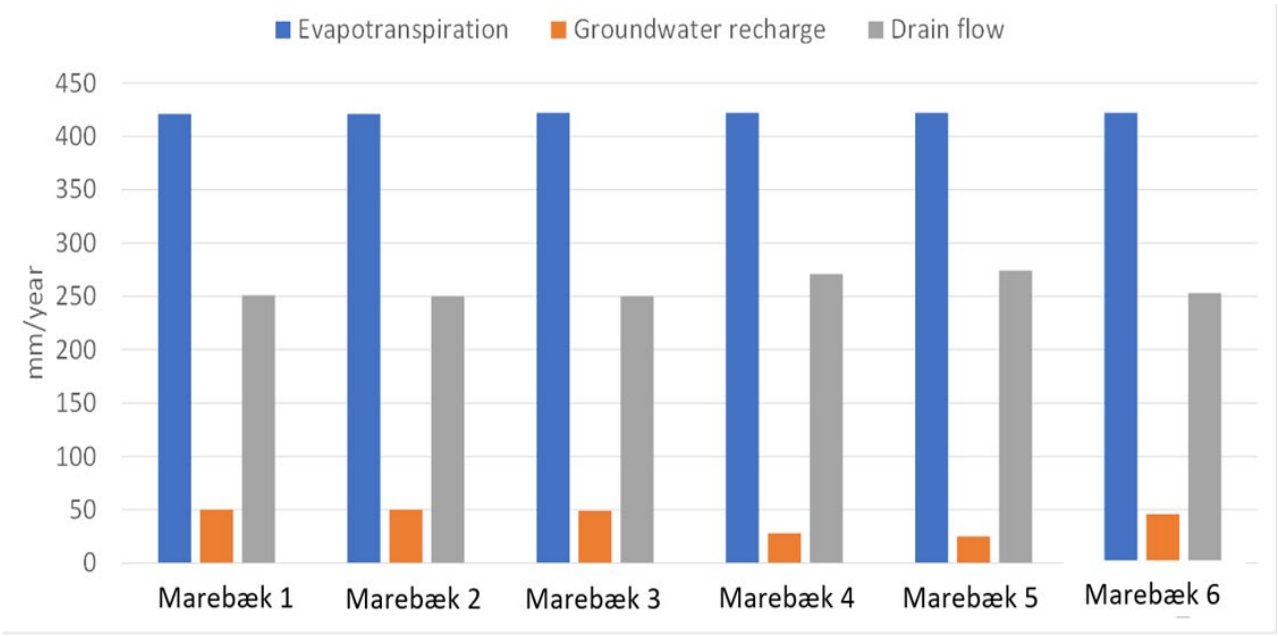

FIGURE 99. Water balance from simulations using the hydraulic properties of the LUC-columns from Havdrup. Low permeability aquitard as lower boundary.

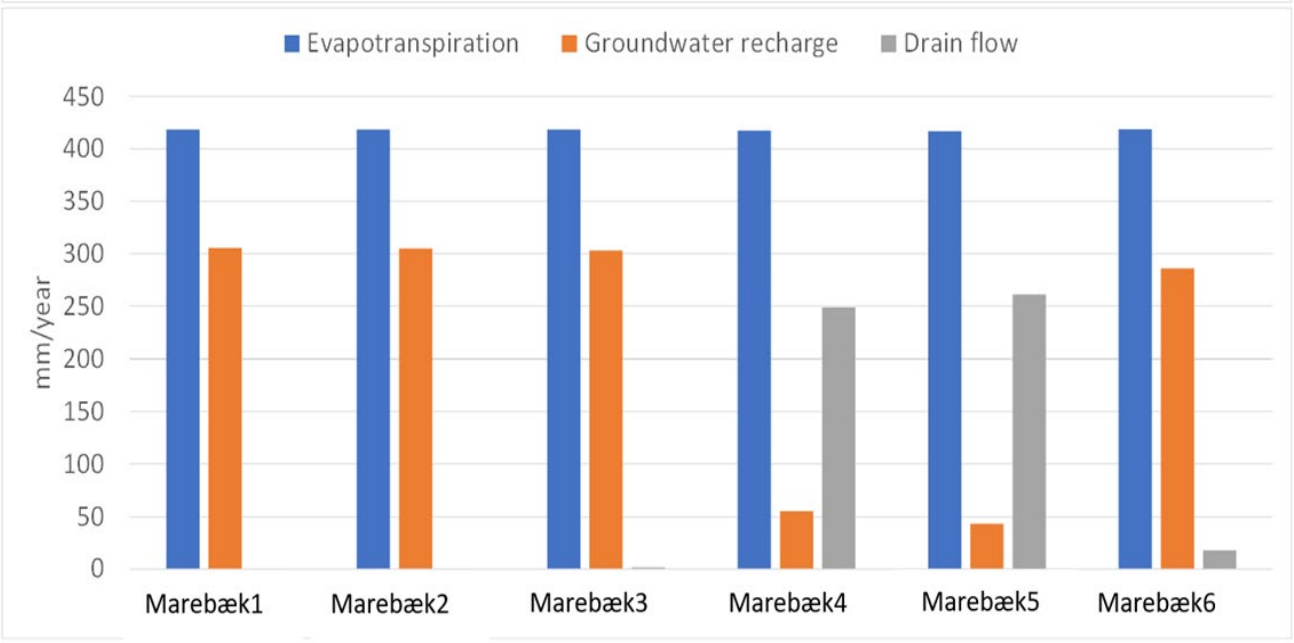

FIGURE 100. *Water balance from simulations using the hydraulic properties of the LUC-columns from Havdrup. Free outflow as lower boundary.*

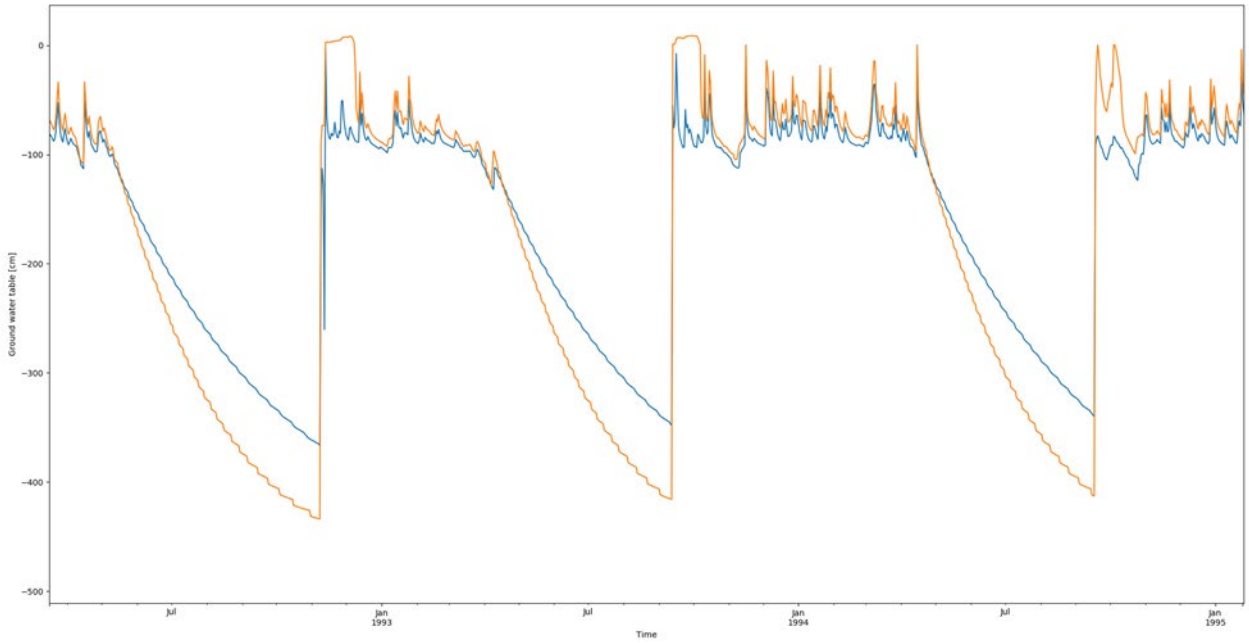

FIGURE 101. Simulated depth to the saturated zone with column properties from Marebæk 1 (blue curve) and Marebæk 4 (orange curve)

Figure 101 shows the simulated water table with the low permeability aquitard as lower boundary for the high conductivity Marebæk1 LUC with root channels along the fractures, and low conductivity Marebæk4 LUC without root channels. Despite 4 orders of magnitude difference between hydraulic conductivity, the water tables are almost similar because they are controlled by the low permeability of the aquitard below and the net precipitation. This pattern compares well with the observed perched water table in the high-ground E1 wells (Figure 21). Also, it shows how the fractures and biopores can become unsaturated during the summer where the evaporation is larger than the precipitation, resulting in negative net precipitation. The simulations illustrate that we cannot calculate a groundwater recharge based on the hydraulic conductivity of the moraine till alone. The boundary conditions are needed in detail, and this will only be possible to do in 1D for very special cases.

Pesticide migration

Pesticide migration was evaluated out by adding pesticide and bromide to the simulations from the previous task. Hence 10 mm of irrigation with 1 g/l of bentazon and bromide was applied to the surface 470 days after the start of the simulation. Bentazon is biodegradable, whereas bromide is conservative. Degradation and sorption constants for Bentazon are given in Jørgensen et al. (2017).

The simulated mass balances after 10 years are shown in Table 29 and Table 30. For Bentazon, most of the mass was degraded in soil, however, a small percentage was lost to the groundwater. With the low conductivity aquitard as lower boundary, most of the bromide was lost to the drains. When comparing the transport of the pesticide with flux of water, it seems that the contaminant does not directly follow the water. This is due to the application time, if the compounds were added at different times, the results would have been different, as ground water recharge and drain flow do not occur evenly over the year. To create preferential flow, the mass transfer coefficient between fracture and matrix was set very low. Setting it higher would have resulted in the same outflow for bromide, however, the timing would be markedly different. The flow rate would be the same, but the porosity would be different, resulting in later arrival of the bromide at the bottom. As was the case for the water flux, the large differences in hydraulic conductivities for the LUC examples, calculated in Table 30. Table 30,

did not result in large differences in the leaking of pesticides. As with the recharge simulations, this was controlled by the simplified 1D description, which does not take the 3D flow processes into account. Hence several orders of difference in pesticide migration into a natural aquifer from fractures (with similar aperture differences, as used in the 1D simulations) was observed in pesticide infiltration experiments in the Marebæk site (Jørgensen et al., 2002a; Regionernes videnscenter, 2008) showing the limitations of the 1D modeling approach. Pesticide migration for a wider range of pesticide properties is evaluated by Aamand et al. in prep. (2020).

TABLE 29. Mass balance of Bentazon and Bromide in % of applied mass. Free outflow as lower boundary.

	Bentazon				**Bromide**		
Site	Ground Water [%]	Drain [%]	Decom-position [%]	Soil [%]	Ground Water [%]	Drain [%]	Soil [%]
Marebæk1	2	0	86	11	45	0	50
Marebæk2	3	0	86	11	47	0	47
Marebæk3	3	0	88	9	22	2	68
Marebæk4	0	12	88	1	2	80	3
Marebæk5	0	11	88	0	1	82	3
Marebæk6	3	2	90	6	31	12	41
Skælskør1.1	1	0	87	12	29	0	63
Skælskør1.2	1	0	87	12	29	0	63
Skælskør1.3	0	11	88	1	2	76	5
Skælskør1.4	0	11	88	1	4	74	6
Skælskør 2.1	0	10	88	1	5	71	8
Skælskør 2.2	1	8	89	2	11	59	12
Skælskør 2.3	0	11	88	1	3	73	8
Skælskør 2.4	2	2	89	6	24	10	49
Ringe1*	2	0	87	11	29	0	64
Ringe2	2	0	87	11	29	0	64
Grundfør1*	3	0	87	11	27	0	67
Grundfør2*	1	8	89	2	12	61	11
Hinnerup1	2	0	87	11	29	0	64
Hinnerup2	2	0	87	11	29	0	64
Farre1	5	0	86	9	91	0	0
Flakkebjerg1	2	2	89	7	20	10	49
Flakkebjerg2	1	0	88	11	16	2	71
Flakkebjerg3	0	11	89	0	1	78	3

** only solitary root channels.*

TABLE 30. Mass balance of Bentazon and Bromide. Aquitard as lower boundary.

	Bentazon				Bromide		
Site	Ground Water [%]	Drain [%]	Decom-position [%]	Soil [%]	Ground Water [%]	Drain [%]	Soil [%]
Marebæk1	1	8	89	3	6	69	10
Marebæk2	1	9	88	2	5	71	8
Marebæk3	0	12	87	1	2	83	4
Marebæk4	0	12	88	0	1	85	2
Marebæk5	0	12	88	0	0	84	2
Marebæk6	0	12	87	1	1	85	3
Skælskør1.1	0	11	87	1	2	80	6
Skælskør1.2	0	11	87	1	2	80	6
Skælskør1.3	0	12	88	0	1	83	3
Skælskør1.4	0	12	88	1	1	83	3
Skælskør 2.1	0	12	87	1	1	84	3
Skælskør 2.2	0	12	87	1	1	85	3
Skælskør 2.3	0	12	87	1	1	82	4
Skælskør 2.4	0	12	87	1	1	84	4
Ringe1*	0	10	88	2	3	77	6
Ringe2	0	10	88	2	3	77	6
Grundfør1*	0	10	88	2	3	77	6
Grundfør2*	0	12	87	1	1	86	2
Hinnerup1	0	10	88	2	3	77	6
Hinnerup2	0	10	88	2	3	77	6
Farre1	0	6	90	3	3	51	10
Flakkebjerg1	0	12	87	1	1	80	5
Flakkebjerg2	0	12	87	1	1	80	5
Flakkebjerg3	0	11	89	0	0	82	3

** solitary root channels*

In summary, in the Daisy 1D simulations, we have varied the properties of the moraine till and the lower boundary. We have not varied the climate, the application time or the interaction with the matrix. This means that we only span a very limited set of the realistic parameter space. The simulations show that in order to describe and analyze the observed heterogeneity and lateral interactions of flow path in the subsoil, a 3D description of the flow system is a requirement.

4. Discussion and Implications

Fossil roots and root channels

Occurrence of relic root channels in the subsoil of glacial tills have been reported in a number of studies (e.g., Ruland et al., 1991; Jørgensen et al., 2004a,b; McKay and Fredericia, 1995; Klint and Gravesen, 1999; Cherry et al., 2006; Jørgensen et al., 2017), however, the phenomenon has not previously been thoroughly investigated. The first hypothesis in this study was that deep relic root channels in farmland mostly originate from pre-historic forest and therefore may be expected to occur widely in moraine landscapes. The study confirmed this hypothesis by providing the first solid evidence that relic root channels in glacial tills are from pre-historic forest, which covered Denmark, and therefore should be anticipated widespread the moraines.

The finding of well-preserved ancient root fossils over the entire Bulbro site was unique and due to its position by foot of the hill where high-groundwater tables and upward anaerobic flow had preserved the roots and channels with minimum influence from weathering processes. By exhibiting ages from 3-7 kyr BP and being exclusively from A. glutinosa, they suggested that a forest dominated by *A. glutinosa* (Rødel, Figure 102) had been covering the low-ground site as part of the Atlantic-Subboreal forest, which covered most of Denmark in the Stone age and much of Eastern Denmark to the Bronze age. This corroborates with the abundant findings of relic root channels dominating preferential flow in previous till studies by e.g., Jørgensen et al. (2002, 2004 a,b, 2017, in prep. 2020); Jensen et al. (1999): Butzbach (2007), and Mosthaf et al. (in review 2020).

Funk (1990) describes *A. glutinosa* to possess an extensive root system of both surface and deep branches, which is in agreement with the current study. This enables it to survive on either waterlogged soils or those with deep water tables. *A. glutinosa* is moreover the only tree species in Denmark to develop roots below groundwater tables (Miljøstyrelsen, 2020), which corroborates with the current study where fossil roots were found to aim for anaerobic sand layers well below the water table in clays with no sign of previously lowered ground water or intense weathering.

FIGURE 102. A. glutinosa (Rødel) shown in its main habitat on moist ground (left). Current distribution in Europe (right). In the native mid-Holocene forest, A. glutinosa was one of the most widespread species occurring both in low and high-ground landscapes.

A. glutinosa was one of the four most common tree species in the native forest in the mid-Holocene climatic optimum from 7,000- 3,000 yr BP (GEUS, 2007; Miljøstyrelsen, 2020). It´s main habitat is moist or wet soils; however, it grows in both low and high-ground landscapes. This implies that relic root channel systems from *A. glutinosa* supposedly are particular widespread in low-ground moraine landscapes, however, also common in high-ground settings where moist and water logged areas were widespread before tile drainage was introduced (Jensen, 2013). In Germany, *A. glutinosa* it is considered to have the deepest roots among indigenous trees (Schmidt-Vogt, 1971).

In the Salløv high-ground site, we found no examples of Holocene aDNA from trees in the oxidized zone, which was probably due to intense weathering of those layers. The aDNA analyses gave evidence that the Fe/Mn-oxide filled root channels (Figure 28 and Figure 67) found in the reduced till pockets in 5-6 m depth in the BB5 and BB6 tracer experiments, were originating from the *Salix* subgroup *Chamaetia/Vetrix*. This suggest that the root channels were likely from the willows *S. caprea* (Seljepil), *S. cinerea* (Gråpil), or *S. myrsinifolia (Sort pil),* which pioneered the open landscape in early post glacial time 11,000-10,000 yr BP (GEUS 2007). As mentioned, the radiocarbon age of the *Salix* aDNA could not be determined accurately due to heterogeneity of the organic carbon in the root channels and matrix in which the aDNA was found (section 3.6.4). However, ages back to early Holocene do not seem unlikely based on (i) only very old radiocarbon ages were determined for the samples (ii) the aDNA patterns were extremely damaged, and (iii) high ages for the root channels were estimated from the accumulation of Fe/Mn-oxides in the channels (section 3.3).

Rooting is known to be highly variable for different tree species, some of which have great ability to adapt to local environment and hydrological conditions (Canadell et al., 1996; Fan et al., 2017; Xi et al., 2018). In general, information of maximum rooting depths is very sparse and uncertain. Canadell et al. (1996) noted that this is due to most of the root biomass occurs within the first 0.5 m in the soil, while only a minimal fraction reaches below that depth. This has led to the assumption that a sufficient understanding of root structures and function can be achived by studying only the upper 0.5 m. Furthermore, the traditionally used technologies to investigate rooting depths have been greatly insufficient (manual digging of trences, road cuts, dynamite, high pressure water). Consequently, tree roots commonly reach far deeper into the

soil than the traditional view has held until recently. Canadell et al. (1996) reported 3.9 ± 0.4 m maximum rooting depth for temperate forest. As mentioned, the investigations were often limited by excavation depths. Overcoming this limitation, Jackson et al. (1999) recorded ecosystem rooting depth in caves of limestone to greater depth than 5 m for at least six North American tree species including Cedar Elm (*U. crassifolia*), and 22 m depth for Texas live Oak (*Q. fusiformis)* in the USA, Texas (humid subtropical climate). Other North American studies have recorded rooting depths to 6-7 m in prairie till soils in eastern Nebraska for a variety of young windbreaker trees (Sprackling et al., 1979).

Among the very few Danish investigations of maximum depths of live tree roots, Holstener-Jørgensen (1959) found roots from Oak, Beech, and Spurce to less than 2 m depth on clayey till soil with shallow groundwater table. In one of the few published recordings from glacial tills outside Denmark, Ruland et al. (1991) reported observations of live roots to 9 m depth in Canadian clayey till. Until more observations become available, similar rooting depths from current and historical trees may be expected possibly also in Danish glacial tills. This is corroborating with the evidence from this study and related previous studies in which connected relic root channel macroprores have been observed from a few meters to more than 5-6 m depth (Klint and Gravesen, 1999; Jørgensen et al., 2002a, 2004a,b, 2017; Butzbach, 2007; Aamand et al. in prep., 2020). In addition to the postdepositional root macropores discussed above, syndepositional root macropores have been reported in thick alluvial aquitards by Timms et al. 2018. Similar root channels penetrating vertically from previous interglacial land surfaces now buried between clayey tills units from older glaciation, may be anticipated to exist locally also in the till aquitards. This was supported by local findings in deep tills of pre-Eemian interglacial organic layers, which were rich in pollen from various trees including e.g., *A. glutinosa* (e.g., Bennike et al., 2018).

Fan et al. (2017) conceptualized that deep rooting from trees is predominantly occurring in topographical elevated settings with relative deep groundwater tables, while rooting is shallow in low-ground places with high groundwater tables. This supported our original hypothesis in the study that groundwater vulnerability in naturally well drained areas (mainly high-ground) would be greater due to deeper root channels, that in originally moist areas (mainly low-ground) where root channels would be absent or very shallow features. Xi et al. (2018) moreover showed that particular deep rooting develops in locations with intense groundwater table fluctuations. This was in agreement with the occurrence of > 6 m deep residual root channels from willows (*Salix* subgroup *Chamaetia/Vetrix*) in the Salløv high-ground E2 site which was coupled with more than 8 m decline of the groundwater table in summer, while by contrast, only about 3 m deep root channels were observed in the other two high-ground E1 and E3 excavation sites where the water tables declined only 2-4 m in summer (Figure 21 and Figure 30). For the low-ground setting, on the contrary, our hypothesis was shown to be invalid by the abundant roots from *A. glutinosas* which were penetrating 1.5- 2 meters below the groundwater table (to 3.2 m depth) in the Bulbro site, and 1-2 m below the groundwater table (to 5 m depth) in the Marebæk site (Jørgensen et al., 2002a). Hence, for Danish conditions the unique ability of *A. glutinosa* to grow roots well below groundwater tables must be anticipated to play a widespread role for the connectivity of macropores into anaerobic groundwater zone due the widespread occurrence of this species now and before.

Hydrologic role of root channels

Subsoil root channels, sometimes with groundwater dripping from them, have been reported from pits in previous studies by e.g., Ruland et al. (1991); Mckay and Fredericia (1995), and Cherry et al. (2006). However, their role as macropore flow paths in tills, and particular inside fractures, have not been investigated before the studies of Jørgensen et al. (2002a, 2004a,b, 2017), and Butzbach (2007). Based on those studies, the current study hypothesized that deep relic root channels would be dominating preferential flow paths in the tills. We found that

relic root channels dominated preferential flow over the fractures, which confirmed the previous studies and hypothesis of this study.

In the Salløv and Bulbro sites, the relic root channels provided dense networks of very rapid macropore flow paths inside the grey fractures or as solitary macropores in the tills to 3-3.5 m depth. As mentioned, in the Salløv site relic root channels actually occurred to > 6 m depth, however, were clogged with Fe/Mn-oxides from about 3.5 m depth, while open root channels along tectonic fractures were found in the field experiments to 5 m depth in the Marebæk site (Jørgensen et al., 2002a) and predecessor PESTPORE field study in Flakkebjerg (Jørgensen et al., 2017).

The same occurrence and depths of rapid flow in relic root macropores (mainly inside fractures), was found in LUC experiments from a number of other clayey till sites investigated with this method. Figure 103 show that Ksat in the LUC experiments containing root channels were 1-4 orders of magnitude higher than in the experiments without containing root channels. This corroborates the current field study in which high saturated flow rates (> 20 m/day) were shown in the BB experiments containing root channels, while very low Ksat values were shown in the BB experiments without occurrence of open root channels (BB0, BB5, and BB8 experiments in Figure 103). The LUC Ksat values in the experiments with root channels followed a decreasing trend over depth due to decreasing root channel frequency in the study sites, which corroberate the observed trend in the current study (Figure 30 and Figure 31).

In the previous Flakkebjerg field study (high-ground), it was shown that vertical fluxes of the pesticides MCPP and Bentazone, were rapidly infiltrated to 4-5 m depth along such root channels. This occurred in root channels in general during build-up of the water table in autumn (Jørgensen et al., 2017), and during winter with high ground water tables in places where the root channels connected with underlying flow regimes with high hydraulic conductivity, such as sand lenses, sand/gravel aquifers and fractures in limestone aquifers (e.g., Jørgensen et al., 2002a, 2017). The same pattern of rapid build-up of high groundwater tables in autumn was observed in the current high ground E2 site. Haria et al. (2002) compared infiltration in a high and low ground limestone area and showed that rapid macropore flow was not activated by strong rainfall in the high ground area with a deep groundwater table due to low moisture content in the matrix, which absorbed infiltration from surplus precipitation. By contrast in the low ground, macropore flow was activated because the matrix was close to saturation due to a higher groundwater tables and capillary fringe near the surface. In the clayey till landscape, similar more frequent activation of root channels as macropore flow paths during summer is likely to occur in many low-ground sites due to typically higher soil moisture content above groundwater tables (e.g., Christiansen et al., 2004). By comparison in the high-ground sites with deep groundwater tables in the tills precipitation surplus is more likely to be absorbed by the matrix (sections 3.1 and 3.6.4). Consequently, pesticide risk and vulnerability due to root channel macropore flow being activated by rain storms in summer is therefore likely often higher in low ground sites.

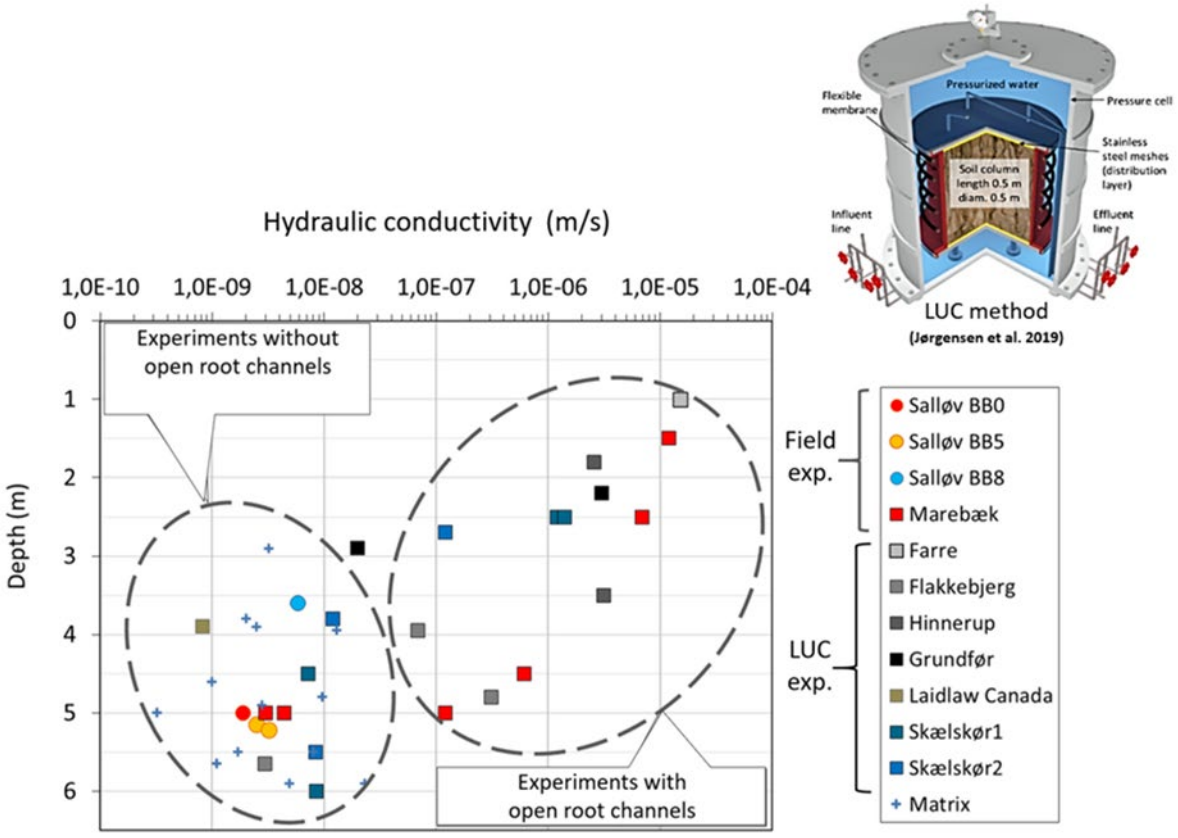

FIGURE 103. Saturated hydraulic conductivity in flow experiments with clayey till with and without flow in root channels. The current BB experiments (Table 17) are compared with 8 other clayey till sites, which were investigated with Large Undisturbed Columns (LUC). LUC data from Jørgensen et al., 1993 (Marebæk); Hinsby et al., 1996 (Skælskør); Jensen et al., 1998, 1999; Jørgensen et al., 1999 (Farre); Jørgensen et al., 1998a, 2002a (Marebæk); Broholm et al., 1999ab (Ringe); O´Hara et al., 2000 (Laidlaw, Canada); Urup, 2000; Jørgensen et al., 2004bc (Hinnerup and Grundfør); Butzbach 2007, (Flakkebjerg); Jørgensen and Spliid, 2016b; Jørgensen et al., 2001, 2016a (Skælskør). Notice logarithmic x-axis.

Despite that most of the tills in the experiments were intensively fractured, Figure 103 shows that the Ksat in the experiments without root channels had low values similar to those of the intact cores of clay matrix without root channels or fractures (collected from the till matrix in the experiments and had Ksat values in the range 10^{-10}- 10^{-8} m/s). This suggest that even intensive fracturing with tectonic fractures played a very minor role for the Ksat values of tills. The same lack of flow in tectonic fractures in tills without root channels was shown in additional LUC experiments by Aamand et al. in prep. (2020).

As mentioned, the relic root channels penetrated to more than 5-6 m depth in Salløv E2 site, Flakkebjerg, and Marebæk sites. In the Salløv site, flow was strongly impeded below 3-3.5 m depth by the clogging of the channels with Fe/Mn-oxides, while the root channels were open throughout in the high-ground PESTPORE Flakkebjerg site as well as in the low-ground Bulbro and Marebæk sites. Hence there appear to be no simple correlation between landscape and depth of open residual root channel macropores. It is unclear, which factors controlled the difference in clogging between the sites, however, the age of the root channels may be one of several factors (see Fe/Mn mass balance age estimates of clogging in Table 8). In conclusion, the LUC and field hydraulic experiments suggests that relic root channels dominate flow in surficial tills in general. Consequently, particularly groundwater risks to pesticide

pollution may be anticipated to exist in areas where the thickness of clay layers above aquifers is smaller than ancient or current rooting depths.

Hydrologic role of fractures

Fractures in clayey tills are widely recognized as governing preferential flow and contaminant pathways in glacial tills (without consideration of possible influence of flow in root channels inside fractures). Some of the natural mechanisms by which fractures are created includes (i) contraction due to drying or freezing (desiccation fractures), (ii) forces from progressing glaciers, and (iii) horizontal stress release from isostatic crustal rebound after melting of ice sheets (Cherry et al. 2006). Mechanisms working to close fracture apertures are (i) increasing *in situ* effective vertical stress with depth, (ii) settlement due to softening and ageing, and (iii) chemical precipitation in fractures (Allred 2000).

The hypothesis in this study was that fractures in subsoils, which are not enlarged by root channels inside, are largely closed. The BB experiments supported this hypothesis by showing that (i) below 1-2 m depth, rapid flow in the tectonic fractures was limited to the root channel macropores inside the shallow grey fractures, (ii) flow was greatly impeded in Fe/Mn-oxide filled red fractures occurring underneath the grey fractures, and (iii) flow was not observed in deeper non-visible ghost fractures.

Figure 104 compare the fracture hydraulic apertures (2b) determined from the current BB field experiments (Table 16) with the LUC experiments from the same 8 sites as were shown in Figure 103.

Figure 104A show that the LUC fractures with root channels inside had large hydraulic apertures in the range 40-170 µm. Those apertures resembled the fractures with abundant root channels inside in the Salløv and Bulbro sites in which observed saturated flow rates were > 20 m/day. In great contrast, the LUC fractures which were not enlarged by root channels had consistently very small apertures in the range 2b = 5-14 µm. This agreed with the apertures in the fractures with no root channels (or only containing root channels clogged with Fe/Mn-oxides) in the current BB field experiments, which exhibited very small hydraulic apertures (2b = 3-10 µm). Those results were furthermore in agreement with additional LUC experiments from the E2 Salløv excavation and Holbæk by Aamand et al. in prep. (2020).

Flow-through hydraulic experiments with conservative tracers in the LUC´s showed that the migration of the tracers in samples with the small aperture fractures (< 10 µm resembling the Salløv BB0-BB8 hydraulic apertures), was very slow and only marginally increased over the migration in the unfractured clay matrix (Aamand et al. in prep. (2020) and Jørgensen et al. in. prep.(2020). This corroborates the modelling of the BB5 experiment by Thalund-Hansen (2018), which showed vertical migration of 1 m/year along the 10 µm aperture fractures that contained Fe/Mn clogged root channels (Table 16), while the migration in the unfractured matrix can be estimated to approximately 0.5-2.3 m/year by Darcy flux calculations based on Aamand et al. in prep. (2020) and matrix Ksat values for the till shown in Table 1. Similarly, low rates of transport were observed for tracers and the pesticides mecoprop (MCPP), metsulfuron (mobile), and prochloraz (strongly adsorbed) along Fe/Mn filled fractures (2b= 12-14 µm) in the field experiment by Jørgensen et al. (2002a). Hence the small fractures without root channels, or only with clogged root channel inside, were not or only marginally increasing vertical tracer migration in the experiments. Those results were consistent with the field experiments obtained in the PESTPORE study by Jørgensen et al. (2017) in which groundwater flow and migration of infiltrated dye tracer and pesticides were absent in the deep tectonic fractures without distinct root channels inside.

In great contrast, the fractures with large root channel apertures provided several orders of magnitude higher water and pesticide fluxes in the LUC and field experiments (Jørgensen et al. 1998a, 2002a, 2017, and Mosthaft et al. 2020 in review), which is due to flow in the fractures varies with the aperture in 3. power (Snow, 1968; Witherspoon et al., 1980). This emphasizes further that places with smaller thickness of the clay layers above aquifers than ancient or current rooting depths, are settings with particularly groundwater risks. Below those depths Cherry et al. (2006) suggested the existence of widely spaced invisible fractures ("ghost fractures") with large apertures. We identified such ghost fractures (section 3.4), however, as mentioned we have found no evidence of active preferential flow along those in the dye tracer experiments in this (e.g., Figure 104) or the previous field studies (Jørgensen et al. 2002a, 2017). This is in accordance with experiments by Aamand et al. in prep. (2020), which showed that small fracture apertures obtained from 3.4-5.9 m depth in Salløv excavation E2 were closing when they were exposed to increasing effective soil stress in LUC experiments that resembled greater soil depth than tested in Figure 104.

Figure 104B show that in addition to increasing vertical soil stress, the closure of fractures was to a high degree controlled by clogging due to chemical precipitation of Fe/Mn in the fractures (red fractures). In the Salløv site, the clogging of the fractures and root channels occurred from ca. 3-3.5 m depth and created a hydrologic barrier in which preferential flow along the fractures and root channels was greatly impeded. This caused several orders of magnitude decline in bulk-hydraulic conductivity of the till, which was very close to that of the uncompromised clay (Figure 103 and Table 17).

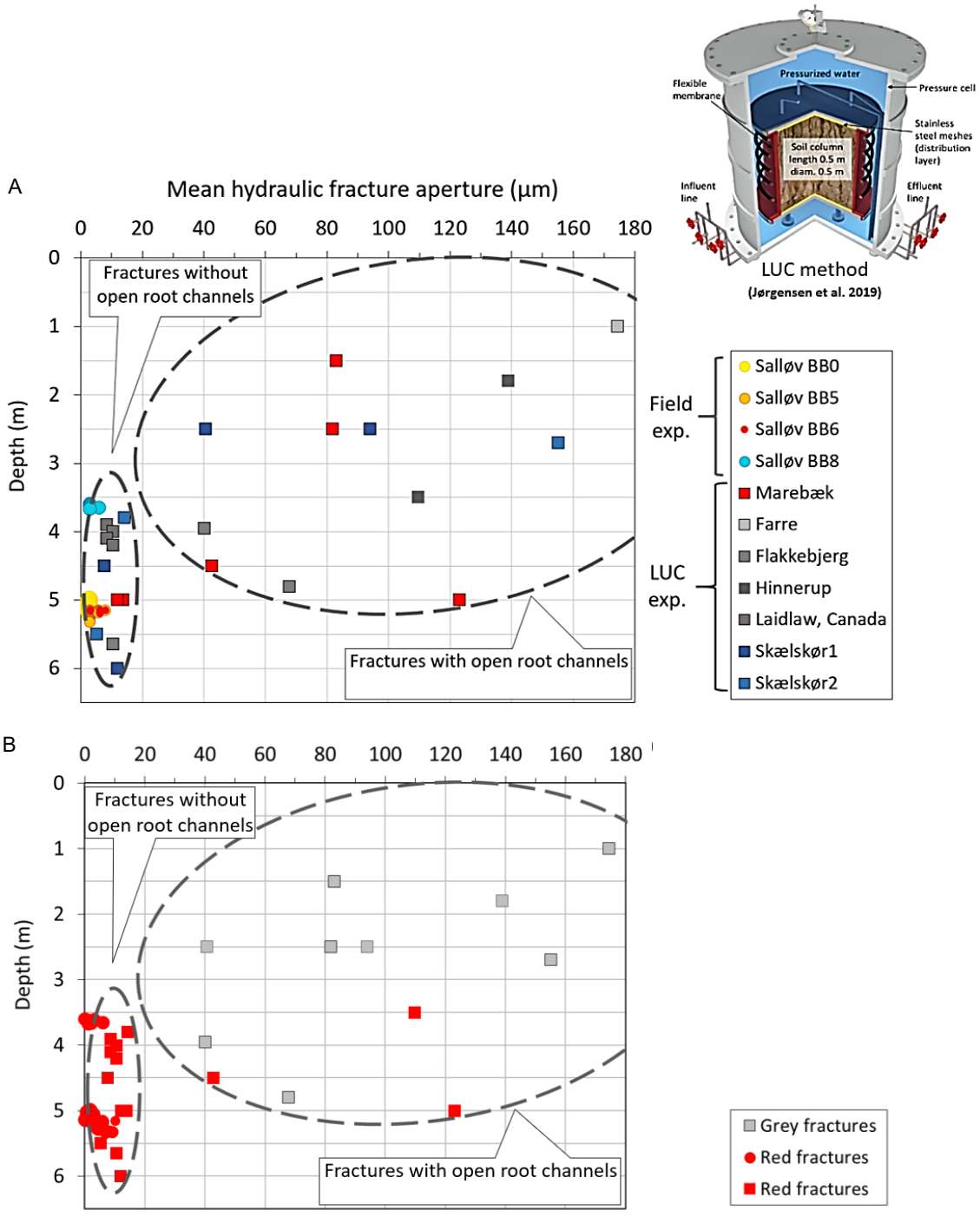

FIGURE 104. Mean hydraulic fracture aperture in fractures with and without root channels inside. The results from the current BB experiments (Table 16) are compared with 8 other clayey till sites, which were investigated with Large Undisturbed Columns (LUC). (A) Values shown for locations. (B) Distribution of values between gray and red fractures. LUC data from Jørgensen et al., 1993 (Marebæk); Hinsby et al., 1996 (Skælskør); Jensen et al., 1998, 1999; Jørgensen et al., 1999 (Farre); Jørgensen et al., 1998a, 2002a (Marebæk); Broholm et al., 1999ab (Ringe); O´Hara et al., 2000 (Laidlaw, Canada); Urup, 2000; Jørgensen et al., 2004bc (Hinnerup and Grundfør); Butzbach, 2007 (Flakkebjerg); Jørgensen and Spliid, 2016b; Jørgensen et

al. 2001, 2016a (Skælskør). Notice, that flow in the fractures varies with the fracture aperture in 3. power.

This barrier created the local perched water tables and reduced groundwater recharge and vulnerability nearby Well 1 and Well 3, (Figure 21).

Figure 104A suggest that similar barriers may be developed in clayey tills in general from the occurrence of Fe/Mn-oxide clogging of red fractures in most of the sites shown in Figure 104B. McKay et al. (2005) showed occurrence of similar developed hydrological barriers in saprolite soils, which diverted shallow groundwater flow laterally and downslope in the landscapes (McKay et al.m 2000). This is likely also an important factor in clayey tills which may potentially redistribute groundwater and leached pesticides significantly in the landscape, e.g., on the edge of the hill slope in the high-ground E3 location (Figure 18 and Figure 21).

Figure 104B show that in some places, the clogging of the red fractures was interrupted by open root channels despite of the Fe/Mn precipitation in the fractures (e.g., Marebæk and Hinnerup). This interrupted the barrier and consequently caused the vertical infiltration into the underlying ground water to changed unpredictably within short range (see also Rivad et al., 2001), which would be difficult to capture with monitoring wells (Jørgensen et al., 2003a). In the Salløv site, the barrier was additionally interrupted by sand lenses, which is discussed in the section below.

In conclusion, the current study provides growing evidence that fractures without root macropores inside are closing with depth and have very small apertures and only marginally influences solute transport below 1-2 m depth unless they contain open root channel macropores. This suggests that fractures have minor or no importance to groundwater risk underneath the depth of historic or current root macropores, where other types of inherent sedimentary heterogeneity in the tills are suggested to played a more important role. Further testing of this evidence would be relevant in early warning sites - VAP sites (GEUS, 2001) and Vendsyssel in Nordjylland, the latter because this part of Denmark has experienced the highest crustal isostatic rebound after retreat of the glaciers from the last ice age and therefore will be most susceptible to opening of deep fractures.

Sand layers and other sedimentary heterogenities

Interbedded sand layers between till units and sand lenses, micro-sandlayers, sand pockets, and other sedimentary heterogeneities with different size, shapes and orientation in individual till units are widespread in Danish glacial tills (e.g., Houmark-Nielsen 1994, Andersen and Pedersen 1998, Kessler et al. 2013, and Aamand et al. in prep., 2020). As mentioned, the hydrologic barrier, which was developed in the Salløv site was interrupted by such random embedded sand lenses. Those caused alternating perched and leaky aquitard conditions local increase vertical hydraulic conductivity in the aquitard, and supposedly, increase of vulnerability of the underlying groundwater (section 3.5.3). This corroborates with studies by Haldorsen and Krüger (1990) who showed that the textual heterogeneities of the till diamicton material can cause several orders of increase in till bulk-hydraulic conductivity. They describe that lodgement tills are typically the densest and least heterogenous till types, while melt-out tills and hummocky tills are more heterogenous, and consequently in general are anticipated to exhibit higher hydraulic conductivities. The most developed heterogeneity would be expected in terminal moraines in which multiple sub-vertical sand layers is a dominating lithofacies (e.g., Milthers 1935). Despite the lodgment tills, according to Haldorsen and Krüger (1990), are the least heterogenous till types, many heterogeneities occurred in both the high and low-ground site in the study (Figure 2).

Reinterpretation of fractures being cause to elevated hydraulic conductivities in deep aquitards

The recognition of fractures as major flow paths in unweathered clayey tills was based on studies of North American tills (e.g., Cherry 1989, Ruland et al. 1991, Cherry et al. 2006). Those studies used conventional hydrological field methods such as pumping tests. They revealed rapid internal hydraulic head responses in the aquitards to the pumping, which were attributed to flow in open fractures. Based on this, it was concluded that fractures were the most likely explanation to the common occurrence of 2 or more orders of magnitude higher hydraulic conductivities of the bulk till aquitards, than for the unfractured clay matrix material of the aquitards (e.g., Cherry et al., 2006). This conclusion was further supported by the wide occurrence of prominent fractures in ecavations and borings to approximately 10 m depth and groundwater dripping from some of the fractures. Furthermore, non-visible fractures (ghost fractures) were suggested to occur with large apertures to even greater depth (Cherry 1989, Cherry et al. 2006). In some of the studies sand lenses were also observed but disregarded as interconnected flow paths in the aquitards (e.g., Cherry 1989, Ruland et al. 1991, McKay & Fredericia 1995).

Prominent fractures were also described in Danish clayey tills by Fredericia (1990), Jørgensen (1990), and Jørgensen and Fredericia,1992. Additionally, Fredericia (1990) showed that the bulk hydraulic conductivities (Ksat) in unweathered aquitards were up to 1-3 orders of magnitude higher than in samples of unfractured clayey matrix from the aquitards (Figure 105). As with the North American studies (Cherry et al. 2006), those observations were interpreted to be the result of active flow in deep fractures.

Since the early studies, a considerable number of direct determinations of flow in fractures have been provided by recent field and the LUC studies, some of which were summarized in Figure 104. Utilizing those newer data, Figure 105 evaluates the interpretations of Frederica (1990) by comparing the observed Ksat values for the aquitards given in the Fredericia (1990) study with corresponding Ksat values calculated for the clay matrix samples, also given by Fredericia (1990), however, with added flow in fractures (imaginary) corresponding to the fractures without internal root channels in Figure104. Hereby, it was tested to what degree the fracture apertures for the fractures without root channels inside can actually explain the observed 1-3 orders of magnitude higher Ksat values of the aquitards than for the aquitard matrix samples. The calculations were carried out using the approach of McKay et al. (1993a) in which the aquitard Ksat = $2b/2B * K_{fracture} + K_{matrix,}$ where 2b = fracture hydraulic aperture (5 µm and 14 µm representing the range of apertures > 0 µm for the fractures without root channels in Figure 104), 2B = fractures spacing (0.5 and 2 m, which represents the range of fracture spacings observed for deep fractures in 32 field excavations across Denmark (GEUS (2014)), $K_{fractures}$ = hydraulic conductivity of fractures (values for fractures without root channels in Table 26), and K_{matrix} = hydraulic conductivity of the matrix (the clay matrix test values from Fredericia (1990) in Figure 105).

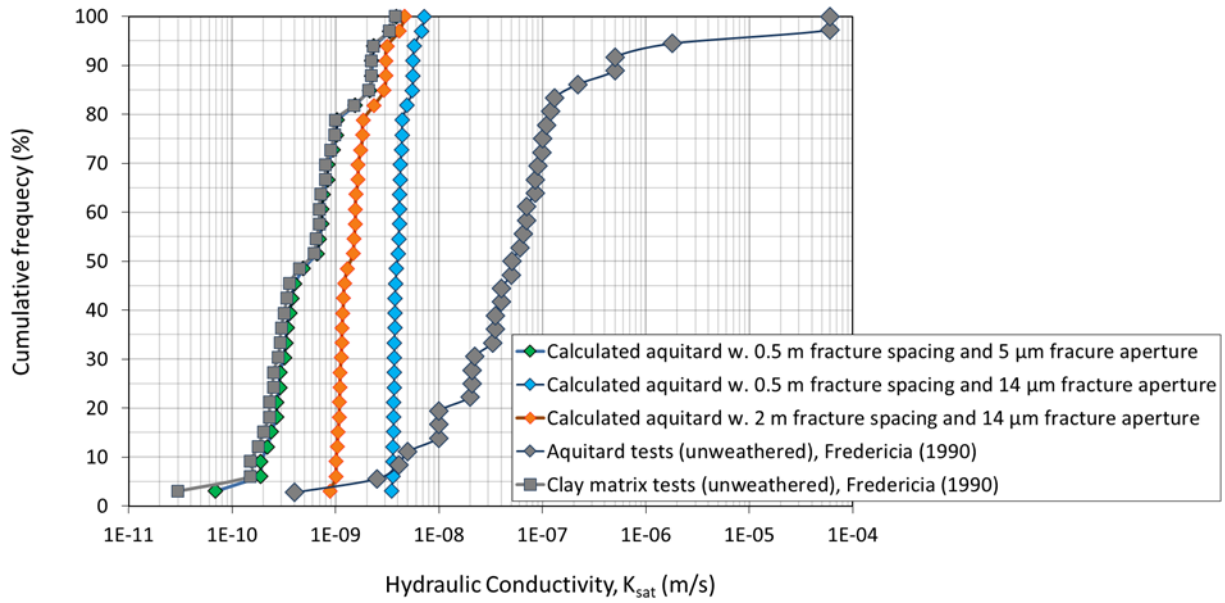

FIGURE 105. Field tested aquitard hydraulic conductivities (Ksat) compared with calculated aquitard Ksat values based on fracture apertures from the BB and LUC experiments in Figure 104. The calculated values show the increase of Ksat over the matrix ("clay matrix tests") by adding flow to those values from fractures with the maximum aperture (5 and 14 µm) for the fractures without enhancement by root channels in Figure 104. The comparison suggest that fractures below assumed depth of root channels, can only explain a minor percentage of the observed aquitard bulk hydraulic conductivities above approximately 10^{-8} m/s (630 mm/yr).

Notice here, that fracture apertures tend to close with greater depth than tested with the LUC and field experiments in Figure 104 (Aamand et al. in prep., 2002). This suggests that the calculated aperture scenario with 14 µm in Figure 105 is likely exaggerating possible fracture contributions in deep unweathered aquitards, while the 5 µm scenario is probably more realistic. Nonetheless, the calculations imply that other geological features with higher flow capacity than fractures in unweathered aquitards are controlling flow in order to explain the high Ksat., which also corroborates the influence of sandlenses in the BB field experiments (Table 17).

This emphasizes the possible role of embedded sand lenses and other sedimentary heterogeneity as those described by Haldorsen and Krüger (1990) and others. Many of those may not be interconnected flow paths throughout aquitards as indicated in the E1 and E3 high-ground examples, and in many of the North American glaciolacustrine tills. However, the general high frequency of sub-horizontal and tectonically inclined sandlayers and lenses in the Danish tills shown by e.g., Houmark-Nielsen (1994), Andersen and Pedersen (1998), Kessler et al. (2913), and Aamand et al. in prep. (2020), makes it probably that those are forming interconnected flow paths through the tills into underlying groundwater in many locations like the local leaky aquitard conditions in E2 (well 2 in Figure 21).

In groundwater catchments with downward flow such aquitard areas with high vertical connected hydraulic conductivity will often manifest themselves as areas with the highest groundwater recharge into aquifers. Jørgensen et al (2004a) showed that vertical connected sand lenses or layers may provide similar pesticide mass flow as large aperture fractures and will greatly enhance pesticide vulnerability of underlying aquifers in the areas with high-groundwater recharge. The recharge and consequently groundwater vulnerability in such areas and locations may be further enlarged in cases where hydraulic heads in underlying aquifers have been lowered by intensive water abstraction, such as in the current study area (Chapter 1) and

e.g., the Copenhagen region. The role of fractures and lithological heterogeneity to groundwater vulnerability for various pesticides in different till types and textures is further evaluated by e.g., Jørgensen et al. (2016a, b), and Aamand et al. in prep. (2020).

Pesticide vulnerability of groundwater

Harrison et al. (1992), showed that widely spaced fractures in idealized homogenic clay with a the low Ksat value of 10^{-10} m/s can cause degradation of water quality in underlying aquifers even for fractures with apertures as small as 10 µm (corresponding to the fractures without root enhancement in Figure 104). However, as mentioned above, matrix hydraulic conductivity in natural aquitards, and in particular in the Danish, varies several order of magnitude (Table 1, and Figure 103) and contains coarse-grained heterogeneities which may significantly increase the hydraulic conductivity of the matrix domain even further (Figure 68 and Figure 105). Figure 106 describes such situations by showing simulated pesticide breakthrough and fluxes resulting from fully penetrating vertical fractures through a 5 m thick aquitard into an aquifer, when varying the aquitard clay matrix Ksat values from 10^{-10} to 10^{-8} m/s (3-315 mm/yr) in order to represent the natural heterogeneity of the matrix domain (Table 1 and Figure 103).

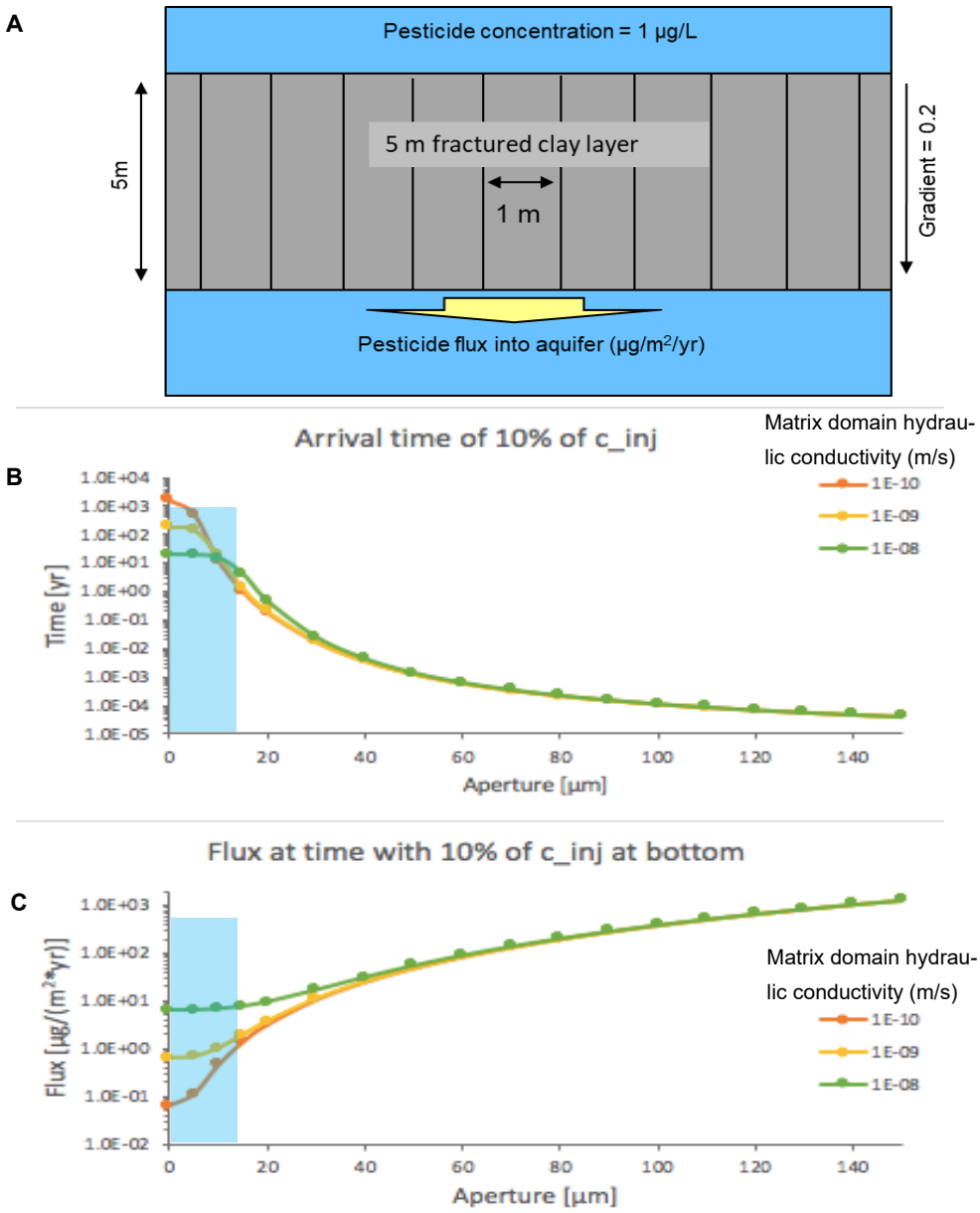

FIGURE 106. Simulated breakthrough times and flux values of pesticide into an aquifer underneath 5 m fractured clay when 10% of the infiltrated pesticide concentration (1µg/L) breaks through into the aquifer (from Aamand et al. in prep., 2020). The impact is shown as function of the fracture's apertures presented in Figure 104 and as function of matrix domain hydraulic conductivity. The pesticide is not degraded or adsorbed. Blue shaded area represents fractures without root channels inside. (A) vertical section of model domain. (B) Arrival time in aquifer of 10% of infiltrated concentration. (C) Pesticide flux into aquifer at time with 10% of infiltrated concentration.

The simulations describe preferential flow in the fractures, and idealized piston flow in the aquitard matrix domain and assume unlimited water supply to the fractures and free drainage into the underlying aquifer.

Figure 106 show that the large fracture apertures representing fractures which are enhanced by root channels (fracture apertures from 40 µm to 150 µm in Figure 104) can completely dominate pesticide transport and provide very high pesticide fluxes in places where they are

connected and well-drained into underlying flow regimes with high hydraulic conductivity (Table 27) such as very coarse-grained embedded layers or aquifers, or fractures in limestone aquifers. This was confirmed in the BB and pesticide experiments in this and previous studies (Jørgensen et al. 2002a, 2017).

For smaller apertures, the simulations show that pesticide breakthrough times and fluxes are under influence of the flow in the till matrix Ksat when the fracture apertures are below ca. 30 µm. This is due to the pesticide flux in the matrix exceeds and therefore obliterates the pesticide flux from the small aperture fractures. Consequently, at small fracture apertures the pesticide flux is controlled by the matrix flow and not by the fractures, which has major implications to the role of fractures below rooting depths for which the fracture apertures are supposedly in the range 0-14 µm (Figure 104 and shaded area in Figure 106). Hence, specifically for the fractures without root channel enlargements, the simulations in Figure 106 suggest that those fractures are not affecting breakthrough times, or increasing pesticide fluxes, in aquitards with hydraulic conductivities about 10^{-8} m/s or more.

Thus, the simulations suggest that fractures generally do not affect pesticide vulnerability of groundwater underneath aquitards with Ksat values above 10^{-8} m/s provided they are below maximum historic or current rooting depths. For aquitards and matrix domains with Ksat < 10^{-8} m/s, breakthrough times for the same small fracture apertures are up to a factor of 5 quicker than with matrix Ksat = 10^{-8} m/s. In such cases where degradation of pesticides is occurring in the aquitard layer, the shorter residence time in the aquitard would mean less removal of the pesticide in the aquitard and consequently greater pesticide impact and vulnerability of underlying groundwater. However, the shorter residence time caused by the fractures is a product of the simplifying piston flow approach used for the modeling of the matrix flow, which does not take into account that the matrix domain typically contains embedded sand lenses and other textural heterogeneity that, when interconnected may provide similar rapid transport as widely spaced large open fractures (Jørgensen et al. 2004a). This show that ranking degrees of aquifer vulnerabilities below rooting depth from Figure 106 depends on the assumptions and premises being used for the contaminant compound.

Gimsing et al. (2019) distinguished between “inherent” and “specific” vulnerability. The former includes geohydrological factors such as precipitation and hydraulic conductivity of soil layers, the latter also take into account pesticide properties such as sorption and degradation. In the case of subsoils and groundwater, pesticide degradation is low or absent (e.g., Miljøstyrelsen 2005, Aamand et al. in prep., 2020), which means it cannot be safely relied upon as pesticide attenuating process. Consequently, the inherent vulnerability needs to be the better criterion for pointing out particular vulnerable areas for the subsoil domain. Also, more or less rapid pesticide breakthrough into the groundwater is not a feasible criterion for vulnerability because sustainability is a mandatory requirement for the groundwater quality, *i.e.,* unpolluted groundwater should also be available for future generations. Hence ranging pesticide vulnerabilities from Figure 106 is most relevant if based on differences between the pesticide fluxes in the simulations, *i.e.,* differences in pesticide mass transfer pr. time unit into aquifers (Figure 106c).

Using this criterion, the simulations in Figure 106 suggests that below rooting depth i.e., the domain where fracture apertures 2b = 0-14 µm, the groundwater is most vulnerable underneath the aquitards with the highest Ksat in the matrix domain (and therefore with the highest bulk-Ksat). This is because those are contributing with the highest pesticide mass fluxes into the aquifer. Those are aquitards in which Ksat equals or are above 10^{-8} m/s for the matrix domain in Figure 106, which are equivalent to the aquitards with Ksat > 10^{-8} m/s in Figure 105. Moreover, Figure 106 show that the small fractures will only influence pesticide vulnerability significantly in the least vulnerable aquitards (Ksat < 10^{-8}), while they will have minor or no influence on pesticide breakthrough times and fluxes in the most vulnerable aquitards. Adding pesticide degradation to the simulations was shown to increase this contrast of vulnerability

even further because degradation is intertwined with diffusion of pesticides from the preferential flow path into the matrix, which further attenuates pesticide migration strongly in the fractures, particularly in fractures with small apertures (Jørgensen et al. 2004c).

Upscaling those results to groundwater catchments, suggest that aquitard areas with large groundwater recharge through the aquitards into underlying aquifers, represents the most vulnerable areas. This corroborates modeling studies by Jørgensen et al. (2004c) and Blessent et al. (2014), which indicated that groundwater vulnerability in groundwater chatchments (expressed as pesticide fluxes into aquifers through fractures or embedded sand layers) will vary orders of magnitude as function of the distribution of aquifer recharge and redox conditions, even if the aquitard thickness in the groundwater catchments is relatively constant. As indicated from the current study, the groundwater vulnerability is suggested to be further increased in areas with small aquitard thickness in which case rapid flow in deep root channel systems may connect directly into underlying aquifers.

Hence differences in aquitard thickness and amount of groundwater recharge in combination are suggested to represent useful key parameters for pointing out areas with overall contrasting groundwater vulnerability without detailed knowledge about differences and location of geological heterogeneity in the aquitards. This was supported by studies of the distribution of environmental tracers (CFC gases) in a regional aquifer by Jørgensen et al. 2003b in which the CFC in water supply wells could be predicted using the modeling approached by Jørgensen et al. 2004c and extended by Stenemo et al. 2005. By using the same approach, the observed concentrations of 2,6-dichlorobenzamid (BAM) were predicted in a clayey till groundwater catchment by Miljøstyrelsen (2005). This approach was also used to successfully predict the overall progression of BAM pollution in groundwater underneath till aquitards by Miljøstyrelsen (2002).

The distribution of aquitard thickness and aquifer recharge has been mapped in many clayey till areas in the national groundwater mapping using geological/geophysical mapping and catchment water balance modeling (Miljøstyrelsen 2020). This suggests that existing data may be utilized or further developed to point out overall clayey till areas with particular aquifer vulnerability to pesticide pollution. Currently such an approach will be limited by absence of info about the local scale variability of aquitard hydraulic conductivity observed in the current and the previous field studies mentioned. More research will be required to provide this level of detail.

5. References

Aamand J., N. Badawi, P. R. Jakobsen, P. R. Jørgensen, K. Mosthaf, L. Troldborg, M. Rolle. Clayfrac project: Mapping groundwater vulnerability to pesticide contamination through fractured clays. Danish Ministry of Environment (in prep., 2020).

Allred, B.J. Survey of fractured glacial till geotechnical characteristics: Hydraulic conductivity, consolidation, and shear strength. Ohio Journ. of Science. V.199, n3-4 (2000).

Andersen, S., S.S Pedersen. Israndslinjer I Norden. TemaNord 1998:584. Nordisk Ministerråd, København (1998).

Bennike, O, L. Hedenäs, K. High, J.S. Korshøj, G. Lemdahl, K. Penkman, R. Preece, K. Rosenlund,

F. A. Viehberg. New interglacial deposits from Copenhagen, Denmark: marine Isotope Stage 7 Boreas. 2018. https://doi.org/10.1111/bor.12342.

Bienert, F., De Danieli, S., Miquel, C., Coissac, E., Poillot, C., Brun, J.-J., & Taberlet, P. (2012). Tracking earthworm communities from soil DNA. Molecular Ecology, 21, 2017–2030. doi: 10.1111/j.1365-294X. 2011.05407.x

Blessent D., P.R. Jørgensen, R. Therrien. Comparing Discrete Fracture and Continuum Models to Predict Contaminant Transport in Fractured Porous Media. Groundwater, 84-95 (2014).

Broholm K., Jørgensen P.R., Hansen A.B., Arvin E., Hansen M. Transport of creosote compounds in a large, intact macroporous clayey till column. Jour. Contamn. Hydrol. 39, 309-329 (1999).

Bronk Ramsey, C. Bayesian analysis of radiocarbon dates. Radiocarbon 51, 337-360. (2009).

Butzbach K. Description of transport mechanisms and hydraulic parameters in fractured glacial till from Flakkebjerg using column experiments. (Master Thesis). Geological Institute, University of Copenhagen, Denmark (2007).

Canadell J., Jackson, Ehleringer J.R., Mooney M.A., Sala-E. O.E., Schulze D. Maximum rooting depth of vegetation types at the global scale. Oecologia. 108. 583-595. (1996).

Carøe, C., Gopalakrishnan, S., Vinner, L., Mak, S.S.T., Sinding, M.H.S., Samaniego, J.A., Wales, N., Sicheritz-Pontén, T., Gilbert, M.T.P. (2018). Single-tube library preparation for degraded DNA. Methods Ecol Evol. 9:410–419. doi: 10.1111/2041-210X.12871

Cherry J.A., B.L. Parker, K.K. Bradbury, T.T. Eaton, M.B. Gotkowitz, D.J. Hart, M.A. Borchardt.Contaminant transport through Aquitards: A-State-of-the-Science Review. Awwa Research Foundation, American Water Works Association, IWA publishing. p.126. (2006).

Cherry, J.A., (1989). Hydrogeological contaminant behaviour in fractured and unfractured clayey deposits in Canada. In: Contaminant transport in groundwater, Kobus V., and Kinzelbach W., (eds) Balkema Rotterdam. 11–20.

Christiansen, J.S., M. Thorsen, T. Clausen, S. Hansen, J.C. Refsgaard. Modelling of macropore flow and transport processes at catchment scale. Journal of Hydrology 299 (2004) 136–158.

Chuoke, R.L., P van Meurs, and C. van der Poel. The instability of slow, immiscible, viscous liquid-liquid displacements in permeable media, Trans. Am. Inst. Min. Metall. Pet. Eng..m, 216,188-194, 1959.

D'Astous A.Y., Ruland W.W. , Bruce J.R.G. , Cherry J.A. , and Gillham R.W. (1989). Fracture effects in the shallow-groundwater zone in weathered Sarnia-area clay. Canadian Geotechnical Journal, 26(1): 43-56.

Ernstsen V. Clay minerals of clayey subsoils of Weichselian Age in the Zealand-Funen area, Denmark. Bulletin of the Geological Society of Denmark, Vol. 45/1, pp. 39-51.

Fan, Y., F., G. Miguez-Machob, E.G. Jobbágyc, R. B. Jackson, C. Otero-Casalb. Hydrologic regulation of plant rooting depth. PNAS, vol. 114, no. 40. 10572–10577, (2017).

Flury, M., Flühler, M. Tracer characteristics of Brilliant Blue FCF. Soil science society of America. 59 (1). 22-27 (1995).
Fredericia J. Saturated Hydraulic Conductivity of Clayey Tills and the Role of Fractures. Nordic Hydrology, 21, (1990), 119-132.
Funk, D.T. (1990). European alder. In: Burns, Russell M., and Barbara H. Honkala. (Eds.) "Silvics of North America: Vol. 2. Hardwoods Agriculture Handbook 654." US Department of Agriculture, Forest Service, Washington, DC. pp. 105-115. www.srs.fs.usda.gov/pubs/misc/ag_654/volume_2/A./glutinosa.htm
GEUS 2001. Etableringsrapport for VAP. The Danish Pesticide Leaching Assessment Programme. Site Characterization and Monitoring Design.
GEUS 2005. De seneste 150.000 år Istidslandskabet og naturens udvikling. Houmark-Nielsen N., J. Krüger, K.H. Kjær. Geoviden, geologi og geografi nr.2. GEUS 2005.
GEUS 2007. Landskabets udvikling i Danmark. Geoviden, geologi og geografi nr.1. GEUS 2007.
GEUS 2014. Vurdering af mulighederne for udpegning af pesticidfølsomme leromåder (SFOler) på grundlag af eksisterende data. Gravesen P, IM Balling, G Vignol, KES Klint, W Brüsch, B Nilsson, CL Larsen, R Juhler, AE Rosenbom. 2014.. Udarbejdet for Naturstyrelsen. GEUS rapport nr 2.
GEUS 2019 Grundvandsovervågning Status og udvikling 1989 – 2017 GEUS (2019).
Ginolhac, A., Rasmussen, M., Gilbert, M. T. P., Willerslev, E. & Orlando, L. mapDamage: Testing for damage patterns in ancient DNA sequences. Bioinformatics 27, 2153–2155 (2011).
Gimsing, A. L. et al. Conducting groundwater monitoring studies in Europe for pesticide active substances and their metabolites in the context of Regulation (EC) 1107/2009. *Journal of Consumer Protection and Food Safety* volume 14, pages 1–93 (2019).
Gryta, H., Paer, C. Van De & Manzi, S. Genome skimming and plastid microsatellite profiling of alder trees (*A.* spp., Betulaceae): phylogenetic and phylogeographical prospects. (2017).
Haldorsen S., and J. Krûger. Till genesis and hydrogeological properties. Nordic Hydroloy 21, 1990, 81-94.
Hansen, S., Abrahamsen, P., Petersen, C.T., and Styczen, M. Daisy: Model Use, Calibration and Validation. (2012a). Transactions of the ASABE 55(4), 1315-1333, doi: 10.13031/2013.42244.
Hansen S., Petersen C.T., Mollerup M., Abrahamsen P., Gjettermann B., Nielsen M.H., Styczen M., Poulsen R., Lørup J.K., Yamagata K., Butts M. (2012b). Flerdimensional modellering af vandstrømning og stoftransport i de øverste 1-2m af jorden i systemer med markdræn. Bekæmpelsesmiddelforskning fra Miljøstyrelsen nr. 138. 276 sider.
Haria H. A, Hodnett M.G., Johnson A.C. Mechanisms of groundwater recharge and pesticide prenetration to a chalk aquifer in southern England. Jour. of Hydrology. 275 (2003), 122-137.
Harrar W., L.C. Murdoch, B. Nilsson, and K.E.S Klint. Field characterization of vertical bromide transport in a fractured glacial till. Hydrogeology Journal (2007) DOI 10.1007/s10040-007-0198-5.
Harrar W., and B. Nilsson. Karakterisering af 3-D strømning og transport i sprækket moræneler: Design af systemer til grundvandsmonitering. I: Sprækker i moræneler - hvordan den nye viden kan anvendes. 8. maj 2001. Geocenter København. (2001).
Harrison, B., Sudicky, E.A. and Cherry, J.A. Numerical analysis of solute migration through fractured clayey deposits into underlying aquifers. Water Resources Research 28: doi: 10.1029/91WR02559. issn: 0043-1397 (1992).
Havrdova, A., Douda, J. & Mandak, B. Higher genetic diversity in recolonized areas than in refugia of A. glutinosa triggered by continent-wide lineage admixture. Mol. Ecol. 24, 4759–4777 (2015).
Richard W. H., and P.G. Cook. Using groundwater levels to estimate recharge. Hydrogeology Journal (2002) 10:91–109.
Hildebrandt S. Et sammenligningsstudie mellem recente og relikte bundmoræneIandskaber på Island og i Danmark. Specialerapport. Geologisk Institut Maj 2000.

Hinsby, K., McKay L.D., Jørgensen P.R., Lenczewski M., Gerba C.P. Fracture aperture Measurements and Migration of Solutes, and Immiscible Creosote in a Column of Clay-Rich Till.Groundwater 3, 34(6), 1996, 1065-1075. (1996).

Holstener-Jørgensen H. (1959). Undersøgelser af rodsystemer hos eg, bøg og rødgran på grundvandspåvirket morænejord med et bidrag til belysning af bevoksningens vandforbrug. Det forstlige forsøgsvæsen. 25. 1958-1959. 225-290.

Homsy G.M. Viscous fingering in porous media. Ann. rev. fluid mech. 1987, (19) 271-311.

Houmark-Nielsen, M.: Late Pleistocene stratigraphy, environmental history and Middle Weichselian glaciation chronology from Klintholm, Møn, Denmark. Bulletin of the Geological Society of Denmark, Vol 41, pp. 181-202. Copenhagen, 1994.

Jackson R. B., L. A. Moore, W. A. Hoffmann, W. T. Pockman, and C. R. Linder. Ecosystem rooting depth determined with caves and DNA. Proc. Natl. Acad. Sci. USA Vol. 96, pp. 11387–11392, September 1999

Jackson, M., Myrholm, C., Shaw, C., & Ramsfield, T. (2017). Using nested PCR to improve detection of earthworm eDNA in Canada. Soil Biology and Biochemistry, 113(Supplement C), 215-218. doi: 10.1016/j.soilbio.2017.06.009

James, S. W., Porco, D., Decaëns, T., Richard, B., Rougerie, R., & Erséus, C. (2010). DNA Barcoding Reveals Cryptic Diversity in Lumbricus terrestris L., 1758 (Clitellata): Resurrection of *L. herculeus* (Savigny, 1826). PLoS ONE, 5(12), e15629. doi: 10.1371/journal.pone.0015629

Jensen J. Danmarks oldtid: Fra stenalder til vikingetid. 1146 p. Gyldensdal A/S (2013).

Jensen, M.B, Jørgensen P.R, Hansen H.C.B, Nielsen N.E. Biopore mediated subsurface transport of dissolved orthophosphate. Jour. Envir. Qual. 27, sept-oct. (1998)

Jensen, M.B., Hansen H.C.B., Jørgensen P.R., Magid J. Subsurface transport of phosphate in structured soil - a two step process. Nordic Hydrol., 30(4/5), 361-378. (1999).

Jørgensen P.R. Spredning af forurening i moræneler. Miljørapport 155. Danish Ministry of Environment (1990).

Jørgensen, P.R, Fredericia J. Migration of nutrients, pesticides and heavy-metals in fractured clayey till. Geotechnique 42: 67-77. (1992).

Jørgensen, P.R., Spliid N.H. Mechanisms and rates of pesticide leaching in shallow clayey till. In: Integrated soil and sediment research: A basis for proper protection. Eds. H.J.P. Eijsackers & Harmers. p.247-253. Kluwer Academic Publishers. (1993).

Jørgensen, P.R., L.D. McKay and N.H. Spliid. Evaluation of chloride and pesticide transport in a fractured clayey till using large undisturbed columns and numerical modeling. Water Resour. Res., 34 (4), 539-553. (1998a).

Jørgensen P.R., Felding, G. Helweg A., Spliid N.H., Thorsen M., Refsgaard J.C. & Jacobsen O.H. Validation and Development of Pesticide Leaching Models. Pesticides Research, 47, Danish Ministry of Environment (1999).

Jørgensen P.R., Spliid N. H., Hansen M., Harrar W., Lindgreen, H. Outzen, S. Brehmer A. Point and Non-point Source Leaching of Pesticides in a Till Groundwater Water Catchment. Pesticide Research no. 52 (Draft). Danish Ministry of Environment, Copenhagen, Denmark (2001).

Jørgensen, P. R., Broholm K., Sonnenborg T.O., Arvin E. DNAPL transport through macroporous clayey till columns. Ground Water, Vol. 36, No. 4, 1998, p. 651 - 660. (1998b).

Jørgensen, P.R. and N.H. Spliid. Migration and biodegradation of pesticides in clayey till. Pesticides Research. No. 37. Ministry of Environment, Copenhagen, Denmark. (1998c)

Jørgensen, P.R., Hoffmann M, Kistrup J.P., Bryde C., Bossi R., Villholt K.G. Preferential flow and pesticide transport in a clay-rich till: Field, laboratory and modeling analyses. Water Resour. Res., 28(11), 2801-2815. (2002a).

Jørgensen, P. R., Eiland, F., Helstrup, T., Jensen, M.B., Vinther, F. & Urup, J. 2002b–12–11: Texturer, strukturer og vand/stof-transportveje i øvre morænelag med fokus på nitrat. DGF grundvandsmøde 31. oktober 2002b. Geologisk Tidsskrift, hæfte 2, pp. 2–5, København.

Jørgensen, P.R., Klint K.E.S., Kistrup J.P. Monitoring well interception with fractures in clayey till. Groundwater. Nov. – Dec. 2003, 772-779. (2003a).

Jørgensen, P.R., H.C.L. Hansen, M. Hoffmann, J. B. Nielsen. An integrated contaminant source and groundwater catchment model for assessment of sustainable land use and groundwater utilization. EGS-AGU-EUG Joint Assembly : Nice, France, 06-11 April 2003b.

Jørgensen, P.R., Helstrup T, Urup J., Seifert D. Modeling of Non-reactive Solute Transport in Fractured Clayey Till During Variable Flow Rate and Time. J.of Contam. Hydrol. 68, 2004, 193-216. (2004a).

Jørgensen, P.R., Urup J., Helstrup T.,Jensen M.B., Eiland F., Vinther F.P. Transport and removal of nitrate in clayey till underneath forest and arable land. J. of Contam. Hydrol., 73, 270 – 286, (2004b).

Jørgensen, P.R., L. McKay, and J. Kistrup. Aquifer Vulnerability to Pesticide Migration Through Till Aquitards. Groundwater. 42. 6. 841-855. (2004c).

Jørgensen, P.R., N.H. Spliid, T. Laier, and S. Outzen. Fate of point source pesticide spill in clayey till after 15 years. Groundwater Monitoring and Remediation 36, no.3, 33-42 (2016a).

Jørgensen, P.R., N.H. Spliid. Accumulation of pesticides in anaerobic clayey till - controls and implications to ground water. Groundwater Monitoring and Remediation 36, no.3, 43-53 (2016b).

Jørgensen P.R., Krogh P.H., Hansen S., Petersen C.P., Habekost-Nielsen M., Rasmussen S.B., Heinrichson K.& Spliid N.H. Occurrence and hydraulic function of deep biopores and their influence on pesticide migration in glacial clayey till (in Danish with extended English summary). Danish Ministry of Food and Environment, BEKF 171, pp.159. (2017).

Jørgensen P.R., K. Mostaf, M. Rolle. A Large Undisturbed Column Method to Study Flow and Transport in Macropores and Fractured Media. Groundwater/ Methods Notes, 1-11. (2019).

Jørgensen P.R., K.Mosthaf, U. Pétursdóttir, J. Aamand, M. Rolle. Groundwater flow in fractures in glacial till controlled by relic root channels. A Paradigm Shift 1. (Manuscript in preparation 2020).

Kalendar, R., Khassenov, B., Ramankulov, Y., Samuilova, O., & Ivanov, K. I. (2017). FastPCR: An in silico tool for fast primer and probe design and advanced sequence analysis. Genomics, 109(3), 312-319. doi: 10.1016/j.ygeno.2017.05.005

Keaveney E. M., Barrett, G. T., Allen, K. and Reimer, P. J. 2020. A new ramped pyroxidation/combustion facility at 827 ^{14}CHRONO, Belfast: setup description and initial results. *Radiocarbon* [in review]

Kessler T.C., Alessandro C., Fabio O., Renard P., Nilsson B., Klint K.E.S., Bjerg P.L. Modeling fine-scale geological heterogeneity-examples of sand lenses in tills. Ground Water, 51, 5: 692-705. (2013)

Klint K.E. S., Nilsson B, Troldborg L., Jakobsen P.R. A poly morphological landform approach for hydrogeological applications in heterogeneous glacial sediments. Hydrogeology Journal 21, 6:1247-1264 (2013).

Klint K.E.S. & P. Gravesen. Fractures and biopores in a Weichselian till aquitard at Flakkebjerg, Denmark. Nordic Hydrology, 30 (4/5) 1999, p. 267-284 (1999).

Kolstrup, E., Buchardt, B., 1982. A Pollen Analytical Investigation Supported by an ^{18}O-Record of a Late Glacial Lake Deposit at Graenge (Denmark). Review of Palaeobotany and Palynology 36, 205-230.

Krûger A/S. Analyse af historiske pejledata. Miljøstyrelsen 1989.

Lichtfouse, É., Dou, S., Houot, S., Barriuso, E., 1995. Isotope evidence for soil organic carbon pools with distinct turnover rates—II. Humic substances. Organic Geochemistry 23, 845-847.

Lindgreen, S. AdapterRemoval: Easy Cleaning of Next Generation Sequencing Reads. BMC Res. Notes 5, 337 (2012).

McKay, L.D., J.A. Cherry, R.W. Gillham. Field experiment in a fractured clay till,1, Hydraulic conductivity and fracture aperture. Water Resour. Res., 29 (4), 1149-1162 (1993a).

McKay, L.D., J.A. Cherry, R.W. Gillham. Field experiment in a fractured clay till, 2,Solutre and colloid transport. Water Resour. Res., 29 (12), 3879-3890 (1993b).

McKay, L.D and Fredericia, J. 1995. Origin, distribution and hydraulic influence of fractures in clay-rich tills glacial tills. Canadian Geotechnical Journal, 32:957-975.

McKay L.D., J. Fredericia, M. Lenczewski, J. Morthorst og K.E.S. Klint 1999. Spatial variability of contaminant transport in fractured till, Avedøre Denmark. Nord. Hydrol. 30, 1999, p. 333-360.

McKay L.D., S. Driese, K.H. Smith, M.J. Vepraskas. Hydrogeology and pedology ofsaprolite formed from sedimentary rock, eastern Tenneseeee, USA. Geoderma 126, 27-45 (2005).

McKay, L.D. W.E. Sandford, J.M. Strong. Field scale migration of colloidal tracers in fractured saprolite. Groundwater 38, 139-147 (2000).

Mehra, O.P. and Jackson, M.L. (1960) Iron Oxide Removal from Soils and Clay by a Dithionite-Citrate System Buffered with Sodium Bicarbonate. Clays and Clay Minerals, 7, 317-327. http://dx.doi.org/10.1346/CCMN.1958.0070122.Meyers, P.A., Teranes, J.L., 2001. Sediment organic matter, In: Last, W.M., Smol, J.P. (Eds.), Tracking Environmental Change Using Lake Sediments, Physicals and Geochemical Methods ed. Kluwer Academic Publishers, Dordrecht, pp. 239-269.

Miljøstyrelsen. Pesticider og vandværker. Udredningsprojekt om BAM forurening. Miljøprojekt Nr. 732 2002.

Miljøstyrelsen. Grundvandskortlægningen (2020).

Miljøstyrelsen. BAM's skæbne i grundvand. Miljøprojekt nr. 1000, 2005

Miljøstyrelsen (2020). Rødel, *A. glutinosa*. Artsleksikon.

Milthers, V. (1935): Nordøstsjællands Geologi. Anden omarbejdede Udgave. – DGU V Rk. Nr. 3.

Mosthaf K., M. Rolle, U. Petursdottir, J. Aamand, P. R. Jørgensen**.** Transport of tracers and pesticides through fractured clayey till: Large Undisturbed Column (LUC) experiments and model-based interpretation. Water Resour. Res. (2020 in review).

Naturstyrelsen, Skov og Landskab. Beskrivelser af udvalgte træ- og buskarter. 2010.

Nissenbaum, A., Schallinger, K.M., 1974. The distribution of the stable carbon isotope (13C/12C) in fractions of soil organic matter. Geoderma 11, 137-145.

Noe-Nygaard, N., Abildtrup, C.H., Albrechtsen, T., Gotfredsen, A.B., Ricther, J., 1998. Palæobiologiske, sedimentologiske og geokemiske undersøgelser af Sen Weichsel og Holocæne aflejringer i Store Åmose, Danmark. Geologisk Tidsskrift 2, 1-65.

Olsen, J., Tikhomirov, D., Grosen, C., Heinemeier, J., Klein, M., 2017. Radiocarbon analysis on the new AARAMS 1MV TANDETRON. Radiocarbon 59, 905-913.

O´Hara, S.K., Parker B.L., Jørgensen P.R., Cherry J.A. Trichloroethene DNAPL flow and mass distribution in naturally fractured clay: 1. Evidence of aperture variability. Water Resour. Res., 36(1), 135-147 (2000).

Petersen, C. T., Nielsen, M. H., Hansen, S., Abrahamsen S. og Koch, C.B. (2013). Undersøgelse af makroporekontinuitet ved markdræn og effekter af direkte forbundne makroporer på jords filterfunktion. Bekæmpelsesmiddelforskning fra Miljøstyrelsen nr. 144, 143 sider.

Philippsen, B., Olsen, J., Sørensen, S.A., Måge, B., 2019. δ13C values of wood and Charcoal Reveal Broad Isotopic ranges at the base of the Food Web. Radiocarbon 61, 2003-2017.

QIAGEN. (2016). DNeasy® PowerMax® Soil Kit Quick start protocol. Retrieved from https://www.qiagen.com/us/resources/download.aspx?id=db06ce1b-deea-4e8f-9096-653caf7a19d6&lang=en

Quigley R.M. and Ogunbadejo. Till geology, mineralogy and geotechnical behavior, Sarnia, Ontario. In: Glacial Till. R.F. Leggett (ed). The royal Society of Canada Special Publication 12 (1976).

Regionernes Videnscenter (2008). SprækkeJAGG Regneark til risikovurdering af sprækker i moræneler Teknik og Administration Nr. 2 2008.

Reimer, P.J., Bard, E., Bayliss, A., Beck, J.W., Blackwell, P.G., Bronk Ramsey, C., Buck, C.E., Cheng, H., Edwards, R.L., Friedrich, M., Grootes, P.M., Guilderson, T.P., Haflidason, H., Hajdas, I., Hatté, C., Heaton, T.J., Hoffmann, D.L., Hogg, A.G., Hughen, K.A., Kaiser, K.F., Kromer, B., Manning, S.W., Niu, M., Reimer, R.W., Richards, D.A., Scott, E.M., Southon, J.R., Staff, R.A., Turney, C.S.M., van der Plicht, J., 2013. IntCal13 and Marine13 Radiocarbon Age Calibration Curves 0–50,000 Years cal BP. Radiocarbon 55, 1869-1887.

Rivad, T, Hasholt, B, Skjernaa, L & P.R. Jørgensen 2001, 'Vandtrykvariationer i moræne- og sandlag', *Vand og Jord*, nr.3, 8. årgang, s. 91-94.
Rosenbom A.E, Ernstsen V, Flühler H, Jensen K.H, Refsgaard J.C, Wydler H. Flourescence Imaging Applied to Tracer Distributions in Variably Saturated Fractured Clayey Till. Journal of Environmental Quality 37, 448-458 (2008).
Rosenbom A.E. (2005). Preferential flow and transport in variably saturated fractured media. Ph.D Thesis. Technical University of Denmark and GEUS. p. 214.
Ruland W.W., Cherry J.A., and Feenstra S. The depth of fractures and active ground-flow in a clayey till plain in southwestern Ontario. Ground Water, 21, 3: 405-417 (1991).
Schmidt-Vogt H. Wachstum und Wurzelentwicklung von Schwarzerlen verschicdener Herkunft. Algemine Forst und Jagdzietung. Heft 6, 149-156, (1971).
Seersholm, F. V. et al. DNA evidence of bowhead whale exploitation by Greenlandic Paleo-Inuit 4000 years ago. Nat. Commun. (2016). doi:10.1038/ncomms13389
Snow, D. T. Rock fracture spacings, openings and porosities, J. Soil Mech.Found. Div. Proc. Am. Soc. Civil Eng., 94, 73– 91, (1968).
Solrød kommune 2016. Tilladelse til vandindvinding Havdrup kildeplads. Solrød kommune, Teknik og Miljø 2016.
Sprackling JA, Read RA. 1979. *Tree Root Systems in Eastern Nebraska* (The Conservation and Survey Division, Institute of Agriculture and Natural Resources, University of Nebraska–Lincoln, Lincoln, NE), Nebraska Conservation Bulletin 37.
Stenemo F., N. Jarvis, P.R. Jørgensen. Linking a one-dimensional pesticide fate model to a three-dimensional groundwater model to simulate pollution risks of shallow and deep groundwater underlying fractured till. Journal of Contaminant Hydrology 79(1-2):89-106 · October 2005
Stuiver, M., Polach, H.A., 1977. Reporting of C-14 data. Radiocarbon 19, 355-363.
Thalund-Hansen R. (2018). Assessment of pesticide transport in fractured clay (master thesis). Department of Environmental Engineering. Technical University of Denmark. 80p.
Timms, W. A., R.I.C Acworth, R.A., Arns, C.H. Arns, J. McGeeney, D.E. Rau, and M.O. Cuthbert. 2018, The influence of syndepositional macropores on the hydraulic integrity of thick alluvial clay aquitards, Water resources research, vol. 54, no. 4, pp. 3122-3138.
Tsakiroglou C.D., K.E.S. Klint, B. Nilsson, M.A. Theodoropoulou, C.A. Aggelopoulos. (2012). From aperture characterization to hydraulic properties of fractures. Geoderma 181–182 (2012) 65–77
Urup J. Undersøgelse og matematisk modellering af nitrattransport og –reduktion i vandmættet makroporøs moræneler på henholdsvis en skov- og en landbrugslokalitet. p. 109. Geological Institute, University of Copenhagen, January (2001).
Vogel JS, Nelson DE, Southon JR. 1987. (super 14) C background levels in an accelerator mass spectrometry system. *Radiocarbon* 29(3):323-33. +Wagner ND, He L, Hörandl E. 2020. Relationships and genome evolution of polyploid Salix species revealed by RAD sequencing data. Frontiers in Plant Sciences11:1077 https://doi.org/10.3389/fpls.2020.01077
Wagner, ND., Gramlich, S., & Hörandl, E. 2018. RAD sequencing resolved phylogenetic relationships in European shrub willows (*Salix* L. subg. *Chamaetia* and subg. *Vetrix*) and revealed multiple evolution of dwarf shrubs. Ecol Evol. 2018a; 00:1–13. https://doi.org/10.1002/ece3.4360
Wagner, S., Lagane, F., Seguin-Orlando, A., Schubert, M., Leroy, T., Guichoux, E., Chancerel, E., Bech-Hebelstrup, I., Bernard, V., Billard, C., Billaud, Y., Bolliger, M., Croutsch, C., Čufar, K., Eynaud, F., Heussner, K.U., Köninger, J., Langenegger, F., Leroy, F., Lima, C., Martinelli, N., Momber, G., Billamboz, A., Nelle, O., Palomo, A., Piqué, R., Ramstein, M., Schweichel, R., Stäuble, H., Tegel, W., Terradas, X., Verdin, F., Plomion, C., Kremer, A., Orlando, L. (2018b). High-Throughput DNA sequencing of ancient wood. Mol. Ecol. 27:1138–1154. doi: 10.1111/ mec.14514.
Westergaard, B., Hansen H.C.B. 1997. Phosphorus in Macropore Walls of a Danish Glossudalf. Acta Agric. Scand Sect. B, Soil and Plant Sci. 1997 (47), 193-200.

Witherspoon P.A., Wang J.S.Y, Iwai K., Gale J.E. Validation of cubic law for fluid flow in deformable roch fractures. Water Res. Resear. 16, no.6, 1016-1024. (1980).

Xi, B., N.Di, J. Liu, R. Zhang, and Z. Cao. Hydrologic regulation of plant rooting depth: Pay attention to the widespread scenario with intense seasonal groundwater table fluctuation. PNAS April 24, (2018), 115 (17).

Ye, J., Coulouris, G., Zaretskaya, I., Cutcutache, I., Rozen, S., & Madden, T. L. (2012). Primer-BLAST: a tool to design target-specific primers for polymerase chain reaction. BMC Bioinformatics, 13, 134. doi: 10.1186/1471-2105-13-134.

Appendix 1. Bore-profiles and well screens

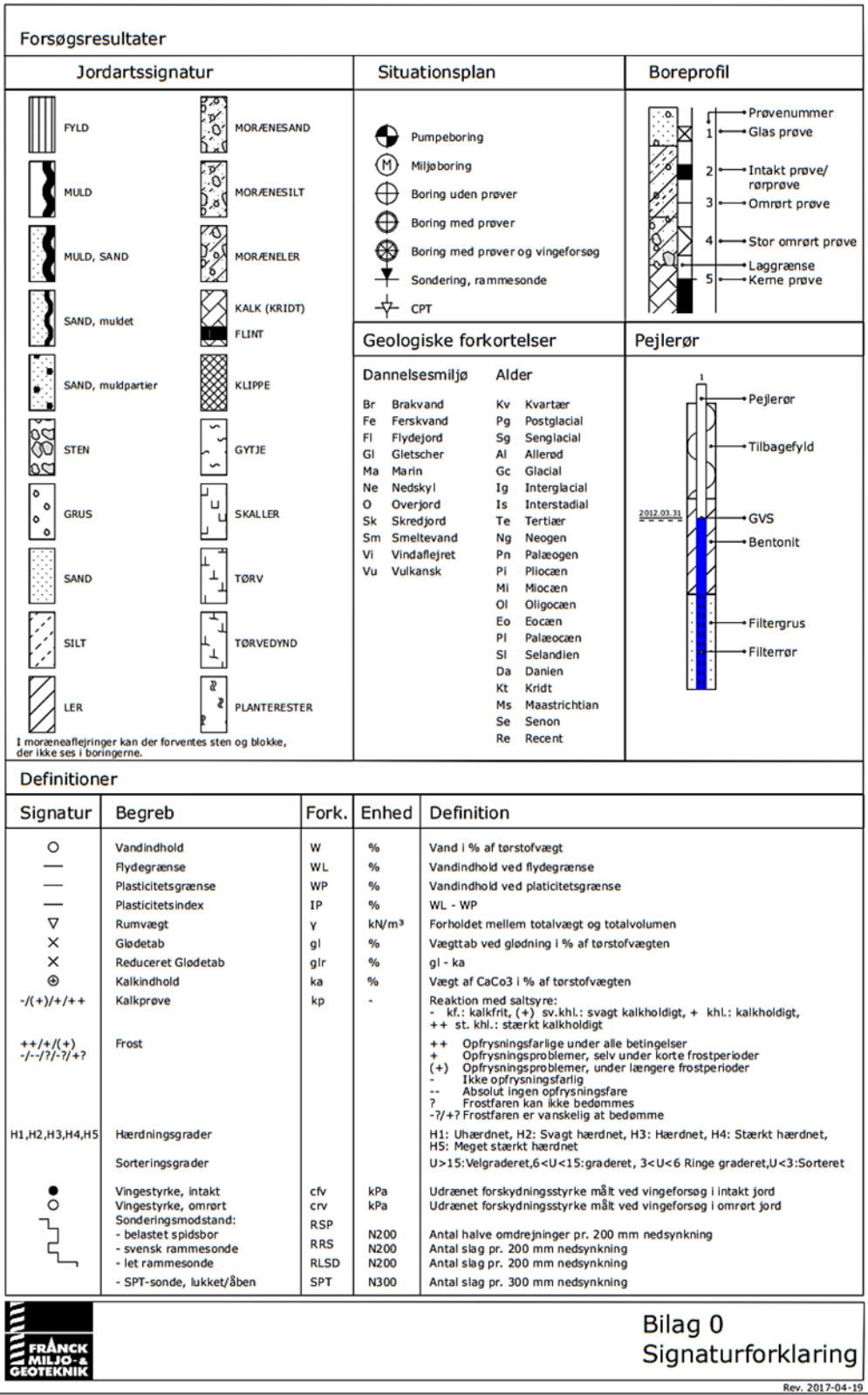

Forsøgsresultater

Jordartssignatur

FYLD
MULD
MULD, SAND
SAND, muldet
SAND, muldpartier
STEN
GRUS
SAND
SILT
LER
MORÆNESAND
MORÆNESILT
MORÆNELER
KALK (KRIDT)
FLINT
KLIPPE
GYTJE
SKALLER
TØRV
TØRVEDYND
PLANTERESTER

I moræneaflejringer kan der forventes sten og blokke, der ikke ses i boringerne.

Situationsplan

Pumpeboring
Miljøboring
Boring uden prøver
Boring med prøver
Boring med prøver og vingeforsøg
Sondering, rammesonde
CPT

Boreprofil

1 Prøvenummer
1 Glas prøve
2 Intakt prøve/ rørprøve
3 Omrørt prøve
4 Stor omrørt prøve
Laggrænse
5 Kerne prøve

Geologiske forkortelser

Dannelsesmiljø

Br	Brakvand
Fe	Ferskvand
Fl	Flydejord
Gl	Gletscher
Ma	Marin
Ne	Nedskyl
O	Overjord
Sk	Skredjord
Sm	Smeltevand
Vi	Vindaflejret
Vu	Vulkansk

Alder

Kv	Kvartær
Pg	Postglacial
Sg	Senglacial
Al	Allerød
Gc	Glacial
Ig	Interglacial
Is	Interstadial
Te	Tertiær
Ng	Neogen
Pn	Palæogen
Pi	Pliocæn
Mi	Miocæn
Ol	Oligocæn
Eo	Eocæn
Pl	Palæocæn
Sl	Selandien
Da	Danien
Kt	Kridt
Ms	Maastrichtian
Se	Senon
Re	Recent

Pejlerør

1 Pejlerør
Tilbagefyld
2012.03.31 GVS
Bentonit
Filtergrus
Filterrør

Definitioner

Signatur	Begreb	Fork.	Enhed	Definition
○	Vandindhold	W	%	Vand i % af tørstofvægt
—	Flydegrænse	WL	%	Vandindhold ved flydegrænse
—	Plasticitetsgrænse	WP	%	Vandindhold ved plasticitetsgrænse
—	Plasticitetsindex	IP	%	WL - WP
▽	Rumvægt	γ	kN/m³	Forholdet mellem totalvægt og totalvolumen
×	Glødetab	gl	%	Vægttab ved glødning i % af tørstofvægten
×	Reduceret Glødetab	glr	%	gl - ka
⊕	Kalkindhold	ka	%	Vægt af CaCo3 i % af tørstofvægten
-/(+)/+/++	Kalkprøve	kp	-	Reaktion med saltsyre: - kf.: kalkfrit, (+) sv.khl.: svagt kalkholdigt, + khl.: kalkholdigt, ++ st. khl.: stærkt kalkholdigt
++/+/(+) -/--/?/-?/+?	Frost			++ Opfrysningsfarlige under alle betingelser + Opfrysningsproblemer, selv under korte frostperioder (+) Opfrysningsproblemer, under længere frostperioder - Ikke opfrysningsfarlig -- Absolut ingen opfrysningsfare ? Frostfaren kan ikke bedømmes -?/+? Frostfaren er vanskelig at bedømme
H1,H2,H3,H4,H5	Hærdningsgrader			H1: Uhærdnet, H2: Svagt hærdnet, H3: Hærdnet, H4: Stærkt hærdnet, H5: Meget stærkt hærdnet
	Sorteringsgrader			U>15:Velgraderet,6<U<15:graderet, 3<U<6 Ringe graderet,U<3:Sorteret
●	Vingestyrke, intakt	cfv	kPa	Udrænet forskydningsstyrke målt ved vingeforsøg i intakt jord
○	Vingestyrke, omrørt	crv	kPa	Udrænet forskydningsstyrke målt ved vingeforsøg i omrørt jord
	Sonderingsmodstand:	RSP		
	- belastet spidsbor	RRS	N200	Antal halve omdrejninger pr. 200 mm nedsynkning
	- svensk rammesonde	RLSD	N200	Antal slag pr. 200 mm nedsynkning
	- let rammesonde	SPT	N200	Antal slag pr. 200 mm nedsynkning
	- SPT-sonde, lukket/åben		N300	Antal slag pr. 300 mm nedsynkning

FRÅNCK MILJØ- & GEOTEKNIK

Bilag 0
Signaturforklaring

Rev. 2017-04-19

Boreprofil

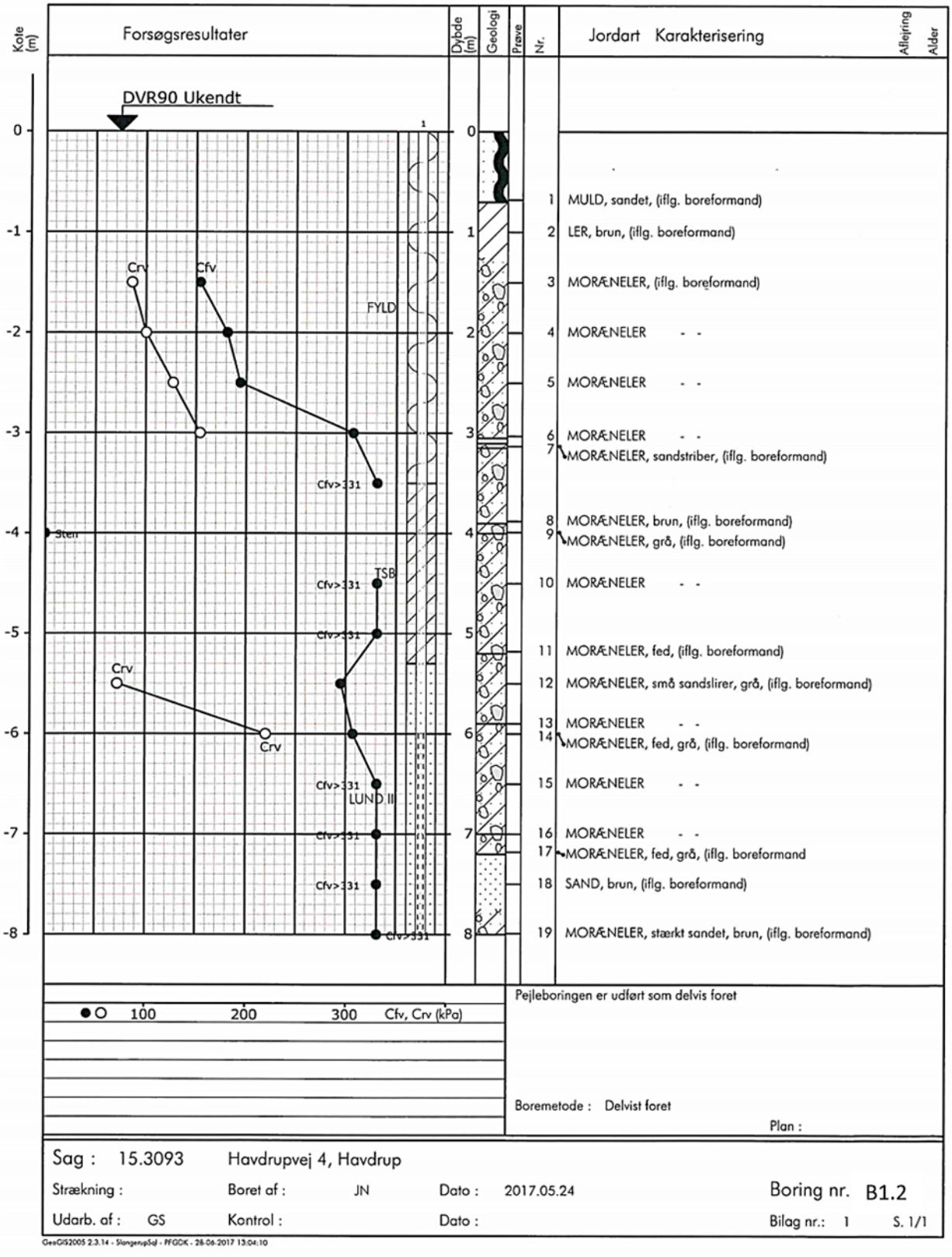
Kote (m)
Forsøgsresultater
Dybde (m)
Geologi
Prøve
Nr.
Jordart Karakterisering
Alder
DVR90 Ukendt
Cfv
Crv
FYLD
Cfv>331
Sten
TSB
LUND II
1 MULD, sandet, (iflg. boreformand)
2 LER, brun, (iflg. boreformand)
3 MORÆNELER, (iflg. boreformand)
4 MORÆNELER
5 MORÆNELER
6 MORÆNELER
7 MORÆNELER, sandstriber, (iflg. boreformand)
8 MORÆNELER, brun, (iflg. boreformand)
9 MORÆNELER, grå, (iflg. boreformand)
10 MORÆNELER
11 MORÆNELER, fed, (iflg. boreformand)
12 MORÆNELER, små sandslirer, grå, (iflg. boreformand)
13 MORÆNELER
14 MORÆNELER, fed, grå, (iflg. boreformand)
15 MORÆNELER
16 MORÆNELER
17 MORÆNELER, fed, grå, (iflg. boreformand
18 SAND, brun, (iflg. boreformand)
19 MORÆNELER, stærkt sandet, brun, (iflg. boreformand)
100 200 300 Cfv, Crv (kPa)
Pejleboringen er udført som delvis foret
Boremetode : Delvist foret
Plan :
Sag : 15.3093 Havdrupvej 4, Havdrup
Strækning :
Boret af : JN
Dato : 2017.05.24
Boring nr. B1.2
Udarb. af : GS
Kontrol :
Dato :
Bilag nr.: 1 S. 1/1
GeoGIS2005 2.3.14 - SlangerupSql - PFGDK - 28.06.2017 13:04:10

Boreprofil

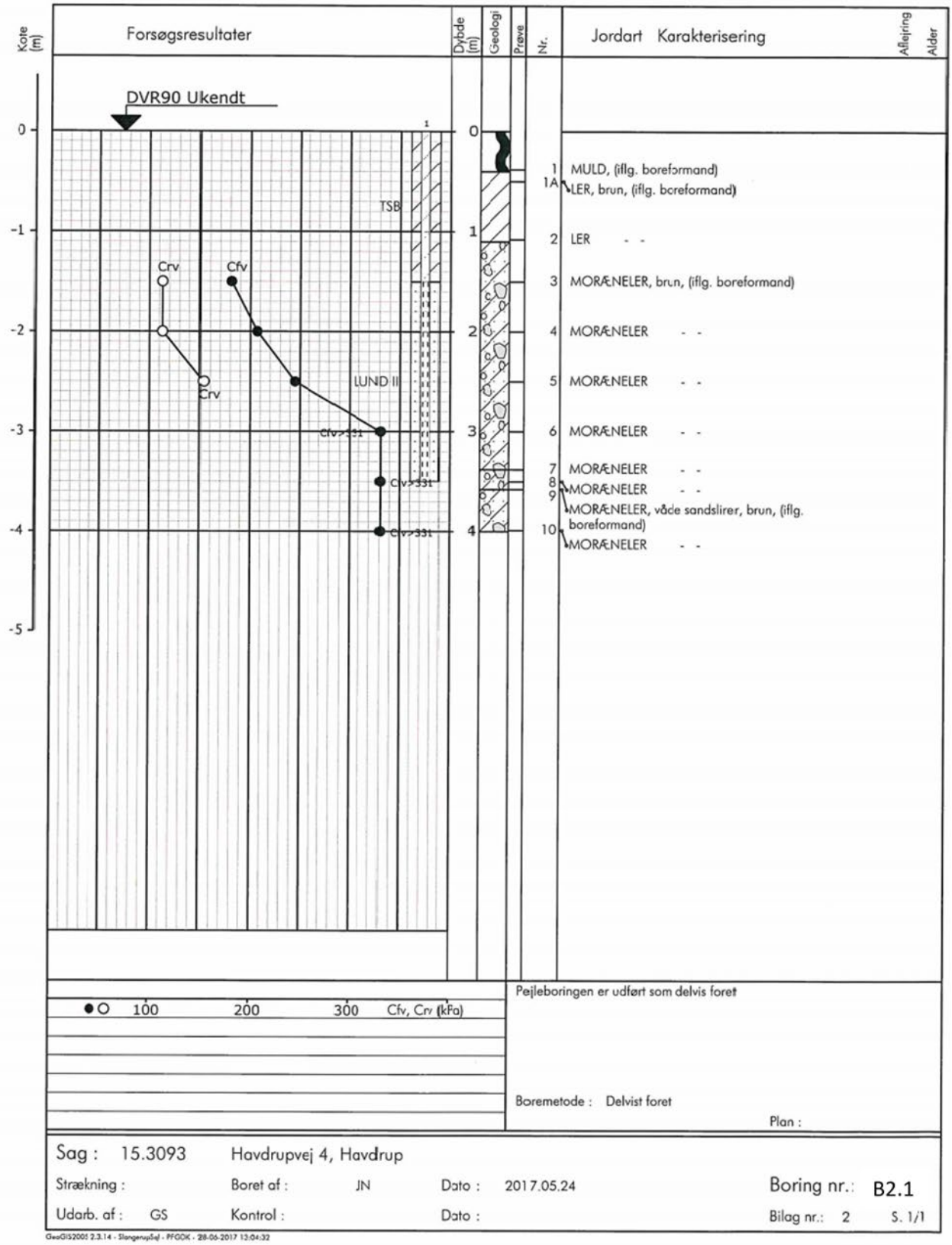
Kote (m)
Forsøgsresultater
Dybde (m)
Geologi
Prøve
Nr.
Jordart Karakterisering
Aflejring
Alder
DVR90 Ukendt
TSB
LUND II
Crv
Cfv
Cfv>331
Crv>331
0
-1
-2
-3
-4
-5
1
2
3
4
1 MULD, (iflg. boreformand)
1A LER, brun, (iflg. boreformand)
2 LER
3 MORÆNELER, brun, (iflg. boreformand)
4 MORÆNELER
5 MORÆNELER
6 MORÆNELER
7 MORÆNELER
8 MORÆNELER
9 MORÆNELER, våde sandslirer, brun, (iflg. boreformand)
10 MORÆNELER
100
200
300
Cfv, Crv (kPa)
Pejleboringen er udført som delvis foret
Boremetode : Delvist foret
Plan :
Sag : 15.3093
Havdrupvej 4, Havdrup
Strækning :
Boret af : JN
Dato : 2017.05.24
Boring nr.: B2.1
Udarb. af : GS
Kontrol :
Dato :
Bilag nr.: 2
S. 1/1
GeoGIS2005 2.3.14 - Slangerup5ej - PFODK - 28-06-2017 13:04:32

Boreprofil

FRANCK MILJØ- & GEOTEKNIK

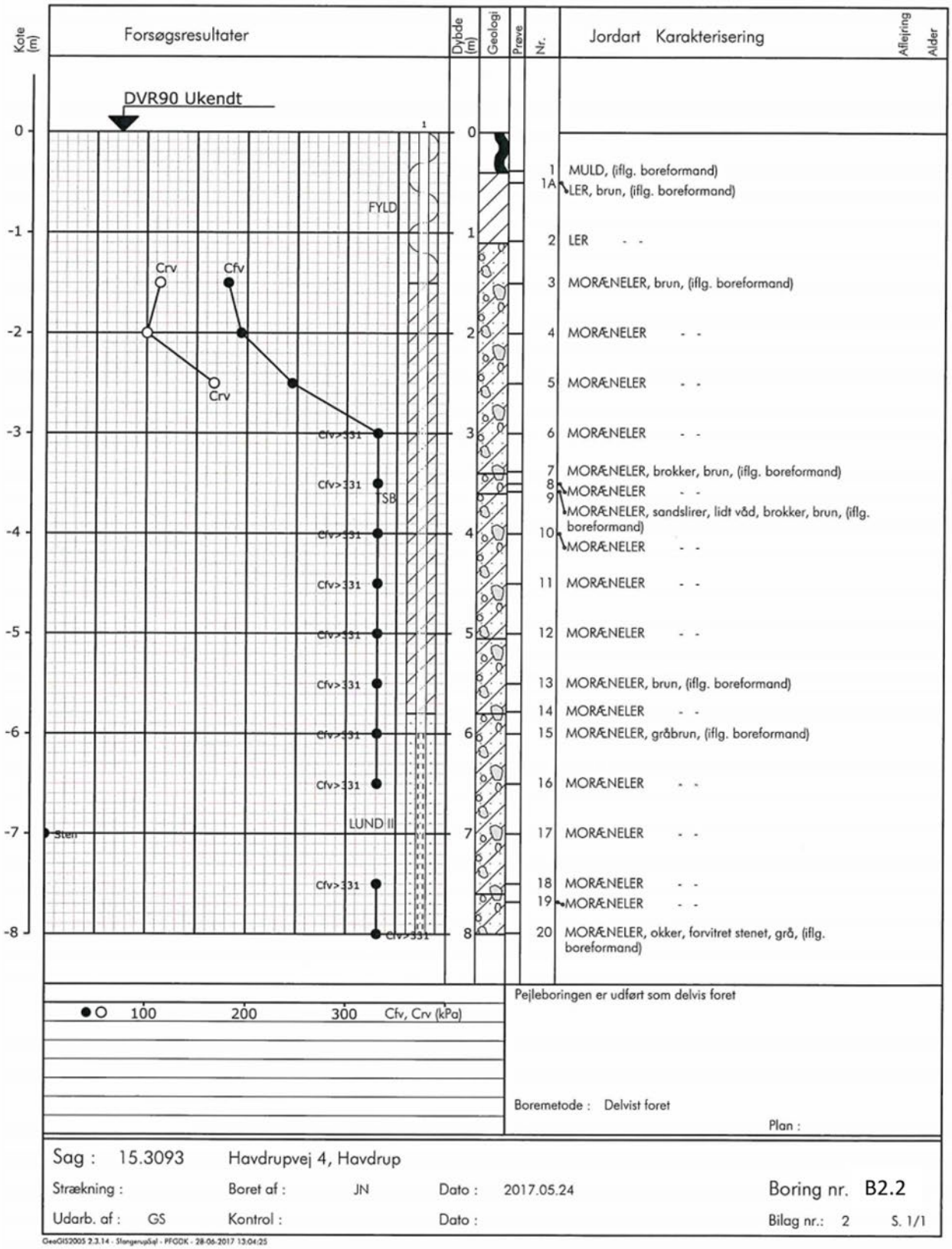

Sag : 15.3093 Havdrupvej 4, Havdrup

Strækning : Boret af : JN Dato : 2017.05.24 Boring nr. B2.2

Udarb. af : GS Kontrol : Dato : Bilag nr.: 2 S. 1/1

GeoGIS2005 2.3.14 - StangerupSøl - PFGDK - 28-06-2017 13:04:25

Boreprofil

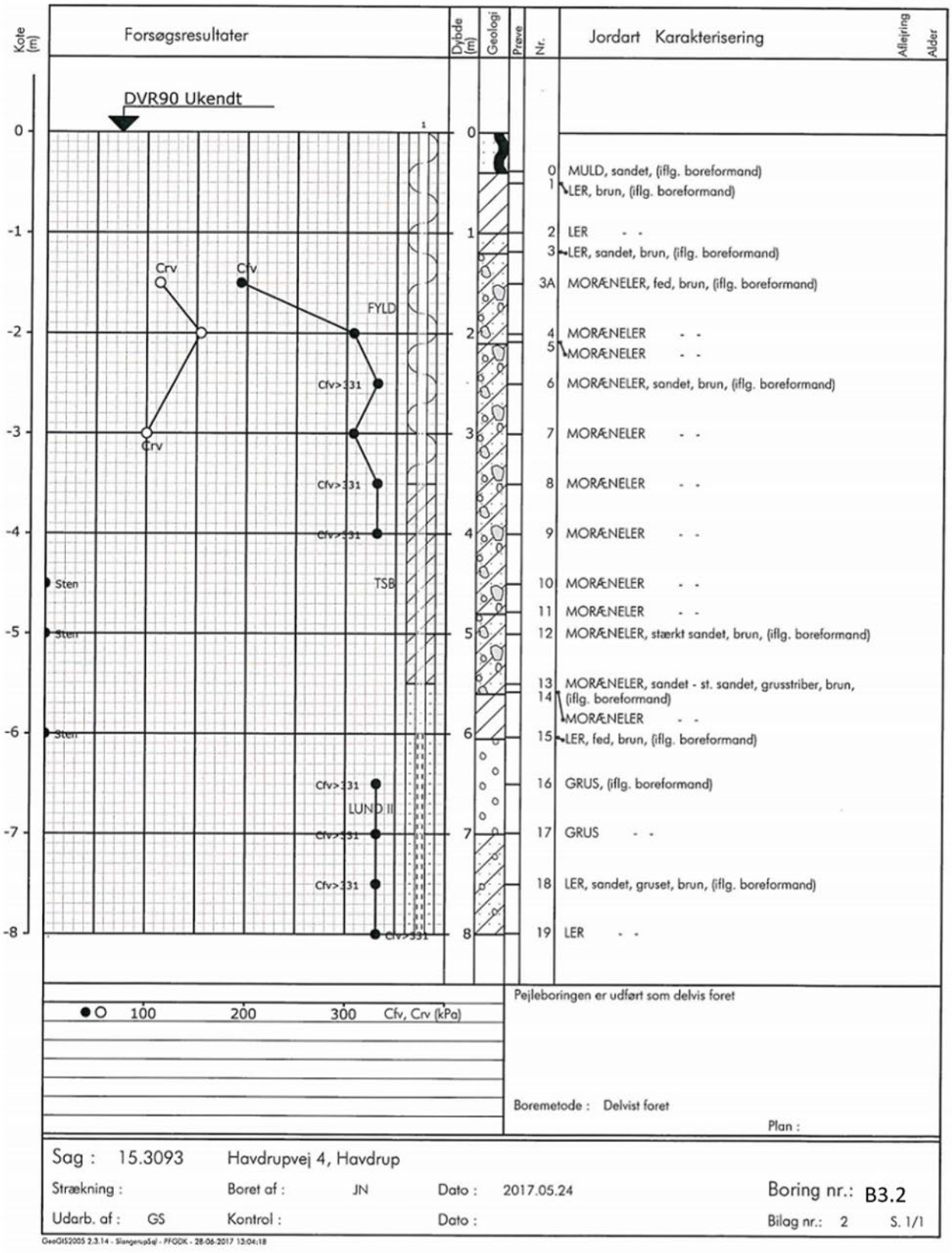
Kote (m)
Forsøgsresultater
DVR90 Ukendt
Dybde (m)
Geologi
Prøve
Nr.
Jordart Karakterisering
Aflejring
Alder
Crv
Cfv
FYLD
Cfv>331
TSB
Sten
LUND II
0 MULD, sandet, (iflg. boreformand)
1 LER, brun, (iflg. boreformand)
2 LER
3 LER, sandet, brun, (iflg. boreformand)
3A MORÆNELER, fed, brun, (iflg. boreformand)
4 MORÆNELER
5 MORÆNELER
6 MORÆNELER, sandet, brun, (iflg. boreformand)
7 MORÆNELER
8 MORÆNELER
9 MORÆNELER
10 MORÆNELER
11 MORÆNELER
12 MORÆNELER, stærkt sandet, brun, (iflg. boreformand)
13 MORÆNELER, sandet - st. sandet, grusstriber, brun,
14 (iflg. boreformand)
MORÆNELER
15 LER, fed, brun, (iflg. boreformand)
16 GRUS, (iflg. boreformand)
17 GRUS
18 LER, sandet, gruset, brun, (iflg. boreformand)
19 LER
100 200 300 Cfv, Crv (kPa)
Pejleboringen er udført som delvis foret
Boremetode : Delvist foret
Plan :
Sag : 15.3093 Havdrupvej 4, Havdrup
Strækning :
Boret af : JN
Dato : 2017.05.24
Boring nr.: B3.2
Udarb. af : GS
Kontrol :
Dato :
Bilag nr.: 2
S. 1/1

Boreprofil

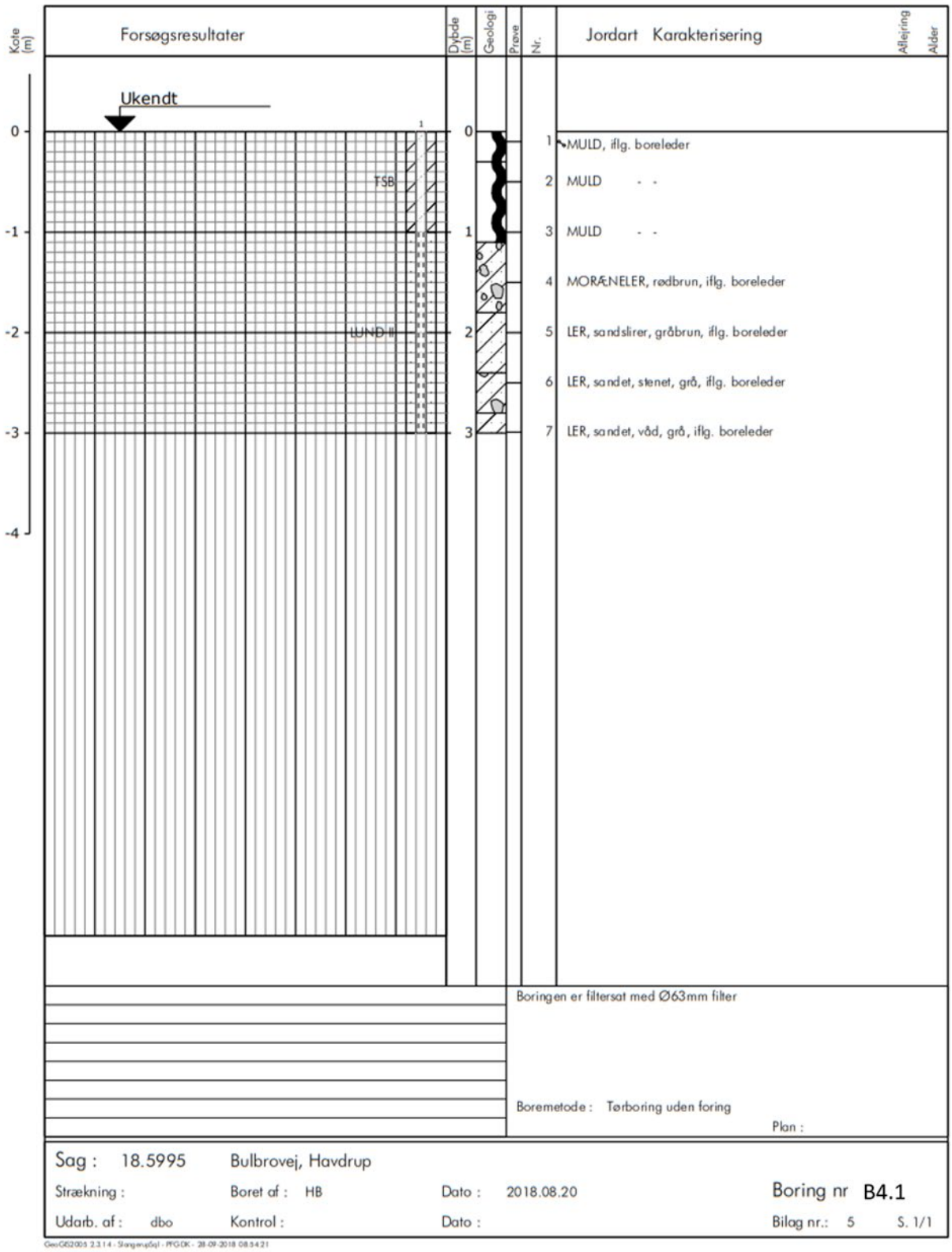
Kote (m)
Forsøgsresultater
Dybde (m)
Geologi
Prøve
Nr.
Jordart Karakterisering
Alder
Ukendt
0
-1
-2
-3
-4
TSB
LUND-II
1
2
3
4
5
6
7
MULD, iflg. boreleder
MULD - -
MULD - -
MORÆNELER, rødbrun, iflg. boreleder
LER, sandslirer, gråbrun, iflg. boreleder
LER, sandet, stenet, grå, iflg. boreleder
LER, sandet, våd, grå, iflg. boreleder
Boringen er filtersat med Ø63mm filter
Boremetode : Tørboring uden foring
Plan :
Sag : 18.5995 Bulbrovej, Havdrup
Strækning :
Boret af : HB
Dato : 2018.08.20
Boring nr B4.1
Udarb. af : dbo
Kontrol :
Dato :
Bilag nr.: 5 S. 1/1

Boreprofil

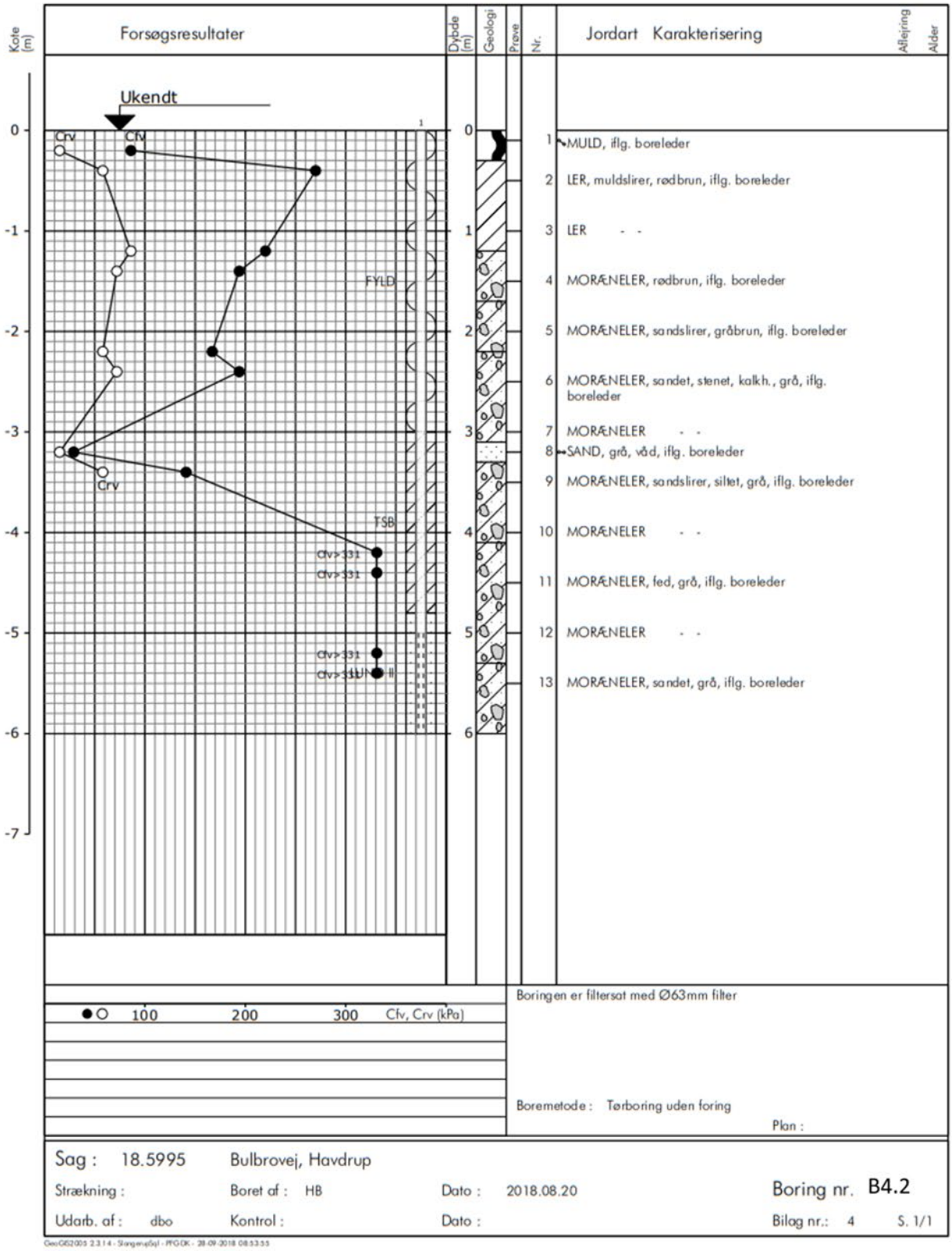
Kote (m)
Forsøgsresultater
Dybde (m)
Geologi
Prøve
Nr.
Jordart Karakterisering
Aflejring
Alder
Ukendt
Cfv
Crv
FYLD
TSB
Cfv>331
1
2
3
4
5
6
7
8
9
10
11
12
13
MULD, iflg. boreleder
LER, muldslirer, rødbrun, iflg. boreleder
LER
MORÆNELER, rødbrun, iflg. boreleder
MORÆNELER, sandslirer, gråbrun, iflg. boreleder
MORÆNELER, sandet, stenet, kalkh., grå, iflg. boreleder
MORÆNELER
SAND, grå, våd, iflg. boreleder
MORÆNELER, sandslirer, siltet, grå, iflg. boreleder
MORÆNELER
MORÆNELER, fed, grå, iflg. boreleder
MORÆNELER
MORÆNELER, sandet, grå, iflg. boreleder
100
200
300
Cfv, Crv (kPa)
Boringen er filtersat med Ø63mm filter
Boremetode : Tørboring uden foring
Plan :
Sag : 18.5995 Bulbrovej, Havdrup
Strækning :
Boret af : HB
Dato : 2018.08.20
Boring nr. B4.2
Udarb. af : dbo
Kontrol :
Dato :
Bilag nr.: 4
S. 1/1

Boreprofil

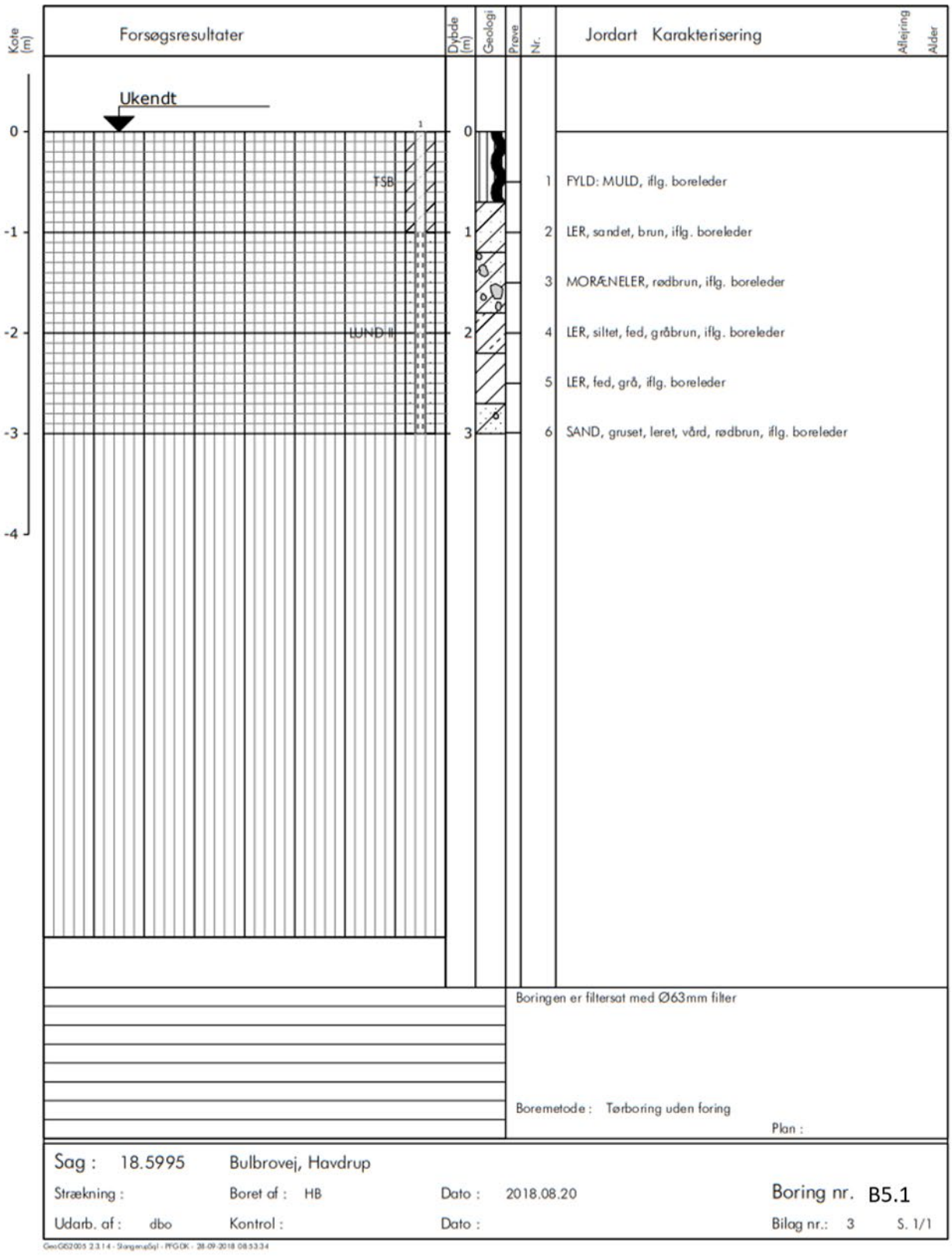
Kote (m)
Forsøgsresultater
Dybde (m)
Geologi
Prøve
Nr.
Jordart Karakterisering
Alleiring
Alder
Ukendt
0
-1
-2
-3
-4
TSB
LUND II
1
2
3
1 FYLD: MULD, iflg. boreleder
2 LER, sandet, brun, iflg. boreleder
3 MORÆNELER, rødbrun, iflg. boreleder
4 LER, siltet, fed, gråbrun, iflg. boreleder
5 LER, fed, grå, iflg. boreleder
6 SAND, gruset, leret, vård, rødbrun, iflg. boreleder
Boringen er filtersat med Ø63mm filter
Boremetode : Tørboring uden foring
Plan :
Sag : 18.5995 Bulbrovej, Havdrup
Strækning :
Boret af : HB
Dato : 2018.08.20
Boring nr. B5.1
Udarb. af : dbo
Kontrol :
Dato :
Bilag nr.: 3 S. 1/1

Boreprofil

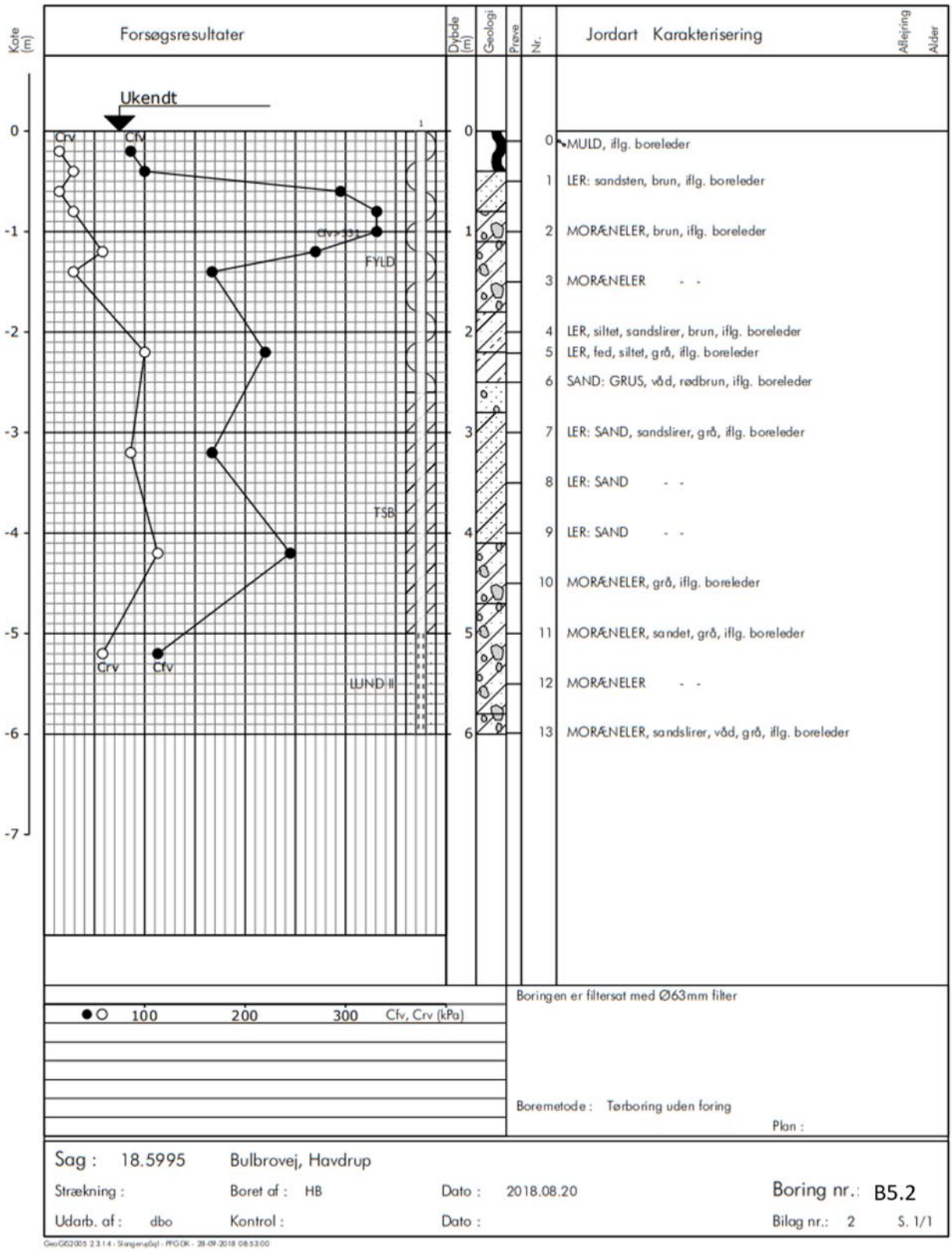
Kote (m)
Forsøgsresultater
Dybde (m)
Geologi
Prøve
Nr.
Jordart Karakterisering
Aflejring
Alder
Ukendt
Cfv
Crv
FYLD
TSB
LUND II
0 MULD, iflg. boreleder
1 LER: sandsten, brun, iflg. boreleder
2 MORÆNELER, brun, iflg. boreleder
3 MORÆNELER - -
4 LER, siltet, sandslirer, brun, iflg. boreleder
5 LER, fed, siltet, grå, iflg. boreleder
6 SAND: GRUS, våd, rødbrun, iflg. boreleder
7 LER: SAND, sandslirer, grå, iflg. boreleder
8 LER: SAND - -
9 LER: SAND - -
10 MORÆNELER, grå, iflg. boreleder
11 MORÆNELER, sandet, grå, iflg. boreleder
12 MORÆNELER - -
13 MORÆNELER, sandslirer, våd, grå, iflg. boreleder
100 200 300 Cfv, Crv (kPa)
Boringen er filtersat med Ø63mm filter
Boremetode : Tørboring uden foring
Plan :
Sag : 18.5995 Bulbrovej, Havdrup
Strækning : Boret af : HB Dato : 2018.08.20 Boring nr.: B5.2
Udarb. af : dbo Kontrol : Dato : Bilag nr.: 2 S. 1/1

Appendix 2. Hydrochemial and geochemical analysis

TABLE A2.1. Concentration of element in the fractures, fracture rims and adjacent clay matrix in fractures from excavation E2. Extracted with the CBD method, and presented in µg g^{-1}.

	Fe	Fe	Fe			Al	Al	Al
Depth	Bleached	Fe (rim)	Matrix		Depth	Bleached	Fe (rim)	Matrix
1.5 m	2347	7649	7046		1.5 m	496	795	823
3.0 m	2429	13583	6962		3.0 m	480	855	686
3.7 m		12558	6962		3.7 m		1105	686
	Mn	Mn	Mn			Cr	Cr	Cr
Depth	Bleached	Fe (rim)	Matrix		Depth	Bleached	Fe (rim)	Matrix
1.5 m	91	188	237		1.5 m	3.6	2.5	2.4
3.0 m	103	263	293		3.0 m	3.1	3.5	2.7
3.7 m		1742	293		3.7 m		2.6	2.7
	Ni	Ni	Ni			Zn	Zn	Zn
Depth	Bleached	Fe (rim)	Matrix		Depth	Bleached	Fe (rim)	Matrix
1.5 m	1.2	4.6	5.3		1.5 m	2.4	10.5	8.9
3.0 m	1.1	7.5	6.0		3.0 m	2.8	16.6	8.0
3.7 m		49.8	6.0		3.7 m		34.3	8.0
	Cu	Cu	Cu			Co	Co	Co
Depth	Bleached	Fe (rim)	Matrix		Depth	Bleached	Fe (rim)	Matrix
1.5 m	1.1	0.9	0.8		1.5 m	1.1	3.4	3.4
3.0 m	0.7	0.9	1.8		3.0 m	0.6	5.7	3.5
3.7 m		17.0	1.8		3.7 m		31.6	3.5
	K	K	K			P	P	P
Depth	Bleached	Fe (rim)	Matrix		Depth	Bleached	Fe (rim)	Matrix
1.5 m	1320	1353	1458		1.5 m	31	59	60
3.0 m	1436	1439	1509		3.0 m	36	125	67
3.7 m		21362	1509		3.7 m		167	67
	B	B	B			V	V	V
Depth	Bleached	Fe (rim)	Matrix		Depth	Bleached	Fe (rim)	Matrix
1.5 m	0.2	1.8	1.8		1.5 m	2.0	7.8	6.8
3.0 m	0.3	5.3	2.9		3.0 m	1.4	11.8	6.2
3.7 m		2.5	2.9		3.7 m		10.7	6.2

Cd, Mo, Pb and Se were all below detection limit

TABLE A2.2. Water analyses from monitoring wells

Water analyses			
Site, Excavation	**Date**	**Well**	**Fe-total (ppb)**
Salløv, E2	27-10-2017	3,1	44
Salløv, E2	08-11-2017	3,1	23
Salløv, E2	08-11-2017	3,1	349
Salløv, E2	24-01-2017	3,1	348
Salløv, E2	09-12-2017	3,1	411
Salløv, E2	22-12-2017	3,1	223
Salløv, E2	02-01-2018	3,1	76
Salløv, E2	16-02-2018	3,1	196
Salløv, E2	01-03-2018	3,1	1483
Salløv, E2	02-03-2018	3,1	1548
Salløv, E2	27-10-2017	3,2	7
Salløv, E2	08-11-2017	3,2	81
Salløv, E2	24-11-2017	3,2	49
Salløv, E2	09-12-2017	3,2	41
Salløv, E2	22-12-2017	3,2	36
Salløv, E2	02-01-2018	3,2	127
Salløv, E2	16-01-2018	3,2	193
Salløv, E2	08-11-2018	3,2	5
Salløv, E2	01-02-2018	3,2	74
Salløv, E2	16-02-2018	3,2	27
Salløv, E2	02-03-2018	3,2	2

Appendix 3. Radiocarbon and DNA analysis

TABEL A3.1. Samples types, and extraction and sequencing working steps.

Sample name	Sample type	Extraction sample input (mg)	Qubit conc. (ng/µL)	Library Input µL	Input (ng)	Modified extraction	Index PCR Cycle number	Sequencing run	G2 DNA/RNA Enhancer	Inhibitor removal
PP2-330	Root fossil	219	1.18	32	37.76		12	1		
PP2-299	Root fossil	247	1.67	32	53.44		12	1		
PP2-300	Root fossil	229	2.78	32	88.96		15	1		
PP2-301	Root fossil	254	3.38	32	108.16		13	1		
PP2-337.1	Root fossil	188	3.5	32	112		15	1		
PP2-337.2	Root fossil	193	2.1	32	67.2		11	1		
Ext. Blank 1	-	-	Too low	32	>0.05		15	1		
PP2-255	Root fossil	185	1.61	32	51.52		18	1		
PP2-262	Root fossil	28	0.97	32	31.04		8	1		
PP2-34	Root channel	923	4.58	32	146.56		14	1		
PP2-35	Soil Matrix	997	Too low	32	>0.05		15	1		
PP2-76a	Root channel	538	0.32	32	10.24		17	1		
PP2-76b	Soil Matrix	1014	Too low	32	>0.05		15	1		
Ext blank 2	-	-	Too low	32	>0.05		18	1		
PP2-179	Sediment	135	0.306	30	6.1	X	12	2	x	x
PP2-192	Sediment	300	0.364	30	7.3	X	14	2	x	x
PP2-197	Sediment	480	2.74	30	54.8	X	20	2	x	x
PP2-358aDNA	Root fossil	501	5.46	30	109.2	X	6	2	x	x
PP2-359aDNA	Root fossil	257	10.2	30	204	X	16	2	x	x
CT1, 1.4m rod-kanal	Channel Sediment	172	2.14	30	42.8	X	12	2	x	x
Brilliant blue FCF (liquid solution)	E-133 CI 42090	500 µL	0.272	30	8.1	X	18	2	x	x
Extraction Blank 3	-	-	0.246	30	4.9	X	20	2	x	x
PP2-351aDNA	Sediment	439	10.1	30	202	X	6	2	x	x

Sample name	Sample type	Extraction sample input (mg)	Qubit conc. (ng/µL)	Library Input µL	Input (ng)	Modified extraction	Index PCR Cycle number	Sequencing run	G2 DNA/RNA Enhancer	Inhibitor removal
PP2-352aDNA	Sediment	500	20.8	16	221.9	X	11	2	x	x
PP2-297	Sediment	500	4.1	30	82	X	11	2	x	x
PP2-246	Sediment	705	38.2	8	203.7	X	20	2	x	x
PP2-297 %G2	Root fossil	500	Too low	30	-	X	6	2	x	x
PP2-267	Root fossil	100	9.9	30	198	X	20	2	x	x
Extraction Blank 4	-	-	0.21	30	4.2	X	20	2	x	x
PP2-248	Sediment	455	20.4	15	204	X	20	3	x	x
PP2-291	Sediment	475	41	7.5	205	X	20	3	x	x
PP2-37_Kanal	Channel Sediment Fe-oxide	505	2.86	30	57.2	X	8	3	x	x
PP2-37_Matrix	Matrix Sediment Fe-oxide	550	1.04	30	20.8	X	12	3	x	x
PP2-355	Channel Sediment Fe-oxide	486	0.536	30	10.7	X	12	3	x	x
PP2-356	Matrix Sediment Fe-oxide	480	2.88	30	57.6	X	11	3	x	x
PP82a_%G2	Channel Sediment Fe-oxide	450	Too low	30	-	X	17	3	x	x
Extraction_Blank 5	-	-	Too low	30	-	X	20	3	x	x
PP2-82a	Sediment Fe-oxide	465	0.616	30	12.3	X	13	3	x	x
PP2-82b	Sediment Fe-oxide	530	1.11	30	22.2	X	17	3	x	x
PP2-Flakkebjerg_5	Concretion sediment Fe-oxide	427	1.37	30	27.4	X	13	3	x	x
PP2-Flakkebjerg_6.1	Concretion sediment Fe-oxide	510	0.862	30	17.2	X	13	3	x	x

Sample name	Sample type	Extraction sample input (mg)	Qubit conc. (ng/µL)	Library Input µL	Input (ng)	Modified extraction	Index PCR Cycle number	Sequencing run	G2 DNA/RNA Enhancer	Inhibitor removal
PP2-Flakkebjerg_6.2	Concretion sediment Fe-oxide	510	1.01	30	20.2	X	14	3	x	x
PP2-Flakkebjerg_Matrix	Sediment Fe-oxide	516	1.75	30	35	X	15	3	x	x
PP2-82b %G2	Sediment Fe-oxide	505	Too Low	30	-	X	20	3	x	x
Extraction_Blank 6	-	-	0.604	30	12.1	X	20	3	x	x

TABLE A3.2. Samples extracted with protocol 1.

Sample	Extraction input (g)	Continued after extraction	Extraction worked
294	1.6		
297	1.2		
179	0.37	X	(+)
181	0.35	X	%
246	1		
192	0.75	X	+
190	0.61	X	+
197	0.91	X	%
248	1	X	%
347	1.9		
348	0.31		
349	1.1		
350	0.77		
351	0.62		
352	0.93	X	%
330	1.02		
331	0.94	X	%
333	0.34		
335	0.94		
337	2.12	X	(+)
338	Not noted		
303	2	X	(+)
308	2	X	%
313	0.98	X	%
327	Not noted		

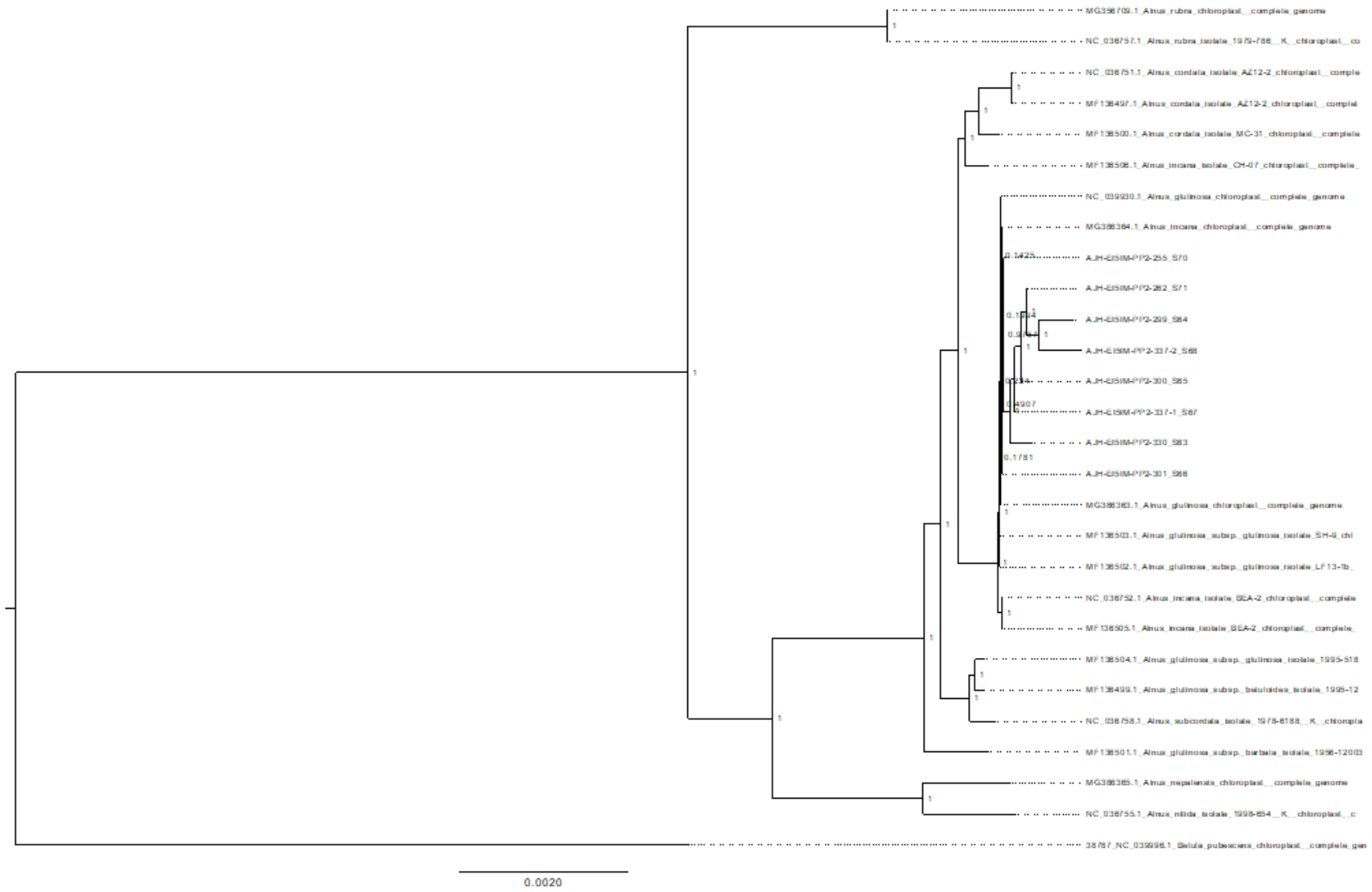

FIGURE A3.1. Tree based on full chloroplast Alnus genomes.

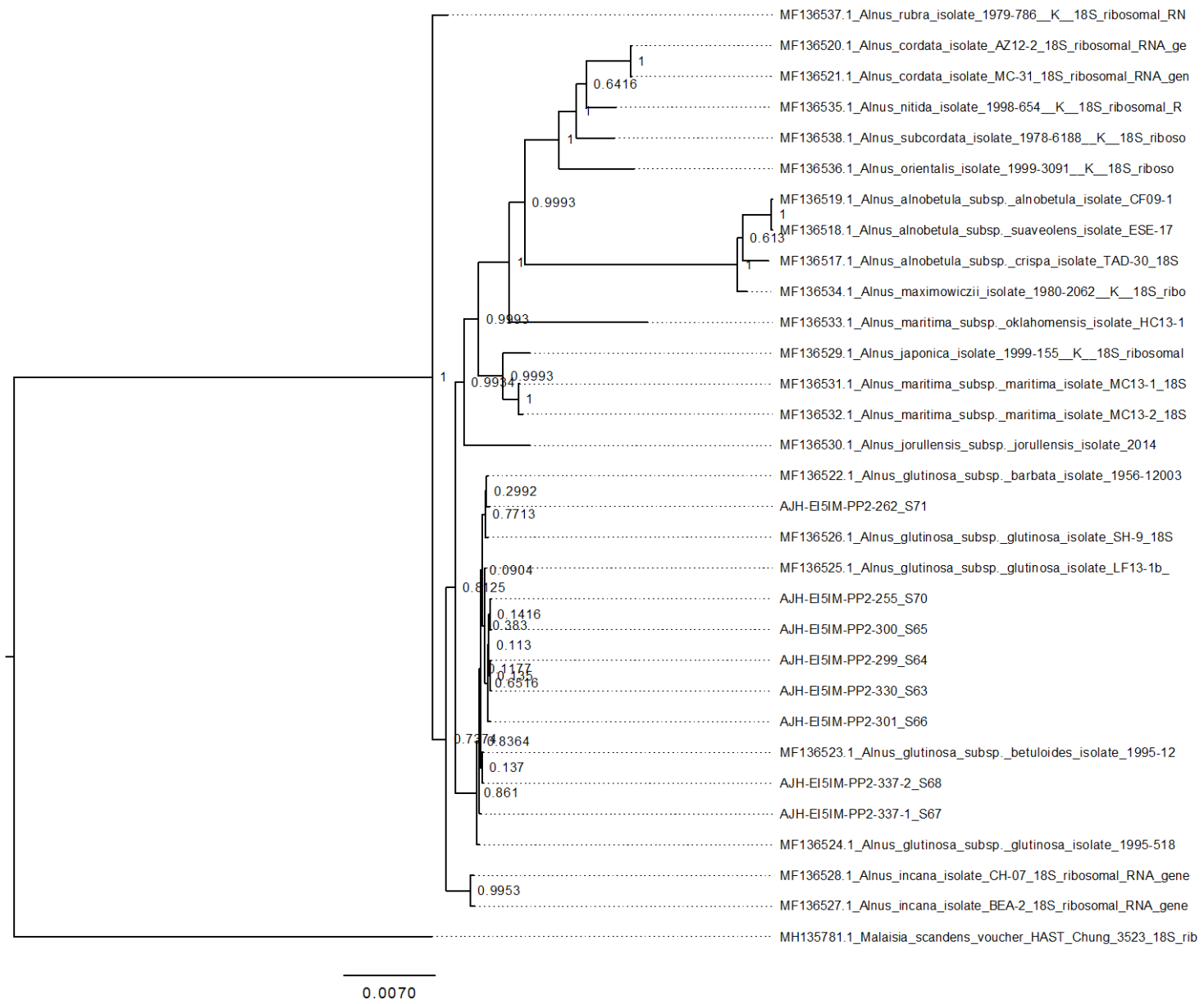

FIGURE A3.2. Phylogenetic tree based on ribosomal RNA Alnus sequences.

TABLE A3.3 Radiocarbon and stable isotope results from paleo-roots and the humic fractions of topsoil, worm burrows, root channels (grey fractures), root channels (red fractures and haloes) and clay matrix. All radiocarbon ages are provided as conventional ^{14}C years before present (BP) where BP is defined as 1950CE.

				Macrofossil		Bulk (humic fraction)		Bulk (humin fraction)	
Sample number	**Lab-ID**	**Sample Origin**	**Depth (m)**	**$\delta^{13}C$ (‰ VPDB)**	**Age (^{14}C yr. BP)**	**$\delta^{13}C$ (‰ VPDB)**	**Age (^{14}C yr. BP)**	**$\delta^{13}C$ (‰ VPDB)**	**Age (^{14}C yr. BP)**
PP2-247, E2, 0.1m	AAR-29073	Topsoil	0.1			-30.4			256 ±19
PP2-249, E3, 0.1m	AAR-29074	Topsoil	0.1			-29.8		-26.7	431 ±19
PP2-292, E4, 0.1m	AAR-29091	Topsoil	0.1			-30.0	170 ±20		1046 ±20
PP2-34, E2, 1.3m	AAR-30410	Worm burrow soil fill	1.3				1424 ±29		4082 ±31
PP2-293, E2, 1.2m	AAR-29092	Worm burrow soil fill	1.2						3851 ±34
PP2-36, E2, 1.2m	AAR-30412	Worm burrow soil fill	1.2				2069 ±27		5172 ±36
PP2-351, E2	AAR-31345	Worm burrow fill XRT1	1.2					-22.8	
PP2-352, E2, 1.3m	AAR-31346	Worm burrow soil fill XRT2	1.3				1307 ±42	-23.4	3420 ±35
PP2-161, E3, 2.5m	AAR-30425	Root channel fill (grey fracture)	2.5					-24.0	10016 ±53
PP2-180, E3, 2.5m	AAR-29068	Root channel fill (grey fracture)	2.5						6656 ±37
PP2-182, E3, 2.5m	AAR-29069	Root channel fill (grey fracture)	2.5						5474 ±49
PP2-194, E3	AAR-30417	Root channel fill (grey fracture)	2.5					-18.3	failed
PP2-158, E3	AAR-30422	Root channel fill (grey fracture)	2.8					-20.9	failed
PP2-198, E3, 2.1m	AAR-29070	Root channel fill (grey fracture)	2.1						5526 ±37
PP2-160, E3, 2.5m	AAR-30424	Root channel fill (grey fracture)	2.5					-22.2	12899 ±95
PP2-334, E5, 2.0m	AAR-29149	Root channel fill (grey fractures)	2.0						17848 ±76
PP2-200, E3, 2.5m	AAR-29143	Root channel fill (grey fractures)	2.5						14412 ±70
PP2-227, E3, 2.0m	AAR-30435	Root channel fill (grey fractures)	2.0			-40.5			15539 ±147
PP2-185, E3, 2.1m	AAR-30674	Root channels (grey fracture)	2.1						9191 ±56
PP2-159, E3, 2.8m	AAR-30423	Root channels infill (grey fracture)	2.8					-23.3	15377 ±74
PP2-255, E6, 1.3m	AAR-30427	Fossil root	1.3	-27.2	5651 ±31				
PP2-256, E6, 0.9m	AAR-30428	Fossil root	0.9	-28.6	5969 ±33				
PP2-358, E5, 1.8m	AAR-31347	Fossil root	1.8		2984 ±28				
PP2-263, E4, 2.0m	AAR-29077	Fossil root	2.0	-28.0	6240 ±25				
PP2-270, E4, 2.0m	AAR-29081	Fossil root	2.0	-27.5	3119 ±23				
PP2-307, E4, 2.1m	AAR-29095	Fossil root	2.1	-29.0	3215 ±23				

				Macrofossil		Bulk (humic fraction)		Bulk (humin fraction)	
Sample number	**Lab-ID**	**Sample Origin**	**Depth (m)**	**$\delta^{13}C$ (‰ VPDB)**	**Age (^{14}C yr. BP)**	**$\delta^{13}C$ (‰ VPDB)**	**Age (^{14}C yr. BP)**	**$\delta^{13}C$ (‰ VPDB)**	**Age (^{14}C yr. BP)**
PP2-312, E4, 2.1m	AAR-29096	Fossil root	2.1	-28.9	3192 ±25				
PP2-302, E4, 2.2m	AAR-29094	Fossil root	2.2	-30.3	3237 ±24				
PP2-262, E4, 2.2m	AAR-30429	Fossil root	2.0	-29.5	6176 ±33				
PP2-359, E5, 2.3m	AAR-31348	Fossil root	2.3		2880 ±33				
PP2-332, E5, 3.0m	AAR-29141	Fossil root	3.0	-29.4	2797 ±26				
PP2-337, E5, 2.0m	AAR-29150	Fossil root	2.0	-30.0	2833 ±22				
PP2-229, E3, 2.3m	AAR-30436	Clay matrix	2.3						25950 ±121
PP2-193, E3, 2.4m	AAR-29140	Clay matrix	2.4						19629 ±59
PP2-202, E3, 2.5m	AAR-29144	Clay matrix	2.5						22014 ±91
PP2-168, E3, 2.8m	AAR-30426	Clay matrix	2.8					-26.8	22412 ±117
PP2 174, E3, 3.0m	AAR-30717	Clay matrix	3.0					-24.0	17346 ±99
PP2-82b, E2	AAR-30421	Clay matrix	5.2				19375 ±104		27952 ±148
PP2-37b, E2	AAR-30416	Clay matrix	5.4						25862 ±115
PP2-296, E2	AAR-29093	Clay matrix	1.2				8209 ±36		8642 ±32
PP2-338, E4	AAR-29496	Bulk sand from sand layer	3.2						20,382 ±79
PP2-338 OM, E4	AAR-29151	Organic fragments from sand layer	3.2				15140 ±66		39702 ±544
PP2-452, E3	AAR-29152	root fragment from till matrix	2.0		35341 ±354				
PP1-13, B5, 0.1m	AAR-24010	Topsoil	0.1				13 ±27		294 ±21
PP1-10, B5, 1.4m	AAR-24007	Wall of worm burrow	1.4				2597 ±36		10197 ±71
PP1-11, B5, 1.5m	AAR-24008	Worm burrow soil fill	1.5				1164 ±31		3205 ±37
PP1-12, B5, 1.5m	AAR-24009	Matrix 3 cm from worm burrow	1.5				3372 ±39		8703 ±48
PP1-15, B5, 2.8m	AAR-24254	Grey halo of root channel	2.8				3805 ±66		16478 ±126
PP1-17, B5, 2.8m	AAR-24255	Red halo of root channel	2.8				4734 ±120		21097 ±163
PP1-18, B5, 2.8m	AAR-24256	Clay matrix	2.8				12011 ±84		28486 ±159
PP1-14, B5, 3.5m	AAR-24011	Clay matrix	3.5				9157 ±89		21325 ±101
PP1-22, B9, 4.5m	AAR-26081	Root channel concretion							18184 ±124
PP1-23, B9, 4.5m	AAR-26082	Root channel concretion	4.5						20520 ±82
PP1-24, B9, 4.5m	AAR-26083	Root channel concretion	4.5						18685 ±81
PP1-19, B9, 4.5m	AAR-26078	Clay matrix	4.5						20502 ±79

				Macrofossil		Bulk (humic fraction)		Bulk (humin fraction)	
Sample number	**Lab-ID**	**Sample Origin**	**Depth (m)**	**$\delta^{13}C$ (‰ VPDB)**	**Age (^{14}C yr. BP)**	**$\delta^{13}C$ (‰ VPDB)**	**Age (^{14}C yr. BP)**	**$\delta^{13}C$ (‰ VPDB)**	**Age (^{14}C yr. BP)**
PP1-20, B9, 4.5m	AAR-26079	Clay matrix	4.5						20824 ±82
PP1-21, B9, 4.5m	AAR-26080	Clay matrix	4.5						20906 ±194
PP1-25, B9, 4.5m	AAR-30430	Clay matrix	4.5						21822 ±110

TABLE A3.4. Photographic documentation of soil sampling and results of radiocarbon dating and aDNA

Sampling excavations (E)

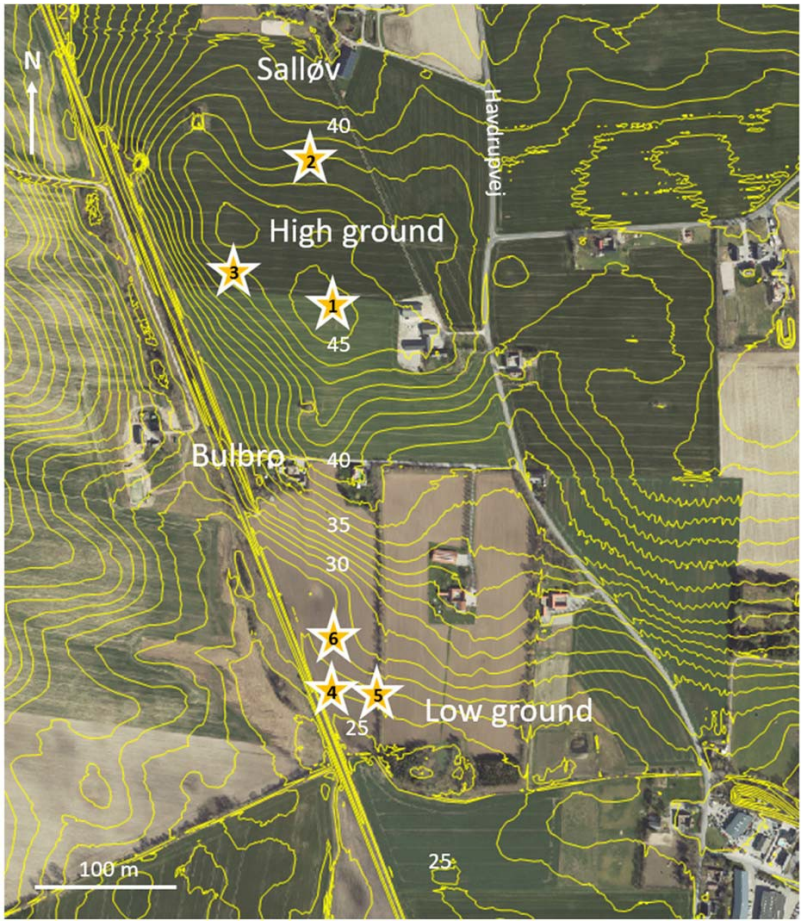

Key:

Red: aDNA

Blue:^{14}C All radiocarbon ages are provided as conventional ^{14}C years before present (BP) where BP is defined as 1950CE.

ND: no plant aDNA detected

NA: not analysed

OM: organic matter

HG: high-ground

LG: low-ground

E2 (HG), topsoil, 0-0.1 m depth

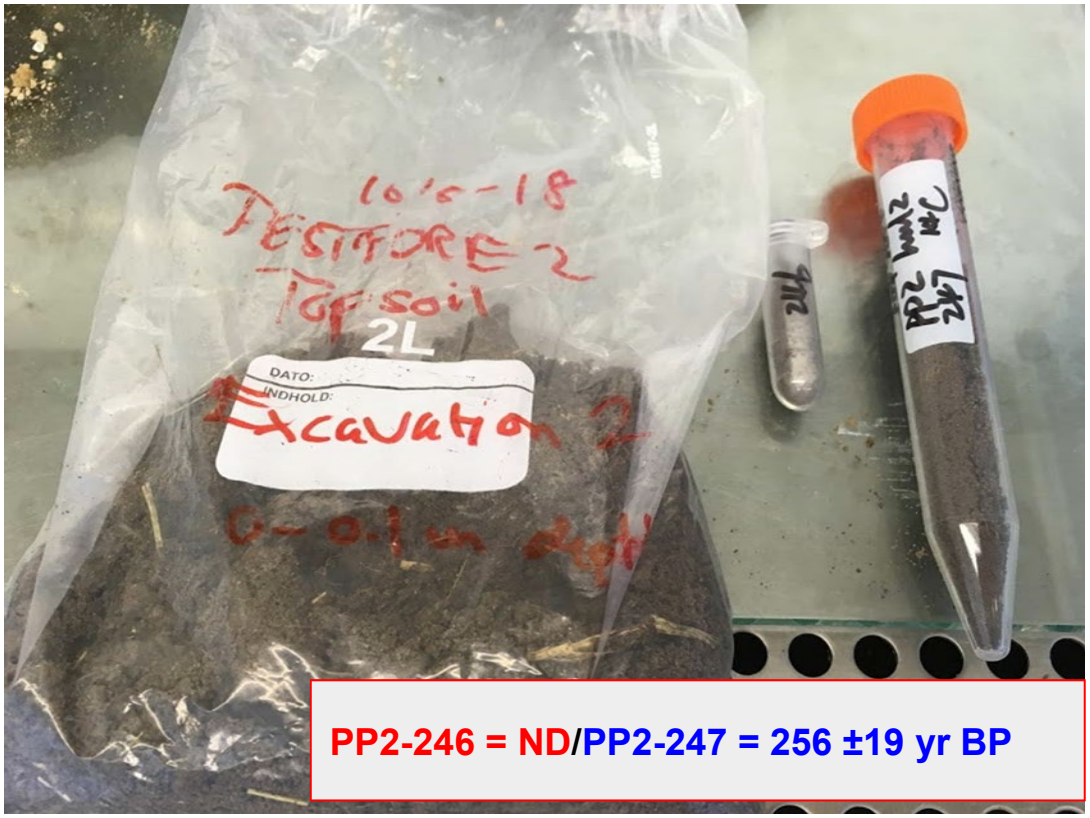

Red No. for aDNA
Blue No. for ^{14}C (humin fraction)

PP2-246 = ND/PP2-247 = 256 ±19 yr BP

E3 (HG), topsoil, 0-0.1 m depth

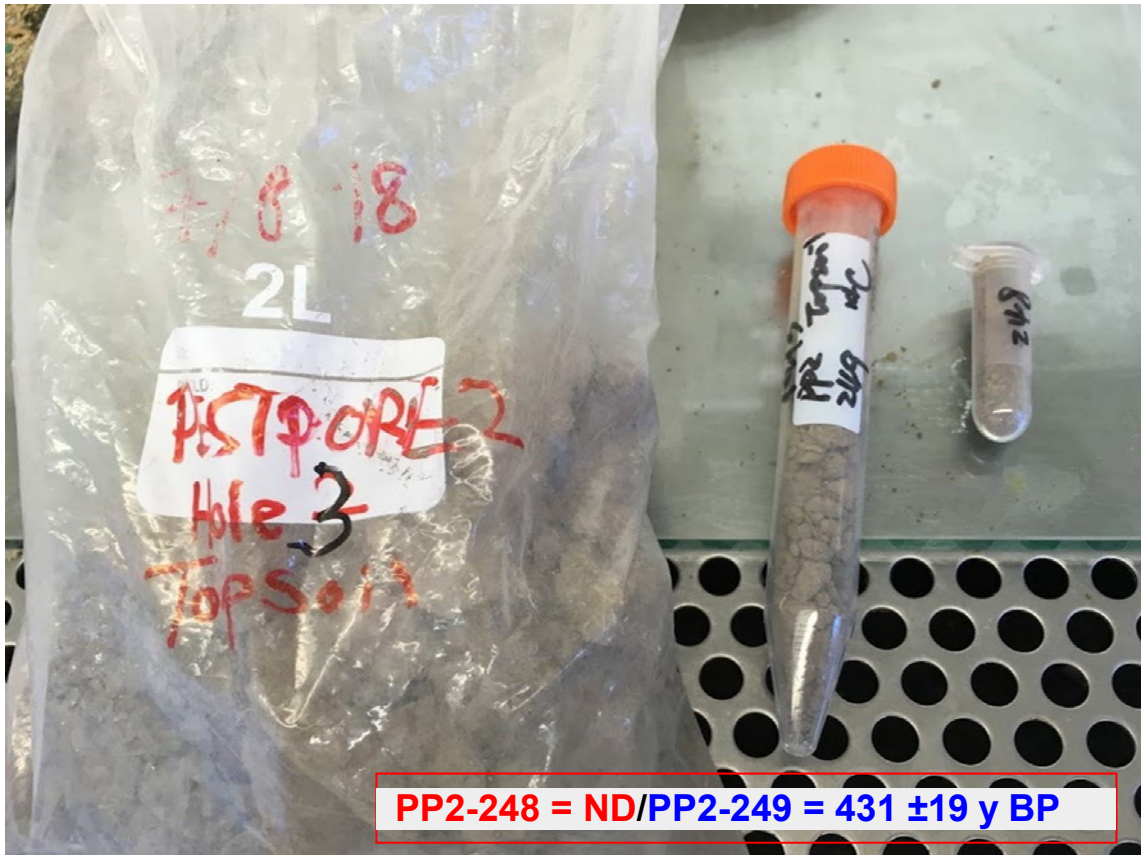

Red No. for aDNA
Blue No. for ^{14}C (humin fraction)

E4 (LG), topsoil, 0-0.1 m depth

Red No. for aDNA
Blue No. for ^{14}C (humin fraction)

PP2-291 = ND/PP2-292 = 1,046 ±20 yr BP

E2 (HG), BB1-exp., 1.2-1.6 m depth

(XRT column 1)

Worm burrow 1.2 m PP2-351=
ND/PP2-351 = failed

Worm burrow 1.3 m PP2-252 =
ND/PP2-252 = 3,420 ±35yr BP

Worm burrow 1.5 m PP2-CT1 =
ND/PP2-CT1 = NA

Red No. for aDNA
Blue No. for ^{14}C (humin fraction)

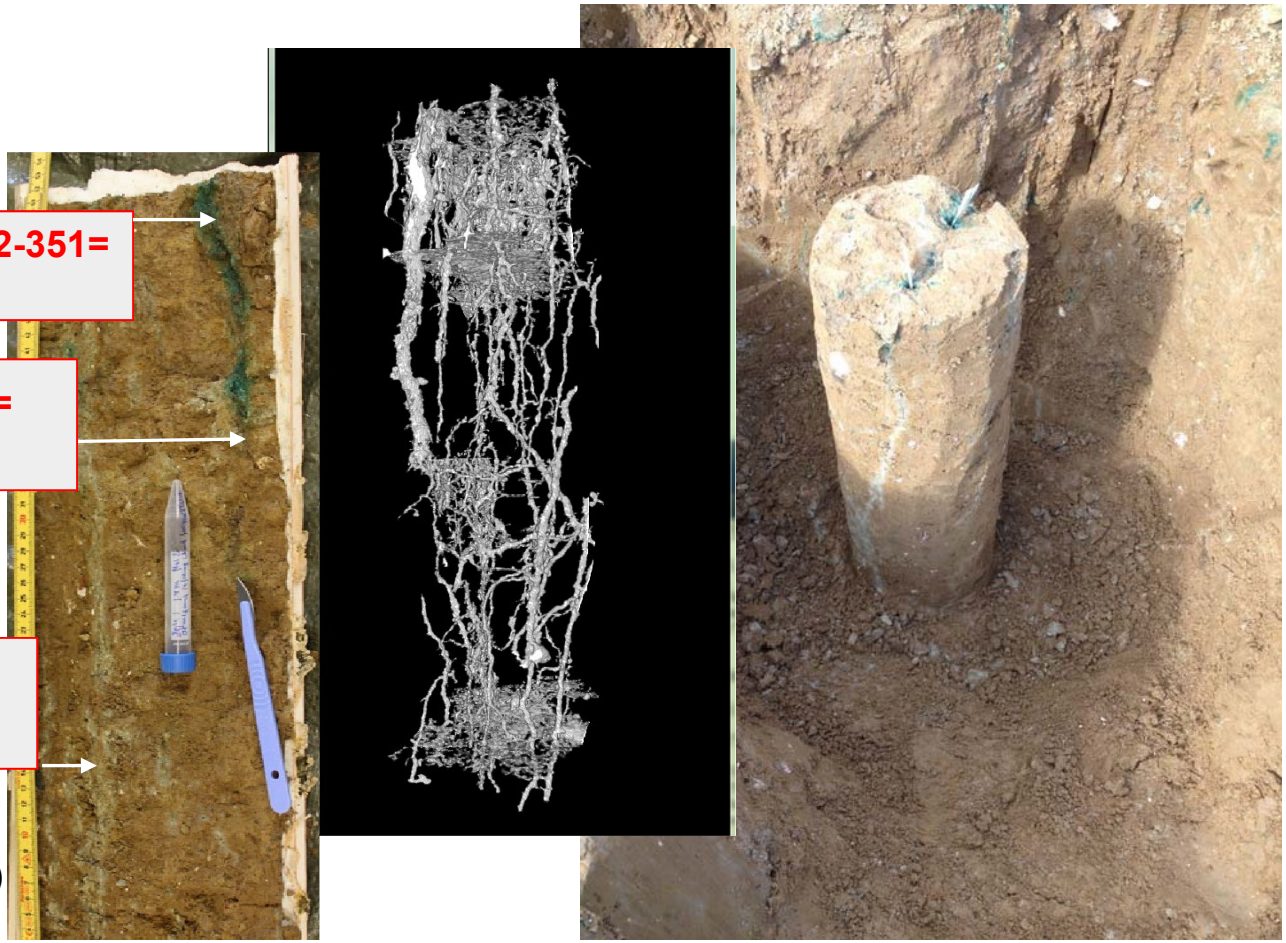

E2 (HG), BB2-exp. 1.1-1.2 m depth

Red No. for aDNA
Blue No. for ^{14}C (humin fraction)

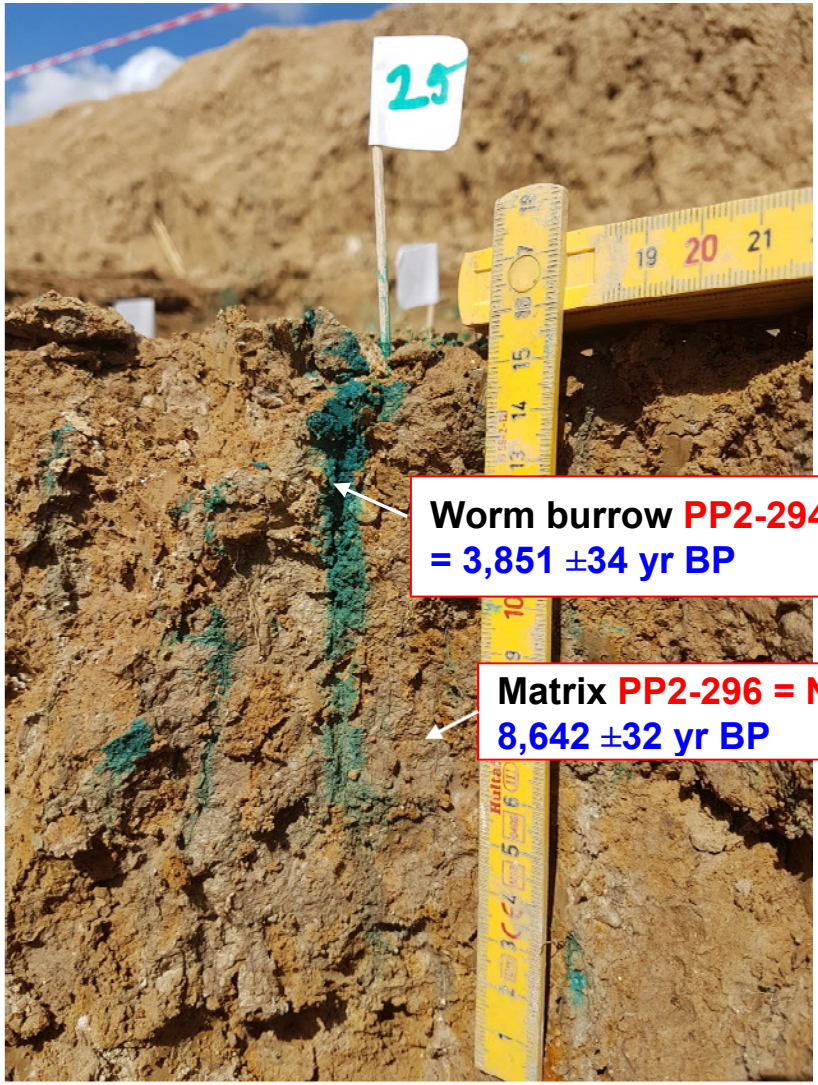

E2 (HG), BB2-exp. 1.1-1.3 m depth

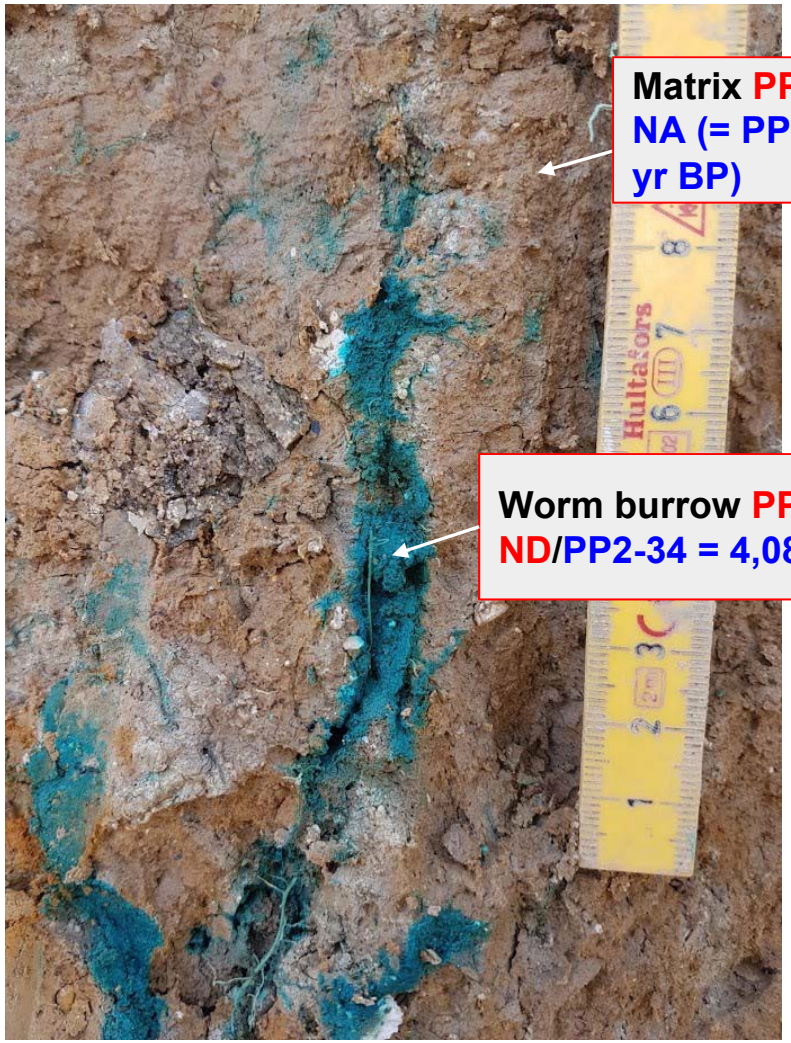

Red No. for aDNA
Blue No. for ^{14}C (humin fraction)

E2 (HG), BB2-exp. 1.1-1.2 m depth

Red No. for aDNA
Blue No. for ^{14}C (humin fraction)

E2 (HG), 2.8 m depth

(root channels in vertical grey fracture),

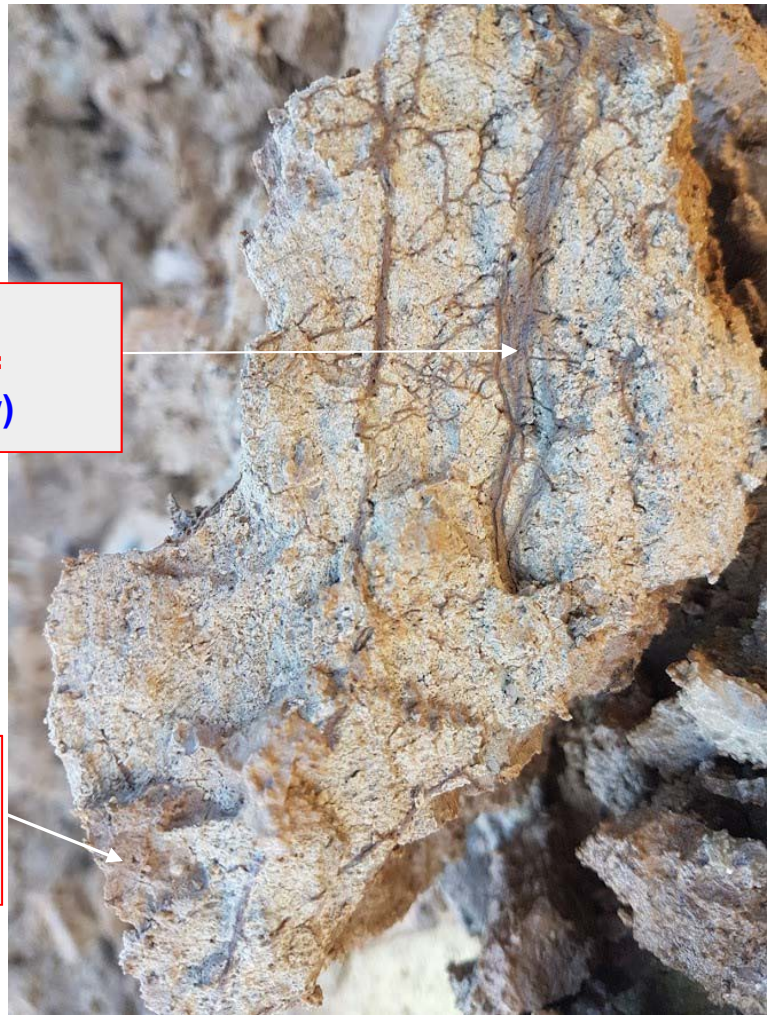

Root channel PP2-76a = ND/76a = NA (OM to low)

Matrix PP2-76b = ND/PP2-76b = NA (OM to low)

Red No. for aDNA

Blue No. for ^{14}C (humin fraction)

E2 (HG), prior to BB6 exp.
5.2 m depth

(Fe/Mn-oxide filled vertical red fracture in reduced matrix)

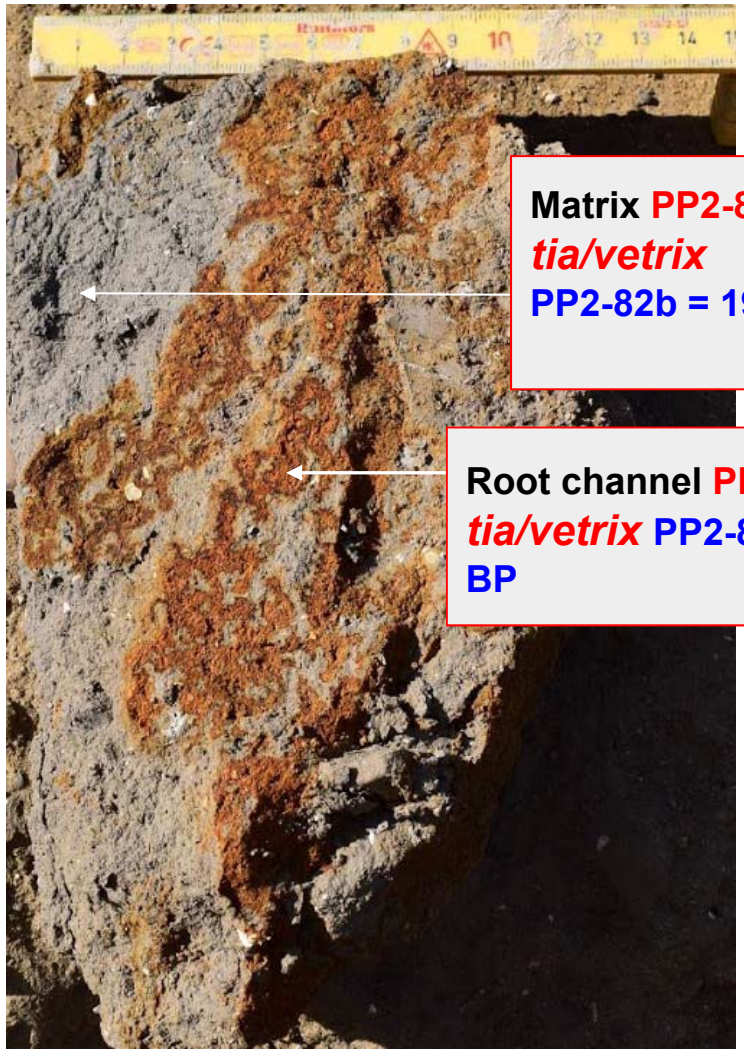

Matrix **PP2-82b** = ***S. chamae-tia/vetrix***
PP2-82b = 19,066 ± 48 yr BP

Root channel **PP2-82a** = ***S. chamae-tia/vetrix*** **PP2-82a = 21,924 ± 100 yr BP**

Red No. for aDNA.
Blue No. for ^{14}C (pyroxidation)

E2 (HG), BB6 exp. 5.4 m depth

(Fe/Mn-oxide filled vertical red fracture in reduced matrix)

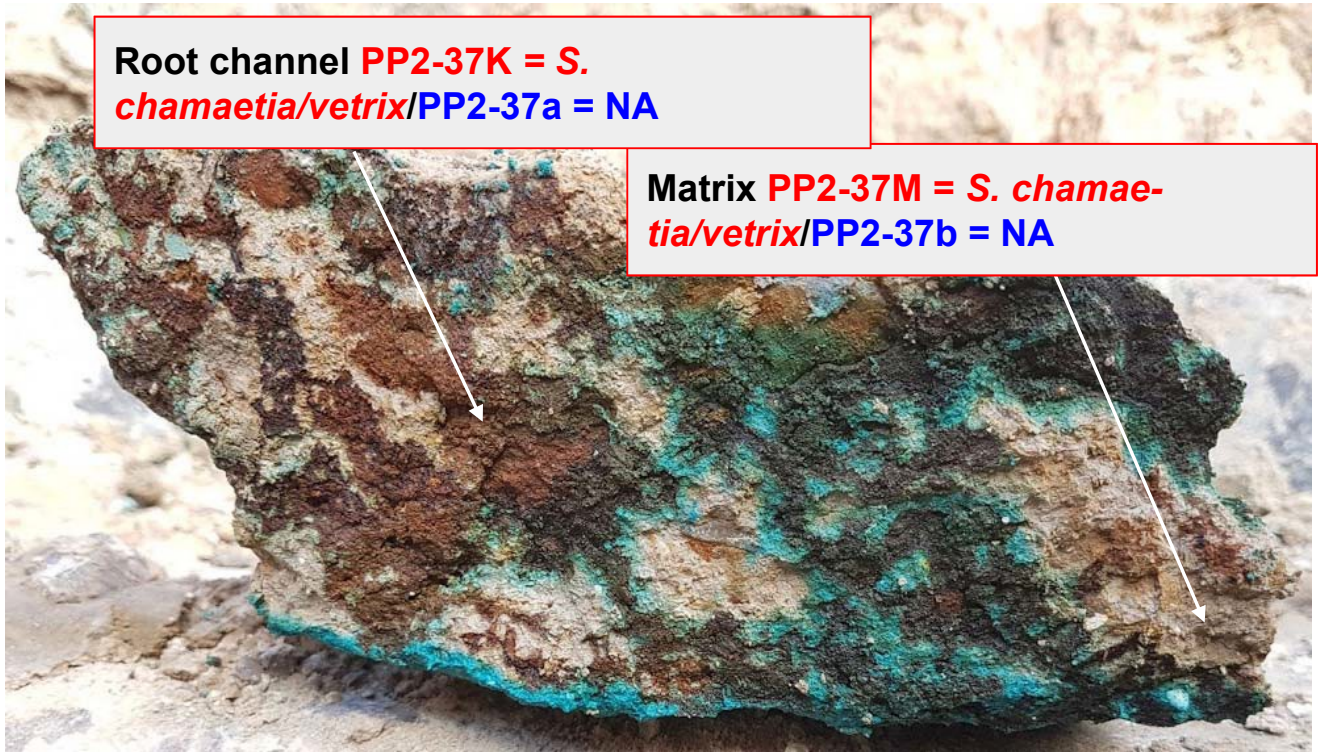

Red No. for aDNA.
Blue No. for ^{14}C.

E2 (HG), BB5 exp. 5.4 m depth

(Fe/Mn-oxide filled vertical red fracture in reduced matrix).

The two sides of main fracture in LUC (large undisturbed column) collected from BB5 exp. for hydraulic lab experiments (Aamand et al. *in prep.2020*).

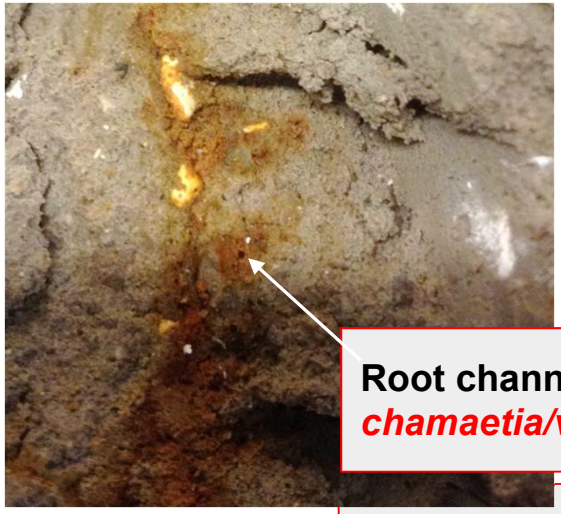

Root channel PP2-355 = *S. chamaetia/vetrix*/PP2-353 NA

Matrix PP2-356 = *S. chamaetia/vetrix* /PP2-356 NA

Red No. for aDNA.
Blue No. for ^{14}C.

E3 (HG), BB8 exp. 2.3 – 2.5 m depth

(dyed root channels along vertical grey fracture in oxidized clay

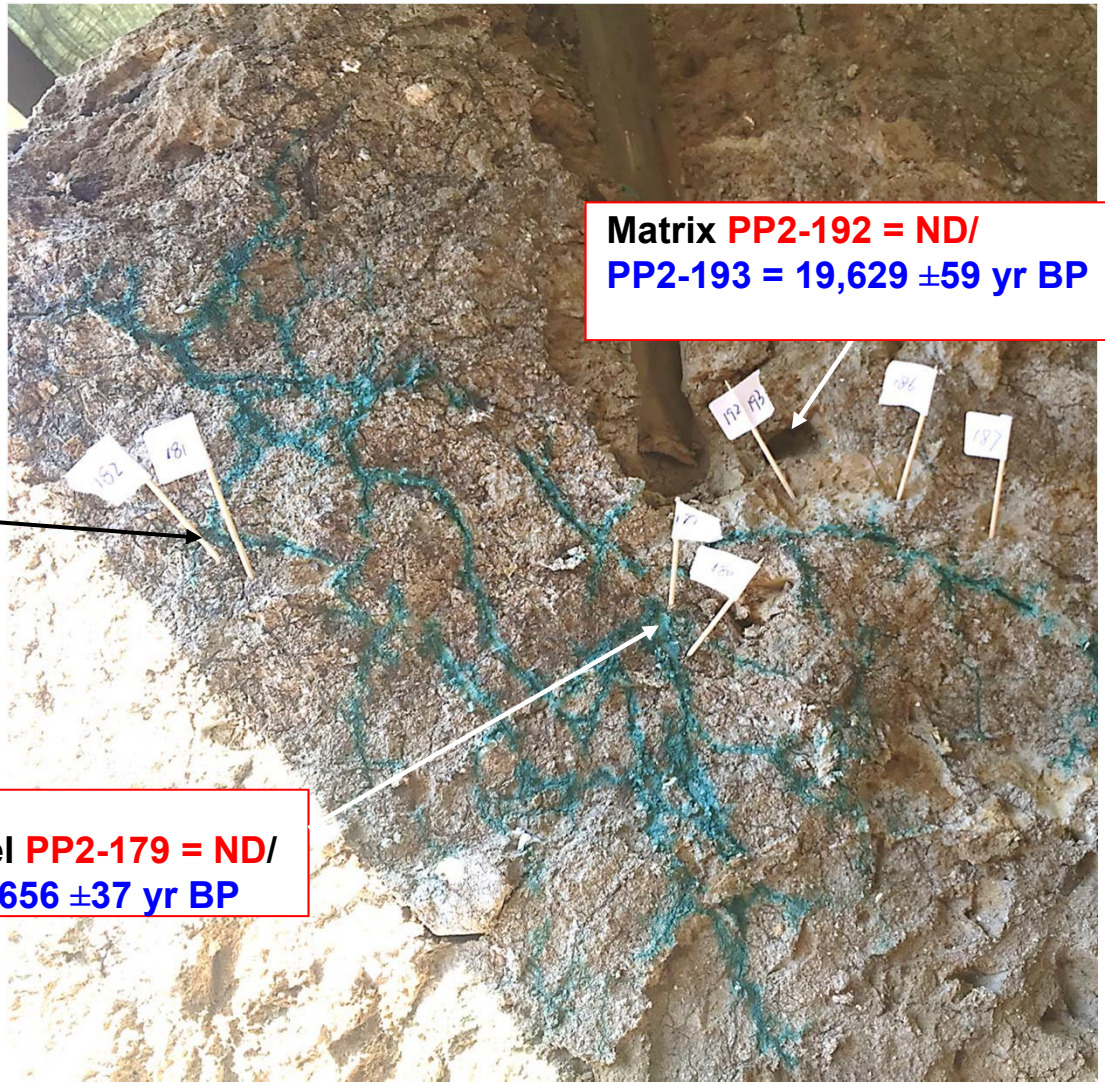

Root channel PP2-181 = NA/ PP2-182 = 5,474 ±49 yr BP

Matrix PP2-192 = ND/ PP2-193 = 19,629 ±59 yr BP

Root channel PP2-179 = ND/ PP2-180 = 6,656 ±37 yr BP

Red No. for aDNA
Blue No. for ^{14}C (humin fraction)

E3 (HG), BB8 exp. 2.5 m depth

(dyed root channels along vertical grey fracture in oxidized clay)

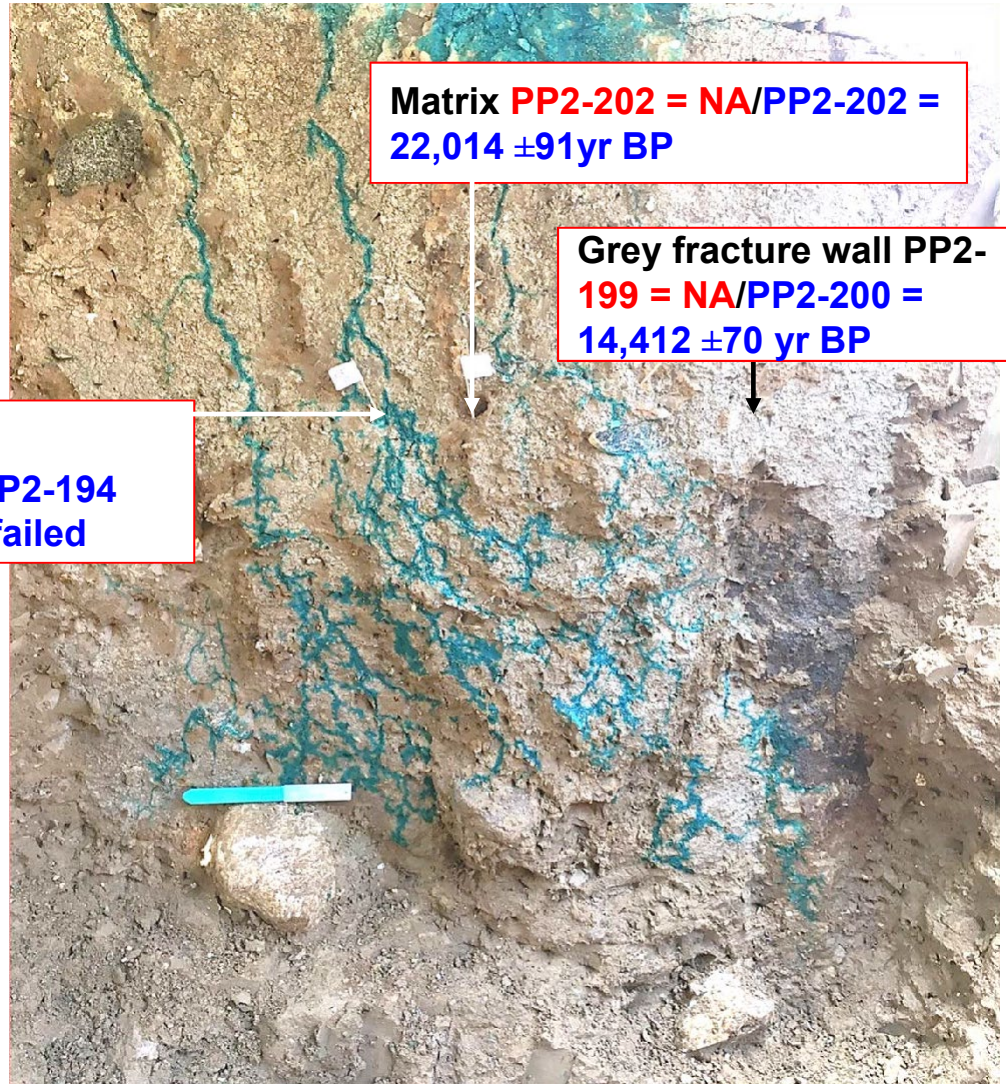

Red No. for aDNA
Blue No. for ^{14}C (humin fraction)

E3 (HG), BB8
2.1 m depth

(dyed root channels along vertical grey fracture in oxidized clay)

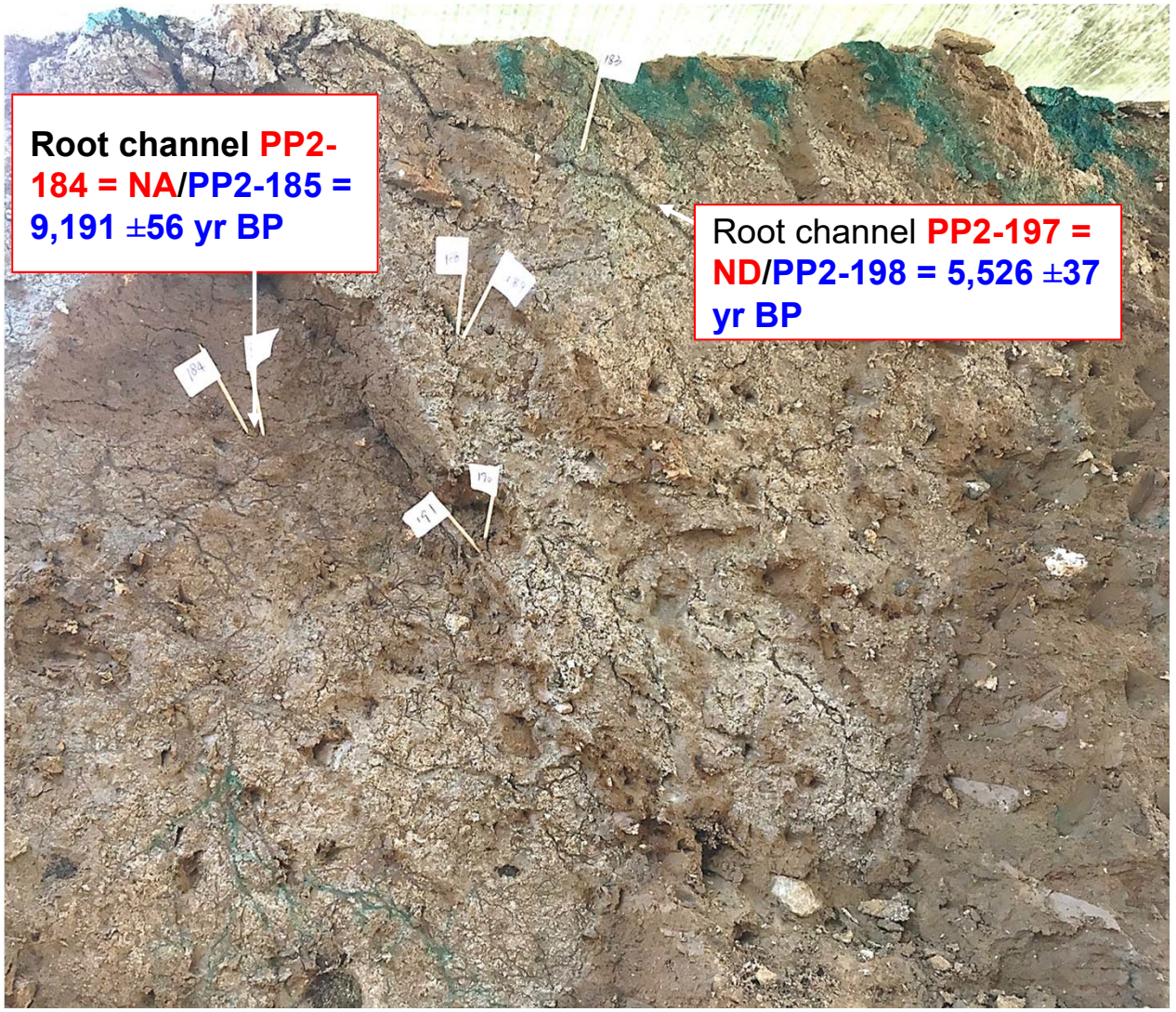

Red No. for aDNA
Blue No. for ^{14}C (humin fraction)

E3 (HG), BB8 exp. 2.8 m depth

(dyed root channels along grey vertical fracture in oxidized clay)

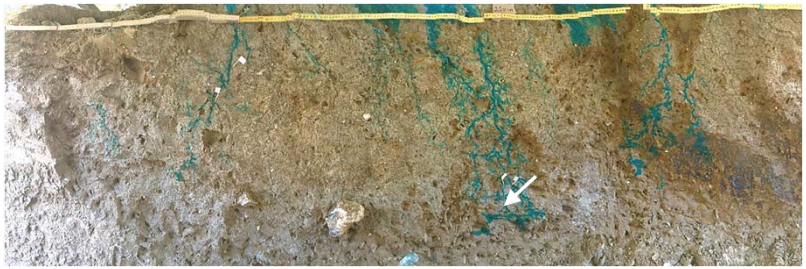

(width =2 m)

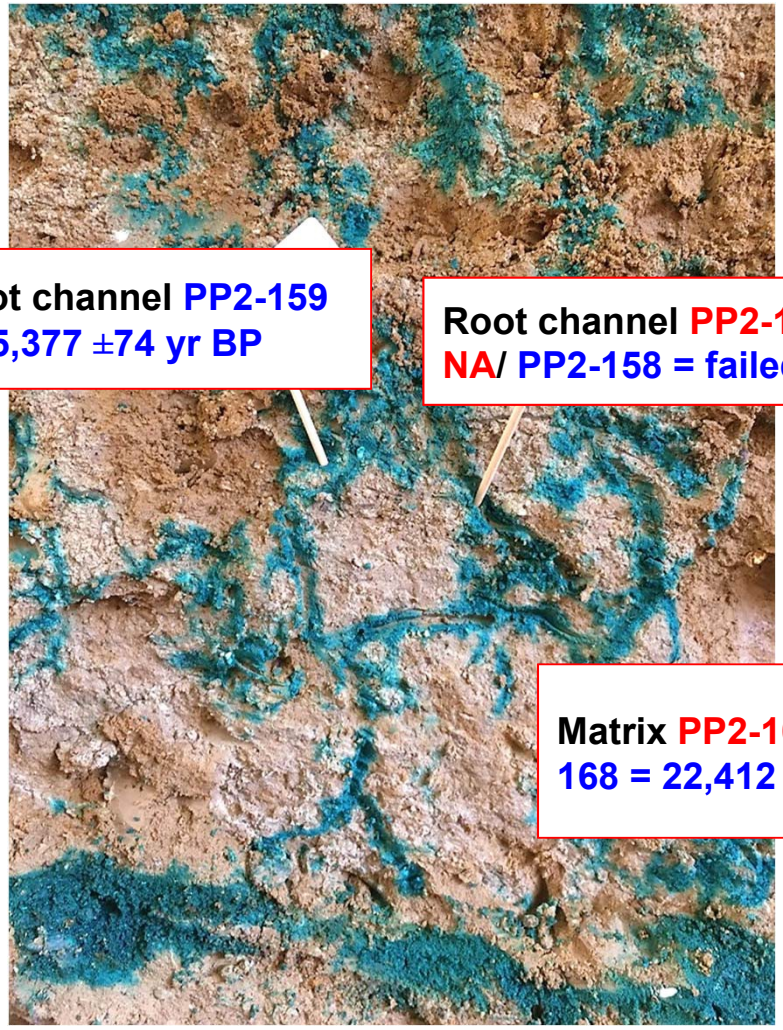

Root channel PP2-159 = 15,377 ±74 yr BP

Root channel PP2-158 = NA/ PP2-158 = failed

Matrix PP2-168 = NA/PP2-168 = 22,412 ±117 yr BP

Red No. for aDNA
Blue No. for ^{14}C (humin fraction)

E3 (HG), BB8, 2.5 m depth

(dyed root channels along grey vertical fracture in oxidized clay)

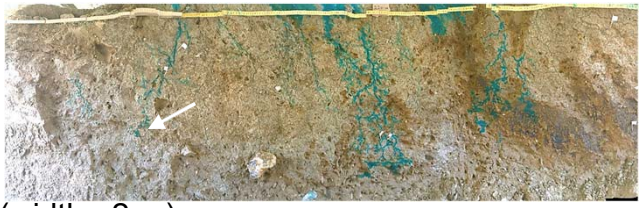

(width =2 m)

Root channel PP2-160 = NA/PP2-160 = 12,899 ±95 yr BP

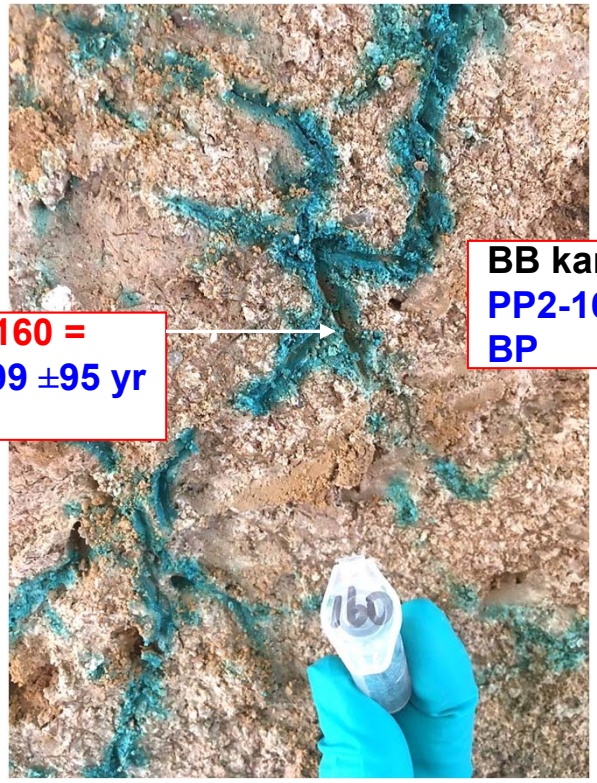

BB kanal 161 = NA/ PP2-161 = 10,016 ±53 yr BP

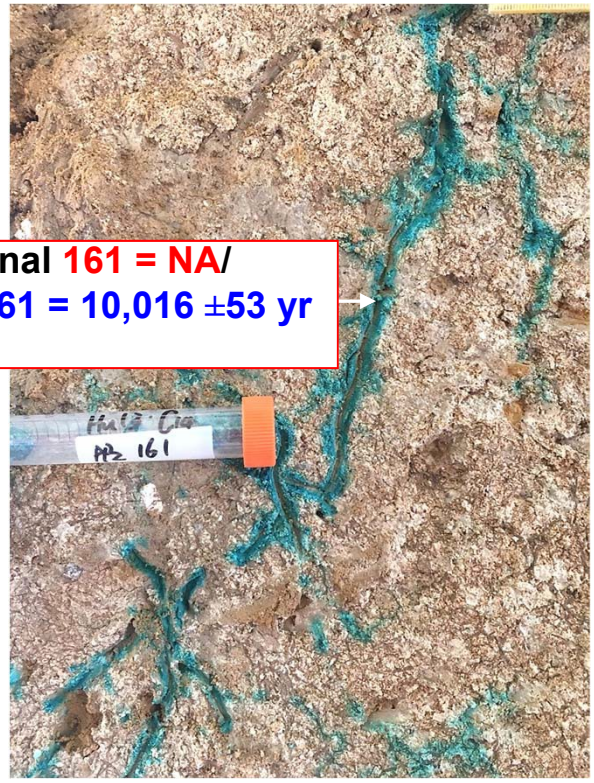

Red No. for aDNA
Blue No. for ^{14}C (humin fraction)

Particular plastic channel fill (allowed for more effective separation of channel fill from till matrix)

E3 (HG), next to BB8, 2 m depth

(root channels along vertical fracture in oxidized clay)

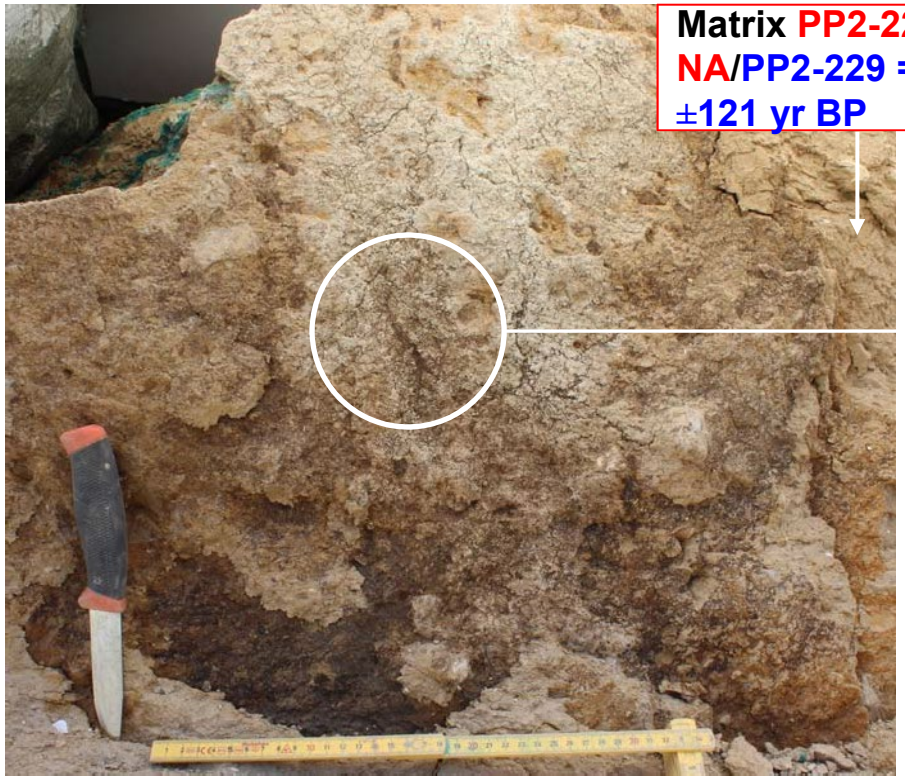

Matrix PP2-229 = NA/PP2-229 = 25,950 ±121 yr BP

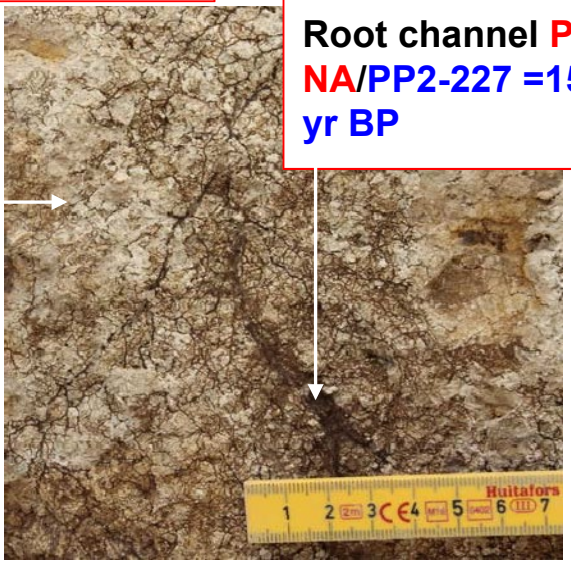

Root channel PP2-227 = NA/PP2-227 =15,539 ±147 yr BP

Red No. for aDNA
Blue No. for ^{14}C (humin fraction)

E4 (LG), wall of excavation next to BB10, 2.3 m depth, (Fossil root in reduced clay)

Red No. for aDNA
Blue No. for ^{14}C

E4 (LG), wall of excavation next to BB10, 2.1 m depth (twin fossil roots in oxidized/reduced clay)

Root 1.1 PP2-301 = *A. glutinosa* /PP2-312 = 3,192 ±25 yr BP

Root1.2 PP2-300 = *A. glutinosa* /PP2-307 = 3215 ±23 yr BP

Red No. for aDNA
Blue No. for ^{14}C

E4 (LG), floor of excavation with BB10, 2 m depth (fossil roots along ghost-fractures in oxidized/reduced clay)

Fossil root PP2-271 = NA/PP2-270 = 3,119 ±23 yr BP

Fossil root PP2-262 = *A. glutinosa*/PP2-262 = 6,176 ±33 yr BP

Fossil root PP2-267 = *A. glutinosa*/PP2-263 = 6,240 ±25 yr BP

E4 (LG), 3.2 m depth

Sand layer with embedded organic fragments

PP2-338 OM = NA/PP2-338 OM = 39,702 ±544 yr BP

PP2-338 = NA/PP2-338 = 20,382 ±79 yr BP

Red No. for aDNA
Blue No. for ^{14}C (humin fraction)

E5 (LG), XRT Column4 next to BB10 and 11, 1.8-2.3 m depth

(2 fossil roots (same system) in oxidized/reduced clay)

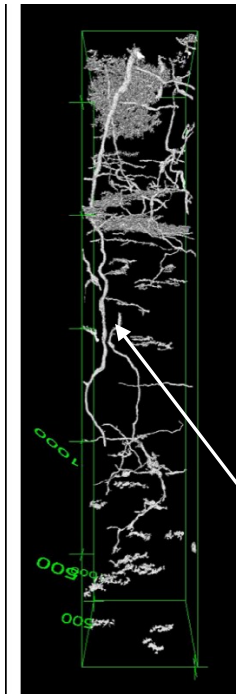

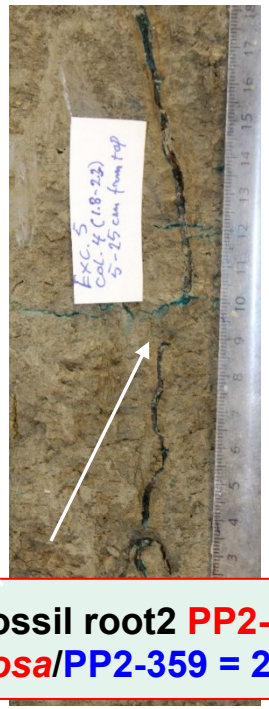

Fossil root2 PP2-359a = *A. glutinosa*/PP2-359 = 2880 ±33 yr BP

Fossil root1 PP2-358a = *A. glutinosa*/PP2-358 = 2984 ±28 yr BP

Red No. for aDNA
Blue No. for ^{14}C (humin fraction)

E5 (LG), ghost-fracture containing fossil root next to BB10 and 11, 2-3 m depth

Fossil root in oxidized/ reduced clay

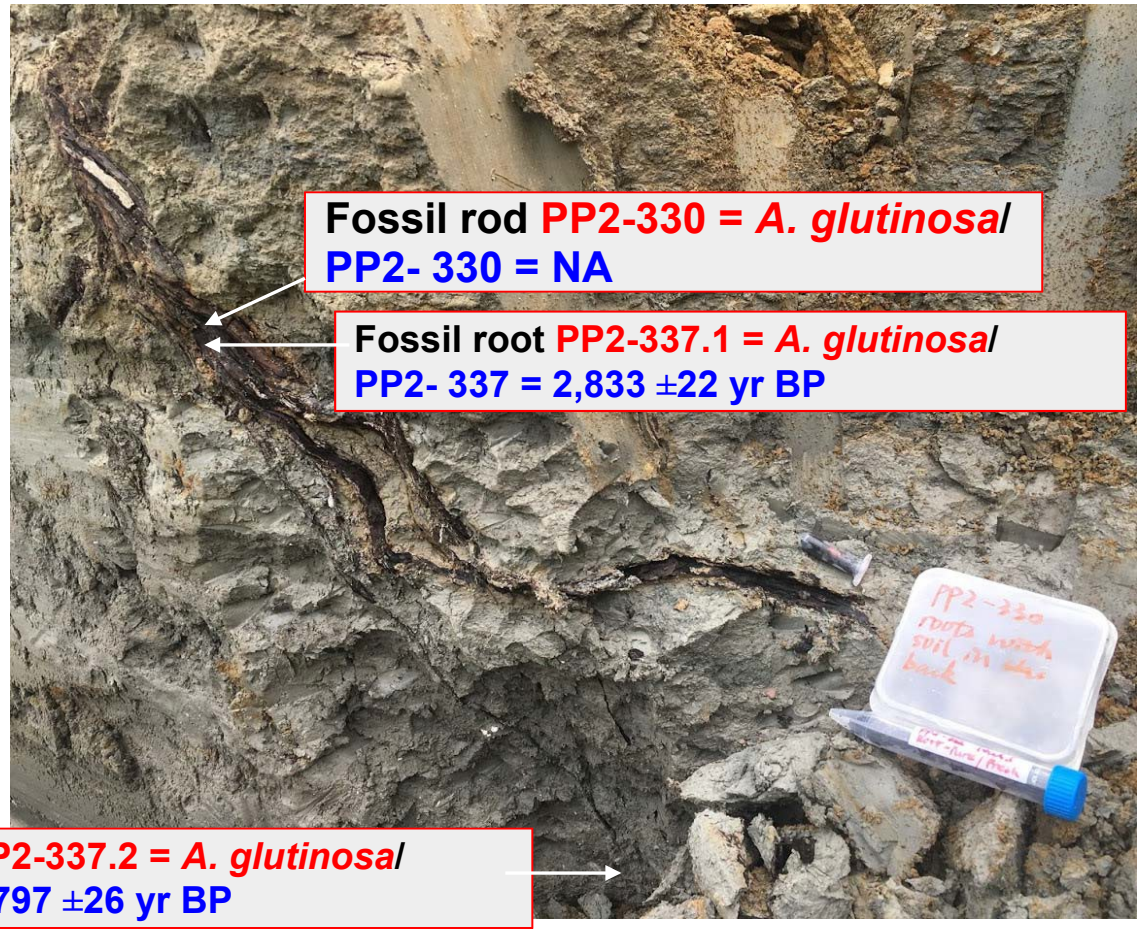

E5 (LG), horizontal surface next to BB10 and BB11, 2 m depth

Residual root hole with Fe-oxide staining in clay

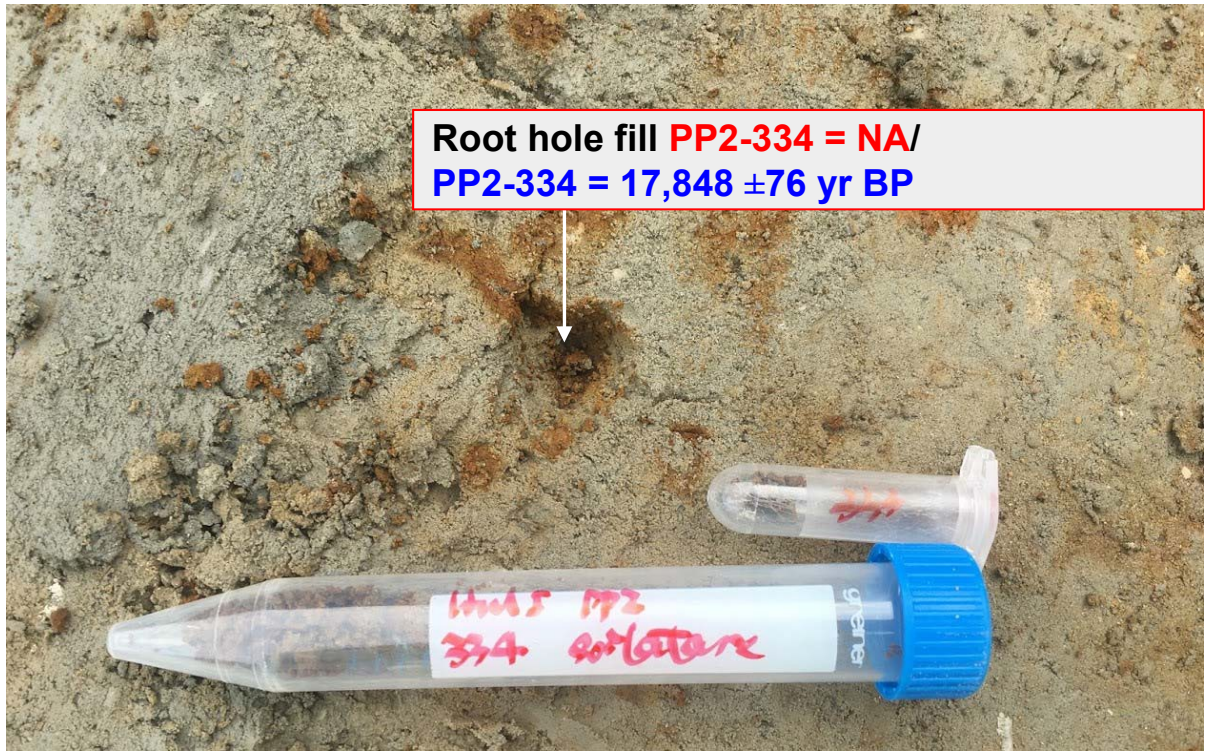

Red No. for aDNA
Blue No. for ^{14}C (humin fraction)

E6 (LG), horizontal surfaces in 0.9 and 1.3 m depth

Fossil roots in local depression

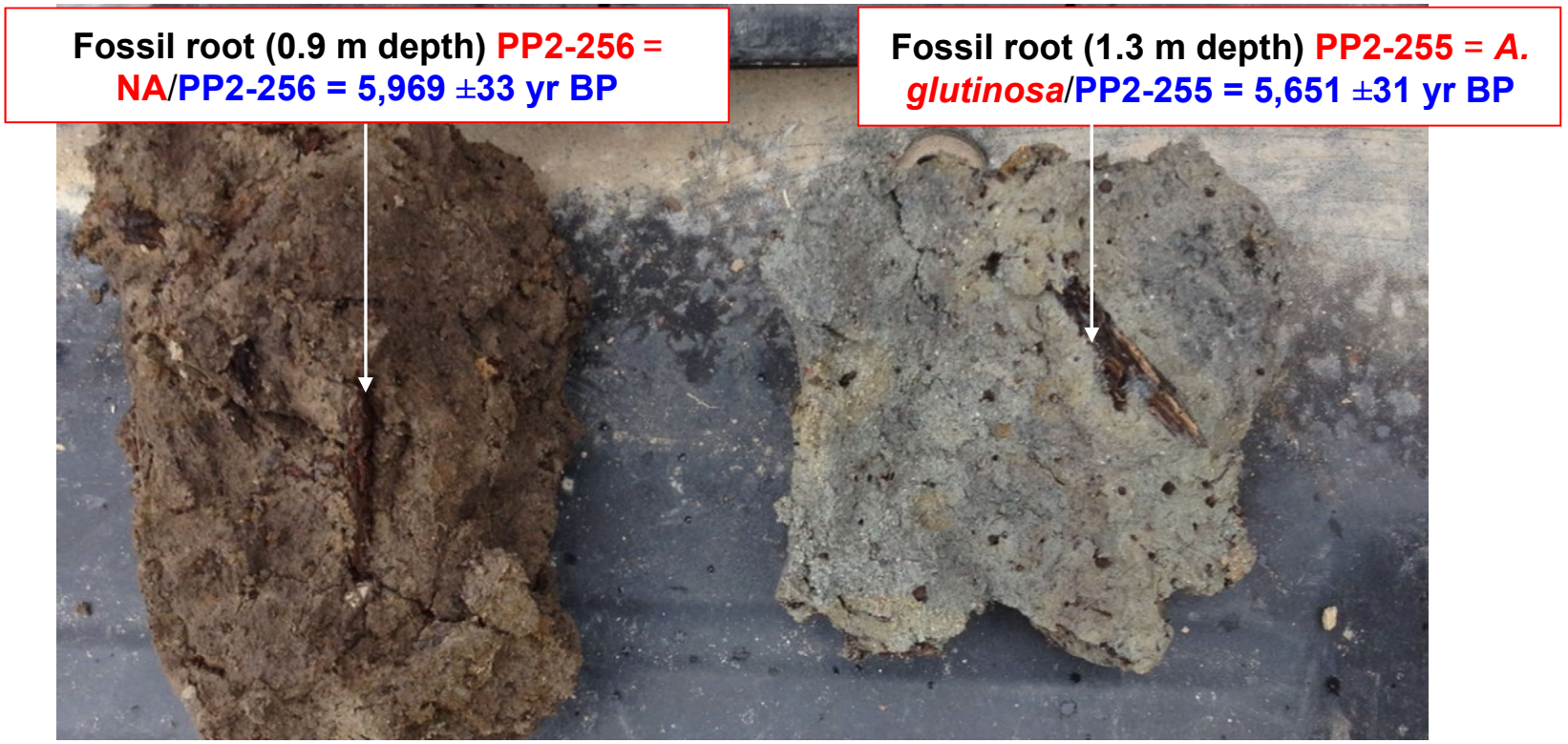

Flakkebjerg site (Jørgensen et al. 2017)

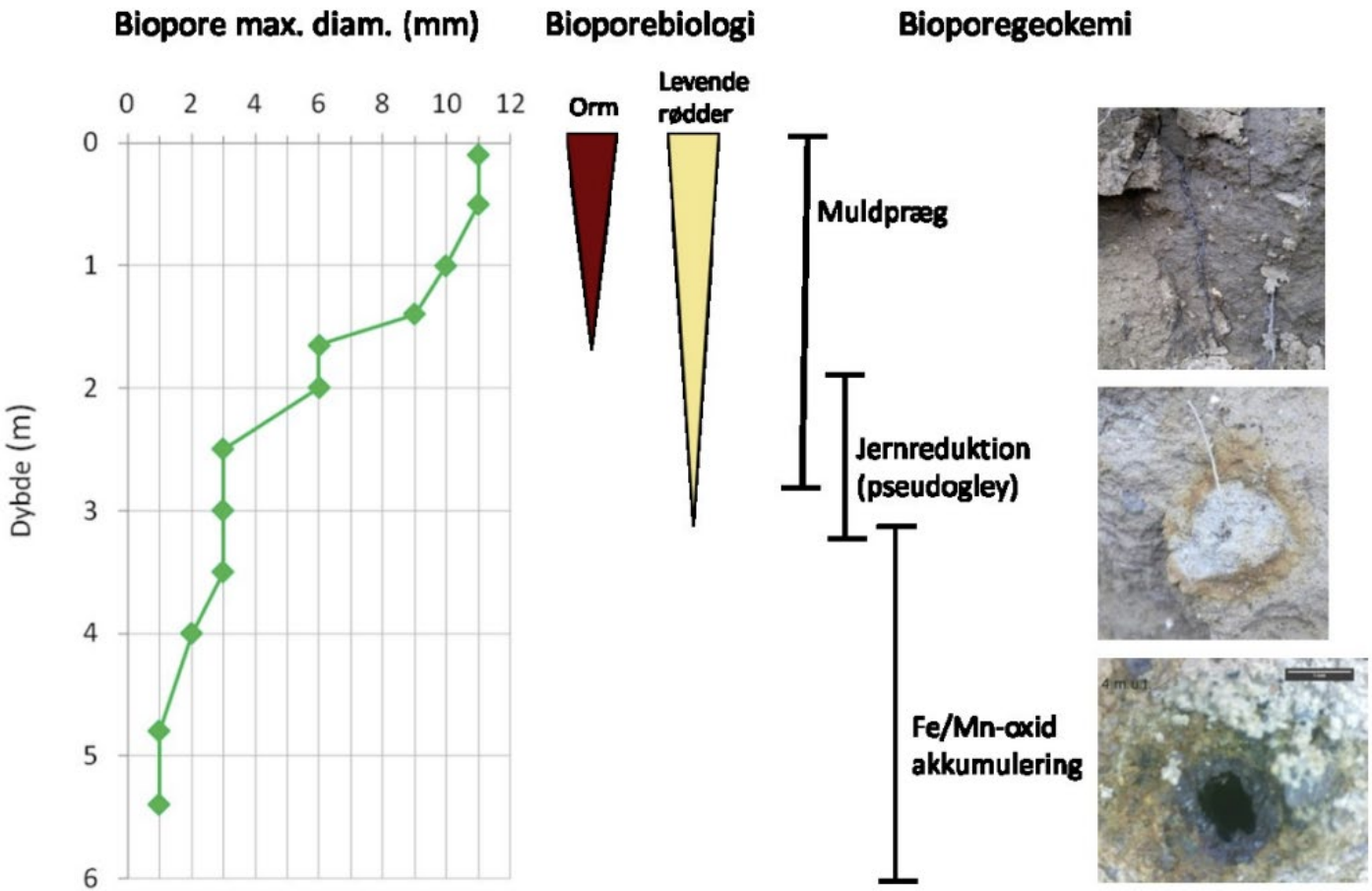

Flakkebjerg site (HG) 0.1 m depth

Topsoil

PP1-13 = NA/PP1-13 = 294 ±21 yr BP

Red No. for aDNA
Blue No. for ^{14}C (humin fraction)

Flakkebjerg site (HG) 1.5 m depth

Fill from worm burrow, wall of burrow, and oxidized matrix

PP1-12 = NA/PP1-11 = 8,703 ±48

PP1-10 = NA/PP1-11 = 10,197 ±71

PP1-11 = NA/PP1-11 = 3,205 ±37

Red No. for aDNA
Blue No. for ^{14}C (humin fraction)

Flakkebjerg site (HG) 2.8 m depth

Root channel, haloe, and oxidized matrix

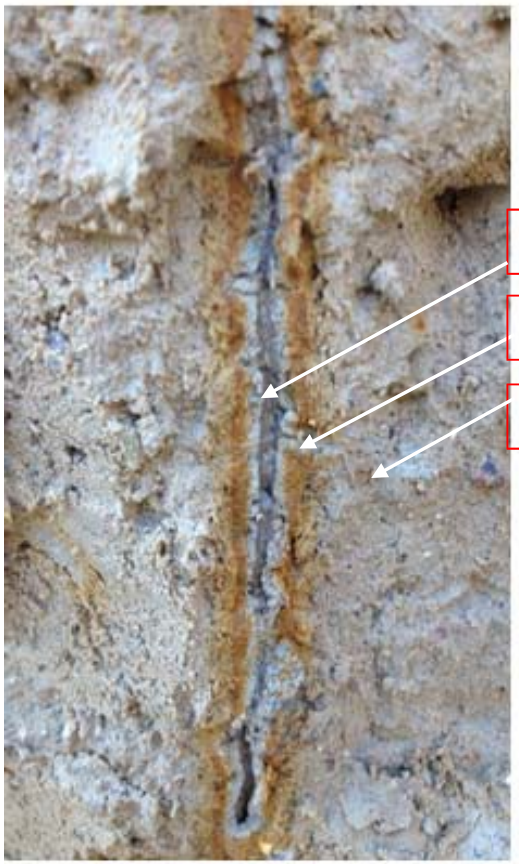

PP1-15 = NA/PP1-15 = 16,478 ±126 yr BP

PP1-17 = NA/PP1-17 = 21,097 ±163 yr BP

PP1-18 = NA/PP1-18 = 28,486 ±159 yr BP

Red No. for aDNA
Blue No. for ^{14}C (humin fraction)

Flakkebjerg site (HG) 4.5 m depth

3 Fe/Mn concretions along root-channel in reduced till

Flakkebjerg PP1-5, PP1-6.1, PP1-6.2 = ND/PP1-3, PP1-16,
= 21,342 ±96 – 25,269 ±169 yr BP/
(different samples of same root system)

Red No. for aDNA
Blue No. for ^{14}C (pyroxidation)

Flakkebjerg site (HG) 4.5 m depth Matrix of reduced till

Flakkebjerg PP1-matrix = ND/
PP1-25 = 15,304 ±34 yr BP
(samples of same root system)

Red No. for aDNA
Blue No. for ^{14}C (pyroxidation)

Appendix 4. Model testing and calibration and scenarios

Code verification

To verify the implementation of the dual-porosity model in Daisy we have modeled the following previously published results.

Jørgensen, P.R., L.D. McKay and N.H. Spliid. Evaluation of chloride and pesticide transport in a fractured clayey till using large undisturbed columns and numerical modeling. Water Resour. Res., 34 (4), 539-553. (1998a).

Jørgensen et al (1998a) made flow experiments on three large undisturbed soil columns of moraine till with varying degrees of fractures and we refer to their paper for details about the experiments and results. Here we just describe how the Daisy model was setup and compare qualitatively with their results. Jørgensen et al (1998a) modeled the results using the discrete fracture model FRACTRAN. The difference between that type of model and a dual-porosity model is that the matrix is also discretized in the direction perpendicular to the fracture as illustrated in Figure A4.1.

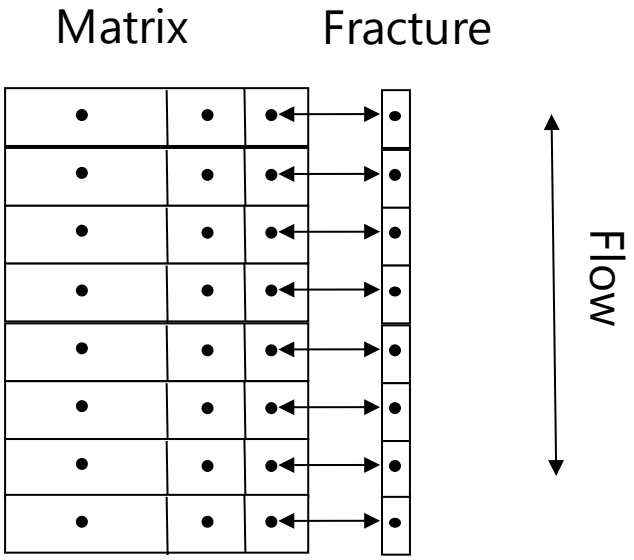

Figure A4.1 Schematic of a discrete fracture model.

Interaction between fracture and matrix is described as normal advection-dispersion, whereas Daisy uses a linear equation. In this particular case, there will be very limited advection in the matrix due to the large difference in hydraulic conductivity and the interaction will therefore be dominated by diffusion.

In Daisy the upper boundary was modeled as “subsurface irrigation” in the upper 1 cm with the measured flowrates. To eliminate ponding, it is necessary to set the “forced_flux” to 0 in the “Surface”. At the lower boundary we maintained a fixed head of 50 cm ensuring that the column would always stay saturated. During the preparation of the column, a 1 cm sand layer was added to the top and bottom. The vertical discretization was 2 cm and the maximum timestep was fixed to 10 seconds. This low timestep was necessary to avoid numerical problems at the start of the experiment for column 1. Hydraulic properties and flow rates for the three experiments are listed in Table 4.1.

Table A4.1 Hydraulic properties of the three column experiments.

Column	Matrix conductivity [m/s]	Fracture spacing* [m]	Fracture aperture [µm]	Matrix porosity	Flow rate $CaCl_2$ [m/d]	Flow rate Pesticide [m/d]
I	$5\ 10^{-10}$	0.06	84	0.32	1.04	1.52
II	$5\ 10^{-10}$	0.10	83	0.31	0.588	0.234
III	$5\ 10^{-10}$	0.16	42	0.25	0.053	0.012

*for orthogonal fractures.

Note that in their model the fractures were orthogonal where Daisy considers them to be parallel. The fracture spacing in Daisy should therefore only be half the fracture spacing in Jørgensen et al (1998a). Also, Daisy requires fracture density, which is the inverse of the fracture spacing. In Table 4.2 the fracture densities of the three setups are listed along with the simulated hydraulic gradients for the $CaCl_2$ experiments.

Table A4.2 Hydraulic properties of the three column experiments and results.

Column	Fracture density [m^{-1}]	Simulated hydraulic gradient [-]
I	32	1.1
II	20	1.1
III	12.5	1.2

In Jørgensen et al (1998a) they used a hydraulic gradient of one, which is very close to the Daisy results. Increasing the hydraulic aperture 2 µm will in all cases make it equal to 1. The small discrepancy may be explained by the temperature dependency of the water viscosity. Based on this, we conclude that the Daisy model gives the same hydraulic results as Jørgensen et al. (1998a).

In Figure A4.2 we have shown the simulated output concentration for the column 1 experiment for varying values of the mass transfer coefficient. As the coefficient increases so does the interaction between the matrix and the fracture resulting in a lower maximum outlet concentration but larger tailing. Note however that the timing is the same for the different values of the coefficient meaning that concentrations start to increase at the exact same time. Thus, the travel time is independent of the interaction with the matrix. The time delay before the concentration increasing is only a function of the flow and the porosity of the fracture.

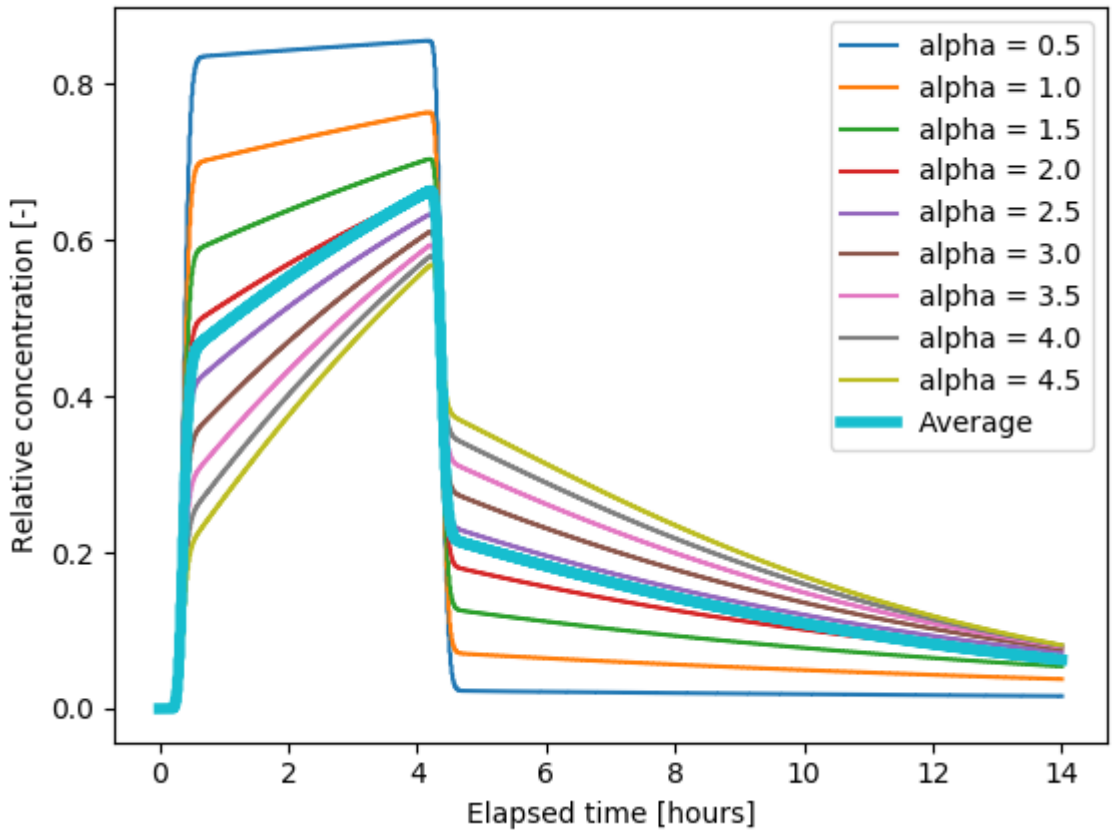

Figure A4.2 Simulated outflow for different values of the mass transfer coefficient. Column 1.

The curves in Figure A4.2 should be compared with the curves in Figure A4.3 for Column 1 with all primary fractures open where the one with the lowest alpha is closest. In fact, the alpha-values are too high to be realistic but we have included them to show the effect of the interaction. Due to the short time of the experiment, there was no significant interaction with the matrix due to diffusion.

The conceptual model in the Jørgensen et al. 1998a was that the fractures were orthogonal and in the Daisy case that the fractures where parallel. We could make an alternative conceptual model where the fractures were still parallel but with different spacing to introduce some heterogeneity. In Daisy this could simply be modelled by varying the exchange coefficient and take an average of the multiple simulations. This is shown by the thick curve labeled “Average” in Figure A4.2. We could also model the experiment by averaging simulations with different fracture apertures. This would correspond very closely to the Fractran simulations with all fractures open.

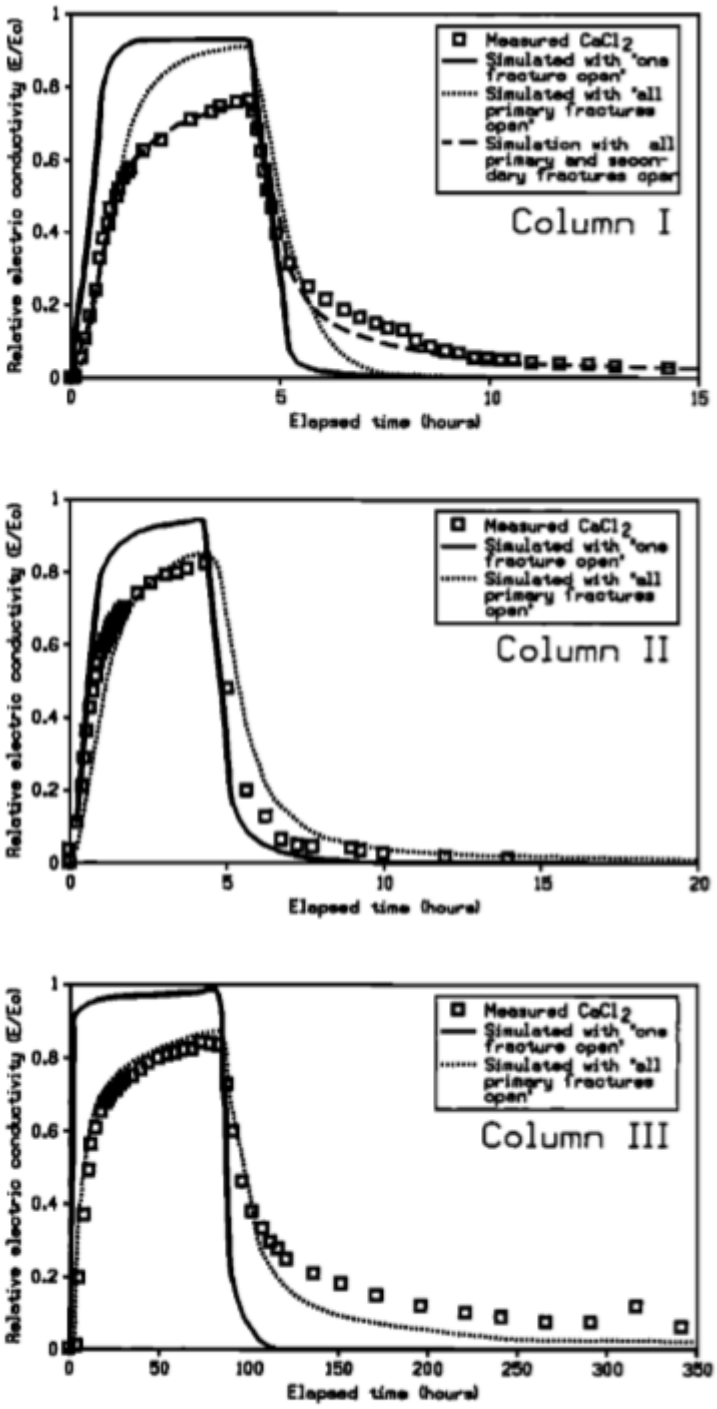

Figure 10. Simulated breakthrough of chloride compared to measured values in effluent from column experiments. Simulations are shown for the conceptual scenarios of fracture flow shown in Figure 9.

Figure A4.3 Breakthrough curves from Jørgensen et al 1998a.

For column 2 and 3 the outputs will be similar but with different values for the exchange coefficient and for column 3 also a different time scale. This is because the coefficient encompasses both the effect of fracture density and the time frame of the experiment.
To illustrate the interaction between the fracture and the matrix Figure A4.4 shows the concentrations in the two domains at four different time steps during experiment 1. After 10 minutes

the solute is approximately half-way through the soil column. Even though there is only advection in the fracture, the front is still smoothed out, which is mainly due to numerical dispersion. After 30 minutes the concentration gradient from top to bottom in the fracture and the matrix are almost linear. When the addition of solute stops the concentration gradient between the fracture and the matrix gets reversed and solute moves from the matrix to the fracture.

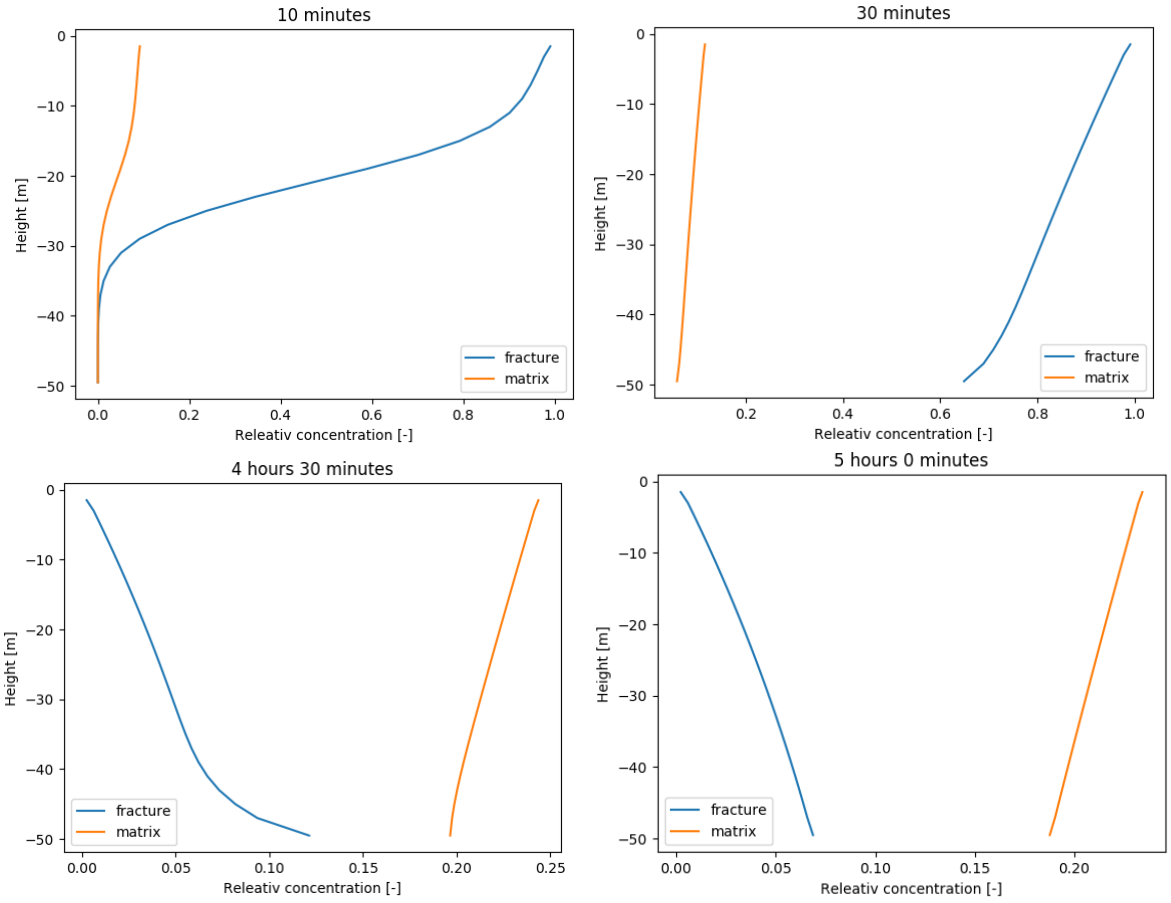

Figure A4.4. Relative concentration in the soil column at various times during experiment 1.

Figure A4.4 above illustrates the challenge with dual-porosity. The fracture interacts with the entire matrix which is not realistic in this case with very rapid flow and changes in concentration. The concentration in the matrix remains low and therefore the diffusive flux between matrix and fracture remains the same during the experiment. In reality, the fracture only interacts with a very limited part of the matrix. In Daisy it is not possible to directly set the volume of the matrix that the fracture interacts with as this is determined by the distance between the fractures. However, we can get the same effect by reducing the porosity.

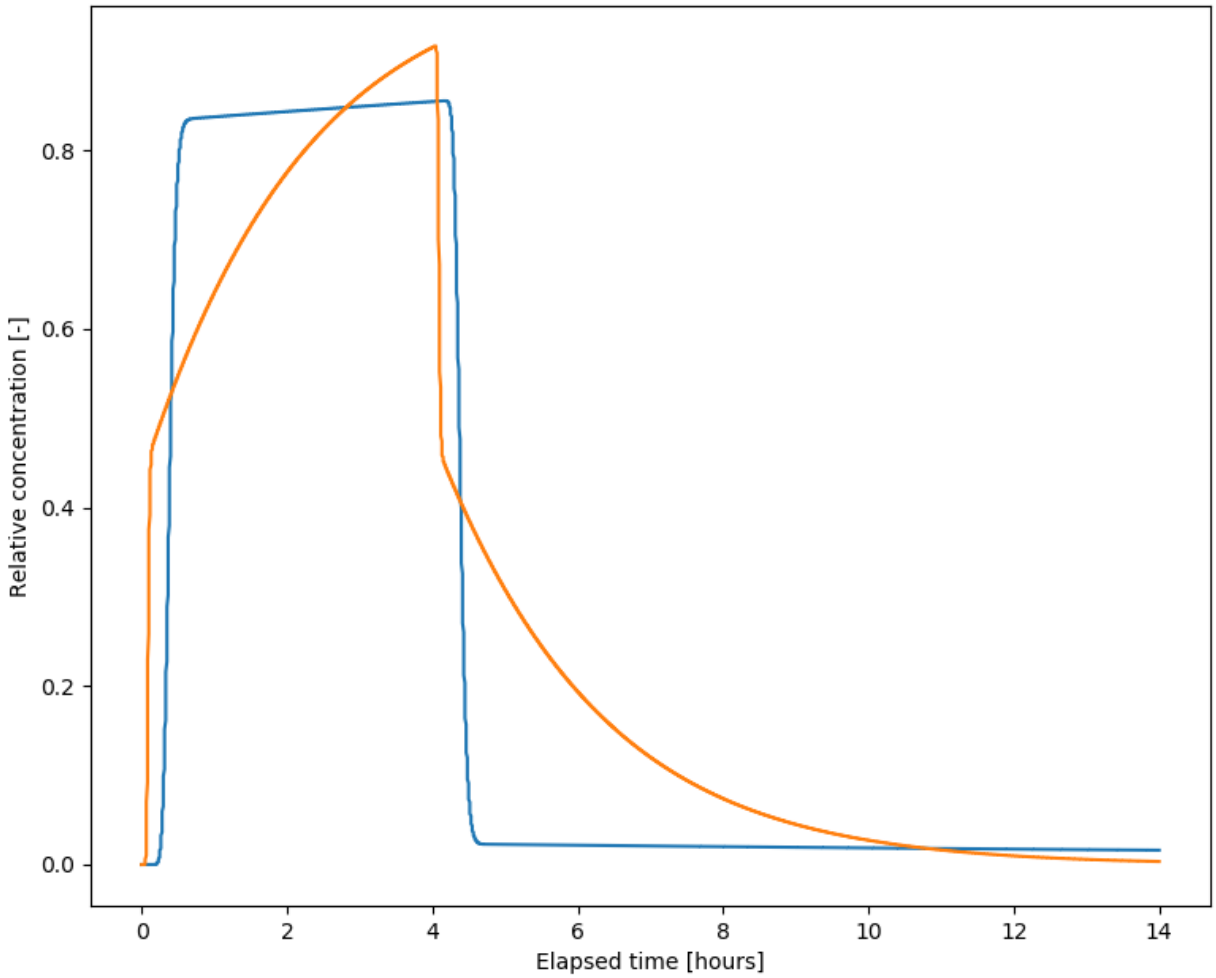

Figure A4.5. Simulated outflow for two sets of porosity and mass transfer coefficient. The blue curve uses a porosity of 0.4 and a mass transfer coefficient of 0.5. The red curve uses a porosity of 0.1 and a mass transfer coefficient of 8.5.

Figure A4.5 shows the simulated outflow when the porosity is reduced from 0.4 to 0.1. The red curve has a more rounded shape because the interaction with the matrix is gradually reduced when the concentration in the matrix increases. The shape of the red curve is also much closer to the experimental results and by adjusting both the interaction volume and the mass transfer coefficient it appears we could get an almost perfect fit. As mentioned previously, preferential flow in Daisy can also be modelled using a biopore model (Figure A4.6).

Currently, the biopores do not allow a positive pressure higher than the hydrostatic pressure. In that case there will be no flow in the biopore. This means that the biopore model cannot be directly used to model the saturated flow experiments. However, by adjusting the pressure potential at the bottom of the cell we can make sure the pressure in the top do not become positive in which case the biopore will become inactive. In this case, there is actually no interaction with the matrix and all the flow occurs through the biopore, however the curve still shows some

dispersion. This is caused by the mixing in top and bottom sand layers as well as in the bio-pore itself.

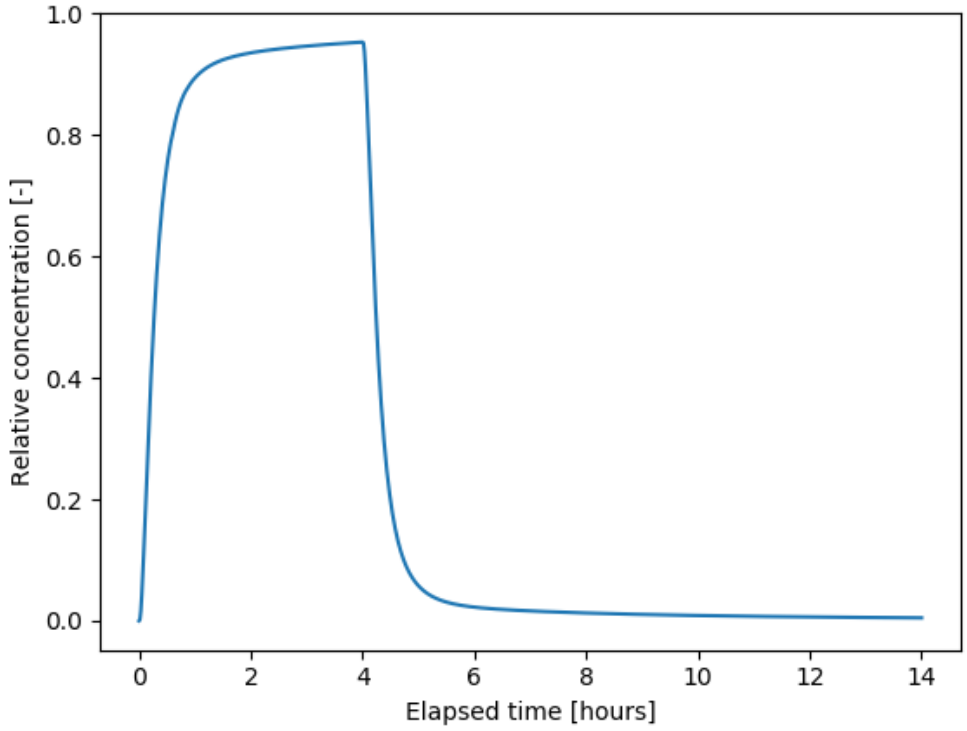

Figure A4.6 Simulated relative concentration in the outflow during experiment 1 modeled with the biopore model.

Jørgensen, P.R., Helstrup T, Urup J., Seifert D. Modeling of Non-reactive Solute-Transport in Fractured Clayey Till During Variable Flow Rate and Time. J. of Contam. Hydrol. 68, 2004, 193-216. (2004a).

In this work they made flow experiments on large undisturbed columns using the same setup as in Jørgensen et al (1998a). However, the flow rates were much lower end different flow rates were used on the same column. We have simulated the same columns with Daisy and we can get the same results as the dual-porosity models CXTFIT and Modflow. We only show results for the first column here.

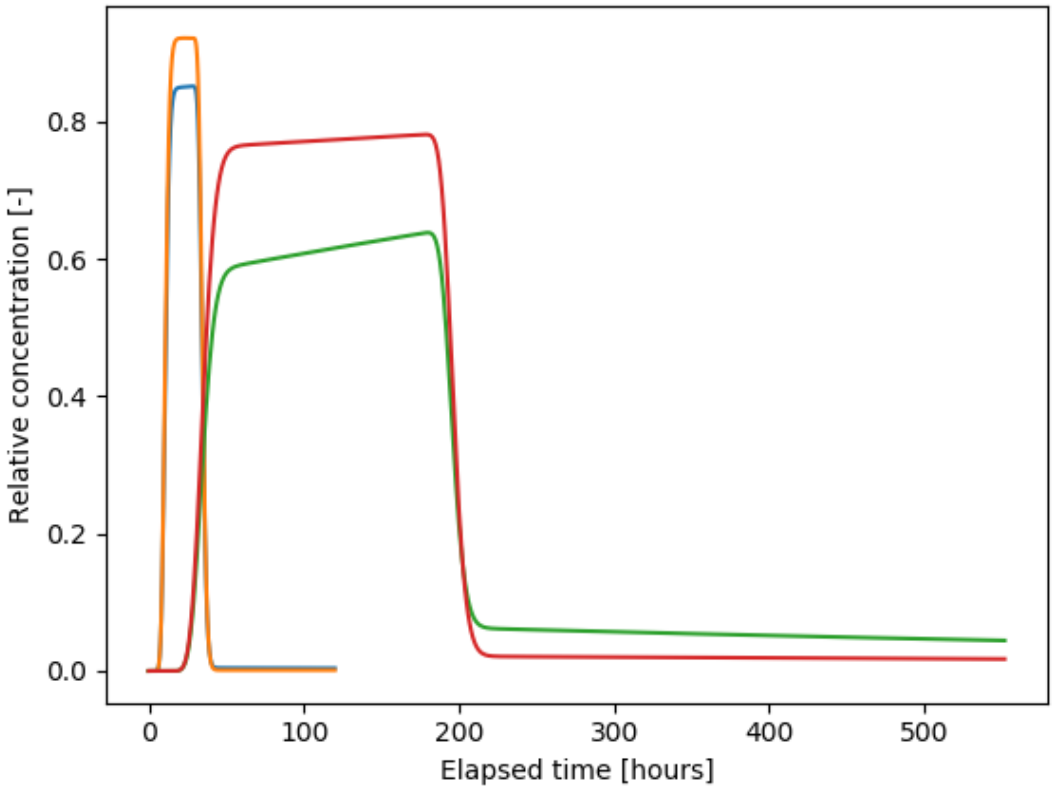

Figure A4.7. Simulated outflow concentration with Daisy of column 1 from Jørgensen et al 2004a. Orange and blue curves are 37 mm/day and red and green are the 11 mm/day experiment. Blue and green curve have a mass transfer coefficient of 0.4 h^{-1} and orange and red have a mass transfer coefficient 0.2 h^{-1}.

Figure A4.7 shows the result for column 1, which should be compared to Figure A4.8 directly from Jørgensen et al (2004a). Note that we use experimental time on the x-axis where it is out-flow-volume in Jørgensen et al. (2004a) but the results are almost exactly the same.

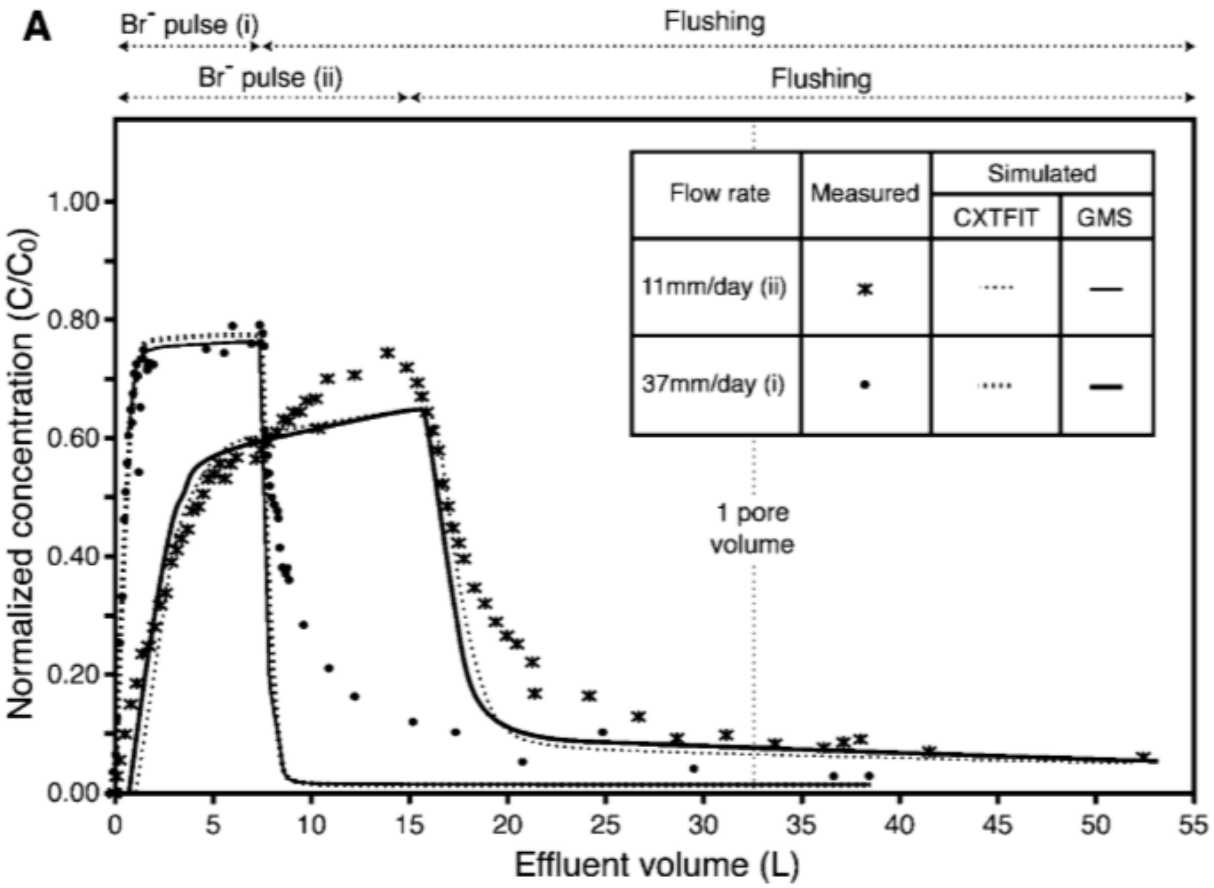

Figure A4.8. Figure 6 from Jørgensen et al (2004a) showing observed and simulated results from column 1.

In the paper they conclude that modeling the experiment results with the dual-porosity concept was unsuccessful as they got different values when they calibrated the models to experiments with different flow rates. In our Figure A4.6 we have shown two simulations for both flow rates with different mass transfer coefficient (0.2 h^{-1} and 0.4 h^{-1}) which corresponds to the two calibrated values. The difference between the curves is not very large compared to the difference between the experimental and simulated results. Based on this, the Daisy modeling disagree with the conclusion that the model cannot be used to simulate the results because different mass transfer coefficients were calibrated. It certainly appears that doing a combined calibration of the two experiments would be able to find a common mass transfer coefficient that would be able to fit the data. Still the dual-porosity models fit the shape of the data very badly when the entire matrix volume is used. In Figure A4.5 we were able to get a curve shape much closer to the experimental results when we reduced the matrix volume. A subsequent dye tracer analysis revealed that a parallel plate fracture was not a good approximation of the flow field.

Ancient Root Macropores and Fractures in Glacial till and Their Contribution to Pesticide Vulnerability of Groundwater in Low and High-ground Agricultural Landscape

Geological layers of glacial clayey till cover almost half of the utilized groundwater in Denmark. This report shows that 3 – 6 m deep root channels are abundant in the glacial till landscape and likely one of the major controls of groundwater flow and pesticide vulnerability in the tills. Most of the root channels were located as rapid flow paths inside deep Ice Age fractures in the tills. The fractures have for decades been recognized as major pesticide flow paths into the groundwater in the tills. However, in the study flow in the fractures was controlled by the root channels, while the fractures themselves were largely closed. DNA sequencing and radiocarbon analyses of root remains in the root channels reveal they originate from the native prehistoric forest that covered Denmark many thousand years ago. Therefore, similar root channels will presumably be widespread in the clayey till landscapes. The possible dominance of flow in the tills by the ancient root channels instead of fractures, have major implications for strategies to protect the underlying groundwater. This is discussed in the report.

The Danish Environmental
Protection Agency
Tolderlundsvej 5
DK - 5000 Odense C

www.mst.dk